Dynamic Analysis of Pavement-Soil System with Piezo-Sensors

A Thesis Submitted
In Partial Fulfillment of the Requirements
for the Degree of

DOCTOR OF PHILOSOPHY

by

Yakshansh Kumar
(Enrollment No. 2K20/PHDCE/502)

Under the Supervision of
Prof. A. Trivedi,
Delhi Technological University
&
Dr. Sanjay Kumar Shukla
Edith Cowan University

Department of Civil Engineering

DELHI TECHNOLOGICAL UNIVERSITY
(Formerly Delhi College of Engineering)
Shahbad Daulatpur, Main Bawana Road, Delhi-110042. India

March, 2026

Acknowledgements

I got the chance to meet many interesting people throughout my time as a Ph.D. candidate. Every interaction has provided me with invaluable insight and experience that has shaped my career and personal growth. Consequently, I am eternally grateful to everyone who has ever touched my life. I believe so many have contributed to my PhD, and it would be an injustice and unethical on my part to overlook the efforts of all the contributors.

First and foremost, I bow in deep reverence to **Lord Shiva**, the eternal source of wisdom and inner strength, whose divine grace has illuminated every step of my research journey. In moments of uncertainty, self-doubt, and exhaustion, it was my faith in him that gave me the courage to persevere and the clarity to walk the right path. I believe it is solely through his will and compassion that I was guided to the right mentors and well-wishers who shaped this journey with their presence and support.

ईशानः सर्वविद्यानां ईश्वरः सर्वभूतानाम्।

ब्रह्माधिपतिर् ब्रह्मणोऽधिपति॒ ब्रह्मा शिवो मे अस्तु सदा शिवोम्॥

(Taittiriya Aranyaka 10.21.1)

"He is the Lord of all knowledge, the ruler of all beings. He is the supreme guide of even the highest knowledge. May that Lord Shiva, the auspicious one, always bless me with divine guidance."

The pursuit of a doctorate degree is a long and winding road that often calls for the wisdom and counsel of seasoned experts. My words cannot express my gratitude and thanks to my PhD supervisors. **Prof. A. Trivedi** and **Dr. Sanjay Kumar Shukla** were an incredible privilege to have as mentors. Their polite nature and empathetic approach provided a sense of comfort and encouragement, especially during the most challenging phases of my academic journey. I could not have gotten anywhere without their selfless sharing of knowledge, fresh perspectives, and useful materials. In addition to their responsibilities as mentors, they have been like guardians, providing unwavering support and direction throughout my life. I know I will never be able to adequately repay them for all the help they have given me, but I am eternally thankful for it.

I do express my sincere gratitude to the Head of the Department **Prof. Awadhesh Kumar**, former Heads of the Department **Prof. K. C. Tiwari and Prof. V. K. Minocha**, the Chairman of the Department Research Committee (DRC), **Prof. Raju Sarkar**, and all the esteemed **faculty members and staff of the Civil Engineering Department** for their continuous support and encouragement. Their guidance, cooperation, and administrative assistance have been invaluable throughout my research journey. The conducive academic environment and prompt help from the department's faculty and staff have greatly contributed to the smooth progress and successful completion of my research work.

I would further like to express my sincere thanks to **Dr. Bharti Singh** from the Applied Physics Department and her Ph.D. scholars for their valuable assistance in the development of piezoelectric sensors. Their technical support and collaborative spirit played a vital role in shaping an important aspect of my research. I also wish to respectfully acknowledge the **Dr. Vikas Rastogi** from the Mechanical Engineering Department. His guidance in understanding finite element methods and his generosity in providing access to the ABAQUS workstation were instrumental in the computational phase of my work. His support and kindness are deeply remembered and appreciated.

I would like to sincerely thank my seniors **Dr. Bhavya Thakur**, and **Dr. Ankita Banwal** for their invaluable guidance and support during the course of my Ph.D. Their willingness to share knowledge, provide clarity on procedures, and supply essential documents for various formal requirements greatly eased many of the practical challenges I faced.

I would like to sincerely thank my juniors **Mr. Kshitij Gaur**, **Mr. Tanuj Kumar**, and **Ms. Preeti Pateriya** for their constant support and companionship throughout this journey.

I would like to warmly thank my friends **Mr. Sushil Kumar Jeenwal**, **Mr. Naresh Nautiyal**, **Mr. Naveen Tushir**, **Ms. Anshul, Mr. Ashwani Sharma**, **Mr. Sandeep Baghel**, **Mr. Abhishek Verma**, **Mr. Abhishek Saini**, **Mr. Navodit Shrivastava, and Ms. Prachi Mishra** for their friendship, camaraderie, and countless joyful moments throughout this journey. I will fondly remember the spirited volleyball and cricket, the laughter we shared.

Finally, I would like to acknowledge the inspiration and motivation that I received from my mother and father, **Mrs. Kamlesh and Mr. Ashwani Kumar**, who always encouraged me to pursue my interests and supported me at my highs and lows. I acknowledge the support of my sisters and their spouses, **Mrs. Sheetal Thakur and Dr. Tez Singh, Mrs. Pooja and Mr. Deepak,** and **Mrs. Chhaya Sailpar and Mr. Vikram Singh Mithila**. They stood by me through every challenge and triumph, providing strength when I felt weak and inspiration when I doubted myself. This achievement is as much theirs as it is mine. Words fail to express the depth of my gratitude for their presence in my life truly, they are the show stoppers of my success.

Dedicated to My Mummy and Papa

DELHI TECHNOLOGICAL UNIVERSITY
(Formerly Delhi College of Engineering)
Shahbad Daulatpur, Main Bawana Road, Delhi-42

CANDIDATE’S DECLARATION

I Yakshansh Kumar hereby certify that the work which is being presented in the thesis entitled Dynamic Analysis of Pavement-Soil System with Piezo-Sensors in partial fulfillment of the requirements for the award of the Degree of Doctor of Philosophy, submitted in the Department of Civil Engineering, Delhi Technological University is an authentic record of my own work carried out during the period from January, 2021 to March, 2026 under the supervision of Prof. A. Trivedi (DTU) and Dr. Sanjay Kumar Shukla (ECU).

The matter presented in the thesis has not been submitted by me for the award of any other degree of this or any other Institute.

Candidate’s Signature

DELHI TECHNOLOGICAL UNIVERSITY
(Formerly Delhi College of Engineering)
Shahbad Daulatpur, Main Bawana Road, Delhi-42

CERTIFICATE BY THE SUPERVISOR(s)

Certified that **Mr. Yakshansh Kumar (**enrollment no. 2K20/PHDCE/502) has carried out their search work presented in this thesis entitled **“Dynamic Analysis of Pavement-Soil System with Piezo-Sensors”** for the award of **Doctor of Philosophy** from the Department of Civil Engineering, Delhi Technological University, Delhi, under our supervision. The thesis embodies results of original work, and studies are carried out by the student himself, and the contents of the thesis do not form the basis for the award of any other degree to the candidate or to anybody else from this or any other University/Institution.

18/11/2025

(Prof. A. Trivedi)
Professor
Department of Civil Engineering
Delhi Technological University,
Delhi-42, India

(Dr. Sanjay Kumar Shukla)
Associate Professor
School of Engineering
Edith Cowan University
Joondalup Campus, Perth, Australia

Date: 18/11/2025

Abstract

The dynamic performance of pavement–soil systems under moving vehicular loads is a complex interaction of load-induced stresses, material damping, and subgrade behavior. Despite significant theoretical progress, practical implementations remain limited due to the lack of integrated modeling frameworks and sensing mechanisms that can capture in situ dynamic responses. This thesis presents a comprehensive investigation that combines finite element-based numerical simulation, experimental validation, and piezoelectric sensing to develop a generalised dynamic framework for pavement–soil systems.

A finite element model incorporating viscoelastic pavement layers over an elastoplastic subgrade was developed using Lagrangian mechanics and multi-degree-of-freedom discretization. The model introduces a Generalised Dissipation Mechanism (GDM) defined by dissipation parameters (α, β, γ) and empirical coefficients (η, ϑ) to quantify damping and amplification characteristics under moving loads. Simulations revealed a 70% increase in load and a 46% increase in displacement compared to static conditions, establishing realistic velocity-dependent amplification zones. The Vibrational Compounded Stress Transfer Mechanism (V-CSTM) was formulated to explain the nonlinear amplification and post-elastic flow behavior of geomaterials, bridging cyclic strength and fatigue responses under high-velocity traffic loads.

Experimental investigations employed flexible PVDF and PVDF–MoS_2 piezoelectric films embedded within confined geomaterials to capture electromechanical responses under vibration. The inclusion of MoS_2 nanoflakes enhanced the electroactive β-phase from 54% to 76%, producing a four-fold increase in voltage output (up to 16.2 V) and confirming superior energy-harvesting efficiency. Correlations between frequency, stress, deflection, and voltage established the films' suitability for vibration sensing and renewable energy generation.

The integrated numerical–experimental framework enables quantification of damping, stress transfer, and energy dissipation across multi-layered pavement systems. The developed piezo-sensors demonstrate strong potential for self-powered monitoring, while the coupled model offers predictive capability for deformation and damage evolution.

Overall, this research advances the understanding of dynamic pavement–soil interaction and contributes to the development of smart, sustainable, and energy-efficient infrastructure systems. The work supports Sustainable Development Goals 9 and 11 by promoting intelligent transport networks capable of real-time monitoring, reduced maintenance, and green energy harvesting.

List of publications

Publications resulting from this thesis work

Articles in international refereed journals:

- Kumar, Y., Trivedi, A. & Shukla, S.K. Impact of moving Load Vibrations on Pavement Damage Supported by Flow-Controlled Geomaterial. *Int. J. of Non-Linear Mech.* 105045, (2025). (IF-2.2) https://doi.org/10.1016/j.ijnonlinmec.2025.105045
- Kumar, Y., Trivedi, A. & Shukla, S.K. Investigating the Influence of Frequency on Piezo-dynamics of Polyvinylidene Fluoride (PVDF) Films Embedded in Confined Geomaterials. *J. Vib. Eng. Technol.* 12, 8867–8886 (2024). (IF-2.7) https://doi.org/10.1007/s42417-024-01395-z
- Kumar, Y., Trivedi, A. & Shukla, S.K. Deflections Governed by the Cyclic Strength of Rigid Pavement Subjected to Structural Vibration Due to High-Velocity Moving Loads. *J. Vib. Eng. Technol.* 12, 3543–3562 (2024). (IF-2.7) https://doi.org/10.1007/s42417-023-01063-8
- Kumar, Y., Trivedi, A. & Shukla, S.K. Damage Evaluation in Pavement-Geomaterial System Using Finite Element-Scaled Accelerated Pavement Testing. *Transp. Infrastruct. Geotech.* (2023). (IF-2.2) https://doi.org/10.1007/s40515-023-00309-y

International conferences:

- Kumar, Y., Trivedi, A. and Shukla, S. K. (2025). Evaluation of Damping and Modulus due to Dynamic Displacements in Cohesionless Subgrade Geomaterial. In ASCE International Conference on Challenges and Innovations for Sustainable Smart Cities (CISSC 2025) held during 7th – 9th February 2025 at Novotel, Chandigarh.

- Kumar, Y., Trivedi, A. and Shukla, S. K. (2024). Velocity Induced Post Elastic Response of Pavements: A Finite Element Based Statistical Investigation. In Sustainable Infrastructure: Innovations, Opportunities, and Challenges (SIIOC 2024) held during 30 April - 1 May 2024 at NITK, Surathkal. (Best Technical Paper Award)
- Kumar, Y., Trivedi, A. and Shukla, S. K. (2023). Role of Flexible Piezo-Electric Nano Generators in Pavement Geomaterial System. In International Online Conference on Basic Science for Sustainable Development (ICBSSD 2022) from December 16-17, 2022, organized by Amal Jyoti College of Engineering & Mahatma Gandhi University, Kottayam, Kerala, India & Gdansk University of Technology, Poland.
- Kumar, Y., Trivedi, A. and Shukla, S. K. (2021). Post Elastic Response of Pavement Subjected to moving load. In International Online Conference on Energy Science (ICES 2021) from December 10-12, 2021, organized by Mahatma Gandhi University, Kottayam, Kerala, India & National University of Science and Technology, Oman & Wroclaw University of Technology, Wroclaw (Best Paper Award)

Publications other than this thesis work

Articles in international refereed journals:

- Boban, A., Pateriya, P., Kumar, Y. et al. Application of machine learning technique for dynamic analysis of confined geomaterial subjected to vibratory load. AI Civ. Eng. 3, 2 (2024). https://doi.org/10.1007/s43503-024-00020-y

International conferences:

- N Boban, A., Kumar, Y. and Trivedi, A. (2023). Numerical and Experimental Investigation of a Confined Geomaterial Subjected to Vibratory Load In Sustainable Infrastructure: Innovations, Opportunities, and Challenges (SIIOC 2023) held during 20 - 21 April 2023 at NITK, Surathkal.

- Kumar, P., Kumar, Y. and Trivedi, A. (2023). “Influence of Jute-Reinforcement on the Stiffness Capacity of Cohesionless Pavement Geo-Materials” International Conference on Interdisciplinary Approaches in Civil Engineering for Sustainable Development (IACESD- 2023).

List of Tables

List of Figures

Page

List of Symbols, Abbreviations, and Nomenclature

Chapter 1: Introduction-Review of the Literature

Symbol/Abbreviation	**Description**
PVDF	Polyvinylidene fluoride
MoS_2	Molybdenum disulfide
PZT	Lead zirconate titanate
FEM	Finite Element Method
BEM	Boundary Element Method
DAF	Dynamic Amplification Factor
FWD	Falling Weight Deflectometer
APT	Accelerated Pavement Testing
LWD	Light Weight Deflectometer
LFWD	Light Falling Weight Deflectometer
IoT	Internet of Things
$[M]$	Mass matrix
$[C]$	Damping matrix
$[K]$	Stiffness matrix
$\{u\}$	Displacement vector
$\{\dot{u}\}$	Velocity vector
$\{\ddot{u}\}$	Acceleration vector
$\{F(t)\}$	Time-dependent applied force vector
GDM	Generalised Dissipation Mechanism
APA	Asphalt Pavement Analyzer

Chapter 2: Development of a Finite Element-Based Numerical Framework for Pavement–Soil System Simulation

Symbol/Abbreviation	**Description**
α, β, and γ	Non-dimensional damping parameters in the generalised dissipation mechanism (GDM)
η, ϑ	Empirical parameters used in numerical simulation for vibration damping and amplification control
ξ_n	Numerical damping ratio
FEM	Finite Element Method
GDM	Generalised Dissipation Mechanism
m	Mass matrix
c	Damper (damping) matrix
k	Stiffness matrix
a, v, and u	Vectors of acceleration, velocity, and displacement, respectively
Q_m	Moving force vector
N_n^i	Shape function for displacement approximation
Π	Non-dimensional frequency parameter
ω	Natural frequency
σ	Stress
E	Strain
ε^e and ε^p	Elastic and plastic strain components

G	Shear modulus
λ	Lame's parameter
Δt	Time increment
D_{mf}	Dynamic load magnification factor
D_{df}	Dynamic displacement magnification factor
v_r	Velocity ratio
E	Young's modulus
v	Poisson's ratio
APT	Accelerated Pavement Testing
Fs-APT	Finite Element scaled Accelerated Pavement Testing
$\Delta\varepsilon$	Total strain increment
$\Delta\varepsilon^p$	Plastic strain increment

Chapter 3: Velocity-Induced Dynamic Response of Pavement–Soil System under Moving Loads

ε_p	is accumulated permanent strain
ε_r	is rebound strain, N is loading repetition
ε_{pn}	is permanent strain after 1 loading cycle
$\varepsilon_r\ (1)$	is permanent strain after one loading cycle
f_{ck}	is the characteristic strength of pavement material
σ^{tr}	is the trial stress
G	is the shear modulus
S_r	is stress ratio

v	is the velocity of the moving load
μ, α, S, a, b, p	are empirical parameters
$[M]$	is the mass matrix
$[C]$	is the damper matrix
$[K]$	is the stiffness matrix
$\{\ddot{x}\}$	is the acceleration vector
$\{\dot{x}\}$	is the velocity vector
$\{x\}$	is the displacement vector
$\{F_E\}$	is the externally prescribed force vector
$\{Q_B\}$	is body force in terms of elemental volume
$\{Q_I\}$	is the inertial force in terms of elemental volume
$\{Q_E\}$	is the externally prescribed force in terms of elemental volume
N_i^N	is the shape function
$\vartheta_{\propto}^{I}$	are the hourglass base vectors
W_B	is the work done by body force,
W_I	is the work done by inertial force
W_E	is the work done by externally prescribed force
M_C^{NM}	are the mass matrices obtained by consistent use of interpolation
I_F^N	is the inertial force vector
Q_F^N	is the external force vector
Φ, ψ, and Γ	free parameters possessing the characteristics of damping
D	is the time-dependent damping factor (DF) matrix

Chapter 4: Dynamic Load-Induced Flow Behavior of Pavement–Soil System

Symbol/Abbreviation	**Description**
d_t, d_c	Damage variables for tensile and compressive damage, ranging from 0 (undamaged) to 1 (complete)
E_0	Initial (undamaged) Young's modulus
σ_t and σ_c	Tensile and compressive stress
p	Hydrostatic (mean) stress
q	Equivalent deviatoric stress magnitude
G	Shear modulus
λ	Lame's first parameter
f	Yield function expression
g	Plastic potential (flow function)
ψ	Dilation angle
e	Eccentricity defining shape of yield surface
R_{mw} and R_{mc}	Meridional and deviatoric radius parameters in flow potential surface
ε^{e} and ε^{p}	Elastic and plastic strain components
δ_{ij}	Kronecker delta
η	Compliance factor related to plastic strain rate
FEM	Finite Element Method
VMST	Vibrational Mechanism of Stress Transfer
K-V model	Kelvin-Voigt spring-dashpot soil model

E	Young's modulus
ν	Poisson's ratio
γ	Unit weight (kN/m³)
ϕ	Friction angle
ψ_d	Dilation angle

Chapter 5: Evaluation of Dynamic Characteristics of Foundation Geomaterial Supporting Pavement using Experimental and Numerical Approaches

Symbol / Abbreviation	**Description**
PVDF	Polyvinylidene fluoride
$[M]$	Mass matrix
$[C]$	Damping matrix
$[K]$	Stiffness matrix
$\{u\}$	Displacement vector
$\{\dot{u}\}$	Velocity vector
$\{\ddot{u}\}$	Acceleration vector
$\{F(t)\}$	Time-dependent applied force vector
$a, b, c, d,$ *and* e	Coefficients used in solving second-order non-homogeneous differential equations
FESEM	Field Emission Scanning Electron Microscopy
XRD	X-ray Diffraction Analysis
DMF	Dimethylformamide (solvent used in PVDF synthesis)

d_{11}, d_{33}	Piezoelectric constants of PVDF
FFT	Fast Fourier Transform
v	Poisson's ratio
E	Young's modulus (GPa or MPa)
C	Cohesion of geomaterial (kPa)
Φ	Angle of internal friction of geomaterial (degrees)
γ	Unit weight of geomaterial ($\mathrm{kN/m^3}$)
f_{th}	Threshold frequency for maximum voltage output

Chapter 6: Development of a Novel Piezo-Sensor for Pressure-Voltage Conversion and Energy Harvesting Applications

Symbol/Abbreviation	**Description**
PVDF	Polyvinylidene fluoride (piezoelectric polymer film)
MoS_2	Molybdenum disulfide (nanoflake doping material for PVDF composite)
PENG	Piezoelectric nanogenerator
F	Fraction of electroactive β-phase content in PVDF
V	Voltage output of PENG patches during vibration
V_{mf}	Voltage magnification factor relative to the reference PVDF patch
T	Thickness of PVDF or PVDF-MoS_2 patches (mm)
Hz	Frequency of applied vibratory load (Hertz)

XRD	X-ray diffraction analysis
Raman Spectroscopy	Technique used to characterize molecular vibrations
FE-SEM	Field Emission Scanning Electron Microscopy for imaging microstructure
FTIR	Fourier Transform Infrared Spectroscopy
Pb	Lead (toxic element in some piezoceramics)
rGO	Reduced graphene oxide (used in some composite nanogenerators)
ΔV	Voltage difference or output range
P	Power output (mW)
R	Resistance in circuit (Ohms)

CONTENTS

1

Chapter

Introduction: Review of the Literature

Highlights

- In this chapter, a review is conducted on dynamic amplification and dissipation as quantified using both numerical and sensor-based data.
- In this chapter, a review is performed on PVDF and PVDF–MoS_2 nanocomposite patches that enhance sensing accuracy and signal strength.
- This chapter presents a coupled electromechanical model linking piezoelectric voltage to stress-strain response.
- The chapter examines the frameworks that enable data-driven calibration of finite-element models.
- This chapter contributes to the review of the development of sustainable, smart, and adaptive transportation infrastructure.

1.1 General

Transportation infrastructure, including highways, railways, airfields, and bridges, forms the physical framework upon which modern economic and social systems depend. Pavements not only sustain the continual movement of people and goods but also serve as dynamic systems subjected to a wide spectrum of mechanical and environmental loads (Banister, 2012; Pradhan & Bagchi, 2013). Over the last two decades, the accelerating pace of freight transport growth and rising vehicle speeds have increased the frequency and magnitude of dynamic loading acting on pavement–

soil systems (Mallela & George, 1994; Mshali & Steyn, 2022). As a result, accurately predicting pavement responses under these dynamic conditions has become a prerequisite for sustainable design, asset management, and long-term serviceability.

Unlike static loads, which generate time-invariant stresses, dynamic loads fluctuate with both space and time. Moving-load effects induce transient stresses, resonant amplifications, and energy dissipation phenomena that traditional static design approaches cannot capture (Wu & Shen, 1996; Machemehl & Lee, 1974). When the velocity of a moving vehicle approaches the natural wave-propagation velocity of the underlying soil, the system experiences velocity resonance, a condition in which displacement and stress amplitudes increase nonlinearly (Beskou & Theodorakopoulos, 2011). For heavy-duty vehicles or high-speed trains, this amplification can reach several times the static response, accelerating fatigue and cracking within pavement layers (Kumar et al., 2024; Beskou & Muho, 2023a). These interactions are further complicated by dynamic loading and environmental influences, such as moisture fluctuations, freeze–thaw cycles, and thermal gradients, which modify the subgrade's stiffness and damping (Guo et al., 2022; Bai et al., 2020).

In transportation networks, the complexity of moving-load behaviour is accentuated by variable axle spacing, suspension properties, and tire–pavement contact dynamics (Lu & Yao, 2013; Zeng et al., 2024). Rigid pavements exhibit amplification around doweled joints or slab interfaces (Riad et al., 2009; Zhang et al., 2022), whereas flexible pavements display distributed viscoelastic damping governed by asphalt modulus and layer thickness (Yan et al., 2021, 2022; Zhu et al., 2022). At higher velocities, the dynamic deflection bowls of flexible systems deepen markedly, revealing the coupling between vehicle speed, load magnitude, and structural configuration (Mshali & Steyn, 2022; Matthews & Pandey, 1991).

Conventionally, the pavement design codes accounted only for static or quasi-static stresses, leaving a critical gap in quantifying dynamic amplification factors (DAF)**,** the ratio of dynamic to static response (Paultre et al., 1992; Han et al., 2018). Contemporary research generalises DAF as an indispensable parameter for assessing fatigue life, vibration comfort, and safety of transportation structures (Ma et al., 2024; Bozyigit & Acikgoz, 2022). Yet, accurate estimation of DAF remains challenging because of the inherent variability in soil heterogeneity, boundary damping, and vehicle–structure interactions (Lei et al., 2025; Gibigaye et al., 2016).

To address these complexities, smart sensing technologies and advanced numerical models are increasingly employed to capture transient responses under realistic moving-load scenarios (Muho & Beskou, 2024; Punetha & Nimbalkar, 2025). Among the available sensing techniques, piezoelectric sensors have emerged as powerful tools for recording strain, acceleration, and pressure within pavement layers (Qiu et al., 2025; Zeng et al., 2024). Their ability to transform mechanical stress into electrical charge with high temporal resolution allows for in-situ calibration of computational models and validation of field performance (Kumar et al., 2025). When integrated with finite-element-based dynamic analysis, piezo-sensor data enable a transition from empirical to mechanistic-empirical and eventually data-driven design frameworks (Lei et al., 2025; Guo et al., 2022).

Moreover, the pressing need for sustainable infrastructure management underscores the urgency of advancing dynamic analysis. Overdesigning pavements to compensate for unknown dynamic effects leads to excessive material use, while underestimating them results in premature failures and increased maintenance (Afshin & Behnood, 2025). Therefore, Fig. 1.1 shows the schematic representation of a pavement-soil system embedded with PVDF piezo sensors under a moving vehicle load.

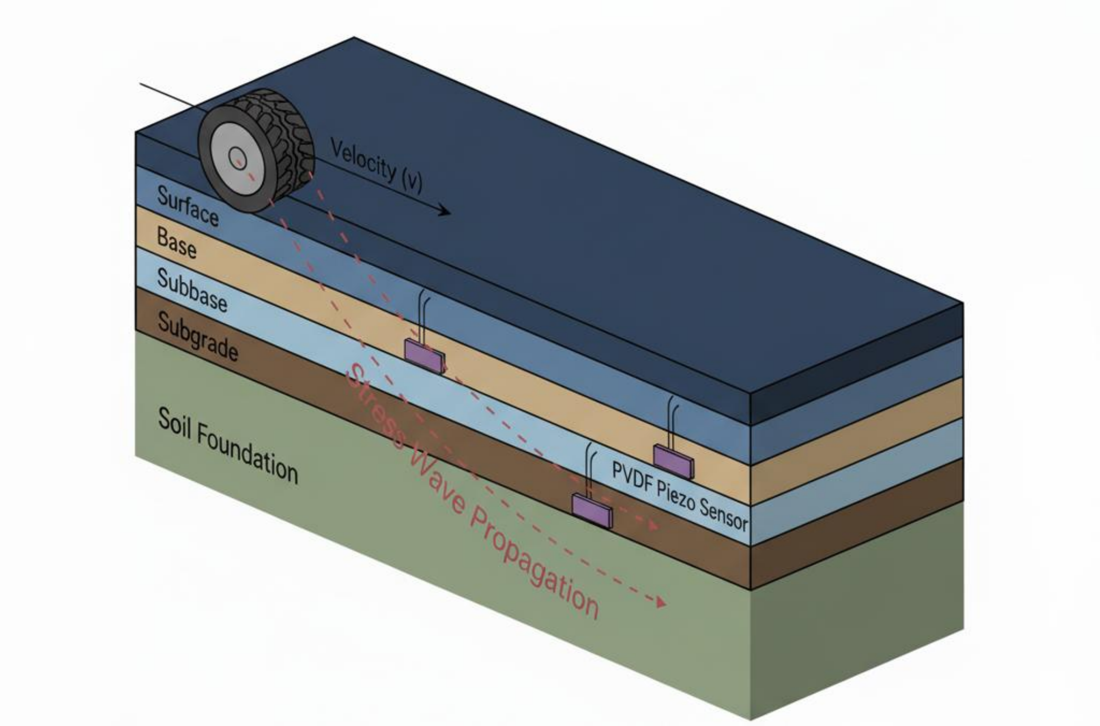

Figure 1.1 Schematic representation of a pavement-soil system embedded with PVDF piezo sensors under a moving vehicle load

1.2 Evolution of Pavement–Soil Dynamic

Understanding the mechanical behaviour of pavement–soil systems under dynamic loading has evolved through decades of theoretical, analytical, and computational advances. Early formulations, namely, the Winkler foundation model, generalise the soil as a series of independent springs reacting linearly to surface loads (Hetényi, 1946). Although conceptually simple, the Winkler model neglected shear interaction within the subgrade, resulting in unrealistic discontinuities at load boundaries (Timoshenko & Goodier, 1970). To overcome these shortcomings, the Pasternak and

Vlasov foundations introduced shear-layer coupling and continuity, representing the soil as an elastic continuum (Selvadurai, 1979).

The mid-twentieth century witnessed a significant expansion of analytical models that incorporated viscoelastic behavior and frequency-dependent damping. Barkan (1962) proposed vibration solutions for rail and road foundations, and the importance of damping ratios for wave-propagation analysis. Later, Richart et al. (1970) provided foundational correlations between dynamic modulus, Poisson’s ratio, and cyclic shear strain, paving the way for modern dynamic soil dynamics.

The numerical computation, namely finite-element (FEM) and boundary-element (BEM) formulations, replaced classical elasticity solutions. One of the early attempts was made by Duncan & Chang (1970), who introduced nonlinear stress–strain relationships for soil under repeated loads. Meanwhile, Zienkiewicz et al. (1971) formalized dynamic finite-element procedures capable of handling transient vibrations. These techniques were later refined through viscoelastic and coupled formulations.

Contemporary research integrates continuum mechanics, rheological modelling, and high-speed computation. Beskou & Theodorakopoulos (2011) examined the response of a layered elastic half-space under moving loads using frequency-domain FEM, demonstrating the influence of vehicle speed on displacement amplification. Their later works extended this approach to non-linear soil constitutive laws and damping calibration (Beskou & Muho, 2023a; Muho & Beskou, 2024).

Experimental validation has remained essential throughout this evolution. Falling-Weight Deflectometer (FWD) and Accelerated Pavement Testing (APT) facilities provide benchmark results for verifying dynamic simulations. These results have supported the development of damping and modulus models that align computational predictions with field responses (Crawford & Katona, 1975). The increasing availability of high-resolution sensors now allows direct measurement of transient strain and acceleration within pavement layers (Qiu et al., 2025).

Numerical schemes combine microscale aggregate–binder mechanics with macroscale continuum representations to evaluate energy dissipation and permanent deformation (Yan et al., 2021; Zhu et al., 2022). This hybridization of analytical and computational approaches bridges the gap between simplified theory and the actual behavior of geomaterials under complex, moving loads (Fig. 1.2).

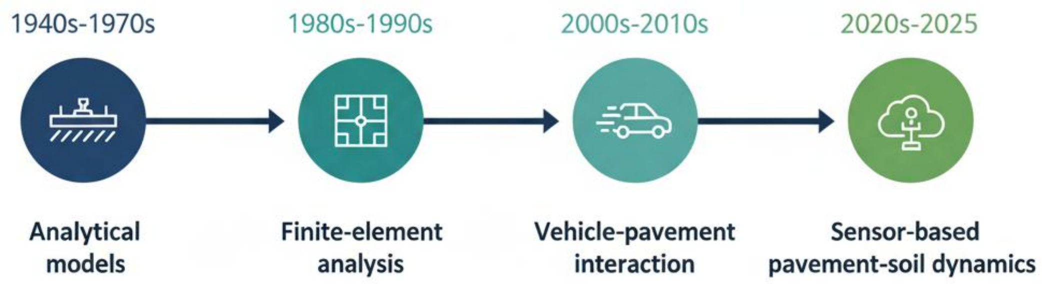

Figure 1.2 Historical evolution of pavement dynamic analysis methodologies

1.3 Piezoelectric Sensing and Smart Pavement Systems

The introduction of smart materials and embedded sensing technologies has transformed the monitoring and diagnosis of pavement–soil systems. Among these technologies, piezoelectric sensors have emerged as the most versatile for capturing dynamic responses due to their high sensitivity, compact geometry, and ability to directly convert mechanical stress into an electrical voltage (Kumar et al., 2024; Qiu et al., 2025). When integrated within pavement layers, piezoelectric transducers can simultaneously record stress, strain, vibration, and temperature, enabling near-real-time evaluation of structural health (Afshin & Behnood, 2025; Mshali & Steyn, 2022).

Polyvinylidene fluoride (PVDF) films and their nanocomposite derivatives have become particularly attractive for such applications because of their mechanical flexibility, chemical resistance, and strong piezoelectric coupling (Kumar et al., 2025; Zhang et al., 2022). Modified PVDF films doped with molybdenum disulfide (MoS_2) nanoparticles exhibit an enhanced β-phase content, resulting in improved sensitivity to micro-strain (Kumar et al., 2025). These composite sensors have been shown to outperform traditional lead-zirconate-titanate (PZT) disks, which are brittle and prone to failure under cyclic traffic loads (Qiu et al., 2025).

Early experimental studies demonstrated that surface-mounted and embedded piezoelectric patches can accurately capture deflection basins and dynamic pressure under moving loads (Guo et al., 2022). Later work extended these experiments to multi-layer configurations, enabling the correlation of voltage outputs with local stiffness variations and fatigue accumulation (Yan et al., 2021, 2022). Recent developments in signal processing, including wavelet transforms and artificial-intelligence-based filtering, have enhanced the interpretation of raw piezoelectric data and facilitated direct comparison with numerical predictions (Beskou & Muho, 2023a; Lei et al., 2025).

Beyond monitoring, piezoelectric materials are now explored for energy harvesting in roadways and rail tracks. The high frequency of vehicle passages can be converted into electrical energy capable of powering roadside sensors or communication devices (Bozyigit & Acikgoz, 2022). Such dual functionality—sensing and energy generation—supports the transition toward self-powered smart pavements (Zeng et al., 2024). The integration of piezoelectric systems with the Internet of Things (IoT) and wireless data acquisition units further enables the distributed monitoring of traffic loading and structural performance (Punetha & Nimbalkar, 2025).

The real strength of piezoelectric sensors lies in its compatibility with computational simulation. When calibrated using both laboratory and field data, voltage-to-stress conversion algorithms enable a direct comparison between sensor output and finite-element predictions (Kumar et al., 2025; Muho & Beskou, 2024). This synergy accelerates the validation of theoretical models and enhances confidence in dynamic analyses of pavement–soil systems (Fig. 1.3).

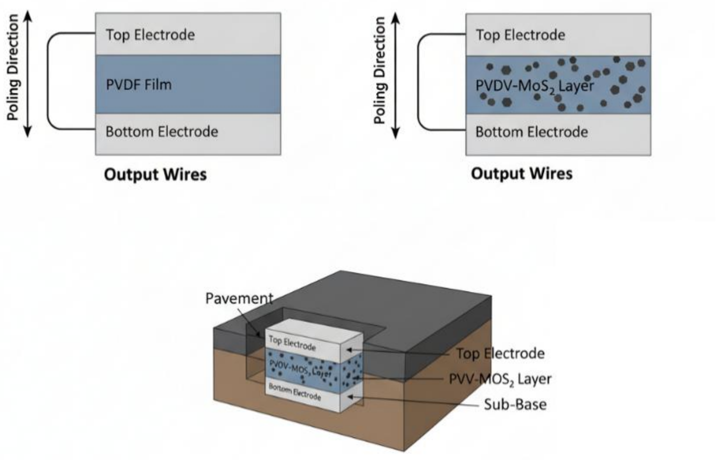

Figure 1.3 PVDF and PVDF–MoS$_2$ piezoelectric sensor likely configurations in the pavement soil system

1.4 Need for Integrated Dynamic Analysis

Despite considerable progress in both modelling and sensing, the accurate prediction of pavement response under moving loads remains a formidable challenge. Many design methodologies continue to rely on simplified static equivalence or linear-elastic assumptions, which cannot fully capture transient wave propagation, boundary damping, and nonlinearity in geomaterials (Han et al., 2018; Lei et al., 2025). The absence of a unified framework capable of coupling vehicle dynamics, pavement structural behaviour, and sensor feedback limits the predictive power of current design tools.

Finite-element simulations often demand high computational cost and depend heavily on constitutive parameters that are difficult to measure in situ (Afshin & Behnood, 2025). Conversely, experimental measurements using FWD, strain gauges, or accelerometers may be affected by noise, drift, or local heterogeneity (Zhang et al., 2022). Bridging this gap requires a hybrid approach wherein sensor data continuously inform and calibrate numerical models, yielding adaptive simulations capable of reflecting actual field conditions (Muho & Beskou, 2024; Qiu et al., 2025).

An integrated dynamic analysis must therefore consider:

- Velocity-induced resonance and its amplification effects on pavement responses;
- Material damping and energy dissipation characteristics of asphalt and subgrade;
- Geometric and boundary effects, including layered heterogeneity and interface stiffness; and
- Sensor feedback coupling, enabling model correction through real-time data assimilation.

Such a framework can reproduce not only the mechanical response but also the electromechanical coupling that occurs when piezoelectric sensors are embedded within the structure (Kumar et al., 2025). It thereby provides a holistic representation of the pavement–soil system as an interactive, dynamic, and intelligent entity.

The integration of sensing, modelling, and control aligns with the broader vision of smart and sustainable infrastructure promoted by modern transportation agencies.

Data-driven numerical models calibrated by embedded sensors can guide maintenance scheduling, energy harvesting, and even traffic management through predictive analytics (Punetha & Nimbalkar, 2025; Mshali & Steyn, 2022). The outcome is not merely improved accuracy in stress–strain estimation but also an evolution toward adaptive pavements that learn from operational data and adjust to changing conditions.

1.5 Advanced Modelling and Experimental Validation

Advances in modelling techniques now permit the simultaneous consideration of nonlinear material behaviour, moving-load kinematics, and sensor-based response. Finite-element formulations employ incremental–iterative solvers that can capture plastic shakedown, damping hysteresis, and progressive damage accumulation in the pavement–soil continuum (Beskou & Muho, 2023a). The governing equations are expressed in matrix form, where the global dynamic equilibrium equation balances inertia, damping, and stiffness forces under time-varying loading (Zienkiewicz et al., 1971).

$$[M]\{\ddot{u}\} + [C]\{\dot{u}\} + [K]\{u\} = \{F(t)\} \tag{1.1}$$

Here, the damping matrix $[C]$is frequently derived through Rayleigh proportionality, linking it to the system's stiffness and mass matrices to approximate viscous energy dissipation (Lei et al., 2025).

For granular and cohesive subgrades, nonlinear stress–strain relationships based on the hyperbolic model of Duncan and Chang (1970) or pressure-dependent yield surfaces (e.g., Mohr–Coulomb, Drucker–Prager) are commonly employed (Afshin & Behnood, 2025). These improvements enable numerical solvers to reproduce the cyclic degradation and recovery behaviour observed in repeated-load triaxial tests (Yan et al., 2021; Zhu et al., 2022).

A distinguishing feature of recent research is the experimental calibration and validation of these numerical frameworks. Laboratory-scale test sections instrumented with PVDF or PVDF–MoS_2 patches provide voltage–time histories that can be directly transformed into stress or strain records (Kumar et al., 2025; Qiu et al., 2025). By matching the simulated and measured peak amplitudes, damping ratios, and phase shifts, researchers can tune soil and asphalt moduli until convergence is achieved (Muho & Beskou, 2024). Field verification using FWD or moving-wheel simulators further bridges the gap between controlled laboratory conditions and real-traffic behaviour (Crawford & Katona, 1975).

Parallel developments in signal processing and machine learning aid in extracting meaningful parameters from complex sensor data. Algorithms employing fast Fourier transforms, Hilbert–Huang decomposition, or convolutional neural networks identify dominant vibration modes and evolving damage signatures (Lei et al., 2025; Punetha & Nimbalkar, 2025). This data-driven refinement reduces dependence on empirical calibration and allows adaptive updating of FEM parameters as new measurements arrive—an approach consistent with digital-twin philosophies in structural engineering (Bai et al., 2020; Bozyigit & Acikgoz, 2022).

1.6 Significance of the Present Study

The increasing demand for high-speed, heavy-traffic transportation networks necessitates an improved understanding of the dynamic behaviour of pavement–soil systems. The significance of the present study lies in developing an integrated approach that unites numerical modelling, experimental verification, and piezoelectric sensing to quantify the transient vibration and dissipation characteristics of layered pavement systems (Kumar et al., 2024; Muho & Beskou, 2024).

From a scientific perspective, this research extends the current state of knowledge by linking electromechanical sensing outputs to mechanical field variables, thereby offering a more precise interpretation of the energy-dissipation mechanisms within geomaterials (Afshin & Behnood, 2025; Lei et al., 2025). The correlation between voltage signals and stress–strain parameters enable the creation of transfer functions that translate electrical measurements into engineering quantities. Such correlations have previously been established in limited laboratory contexts; however, their extension to full-scale dynamic simulations remains novel (Kumar et al., 2025; Qiu et al., 2025).

From an engineering standpoint, the study responds to pressing infrastructure challenges: premature cracking, rutting, and differential settlement of pavements subjected to repeated traffic loads. Incorporating dynamic effects into design can improve fatigue prediction, enhance service life, and reduce maintenance costs (Hanet al., 2018; Mshali & Steyn, 2022). Embedding piezoelectric sensors allows for condition-based maintenance rather than schedule-based intervention, aligning with modern asset management philosophies (Zeng et al., 2024).

The societal and environmental relevance of the work is also considerable. By preventing overdesign and facilitating timely rehabilitation, the approach generalises material wastage and energy consumption, supporting sustainability goals embedded in global transportation policies (Bozyigit & Acikgoz, 2022; Punetha & Nimbalkar, 2025). Moreover, the dual-use capability of piezoelectric sensors for both energy harvesting and structural monitoring provides opportunities for self-powered smart pavements, reducing dependency on external power sources (Zhang et al., 2022; Kumar et al., 2025).

1.7 Literature Review

The literature review performed to conduct the presented research is shown in Tables 1.1 and 1.2.

Table 1.1 Literature Review (Part 1): Analytical & Numerical studies

Methodology and Focus	System Studied	Key Findings and Contributions
Analytical review of moving-load effects on pavements	[a]Layered pavement systems	Comprehensive synthesis of resonance and velocity effects on pavement response under moving loads. Emphasised the need for layered formulations.
3D analytical/numerical modelling of concrete pavements with moving loads	[b]Rigid concrete pavements	Early three-dimensional treatment demonstrating dynamic stress distribution and importance of 3D effects.
Time integration and numerical dissipation methods (Hilber–Hughes–Taylor)	[c]Numerical algorithms for dynamics	Introduced improved numerical dissipation for time integration to reduce spurious high-frequency noise.
Analytical and FEM solutions for plates under moving loads	[d]Plates and slabs on elastic foundations	Presented finite-element transient solutions and structural impedance methods for moving loads.
Early amplification factor formulations for moving loads	[e]Beam/plate models	Classic empirical/analytical amplification relations used as baseline cases.
Timoshenko beam theory handbooks & beam models	[f]Beam models for pavement dynamics	Compendium of beam and plate theories (Timoshenko) relevant to dynamic pavement modelling.
Vibration analysis of 3D Timoshenko beams under moving vehicles	[g]Beam models with moving mass	Showed importance of shear and rotary inertia for dynamic response at higher speeds.
Vehicle–pavement coupled vibration using Timoshenko beam on nonlinear foundation	[h]Coupled vehicle–pavement systems	Demonstrated coupling effects and role of foundation nonlinearity on dynamic amplification.
Moving harmonic rectangular load on unsaturated half-space (Fourier method)	[i]Unsaturated half-space soils	Presented FT-based solutions showing displacement/stress variation with saturation/permeability.
Vehicle–road dynamic interaction effects	[j]Pavement vibration due to traffic	Demonstrated how vehicle dynamics and road roughness amplify pavement vibration.

Recent reviews: rigid and flexible pavements under moving vehicles	[k]Rigid & flexible pavements	Synthesised modern insights into moving-load responses differentiated by pavement type; highlighted research gaps.
Finite-element dynamic solutions for plates	[l]Plate dynamic FEM	FEM methodology to obtain transient plate responses to moving loads; numerical validation.
3D FE effects of vehicle dynamic loading on continuously reinforced concrete pavement (CRCP)	[m]CRCP systems	Explored dynamic loading effects and need for 3D FE to capture real stress fields.
Parallel FEM implementation for moving load beam problems	[n]Parallel/numerical computation	Addressed computational performance for moving load FEM problems.
Kalman filtering for pavement profile estimation from passing vehicles	[o]Vehicle–pavement sensing & estimation	Showed data assimilation techniques for extracting pavement properties from vehicle responses.
Dynamic pavement response under moving truck loads with random amplitudes	[p]Stochastic dynamic loading	Investigated effects of random amplitude variations on pavement response.
Viscoelastic/viscoplastic FE models for rutting and anti-rutting strategies	[q]Asphalt pavements under repeated loads	Demonstrated viscoplastic modelling for rutting prediction and design implications.
Series: FE-scaled APT, deflections & damage, moving-load impact on flow-controlled geomaterials	[r]Pavement–geomaterial systems with piezo/sensor integration	Developed FE-scaled APT methodology, generalised numerical damping (GDM), and amplification frameworks; calibrated with experiments.
Vehicle–pavement dynamic interaction and vehicle dynamics overview	[s]Vehicle–pavement systems	Provided modelling strategies and reduced symmetric FE modelling arguments to save computation.

[a]Beskou & Theodorakopoulos (2011); [b]Wu & Shen (1996); [c]Hilber et al. (1977); [d]Taheri & Ting (1989, 1990);[e]Yoshida & Weaver (1971); [f]Elishakoff (2020); [g]Ju (2011); [h]Ding et al. (2014); [i]Lu et al. (2018); [j]Lu & Yao (2013); [k]Beskou & Muho (2023a, 2023b); [l]Taheri & Ting (1990); [m]Wang & Yang (2008); [n]Froio et al. (2021); [o]He & Yang (2021); [p]Zhao & Wang (2020); [q]Cao et al. (2012); [r]Kumar et al. (2024a, 2024b, 2025); [s]Yang et al. (2010, 2013)

Table 1.2 Literature Review (Part 2): Experimental and Standard Reviews

Methodology and Focus	System Studied	Key Findings and Contributions

Full-scale Accelerated Pavement Testing (APT) overview	[a]Full-scale APT facilities	Summarised the APT methodology and benefits for performance evaluation.
APT in highway engineering review	[b]APT practice and interpretation	Discussed APT applications and interpretation challenges for pavement performance.
HVS APT efforts and findings	[c]Heavy Vehicle Simulator APT	Showed the value of HVS in reproducing long-term traffic damage faster.
Fs-APT experimental facility and path (CSIR-CRRI)	[d]Finite-scale APT tests	Provided experimental rutting and deflection data used for numerical mapping.
Inverted pavement structure APT evaluation	[e]Inverted pavements	Demonstrated APT utility for alternative pavement structures.
Rutting prediction — lab to APT numerical modelling	[f]Asphalt pavement rutting	Bridged lab tests and APT for rutting prediction using numerical models.
Lab APT: bamboo/jute geocell overlay behaviour	[g]Geocell overlays on soft subgrade	Documented cyclic response and reinforcement benefits under repeated loads.
LWD measurement comparison	[h]Pavement foundation materials	Compared LWD results and recommended practices for field characterization.
LWD quality control review	[i]Compaction & LWD use	Reviewed LWD as a QC tool; discussed limitations and procedures.
FWD and pervious concrete pavements	[j]Pervious pavement structural response	Applied FWD for structural evaluation; discussed interpretation nuances.
Enhancing FWD testing procedures review	[k]FWD testing practices	Proposed robust FWD procedures and improvements.
LFWD on geosynthetic bases	[l]Aggregate layers on geosynthetics	Demonstrated LFWD applicability for thin layer stiffness assessment.
Correlative study: LWD, plate loading, CBR (GA)	[m]Unbound pavement layers	Used GA to correlate different site tests for robust assessment.
FWD relationships for recycled/virgin aggregate bases	[n]Field FWD & nonlinear parameter correlation	Related FWD deflections to nonlinear parameters for field mix evaluation.
FWD characterization of composite pavements	[o]Composite pavements & FWD	Characterised composite pavement responses and recommended analysis methods.
FE applications using ABAQUS	[p]FE method application examples	Provided practical guidance for ABAQUS modelling and applications.

FE-scaled APT: damage evaluation	[r]Pavement–geomaterial systems	Developed FE-APT methodology and calibration against APT/field results.
Deflections & cyclic strength for rigid pavement	[s]Rigid pavement under high-velocity loads	Quantified deflection governance by cyclic strength; velocity influence.
Moving-load vibrations & flow-controlled geomaterials	[t]Pavement damage with flow control geomaterials	Demonstrated moving-load vibration impacts and flow-controlled material behaviours.
ML for dynamic analysis of confined geomaterial	[u]Confined geomaterials under vibratory load	Applied machine learning to predict confined geomaterial responses.
Numerical & experimental confined geomaterial study	[v]Vibratory loading on confined geomaterial	Combined lab experiments and numerical models for confined geomaterials.
Performance prediction models for asphalt	[w]Asphalt binder & mix performance	Provided empirical relationships and performance prediction frameworks.
Rutting change-rule analysis	[x]Asphalt pavement overlay rutting	Studied rutting progression and provided change-rule insights.
Elastic–viscoplastic models & APA comparisons	[y]APA lab vs numerical predictions	Related lab APA tests to numerical viscoplastic models for rutting.
3D FE viscoelastic–viscoplastic analysis for rutting	[z]Road surfaces under moving load	Examined viscoplastic behaviour and rutting mitigation strategies.
Anti-rutting performance tests for big-interspaced asphalt	[aa]Asphalt mixtures with rubber content	Studied anti-rutting performance under repeated load tests.
Rutting analysis on overlays (APA)	[ab]Rutting evolution studies	Correlated rutting depth with load cycles and temperature.
Vibroacoustic analysis & attached mass-spring-damper effects	[ac]Asphalt pavements with vehicle dynamics	Analysed added mass-spring-damper systems effect on pavement vibroacoustics.
Dynamic responses of unsaturated multilayer road systems	[ad]Multi-layer unsaturated pavement systems	Highlighted unsaturated soil effects with impermeable pavements under moving vibratory loads.
Dowel joint mechanical behaviour review	[ae]Dowelled concrete pavements	Reviewed dowel behaviour and their role in localized amplification.
Unsaturated half-space dynamic analysis (FT method)	[af]Unsaturated soils under moving harmonic loads	Showed displacement/stress sensitivity to saturation and permeability.
Structural behaviour of asphalt pavements	[ag]Integrated asphalt pavement analysis	Comprehensive treatment of asphalt pavement structural response.

Asphalt pavements handbook (editor)	[ah]Asphalt pavement fundamentals	Source for practical pavement material and design parameters.
Plate transient solutions & structural impedance	[ai]Plates under moving loads	Demonstrated transient solution strategies for moving loads.

[a]Metcalf (1996); [b]Brown (2004); [c]Du Plessis et al. (2018); [d]Khan et al. (2016); [e]Jiang et al. (2022); [f]Liu et al. (2023); [g]Biswas et al. (2024); [h]Vennapusa & White (2009); [i]Duddu & Chennarapu (2022); [j]Suleiman et al. (2011); [k]Pandya et al. (2024); [l]Sulewska & Bartnik (2017); [m]Khaksar et al. (2025); [n]Zulfiqar et al. (2025); [o]Zhang et al. (2025); [p]Zhuang et al. (2009); [r]Kumar et al. (2024a); [s]Kumar et al. (2024b); [t]Kumar et al. (2025); [u]Boban et al. (2024); [v]Boban et al. (2023); [w]Lytton et al. (1993); [x]Yao et al. (2012); [y]Pirabarooban et al. (2003); [z]Cao et al. (2012); [aa]Imanninasab et al. (2016); [ab]Yao, Zhou et al. (2012); [ac]Zeng et al. (2024); [ad]Qiu et al. (2025); [ae]Zhang et al. (2022); [af]Lu et al. (2018); [ag]Sun (2016); [ah]Kim (2014); [ai]Taheri & Ting (1989)

1.8 Research Gaps Identified from the Review of Literature

The following are the research gaps identified from the literature as listed below:

I. The available studies consider only linear behaviour and deformations in pavements, and only a few are characterized by nonlinear behaviour, corresponding to more realistic cases for the problem.

I. Available literature on pavement dynamics is mainly theoretical and lacks calibration based on field experiments on the problem.

II. The available studies lack flow control characteristics with fatigue and permanent deformation features for the problem.

III. Further efforts are required in the direction of dynamic pavement-soil interaction philosophies and successful implementation in the field.

IV. The literature prevails the complexity and difficulty in the use of the numerical approach for field engineers and practitioners.

1.9 Research Objectives

To address the research gaps, the entire work in the present thesis is divided into seven chapters based on the following objectives listed below:

(a) To develop an efficient numerical program for the simulation of the pavement-soil system using FEM.

(b) To examine the velocity-induced load-displacement response and amplification characteristics of the pavement-soil system subjected to a concentrated-distributed load with varied velocity.

(c) To investigate the flow characteristics of pavement-soil systems subjected to dynamic load.

(d) To examine the dynamic response of foundation geomaterial supporting the pavement using piezo-sensors and numerical simulations.

(e) To develop a novel piezo-sensor using voltage output into pressure, providing a more effective basis for energy harvesting and deformation measuring instruments.

1.10 Organisation of the Thesis

This thesis is organized into seven chapters to accommodate all the research objectives.

Chapter 1.	Introduction: Review of literature
Chapter 2.	Development of a Numerical Framework for Pavement–Soil System Simulations
Chapter 3.	Velocity-Induced Dynamic Response of Pavement–Soil System
Chapter 4.	Dynamic Load-Induced Flow Behavior of Pavement–Soil System
Chapter 5.	Dynamic Load-Induced Flow Characterization of Pavement–Soil System
Chapter 6.	Development of a Novel Piezo-Sensor for Sensing and Energy Harvesting Applications
Chapter 7.	Conclusions, Future Scope, and Social Impact

1.11 Conclusions

The present thesis establishes a holistic framework for dynamic analysis of pavement–soil systems with embedded piezo-sensors. It generalises the interplay between moving-load dynamics, geomaterial behaviour, and sensor-based feedback mechanisms, bridging theoretical, numerical, and experimental domains. The conceptual model represents the pavement as a multi-layered viscoelastic system resting on a semi-infinite subgrade, excited by distributed moving loads. Piezoelectric patches, placed at strategic interfaces, transduce mechanical deformation into electrical voltage, creating a coupled electromechanical field that serves as both a diagnostic and analytical tool.

The workflow proposed herein involves three major modules:

1. Formulation of governing equations through the Lagrangian method and finite-element modelling for multi-degree-of-freedom systems.
2. Use of PVDF and PVDF–MoS_2 piezoelectric patches to record dynamic responses and calibrate model parameters.
3. Post-processing of sensor signals and FEM outputs to derive energy-dissipation and amplification indices.

This integrated approach allows systematic evaluation of velocity-dependent response amplification, damping distribution, and energy-dissipation mechanisms within the pavement–soil system. It directly supports the thesis aim of developing generalised parameters that capture vibration dissipation and dynamic amplification across different pavement configurations.

References

1. Bai, W., Mu, K., Kong, L., Zhang, W., & Yue, X. (2020). Dynamic response and its frequency domain characteristics of lateritic soil subgrade under traffic load during construction. Advances in Civil Engineering, 2020(1), 8899482. https://doi.org/10.1155/2020/8899482

2. Banister, D. (2012). Transport and economic development: reviewing the evidence. Transport Reviews, 32(1), 1-2. https://doi.org/10.1080/01441647.2011.603283
3. Barkan, D. D. (1962). Dynamics of Bases and Foundations. McGraw-Hill.
4. Beskou, N. D., & Muho, E. V. (2023a). Review on dynamic response of road pavements to moving vehicle loads; part 1: Rigid pavements. Soil Dynamics and Earthquake Engineering, 175, 108249. https://doi.org/10.1016/j.soildyn.2023.108249
5. Beskou, N. D., & Muho, E. V. (2023b). Review on dynamic response of road pavements to moving vehicle loads; part 2: Flexible pavements. Soil Dynamics and Earthquake Engineering, 175, 108248. https://doi.org/10.1016/j.soildyn.2023.108249
6. Beskou, N. D., & Theodorakopoulos, D. D. (2011). Dynamic effects of moving loads on road pavements: a review. Soil Dynamics and Earthquake Engineering, 31(4), 547-567. https://doi.org/10.1016/j.soildyn.2010.11.002
7. Biswas, S., Hussain, M., & Singh, K. L. (2024). Behavior of bamboo and jute geocell overlaying soft subgrade under repeated wheel loading. Journal of Materials in Civil Engineering, 36(2), 04023570. https://doi.org/10.1061/JMCEE7.MTENG-16528
8. Boban, A., Kumar, Y., & Trivedi, A. (2023). Numerical and Experimental Investigation of a Confined Geomaterial Subjected to Vibratory Load. In International Conference on Sustainable Infrastructure: Innovation, Opportunities and Challenges (549-562). Singapore: Springer Nature Singapore. https://doi.org/10.1007/978-981-97-4852-5_44

9. Bozyigit, B., & Acikgoz, S. (2022). Dynamic amplification in masonry arch railway bridges. Structures*,* *45*, 1717-1728. https://doi.org/10.1016/j.istruc.2022.09.100
10. Brown, S. F. (2004). Accelerated pavement testing in highway engineering. In Proceedings of the Institution of Civil Engineers-Transport*,* 157(3), 173-180. https://doi.org/10.1680/tran.2004.157.3.173
11. Crawford, J. E., & Katona, M. G. (1975). State-of-the-art for prediction of pavement response. US Army Engineer Waterways Experiment Station.
12. Cao, P., Feng, D. C., & Jing, R. X. (2012). Based on FE method to research resistant rutting ability of pavement structure in Heilongjiang province. Applied Mechanics and Materials. https://doi.org/10.4028/www.scientific.net/AMM.128-129.1349
13. Ding, H., Yang, Y., Chen, L. Q., & Yang, S. P. (2014). Vibration of vehicle–pavement coupled system based on a Timoshenko beam on a nonlinear foundation. Journal of Sound and Vibration, 333(24), 6623–6636. https://doi.org/10.1016/j.jsv.2014.07.016
14. Du Plessis, L., Ulloa-Calderon, A., Harvey, J. T., & Coetzee, N. F. (2018). Accelerated pavement testing efforts using the Heavy Vehicle Simulator. International Journal of Pavement Research and Technology, *11*(4), 327-338. https://doi.org/10.1016/j.ijprt.2017.09.016
15. Duncan, J. M., & Chang, C. Y. (1970). Nonlinear analysis of stress and strain in soils. Journal of the soil mechanics and foundations division, *96*(5), 1629-1653. https://doi.org/10.1061/JSFEAQ.000145

16. Duddu, S. R., & Chennarapu, H. (2022). Quality control of compaction with lightweight deflectometer (LWD) device: a state-of-art. International Journal of Geo-Engineering, 13(1), 6. https://doi.org/10.1186/s40703-021-00171-2
17. Elishakoff, I. (2020). Handbook on Timoshenko-Ehrenfest beam and Uflyand-Mindlin plate theories. World Scientific.
18. Froio, D., Verzeroli, L., Ferrari, R., & Rizzi, E. (2021). On the numerical modelization of moving load beam problems by a dedicated parallel computing FEM implementation. Archives of Computational Methods in Engineering, 28(4). https://doi.org/10.1007/s11831-020-09459-5
19. Gibigaye, M., Yabi, C. P., & Alloba, I. E. (2016). Dynamic response of a rigid pavement plate based on an inertial soil. *International Scholarly Research Notices*, *2016*(1), 4975345. https://doi.org/10.1155/2016/4975345
20. Guo, M., Hou, F., Zhang, S., Li, X., Li, Y., & Bi, Y. (2022). Research and evaluation on dynamic response characteristics of various pavement structures. *Advances in Materials Science and Engineering*, *2022*(1), 5302142. https://doi.org/10.1155/2022/5302142Digital Object Identifier (DOI)
21. Han, F., Dan, D. H., & Wang, H. (2018). A study on dynamic amplification factor and structure parameter of bridge deck pavement based on bridge deck pavement roughness. *Advances in Civil Engineering*, *2018*(1), 9810461. https://doi.org/10.1155/2018/9810461
22. He, Y., & Yang, J. P. (2021). Using Kalman filter to estimate the pavement profile of a bridge from a passing vehicle considering their interaction. Acta Mechanica, 232(11), 4347–4362. https://doi.org/10.1007/s00707-021-03055-9

23. Hetényi, M. (1946). *Beams on elastic foundation.* (16), Ann Arbor: University of Michigan Press.

24. Hilber, H. M., Hughes, T. J., & Taylor, R. L. (1977). Improved numerical dissipation for time integration algorithms in structural dynamics. Earthquake Engineering & Structural Dynamics, 5(3), 283–292. https://doi.org/10.1002/eqe.4290050306

25. Imaninasab, R., Bakhshi, B., & Shirini, B. (2016). Rutting performance of rubberized porous asphalt using finite element method (FEM). Construction and Building Materials, 106. https://doi.org/10.1016/j.conbuildmat.2015.12.134

26. Jiang, X., Titi, H., Ma, Y., Polaczyk, P., Zhang, M., Gabrielson, J., ... & Huang, B. (2022). Evaluating the performance of inverted pavement structure using the accelerated pavement test (APT). *Construction and Building Materials*, *346*, 128489. https://doi.org/10.1016/j.conbuildmat.2022.128489

27. Ju, S. H. (2011). Vibration analysis of 3D Timoshenko beams subjected to moving vehicles. Journal of Engineering Mechanics, 137(11), 713–721. https://doi.org/10.1061/(ASCE)EM.1943-7889.0000276

28. Khan, S., Nagabhushana, M. N., Tiwari, D., & Jain, P. K. (2016). Comparison of uni and bi-directional load induced rutting in flexible pavement with accelerated pavement testing facility (APTF). *Transportation Research Procedia*, *17*, 521-528. https://doi.org/10.1016/j.trpro.2016.11.106

29. Khaksar, M., Khavandi, A., Khabiri, M. M., & Bakhtiari, J. (2025). Correlative Study of Light-Weight Deflectometer, Plate Loading, and California Bearing Ratio Tests for Unbound Pavement Layers Using Genetic

Algorithm. *Transportation Infrastructure Geotechnology*, *12*(1), 6. https://doi.org/10.1061/(ASCE)EM.1943-7889.0000276

30. Kim, Y. R. (Ed.). (2014). Asphalt pavements. CRC Press.
31. Kumar, Y., Trivedi, A., & Shukla, S. K. (2024a). Damage evaluation in pavement-geomaterial system using finite element-scaled accelerated pavement testing. Transportation Infrastructure Geotechnology. https://doi.org/10.1007/s40515-023-00309-y
32. Kumar, Y., Trivedi, A., & Shukla, S. K. (2024b). Deflections governed by the cyclic strength of rigid pavement subjected to structural vibration due to high-velocity moving loads. Journal of Vibration Engineering & Technologies, 12(3), 3543–3562. https://doi.org/10.1007/s42417-023-01063-8
33. Kumar, Y., Trivedi, A., & Shukla, S. K. (2025). Impact of moving load vibrations on pavement damage supported by flow-controlled geomaterials. *International Journal of Non-Linear Mechanics*, *172*, 105045. https://doi.org/10.1016/j.ijnonlinmec.2025.105045Get rights and content
34. Lei, H., Huang, C., & Qian, J. G. (2025). Dynamic response of saturated ground subjected to moving loads with variable speeds. *Soil Dynamics and Earthquake Engineering*, *197*, 109532. https://doi.org/10.1016/j.soildyn.2025.109532
35. Liu, Z., Gu, X., & Ren, H. (2023). Rutting prediction of asphalt pavement with semi-rigid base: Numerical modeling on laboratory to accelerated pavement testing. *Construction and Building Materials*, *375*, 130903. https://doi.org/10.1016/j.conbuildmat.2023.130903

36. Lu, Z., & Yao, H. (2013). Effects of the dynamic vehicle-road interaction on the pavement vibration due to road traffic. *Journal of Vibroengineering*, *15*(3), 1291-1301.
37. Lu, Z., Fang, R., Yao, H., Dong, C., & Xian, S. (2018). Dynamic responses of unsaturated half-space soil to a moving harmonic rectangular load. International Journal for Numerical and Analytical Methods in Geomechanics, 42(9), 1057–1077. https://doi.org/10.1002/nag.2780
38. Lytton, R. L., Uzan, J., Fernando, E. G., Roque, R., Hiltunen, D., & Stoffels, S. M. (1993). Development and validation of performance prediction models and specifications for asphalt binders and paving mixes, 357, Strategic Highway Research Program.
39. Mallela, J., & George, K. P. (1994). Three-dimensional dynamic response model for rigid pavements. *Transportation Research Record*, *1448*, 92-99.
40. Ma, L., Li, Z., Xu, H., & Cai, C. S. (2024). Numerical study on the dynamic amplification factors of highway continuous beam bridges under the action of vehicle fleets. *Engineering Structures*, *304*, 117638. https://doi.org/10.1016/j.engstruct.2024.117638
41. Matthews, J. M., & Pandey, B. B. (1991). Performance of flexible pavements. *Transportation Research Record*, 1307, 51-62.
42. Metcalf, J. B. (1996). Application of full-scale accelerated pavement testing. *Transportation Research Board*, 235.
43. Mshali, M. R., & Steyn, W. J. (2022). Effect of truck speed on the response of flexible pavement systems to traffic loading. *International Journal of Pavement Engineering*, *23*(4), 1213-1225. https://doi.org/10.1080/10298436.2020.1797733

44. Muho, E. V., Beskou, N. D., & Qian, J. (2025). Models and methods for dynamic response of 3D flexible and rigid pavements to moving loads: A review by representative examples. *Journal of Road Engineering*. https://doi.org/10.1016/j.jreng.2024.07.003
45. Pandya, H. I., Ali, A. A., & Mehta, Y. A. (2024). Enhancing falling weight deflectometer (FWD) testing: comprehensive review and development of robust procedure in the United States. *Journal of Testing and Evaluation*, *52*(4), 2039-2054. https://doi.org/10.1520/JTE20230389
46. Paultre, P., Chaallal, O., & Proulx, J. (1992). Bridge dynamics and dynamic amplification factors—a review of analytical and experimental findings. *Canadian Journal of Civil Engineering*, *19*(2), 260-278. https://doi.org/10.1139/l92-032
47. Pirabarooban, S., Zaman, M., & Tarefder, R. A. (2003). Evaluation of rutting potential in asphalt mixes using finite element modeling. TAC/ATC Annual Conference and Exhibition of the Transportation Association of Canada: The Transportation Factor.
48. Pradhan, R. P., & Bagchi, T. P. (2013). The Effect of Transportation Infrastructure on Economic Growth in India: A VECM Approach. *Research in Transportation economics*, *38*(1), 139-148. https://doi.org/10.1016/j.retrec.2012.05.008
49. Punetha, P., & Nimbalkar, S. (2025). Numerical investigation on the dynamic behaviour of unpaved roads under realistic moving loads. *Road Materials and Pavement Design*, 1-46. https://doi.org/10.1080/14680629.2025.2533350

50. Qiu, Z., Li, L., Chen, Z. L., Zhang, X., & Gong, W. (2025). Dynamic responses of a multi-layered unsaturated road system with impermeable pavement under moving-vibratory vehicle load. *Transportation Geotechnics*, 101675. https://doi.org/10.1016/j.trgeo.2025.101675
51. Richart, F. E., Hall, J. R., & Woods, R. D. (1970). *Vibrations of Soils and Foundations.* Prentice-Hall.
52. Selvadurai, A. P. S. (1979). *Elastic Analysis of Soil–Foundation Interaction.* Elsevier.
53. Suleiman, M. T., Gopalakrishnan, K., & Kevern, J. T. (2011). Structural response of pervious concrete pavement systems using falling weight deflectometer testing and analysis. *Journal of Transportation Engineering*, *137*(12), 907-917. https://doi.org/10.1061/(ASCE)TE.1943-5436.00002
54. Sulewska, M. J., & Bartnik, G. (2017). Application of the light falling weight deflectometer (LFWD) to test aggregate layers on geosynthetic base. *Procedia* Engineering, 189, 221-226. https://doi.org/10.1016/j.proeng.2017.05.035
55. Sun, L. (2016). Structural behavior of asphalt pavements: Intergrated analysis and design of conventional and heavy duty asphalt pavement. Butterworth-Heinemann.
56. Taheri, M. R., & Ting, E. C. (1989). Dynamic response of plate to moving loads: Structural impedance method. Computers & Structures, 33(6), 1379–1393. https://doi.org/10.1016/0045-7949(89)90478-1
57. Taheri, M. R., & Ting, E. C. (1990). Dynamic response of plates to moving loads: Finite element method. Computers & Structures, 34(3), 509–521. https://doi.org/10.1016/0045-7949(90)90276-8

58. Timoshenko, S. P., & Gere, J. M. (2012). Theory of elastic stability. Courier Corporation.
59. Vennapusa, P. K., & White, D. J. (2009). Comparison of light weight deflectometer measurements for pavement foundation materials. *Geotechnical Testing Journal*, *32*(3), 239-251. https://doi.org/10.1520/GTJ101704
60. Wang, B., & Yang, J. (2008). Effects of vehicle dynamic loading on CRCP by 3D finite element method. Journal of South-east University: Natural Science Edition, 38(5), 850–855.
61. Wu, C. P., & Shen, P. A. (1996). Dynamic analysis of concrete pavements subjected to moving loads. Journal of Transportation Engineering, 122(5). https://doi.org/10.1061/(ASCE)0733-947X(1996)122:5(367)
62. Yan, Z., Liang, J., Bai, Y., Cao, L., & Zhao, G. (2021). Response of asphalt pavement structure layer and particle movement velocity based on particle flow theory. *Journal of Construction Engineering and Management*, *147*(12), 04021170. https://doi.org/10.1061/(ASCE)CO.1943-7862.0002199
63. Yao, G., Wu, L., Yang, Y., Zheng, Y., Qin, B., & Chen, Y. (2023). A scientometric research and critical analysis of road-rail bridge. *Vibroengineering Procedia*, *51*, 69-75. https://doi.org/10.21595/vp.2023.23552
64. Yang, S., Li, S., & Lu, Y. (2010). Investigation on dynamical interaction between a heavy vehicle and road pavement. Vehicle System Dynamics, 48(8). https://doi.org/10.1080/00423110903243166
65. Yang, S., Lu, Y., & Li, S. (2013). An overview on vehicle dynamics. International Journal of Dynamics and Control, 1(4), 385–395. https://doi.org/10.1007/s40435-013-0032-y

66. Zeng, F., Chen, F., & Eghbal, S. (2024). Vibroacoustic analysis of asphalt pavement responses to moving loads and attached mass-spring-damper systems. *Soil Dynamics and Earthquake Engineering*, *185*, 108887. https://doi.org/10.1016/j.soildyn.2024.108887

67. Zhang, J., Zhang, G., Wang, Y., & Yuan, J. (2022). Mechanical behavior of doweled joints in concrete pavements: A review. Journal of Transportation Engineering, Part B: Pavements, 148(4), 03122002. https://doi.org/10.1061/JPEODX.0000399

68. Zhang, C., Cho, S., Park, B., Orosa, P., Li, J., & Haddock, J. E. (2025). Characterizing Mechanical Responses of Composite Pavements in Falling Weight Deflectometer Testing for Structural Condition Evaluation. *Transportation Research Record*, 03611981251341340. https://doi.org/10.1177/03611981251341340

69. Zulfiqar, Q., Waqar Haider, S., Cetin, B., & Sinan Coban, H. (2025). Establishing a Relationship between Falling Weight Deflectometer Field Deflections and Nonlinear Parameters to Quantify Stress State for Recycled and Virgin Aggregate Bases. *Geotechnical Testing Journal*, *48*(5). https://doi.org/10.1520/GTJ20230553

2

Chapter

Development of a Numerical Framework for Pavement–Soil System Simulations

Highlights

- In this chapter, a finite element-based numerical framework has been developed for simulating the dynamic response of the pavement–soil system.
- A generalised dissipation mechanism (GDM) has been presented, which introduces the three dissipation parameters (α, β, γ) and two empirical parameters ($\acute{\eta}, \vartheta$) in numerical simulation for vibration damping and amplification control.
- This family of numerical parameters in GDM eliminates computational noise and enhances the accuracy of finite-element-based dynamic pavement response models.
- The GDM demonstrates effective noise reduction in stress response estimation, reducing numerical noise from 16% to near-negligible levels as the numerical damping ratio (ξ_n) approaches 0.03.
- The GDM quantifies dynamic amplification effects, revealing up to a 70% increase in load and 46% in displacement in pavement layers compared to static loading at threshold velocities.
- The research presented in this chapter has practical implications for improving the prediction of in-situ pavement responses and guiding future revisions of pavement design and analysis methodologies under moving loads.

2.1 General

Analytical solutions to the problem of pavement dynamic response have been presented in the classical literature of pavement engineering. The Timoshenko beam theory has been extensively used to investigate the dynamic response of pavements by modeling them as Timoshenko beams resting on an elastic spring foundation (Elishakoff, 2020). The vehicle-pavement interaction effects are considered crucial for investigating the dynamic response of pavements (Beskou & Muho, 2023a; b). Time integration dissipation in the three-dimensional numerical algorithm is crucial for establishing a dependable solution in the dynamic analysis of pavement-geomaterial assemblies (Kumar et al., 2025). The Timoshenko beam was adopted in 3D FEM numerical programs to investigate the impact of vehicle vibration on pavement dynamics coupled with a non-linear dynamic foundation (Ju, 2011; Ding et al., 2014; Xu et al., 2022; Froio et al., 2021; Xu et al., 2023). The effect of subgrade stress is a critical issue in pavement dynamics. Several three-dimensional numerical schemes have been proposed in the literature to investigate the transfer mechanism in subgrades supporting the pavements (Wu & Shen, 1996; Ling & Liu, 2003; Beskou & Theodorakopoulos, 2011; Xu et al., 2023). These studies established the involvement of complex mathematics in investigating the dynamics of pavement-soil systems, which require further investigative efforts with damping stabilization (Wang & Yang, 2008; Huang et al., 2022; Kumar et al., 2024a).

Moreover, past studies have reported that vehicle guideways, as dynamic systems, are greatly influenced by the velocity of moving loads (Wu & Shen, 1996; Kansake et al., 2023). The keen interest of researchers in the dynamic response of pavements has been increasing due to their complex and unsolved nature (Zhao & Wang, 2020; Snehasagar et al., 2020; Liu et al., 2021; Rith et al., 2021; Ai et al., 2022; Kumar et al., 2024b). The pavement-geomaterial system is a complex dynamic system subjected to varied velocities of moving load during its designed life, and can be solved using a versatile numerical simulation (Yang et al., 2013; Kumar, 2020; Xu et al., 2022; Sadripour et al., 2024). The numerical noise is a crucial parameter that is inadvertently introduced in numerical simulations, influencing the accuracy and reliability of the numerical model (Hilber et al., 1977). These noises are produced in extreme dynamic environments, such as pavement subjected to varying velocities of moving loads (He & Yang, 2021; Kumar et al., 2024a). The solution presented by Hilber et al. (1977) can be improved and applied to remove the numerical noise by numerical damping factors. The high-speed guideways are a crucial issue related to dynamic systems that must be investigated for the time integration dissipation solution (Kumar et al., 2024b). Yet no trace of literature has been found on numerical analysis of pavements subjected to moving loads of varied velocity with time integration dissipation control.

The literature surveyed for conducting the presented research has led to the observation that time integration dissipation solutions for pavement geomaterials subjected to varied velocities of moving loads, as dynamic systems, are very rare. The stress response in pavement-geomaterial dynamic systems needs further investigation. Additionally, the literature is limited to load amplification and lacks the determination of displacement amplification in layers of pavement geomaterial systems at varying input velocities. These situations may lead to failure if underestimated. Hence, the following objectives have been set to conduct the present research:

- To formulate a novel time integration dissipation control using a family of numerical damping parameters, and

- To investigate the dynamic response of the pavement-geomaterial system with the inclusion of numerical damping, with calculation of amplification of load and displacement in the pavement-geomaterial system.
- To calibrate the numerical model with field observations by developing a finite element scaled accelerated pavement testing.

Considering the defined objectives, an attempt has been made to develop a time integration dissipation solution for pavement-geomaterial dynamic systems. A novel damping evolution theory with a family of numerical damping parameters has been formulated to implement the time integration dissipation control. A relatively dependable solution for the dynamic response of pavement-geomaterial assembly as a dynamic system has been presented by numerically varied algorithms. The load and displacement amplification factors have been mathematically captured, and a generalised solution is proposed to estimate amplification due to a moving load.

2.2 Model Definition

2.2.1 Geometric Modelling

To conduct numerical investigations, the pavement has been numerically modelled as a meshed geometry resting on layers of geomaterial (granular base course and subgrade soil layers). To reduce the computational timing in the numerical model, the work reported in the literature considered the dimensionally half-symmetric models (Yang et al., 2010). Since the symmetric model can comprehensively reduce computation time in numerical simulations, the numerical model with symmetry along depth has been adopted €n the presented research. Fig. 2.1 portrays the schematic isometric diagram of the symmetric pavement-geomaterial assembly considered as a dynamic system, along with the representative dimensions of the layers.

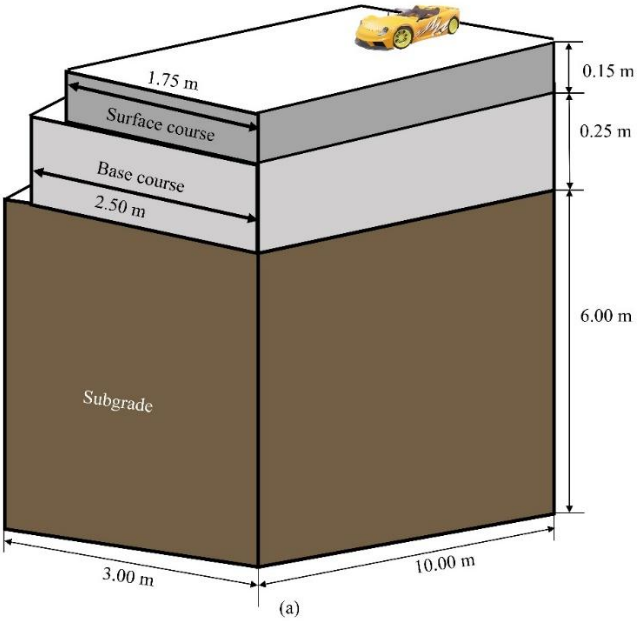

Figure 2.1 Schematic representation showing an isometric view with layered dimensional specifications (not drawn to the scale)

Fixed boundary conditions have been applied at the bottom, and symmetric boundary conditions have been used along the depth at the face of the numerical model. The material properties were adopted from the research article by Kumar et al. (2024a). The input material properties of each layer have been tabulated in Table 2.1.

Table 2.1 Input material properties

Input property, symbol (unit)	Layer	Magnitude [a]
Young's modulus, *E* (MPa)	Pavement	2.48×10^7
	Base course	2.76×10^5
	Subgrade	5.15×10^4
Poisson's ratio, *ν*	Pavement	0.15
	Base course	0.30
	Subgrade	0.40
Unit weight, *γ* (kN/m^3)	Pavement	23.24
	Base course	17.60
	Subgrade	18.40

[a] Kumar et al. (2024a)

2.2.2 Finite-Element-Scaled Accelerated Pavement Testing

Further, the present study has been conducted in terms of deflection, equivalent and principal stress, and rutting characteristics of finite element scaled APT. The investigations involving moving load issues have been modelled using a commercial finite element software program, Abaqus (Wang & Fu, 2010; Zhuang et al., 2009), for the pavement Fes-APT (Fig. 2.2). A few researchers favoured full-scale models and reduced dimensional analysis, while considering varied dimensional tire models to model the quarter and half models of the car. The full-scale model of symmetry has been considered to reduce the computation time (Yang et al., 2013). Various numerical techniques have been adopted in the literature to simulate moving loads, including moving-coordinate-frame approaches, time-dependent nodal force application, contact-based wheel–pavement interaction modelling, and explicit dynamic formulations (Kim 2026). In the present study, a controlled DLOAD subroutine in Fortran language has been coded to define velocity-dependent moving loads, enabling systematic evaluation of amplification and dissipation characteristics while maintaining numerical stability. A linear shape function of the 3D stress family, specifically the C3D8R, an 8-noded cuboidal brick element, has been adopted in a weak form of a reduced integration scheme with hourglass control to conduct the Fes-APT. To model field-scaled accelerated pavement testing at the finite element scale, the prerequisite parameters are elastic modulus, Poisson's ratio, and layer thickness.

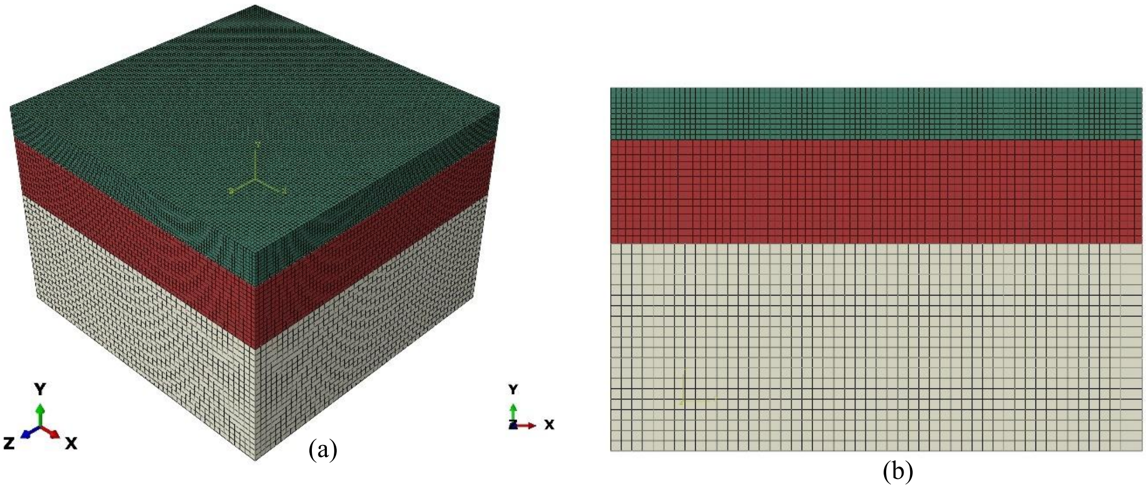

(a)

(b)

Figure 2.2 Mesh profile of the numerical model for FEM scaled-APT

There have been very limited studies on the determination and effect of elastic modulus, Poisson’s ratio, and layer thickness for accelerated pavement testing. Unfortunately, these parameters altogether are not available in one article. The material adopted in the present study has the following possible range of values for wearing course, base course, and subgrade layer. The layer thickness, modulus, and Poisson’s ratio typically vary from 25 mm to 250 mm, 5 MPa to 1500 MPa, and 0.15 to 0.45, respectively, for the wearing course, base course, and subgrade layer. Considering the above fact, the properties of the pavement, granular base, and soil subgrade were obtained from different sources (Kim, 2014; Sun, 2016; Ma et al., 2022). The material properties adopted to model the pavement are listed in Table 2.2:

Table 2.2 Input properties in the FE-s APT considered in the present study

Layers	Thickness (mm)	Modulus (MPa)	Poisson’s Ratio
Wearing Course	50	1200	0.35
Base Course Layer	100	110	0.35
Subgrade Layer	200	20	0.3

In finite element scaled accelerated pavement testing, the unidirectional mode of traffic was adopted. For the presented pavement with the design parameters, the mode of traffic has a significant potential for distress in terms of permanent deformation. The simulation for unidirectional single testing was kept running in the commercialised software package ABAQUS. The unidirectional mode of traffic was adopted with the following traffic conditions, as shown in Table 2.3:

Table 2.3 Input traffic condition* for the present study

Traffic Inputs	Magnitude	Unit
Velocity	10	Kmph
Load	80	KN
Vehicle movement direction	Unidirectional	-

*Khan et al. (2016)

These test settings were all maintained at their original values throughout the whole test. The test section was divided into 16 points with uniform spacing. To measure the depth of rutting, the meshed nodes along the pavement's width were selected in the center of the pavement.

2.2.3 Evolution of Damping Parameters in Pavement-geomaterial System Subjected to Moving Loads

Using D'Alembert's principle, the generalised equation for motion has been conceptualized as:

$$ma + ku + cv = Q_m \tag{2.1}$$

where m is the mass matrix, c is the damper matrix, and k is the stiffness matrix in the equation of motion, and a, v, u, and Q_m are respectively the acceleration, velocity, displacement, and moving force vector associated with these matrices. A simple pilot problem, i.e., $Q_m \equiv 0$, has been adopted to solve the numerical algorithm. The displacement on the nodes of pavement geomaterial assembly due to moving load has been generalised as per the equations provided by Kumar et al. (2024b) as detailed below:

$$u = \sum_{n=1}^{N} N_i^n u_n \tag{2.2}$$

$$N_i^n(u, v, w) = \frac{1}{8}(1+x_i u)(1+y_i v)(1+z_i w) \tag{2.3}$$

The shape function (N_i^n) is independent of displacement at nodes and used as an approximation function for estimating displacement fields. In a dynamic system, damping is generally conceived as a rate of change of momentum introduced into the system as a mechanical modulator, which is dissipated as the vibrational energy of actual structures. Thus, the vibration experiments on actual pavement systems provide data for evaluating the damping coefficient. In the present work, this damping is numerically split up using an algorithm that has been developed to obtain a dependable solution for the dynamic response of the pavement-geomaterial assembly. The time integration dissipation solution has been conceptulised as a function of acceleration, velocity, displacement, and time. The iterative compact form can be expressed as:

$$U_{m+1}=\zeta U_m \qquad m \in \{0, 1, 2, ..., M-1\} \tag{2.4}$$

$$U_m=(u_m, \Delta t v_m, \Delta t^2 a_m)^T \tag{2.5}$$

where ζ is the governing damping matrix that depends on time and induces time integration dissipation control during the numerical solution integration. The equation defining the characteristic state can be expressed as:

$$det(\zeta - \lambda I) = \lambda^3 - 2\zeta_1\lambda^2 + \zeta_2\lambda - \zeta_3 = 0 \tag{2.6}$$

where λ and I have been designed to represent the eigenvalue and identity matrix, respectively, with

$$\left.\begin{array}{l}\zeta_1 = \frac{1}{2}\ \textit{trace of}\ \zeta \\ \\ \zeta_2 = \textit{summation of principal minors associated with}\ \zeta \\ \\ \zeta_3 = \textit{determinant of}\ \zeta\end{array}\right\} \tag{2.7}$$

as the invariants of ζ. The difference equation has been acquired in terms of the displacement vector to obtain the deflection as:

$$u_{m+1} - 2\zeta_1 u_m + \zeta_2 u_{m-1} - \zeta_3 u_{m-2} = 0 \qquad m \in \{2, 3, ..., M\text{-}1\} \tag{2.8}$$

The time integration dissipation control in explicit terms defined using non-dimensional damping parameters α, β, and γ can be expressed as:

$$B \times \zeta = \begin{bmatrix} 1+\alpha\beta\Pi^2 & 1 & \frac{1}{2}\text{-}\beta \\ \text{-}\ \gamma\Pi^2 & 1\text{-}(1+\alpha)(\gamma-\beta)\Pi^2 & (1-\gamma)\text{-}(1+\alpha)\left(\frac{1}{2}\gamma-\beta\right)\Pi^2 \\ \Pi^2 & \text{-}(1+\alpha)\Pi^2 & \text{-}\ (1+\alpha)\left(\frac{1}{2}-\beta\right)\Pi^2 \end{bmatrix} \tag{2.9}$$

where

$$\left.\begin{array}{l} B = 1 + (1 + \alpha)\,\beta\Pi^2 \\ \\ \Pi = \omega\Delta t \\ \\ \omega = \sqrt{K/_M} \end{array}\right\} \tag{2.10}$$

with damping characteristics related to ζ_1, ζ_2, and ζ_3 is given as:

$$\left.\begin{array}{l} \zeta_1 = 1 - \Pi^2[(1 + \alpha)\left(\gamma + \frac{1}{2}\right) - \alpha\beta]/2\zeta \\ \\ \zeta_2 = 1 - \Pi^2[\gamma - \frac{1}{2} + 2\alpha(\gamma - \beta)]/\zeta \\ \\ \zeta_3 = \alpha\Pi^2\,[1 - \Pi^2[(\beta - \gamma + \frac{1}{2})]/\zeta \end{array}\right\} \tag{2.11}$$

and

$$\frac{u_{m+1} - 2u_m + u_{m-1}}{\Delta t^2} + \frac{\omega \Pi(\alpha + \gamma - \frac{1}{2})}{B} . \frac{u_m - u_{m-1}}{\Delta t} + \frac{\omega^2}{B} u_m - A_3 \frac{u_m - 2u_{m-1} + u_{m-2}}{\Delta t^2} = 0 \quad (2.12)$$

The Newmark's solution modified with non-dimensional parameters for estimating the displacement and velocity with time integration dissipation control can be expressed as:

$$\{u\,|_{t+\Delta t}\} = \{u\,|_t\} + \Delta t.\{v\,|_t\} + \Delta t^2.(\beta).\{a\,|_t\} + \left(\frac{1}{2} - \beta\right).\{a\,|_{t+\Delta t}\}) \quad (2.13)$$

$$\{v\,|_{t+\Delta t}\} = \{v\,|_t\} + \Delta t.((\gamma).\{a\,|_t\} + (1 - \gamma).\{a\,|_{t+\Delta t}\}) \quad (2.14)$$

and the boundaries of these non-dimensional parameters for time integration dissipation control have been established as expressed below:

$$-1 < \alpha < 0,\ 4\beta = 2 - \left(\frac{1}{1+\alpha}\right)^2,\ \text{and}\ \gamma = \frac{1}{2}\left(\frac{1+3\alpha}{1+\alpha}\right)$$

2.2.3.1 Distinction Between Physical and Numerical Damping

Physical damping represents actual material energy dissipation due to viscoelastic behaviour of asphalt layers and hysteretic response of geomaterials. Numerical damping, on the other hand, arises from time integration algorithms such as Newmark-β or Backward Euler methods, primarily to suppress spurious high-frequency oscillations. The damping ratio range adopted in the present study (ξ_n = 0.001–0.03) corresponds to reported small-strain damping values for pavement geomaterials and ensures a balance between computational stability and response accuracy.

2.2.4 Estimation of Stress in Pavement-geomaterial Assembly due to Moving Load

At any nodal point on pavement, the stress-strain due to the moving load using Hoek's law in terms of compliance matrix can constitutively be expressed as (Kumar et al., 2024b; Kumar et al., 2025):

$$\sigma = C\varepsilon^{e} \ = C\ (\varepsilon - \varepsilon^{p}) \tag{2.15}$$

Solution to which is conceived through the effective stress tensor, which can be expressed as:

$$\sigma_{e} = \sqrt{\frac{3}{2}\acute{\sigma}\colon\acute{\sigma}} \tag{2.16}$$

and effective trial stress tensor expressed as:

$$\sigma_{e}^{tr} = \sqrt{\frac{3}{2}\acute{\sigma}^{tr}\colon\acute{\sigma}^{tr}} \tag{2.17}$$

where, $\acute{\sigma}\colon\acute{\sigma} = \sum_{i=1}^{3}\sum_{i=1}^{3}\acute{\sigma}_{ij}\acute{\sigma}_{ij}$, is the double contracted product. Using Hoek's law, the behaviour of pavement subjected to a moving load has been predicted, and the numerical formulation can be expressed as:

$$\begin{bmatrix}\sigma_{11}\\ \sigma_{22}\\ \sigma_{33}\\ \sigma_{12}\\ \sigma_{13}\\ \sigma_{23}\end{bmatrix} = \lambda \begin{bmatrix} \frac{2G}{\lambda}+1 & 1 & 1 & 0 & 0 & 0 \\ 1 & \frac{2G}{\lambda}+\lambda & 1 & 0 & 0 & 0 \\ 1 & 1 & \frac{2G}{\lambda}+1 & 0 & 0 & 0 \\ 0 & 0 & 0 & \frac{G}{\lambda} & 0 & 0 \\ 0 & 0 & 0 & 0 & \frac{2G}{\lambda} & 0 \\ 0 & 0 & 0 & 0 & 0 & \frac{2G}{\lambda} \end{bmatrix} \begin{bmatrix}\varepsilon_{11}\\ \varepsilon_{22}\\ \varepsilon_{33}\\ \varepsilon_{12}\\ \varepsilon_{13}\\ \varepsilon_{23}\end{bmatrix} \tag{2.18}$$

where G is the shear modulus, λ is Lame's parameter. As shear modulus (*G)* exists in all the diagonal elements of the stiffness matrix, the stress and strain components can be related and expressed as:

$$\sigma_{ij} = \lambda\left(\frac{2G\varepsilon_{ij}^{e}}{\lambda} + (\varepsilon_{11}^{e} + \varepsilon_{22}^{e} + \varepsilon_{33}^{e})\Delta_{ij}\right)\begin{cases}\Delta_{ij} = 0\ for\ i \neq j\ (shear\ stresses)\\ \Delta_{ij} = 1\ for\ i = j\ (normal\ stresses)\end{cases} \tag{2.19}$$

where, Δ_{ij} is Kronecker delta and $\varepsilon_{11}^{e} + \varepsilon_{22}^{e} + \varepsilon_{33}^{e}$ can be written as $tr(\varepsilon^{e})I$ and hence Eq. (2.19) can be written as:

$$\sigma = \lambda\left(\frac{2G\varepsilon^e}{\lambda} + tr(\varepsilon^e)I\right) \tag{2.20}$$

Equation (2.20) is valid for all strain computations and used at the end of the increment. For n+1 increment, Eq. (2.20) can be expressed as:

$$\sigma_{n+1} = \lambda\left(\frac{2G\varepsilon_{n+1}^e}{\lambda} + tr(\varepsilon_{n+1}^e)I\right) \tag{2.21}$$

Now the elastic strain at the end of the increment is calculated based on the strain at the beginning of the increment. Total and plastic strain increments can be expressed as:

$$\varepsilon_{n+1}^e = \varepsilon_n^e + \Delta\varepsilon^e = \varepsilon_n^e + (\Delta\varepsilon - \Delta\varepsilon^p) \tag{2.22}$$

Substituting the value of ε_{k+1}^e into Eq. (2.21)

$$\sigma_{n+1} = \lambda\left(\frac{2G\big(\varepsilon_n^e + (\Delta\varepsilon - \Delta\varepsilon^p)\big)}{\lambda} + tr\big(\varepsilon_n^e + (\Delta\varepsilon - \Delta\varepsilon^p)\big)I\right) \tag{2.23}$$

As the material is incompressible therefore rearranging Eq. (2.23) as:

$$\sigma_{n+1} = \lambda\left(\frac{2G(\varepsilon_n^e + \Delta\varepsilon) - 2G\Delta\varepsilon^p}{\lambda} + tr(\varepsilon_n^e + \Delta\varepsilon)I\right) \tag{2.24}$$

The term $2G(\varepsilon_n^e + \Delta\varepsilon) + \lambda tr(\varepsilon_n^e + \Delta\varepsilon)I$ is equal to the strain at the beginning of the increment plus the stiffness matrix multiplied by the total strain increment expressed as:

$$\sigma_{n+1} = \sigma_n + C\Delta\varepsilon - 2G\Delta\varepsilon^p \tag{2.25}$$

The stress at the end of the first increment has been calculated by assuming that the strain at the beginning of the increment is elastic and is known as elastic predictor trial stress expressed as:

$$\sigma^{tr} = \lambda\left(\frac{2G(\varepsilon_n^e+\Delta\varepsilon)}{\lambda} + tr(\varepsilon_n^e + \Delta\varepsilon)I\right) = \sigma_k + C\Delta\varepsilon \tag{2.26}$$

Hence, Eq. (2.26) can be written as:

$$\sigma_{n+1} = \sigma^{tr} - 2G\Delta\varepsilon^{p} \tag{2.27}$$

2.2.5 Computational Algorithm

The steps, as shown in Fig. 2.3, to introduce time integration dissipation control in pavement-geomaterial assembly considered as a dynamic system, are given below:

- The Abaqus standard and implicit solvers with mesh convergence have been adopted to conduct simulations with the initial input parameters as specified in Tables 2.1, 2.2, and 2.3.
- Damping control in the algorithm has been provided using Eq. (2.20), stability checks were performed using Eq. (2.22), and the time integration dissipation-controlled dynamic displacements and stresses have been captured by Eqs. (2.13) and (2.27), and the process has been repeated to obtain a dependable solution.

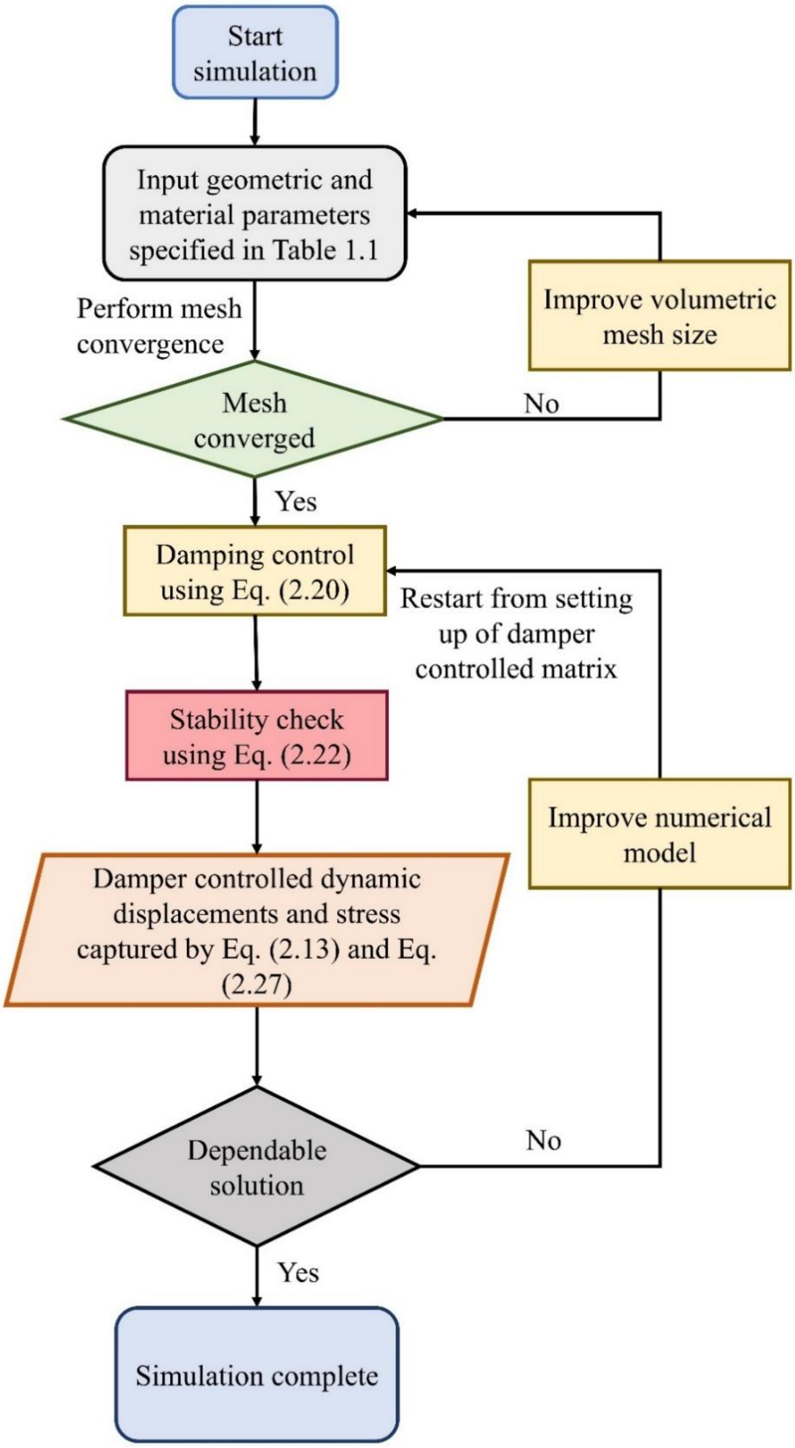

Figure 2.3 Pictorial flow chart of the simulation process

2.3 Results and Discussion

The present study is the first of its kind to investigate the dissipation-stabilized finite element testing of pavement geomaterial systems subjected to moving loads. The results are discussed under the following headings: (2.3.1) mesh convergence, model calibration, and FE-APT validation; (2.3.2) estimation of damping; (2.3.3) stress response; and (2.3.4) load and displacement magnifications.

2.3.1 Mesh Convergence, Model Calibration, and FE-APT Validation

The numerical model presented has been studied and tested for mesh convergence, and the findings have been analyzed in comparison with the results available in the literature. The mesh convergence has been performed from coarser to relatively finer mesh sizes to remove any noise that may arise due to inappropriate mesh sizes. The mesh size has been volumetrically varied with global seeding for the mesh convergence test. The change in volumetric mesh size with increasing global seeding magnitude is shown in Fig. 2.4(a). An increasing magnitude of global seeding points tends to align with a coarser mesh, and vice versa. The number of elements exponentially increases with a decrease in the magnitude of global seeding.

The central deflection along the length of the pavement, with an increasing global seeding ranging from 0.2 to 0.5, is shown in Fig. 2.4(b). It can be observed from Fig. 2.4(b) that the variation in central deflection for a global seeding magnitude of 0.2 compared to 0.3 is less than 1%. Hence, the present work was carried out with a global seeding magnitude of 0.2 to save computation time.

The radar (ternary) plots compare pavement performance across three different studies, namely, Wu & Shen (1996), Yang et al. (2010), and the present work, as shown in Fig. 2.5. These plots visualize pavement deformation or strain under varying pavement thicknesses of 15 cm, 30 cm, and 45 cm, with measurements given in millimeters. The coloured regions represent the extent of deformation, where a larger and more extended region indicates higher deformation, suggesting weaker pavement performance, while a more compact region signifies better structural integrity.

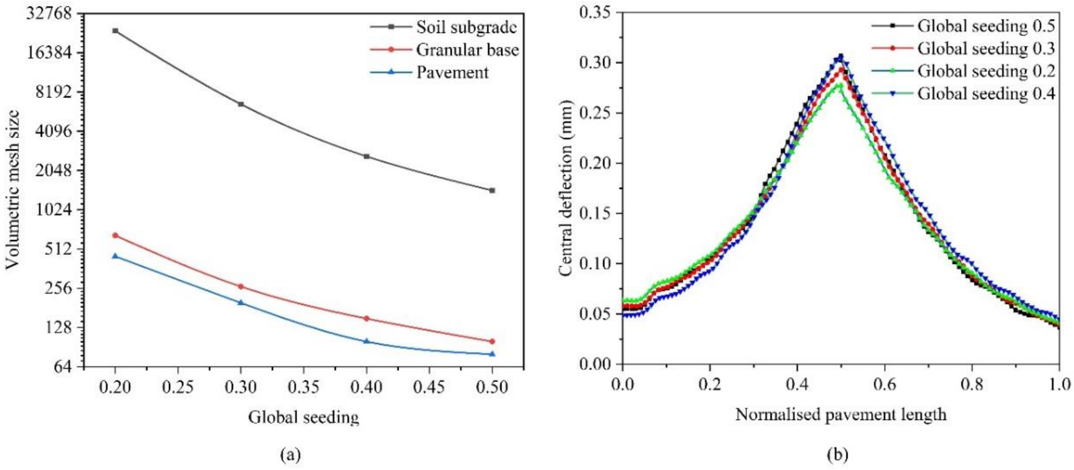

Figure 2.4 (a) Variation in volumetric size of the mesh with the varied magnitude of global seeding used to perform the convergence of meshed results, and (b) central deflection along pavement length for the varied magnitude of global seeding ranging from 0.2 to 0.5

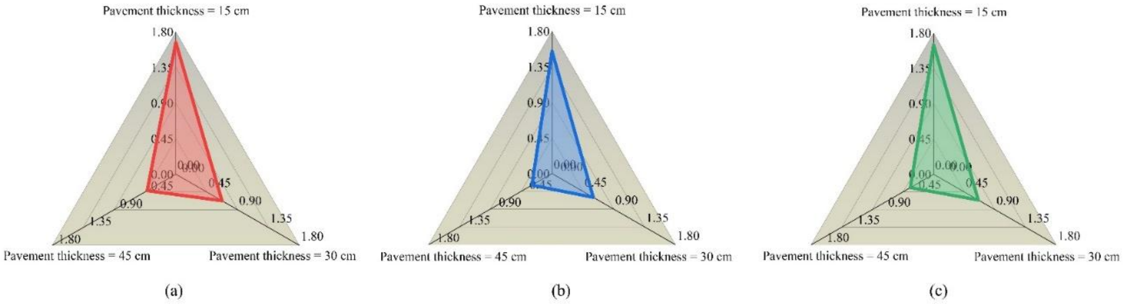

Figure 2.5 Comparison of pavement deformation across different studies using radar plots. (a) Wu & Shen (1996), (b) Yang et al. (2010), and (c) Present Work. The colored regions represent deformation measurements at pavement thicknesses of 15 cm, 30 cm, and 45 cm

Figure 2.5(a) shows that the red region as studied by Wu & Shen (1996) is more elongated, particularly towards the 15 cm pavement thickness, indicating significant deformation at lower thicknesses, with values approaching 1.8 mm. Even at a thickness of 45 cm, deformation is still relatively high. The results in Fig. 2.5(b), as reported by Yang et al. (2010), show a slightly more compact region compared to Wu & Shen

(1996). Although the highest deformation still occurs at 15 cm thickness, the values are lower, and the spread at 45 cm is less pronounced, implying better pavement performance. The present work, as shown in Fig. 2.5(c), illustrated in green, shows the most compact region, indicating significantly lower deformation across all pavement thicknesses.

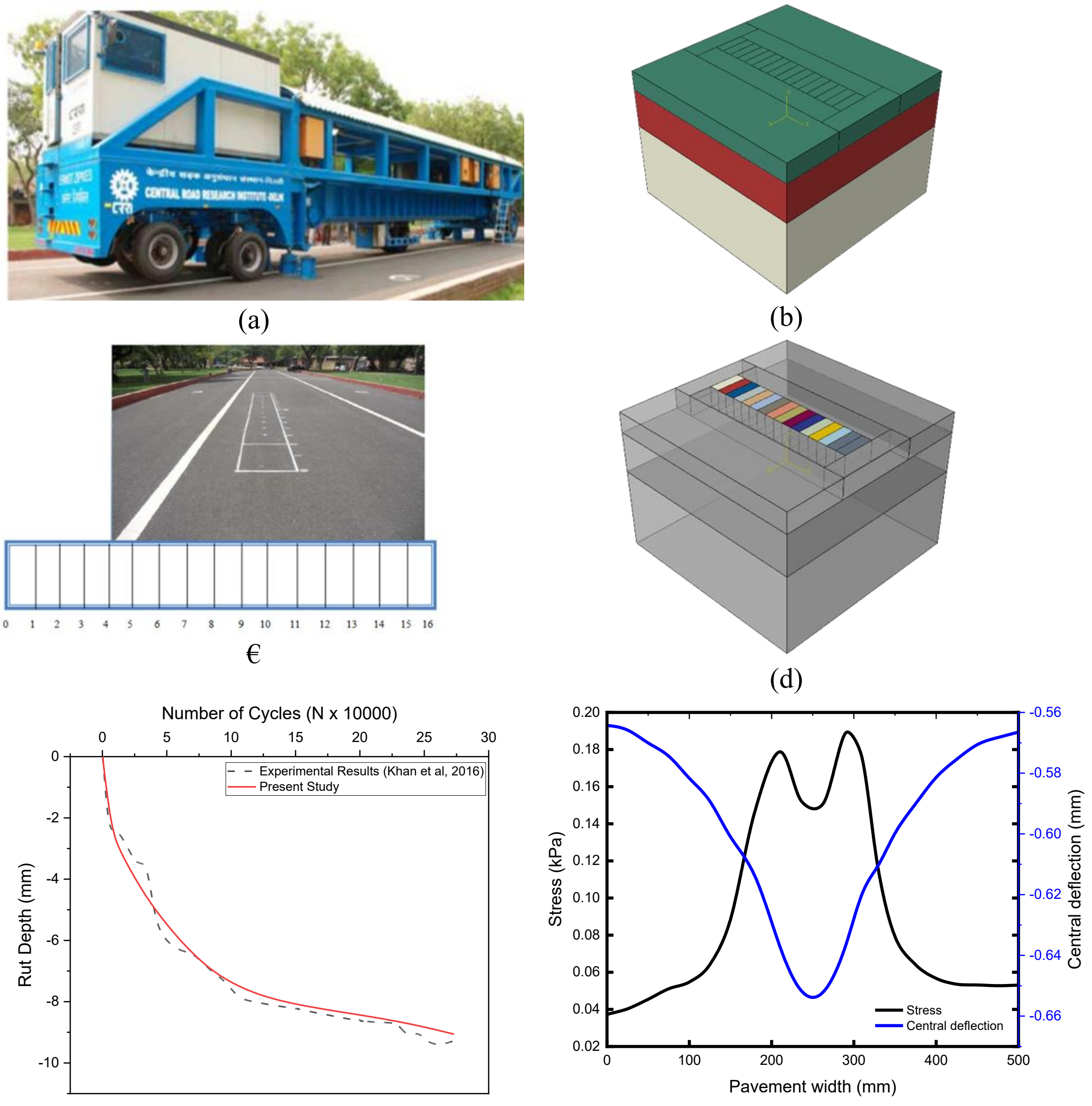

(a) (b)

€ (d)

€ (f)

Figure 2.6 (a) Fs-APT facility at CSIR-CRRI, (b) Finite Element Scaled APT, (c) experimental path for the movement of Fs-APT test facility, (d) projected finite element loading path of experimental Fs-APT testing facility, (e) comparison between the rut depth obtained by numerical results and experimental Fs-APT testing facility, and (f) stress and central deflection in pavement along the pavement width

Additionally, the finite element scaled APT has been validated and tested for mesh sensitivity. The validation process has been further carried out with experimental findings (Khan et al., 2016). The original experimental data points presented in Fig. 2.6(a) have been used without any data fitting to validate our study. The FS-APT facility at CSIR-CRRI, shown in Fig. 2.6 (a), is mapped in the FE model as shown in Fig. 2.6(b), and the experimental testing path for moving load testing, shown in Fig. 2.6(c), is numerically simulated using the DLOAD subroutine (Fig. 2.6(d)). The numerical findings are calibrated with the experimental findings of Fs-APT (Fig. 2.6€). The rut depth along the pavement length with residual edge deflection and stress has been portrayed in Fig. 2.6(f). It has been analyzed that the stress and deflection response along the pavement center and edges for each cycle are stored which forms the fundamental for next cycle in the development of rut width along the pavement.

2.3.2 Estimation of Damping

In numerical time integration, a non-dimensional time factor (τ) has been introduced to account for damping effects. The non-dimensional time factor (τ) has been defined as the ratio of the time increment in one iteration step to the total simulation time. The consideration of τ becomes crucial in dynamic systems, particularly at varying velocities of moving loads, such as pavement-geomaterial assemblies, where unwanted numerical noise is introduced during numerical time integration. These numerical disturbances, if not properly managed, can lead to unreasonable and inaccurate results, affecting the reliability of the simulation. Fig. 2.7 presents the numerical damping ratio (ξ_n) as a function of the non-dimensional time factor (τ) for various numerical algorithms with differing levels of precision to mitigate the issue of numerical noise and ensure a stable as well as dependable solution.

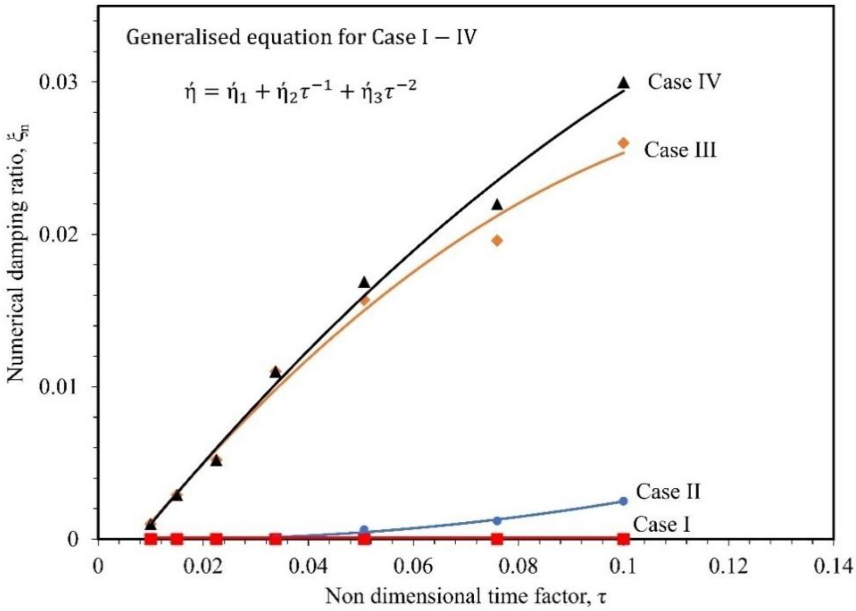

Figure 2.7 Damping ratio versus non-dimensional factor of time for varied precision-based numerical algorithms with generalised equation

Therefore, to increase the reliability of the presented research, the authors have provided a generalised concept for amplification for load and displacement, which incorporates the amplification factors proposed by various researchers with varied regional data, as,

$$\left.\begin{aligned} \xi_n &= \acute{\eta}\,\tau^2 \\ \acute{\eta} &= \acute{\eta}_1 + \acute{\eta}_2\tau^{-1} + \acute{\eta}_3\tau^{-2} \end{aligned}\right\} \tag{2.28}$$

The generalised Eq. (2.28) suggests that numerical damping is influenced by both constant and inverse-power terms of τ, where the damping ratio is more prominent at lower values of τ and conceptual as τ increases. The numerical results classify and compare four different cases based on their damping behaviour. Case I, i.e., Newmark's β method, exhibits almost negligible damping, indicating a highly energy-conserving numerical scheme. Case II, i.e., the present research conducted via the proposed transient precision, shows a slight increase in damping, which may help in computations while still maintaining accuracy. Case III, i.e., the present research conducted via the proposed moderate precision, introduces a moderate level of damping, effectively balancing stability and accuracy. Case IV, i.e., Backwards Euler method, demonstrates the highest damping, with a steep increase in ξ_n as τ increases, indicating a numerical scheme that strongly dissipates energy. The increasing trend in numerical damping across these cases highlights how different numerical algorithms manage energy dissipation during time integration.

Numerical damping, conceived as a function of precision in the numerical model, ensures a reliable and stable solution. A carefully controlled damping ratio is crucial for achieving an optimal balance between stability and accuracy in simulations. For transient and moderate precision, a maximum of 0.001 and 0.03 damping ratios have been specified using non-dimensional numerically varied damping parameters, as tabulated in Table 2.4.

Table 2.4 Input time integration dissipation control parameters

Methodology	Input parameter		
	α	β	γ
Present work using moderate precision	0.7	2.41	1.91
Present work using transient precision	0.05	0.22	0.44

The selection of appropriate numerical damping depends on the nature of the simulation, where lower damping is preferable for energy-conserving applications (e.g., long-term dynamic simulations), whereas higher damping may be beneficial in scenarios requiring numerical stability (e.g., high-speed impact analysis or moving load problems). Ultimately, the insights drawn from Figure 2.7 emphasize the necessity of incorporating numerical damping to eliminate computational noise and ensure accurate, dependable numerical solutions in dynamic system simulations.

Table 2.5 shows that the methods to estimate numerical damping in the literature (Newmark's β method and Backwards Euler method) are special cases of the generalised solution presented in this work. Therefore, the generalised numerical damping factor can be effectively implemented in a finite element algorithm to obtain a reliable dynamic response of the pavement geomaterial system.

Table 2.5 Non-dimensional coefficients for estimating the numerical damping

Non-dimensional coefficients			Universality of generalised numerical damping factor
$\acute{\eta}_1$	$\acute{\eta}_2$	$\acute{\eta}_3$	
0	0	0	Case I [a]
0.3293	-0.0086	-0.00004	Case II [b]
-1.4876	0.4335	-0.0031	Case III [c]
-1.0695	0.4337	-0.0033	Case IV [d]

[a] Newmark's β method; [b] Present work using transient precision; [c] Present work using moderate precision; [d] Backward Euler method

2.3.3 Stress Response

Figs. 2.8 (a) and (b) show the effect of damping on the reliability of stress behaviour over the pavement length with velocity ratio (v_r). The velocity ratio is defined as the moving load velocity (v_m) divided by the threshold critical velocity (v_{cr}). A magnitude of 20 to 40 kPa of fluctuating stress has been observed towards the near and far ends of the pavement, with two peaks of stress at the pavement center for a numerical damping ratio (ξ_n) of 0.001. With an increase in numerical damping, it has been observed that the stress response stabilizes, as evidenced by the near, far end, and center of the pavement. The increase in the magnitude of velocity increases the stress over pavement length, and this happens because increasing velocity magnifies the magnitude of the moving load. It has been observed that stress varies between 90 to 120 kPa for ξ_n equal to 0.001 at the center and 100 to 140 kPa for ξ_n equal to 0.03. For

ξ_n equal to 0.03, peaks become distinct, indicating that numerical damping improves the response.

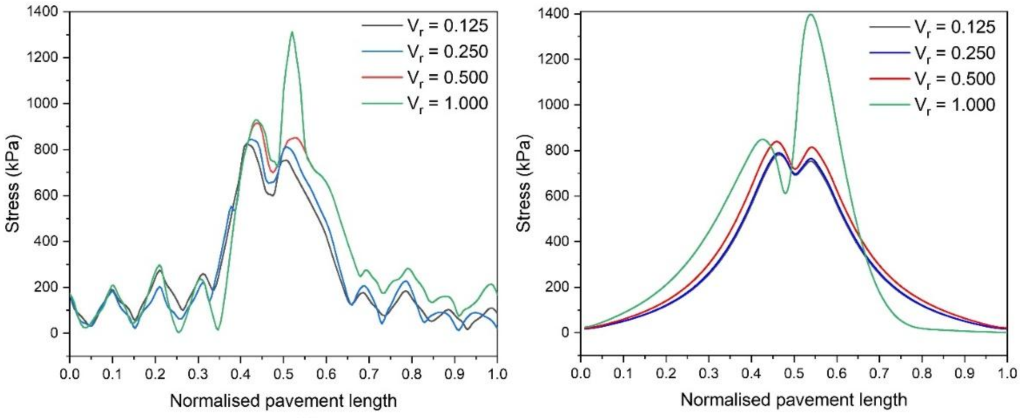

(a) (b)

Figure 2.8 Velocity-induced time integration dissipation-controlled stress response of pavement for varied input velocity ratio ranging from 0.125 to 1.0 with (a) ξ_n = 0.001; (b) ξ_n = 0.03

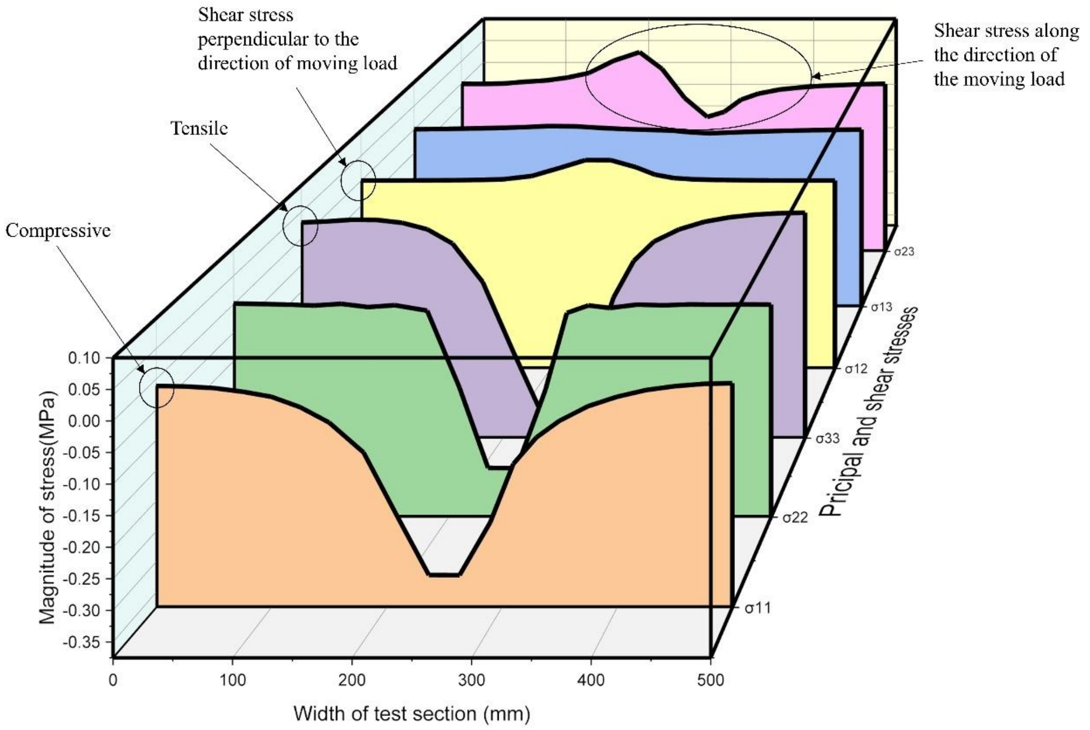

Figure 2.9 Variation of the principal stress along the pavement width

Fig. 2.9 shows the variation of principal stress along the pavement width. It has been observed that principal lateral stresses at edges, i.e., σ_{11} and σ_{33} are compressive and tensile in nature, respectively, and principal longitudinal stresses along shear stress contribute towards the permanent deformations. The shearing stresses σ_{12} support the rutting behaviour by producing a tensile action in 1-2 plane, i.e., XY plane and σ_{23} support the rutting behaviour by producing alternative compressive and tensile action in 2-3 plane, i.e., YZ plane. The aforementioned observation concludes that the displacement behaviour, stress along the pavement, and principal stress distribution best explain the basis of rutting in pavement subjected to moving load.

2.3.4 Load and Displacement Magnification

The dynamic load magnification factor (D_{mf}) is expressed as a ratio of the load under moving conditions (dynamic load) to the load at rest (static load). Furthermore, the dynamic displacement magnification factor (D_{df}) is expressed as the ratio of the displacement observed in the pavement-geomaterial assembly under moving load conditions (dynamic displacement) to the displacement observed when the load is at rest (static displacement). The non-dimensional factors have been Conceptualized to observe the velocity-induced load and displacement magnifications. These magnification factors have been estimated and implemented as multipliers to account for the effects of moving loads on pavement dynamics. The load magnification obtained using moderate precision has been increased by 4-7% more than the load magnifications calculated using the transient precision for selected input velocities (15-250 m/s). It has been observed that, up to a velocity ratio of 0.125, the magnification effects exhibit a similar trend to those under static loading. The dynamic load magnification factor (D_{mf}) escalates with a rise in the magnitude of moving load velocity up to a critical velocity input, as evident from Fig. 2.10 (a). The magnitude of dynamic magnification at this critical threshold velocity ($v_{cr} \sim 125$ m/s) has increased by 70%. Beyond this point, the D_{mf} has been observed to be significantly reduced, dropping to 54%. From Fig. 2.10(b), it is observed that the displacement amplification effects are analogous to static loading for a load moving up to a velocity ratio of 0.125. Afterwards, the dynamic displacement factor (D_{df}) increases with a rise in the magnitude of the moving load velocity up to a critical velocity, as evident from Fig. 2.10(b). It has been observed that the magnitude of D_{df} at critical threshold velocity (v_{cr} ~ 125 m/s) has increased up to 46% in pavement and approximately 40% in granular base and soil subgrade layer.

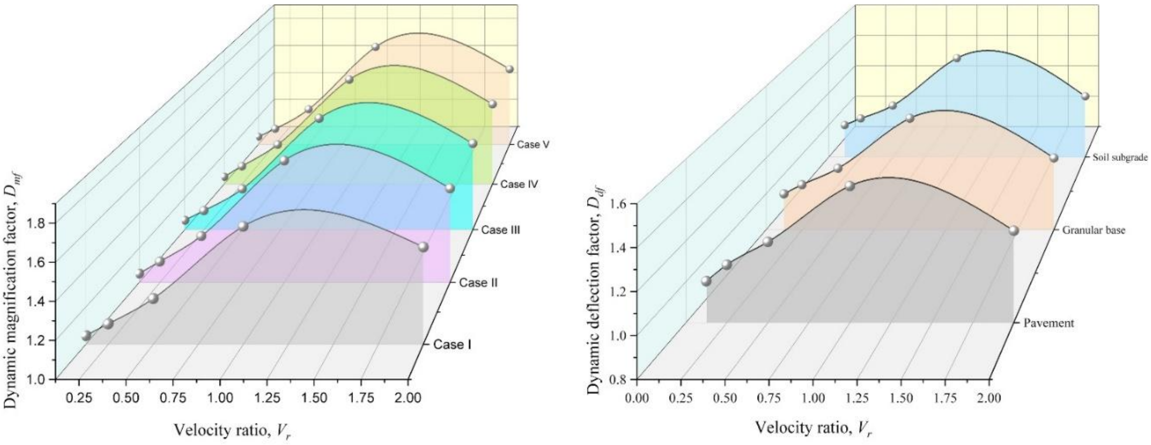

Figure 2.10 Variation in magnitude of dynamic magnification factor (D_{mf}) with velocity ratio (V_r) obtained using generalised empirical model and variation in magnitude of dynamic deflection factor (D_{df}) for pavement, granular base, and soil subgrade

Table 2.6 Non-dimensional coefficients for estimating the amplification factor

Non-dimensional coefficients			Universality of the generalised magnification factor
ϑ_1	ϑ_2	ϑ_3	
0.84112	1.20284	-0.42789	Case I [a]
0.84018	1.2236	-0.43878	Case II [b]
0.84949	1.18902	-0.42289	Case III [c]
0.8419	1.22656	-0.43846	Case IV [d]
0.86269	1.07557	-0.37497	Case V [e]

[a] Yoshida & Weiver (1971); [b] Taheri & Ting (1990); [c] Wu & Shen (1996); Present work using [d] moderate precision; [e] transient precision

Based on these findings, a generalised empirical amplification factor has been presented by Eq. (2.29).

$$\left.\begin{aligned} D_{mf} &= \vartheta v_r^2 \\ \vartheta &= \vartheta_1 + \vartheta_2 v_r^{-1} + \vartheta_3 v_r^{-2} \end{aligned}\right\} \tag{2.29}$$

Generalised Eq. (2.29) has special cases, namely Cases I to V, which were validated against the observed values in the references. Table 2.6 shows that the solutions available in the literature (Yoshida & Weiver, 1971; Taheri & Ting, 1990; Wu & Shen, 1996) are special cases of the solution presented in this work. This indicates that time integration dissipation control has improved the dependability and accuracy of numerical solutions for designing and analysing pavement-geomaterial systems.

Table 2.7 Systematic representation of amplification factors with velocity ratio and velocity (in m/s and km/h) for engineering implications and benefit to researchers

Velocity ratio, V_r	Velocity, V		Load amplification factor	Displacement amplification factor			Application
	m/s	km/h		Pavement	Granular base	Soil subgrade	
0 to 0.25	0 to 31.25	0 to 112.5	1.0 to 1.1	1.0 to 1.08	1 to 1.05	1 to 1.04	Expressways with controlled access*
0.25 to 0.5	31.25 to 62.5	112.5 to 225	1.1 to 1.2	1.08 to 1.19	1.05 to 1.14	1.04 to 1.12	Future super expressways**
0.5 to 1.0	62.5 to 125	225 to 450	1.2 to 1.7	1.19 to 1.46	1.14 to 1.42	1.12 to 1.41	High-speed guideways (F1-racing tracks) ***
1.0 to 2.0	125 to 250	450 to 900	1.7 to 1.5	1.46 to 1.25	1.42 to 1.20	1.41 to 1.18	The projected values are obtained in order to explore responses beyond the threshold.

$V_r = V/V_{cr}$; $V_{cr} = 125$ m/s
*Ministry of Road Transport and Highways (MORTH) S.O. 1522€: [F. No. RT-11028/07/2017-MVL]
** Kumar et al. (2024b)
***Mercedes w11 (2020)

The validity of the previous parameters, namely load and displacement amplifications, has been enhanced by testing the data in real-world applications from expressways with controlled access, future super expressways, and high-speed guideways (e.g., F1 Racing tracks). Beyond that, the projected values are obtained to explore responses beyond the threshold in situations such as complex calculations in large-scale experiments or when the measurement system may not function properly. A systematic representation of amplification factors, including velocity ratio and velocity (in m/s and km/h), is presented in Table 2.7 for engineering implications and benefits to researchers.

2.4 Conclusions

In this study, a comprehensive and novel theory of numerical damping evolution has been developed by introducing a new family of dimensionless damping parameters for pavement–geomaterial systems. This generalised framework advances the numerical modelling of dynamic load propagation in pavements by systematically integrating damping behaviour into numerical simulations. Based on the analyses, the following key conclusions have been drawn:

- Introduction of a generalised numerical damping ratio (ξ_n): The concept of numerical damping ratio (ξ_n) significantly enhances the fidelity of dynamic simulations by mitigating numerical noise. The proposed damping parameters (α, β, γ, $\acute{\eta}$, and ϑ) enable a tunable ξ_n ranging from 0.001 to 0.03. This provides both transient-level precision (in similitude with Newmark's β-method) and moderate precision (analogous to the Backwards Euler method), allowing for flexible control of stability and accuracy in numerical models.

- Development of a generalised dissipation amplification framework: The study introduces a unified mechanism that subsumes existing models in the literature as special cases. The generalised amplification factor derived herein spans a broader range of velocity and material scenarios, offering a more robust predictive capability for dynamic amplification phenomena under moving loads.
- Velocity-driven stress response: A strong correlation was observed between increasing load velocity and rising stress magnitudes along the pavement length. Stress values ranging from 90 to 140 kPa were reported for ξ_n between 0.001 and 0.03, with clearer peak formation at $\xi_n = 0.03$. This evidences the role of damping in refining stress resolution and eliminating spurious oscillations.
- Load and displacement magnification: The amplification factors for load and displacement are notably higher (by 4–7%) under moderate damping conditions than those under transient damping, across velocity ranges of 15–250 m/s. At the threshold velocity (v_{cr}), dynamic load and displacement were amplified by up to 70% and 31%, respectively, clearly indicating the significance of generalised damping in realistic pavement response modelling.
- The stress and deflection response along the pavement centre and edges for each layer in the pavement geomaterial system serve as the basis for the growth of ruts and permanent deformation. It is observed that the deflection of the pavement-geomaterial system in the numerical model is 0.56 mm and 0.6 to 0.64 mm at the edges and centre of pavement, granular base course, and soil subgrade layers respectively. The permanent deformations and stresses are seen to exist throughout the pavement width in all the layers of pavement-geomaterial system.

- The equivalent stress at the edges and the center has been reported in the range of 10^{-3} to 10^{-2} MPa and 0.05 to 0.18 MPa respectively, for pavement-geomaterial system. It is observed that principal lateral stresses at edges are compressive and tensile in nature and principal longitudinal stresses along with shear stresses contribute towards permanent deformations. The shearing stresses in the XY plane support the rutting behaviour by producing a tensile action, and shearing stresses in the YZ plane support the rutting behaviour by producing alternative compressive and tensile action.

This study presents the first generalised numerical dissipation framework specifically tailored for pavement-geomaterial systems subjected to moving loads. It not only bridges a critical gap in pavement dynamics but also provides a foundation for revising current pavement design philosophies. The proposed damping model, with its capability to predict realistic in-situ responses and remove computational instabilities, can be effectively adopted by geotechnical engineers and transportation agencies in both design and performance evaluation of roadway infrastructures.

References

1. Ai, Z. Y., Wang, X. M., Song, X., & Yang, J. J. (2022). Dynamics of plates resting on layered transversely isotropic poroelastic media under moving loads. Journal of Sound and Vibration, 533, 117022. https://doi.org/10.1016/j.jsv.2022.117022
2. Beskou, N. D., & Muho, E. V. (2023a). Review on dynamic response of road pavements to moving vehicle loads; part 1: Rigid pavements. Soil Dynamics and Earthquake Engineering, 175, 108249. https://doi.org/10.1016/j.soildyn.2023.108249

3. Beskou, N. D., & Muho, E. V. (2023b). Review on dynamic response of road pavements to moving vehicle loads; part 2: Flexible pavements. Soil Dynamics and Earthquake Engineering, 175, 108248. https://doi.org/10.1016/j.soildyn.2023.108248
4. Beskou, N. D., & Theodorakopoulos, D. D. (2011). Dynamic effects of moving loads on road pavements: A review. Soil Dynamics and Earthquake Engineering, 31(4), 547–567. https://doi.org/10.1016/j.soildyn.2010.11.002
5. Ding, H., Yang, Y., Chen, L. Q., & Yang, S. P. (2014). Vibration of vehicle–pavement coupled system based on a Timoshenko beam on a nonlinear foundation. Journal of Sound and Vibration, 333(24), 6623–6636. https://doi.org/10.1016/j.jsv.2014.07.016
6. Elishakoff, I. (2020). Handbook on Timoshenko-Ehrenfest beam and Uflyand-Mindlin plate theories. World Scientific.
7. Froio, D., Verzeroli, L., Ferrari, R., & Rizzi, E. (2021). On the numerical modelization of moving load beam problems by a dedicated parallel computing FEM implementation. Archives of Computational Methods in Engineering, 28(4), 2253–2314. https://doi.org/10.1007/s11831-020-09459-5
8. He, Y., & Yang, J. P. (2021). Using Kalman filter to estimate the pavement profile of a bridge from a passing vehicle considering their interaction. Acta Mechanica, 232(11), 4347–4362. https://doi.org/10.1007/s00707-021-03055-9
9. Hilber, H. M., Hughes, T. J., & Taylor, R. L. (1977). Improved numerical dissipation for time integration algorithms in structural dynamics. Earthquake Engineering & Structural Dynamics, 5(3), 283–292. https://doi.org/10.1002/eqe.4290050306
10. Huang, J., Li, X., Zhang, J., Sun, Y., & Ren, J. (2022). Determining the Rayleigh damping parameters of flexible pavements for finite element modeling. Journal of

Vibration and Control, 28(21-22), 3181–3194.
https://doi.org/10.1177/107754632110267

11. Ju, S. H. (2011). Vibration analysis of 3D Timoshenko beams subjected to moving vehicles. Journal of Engineering Mechanics, 137(11), 713–721. https://doi.org/10.1061/(ASCE)EM.1943-7889.0000276
12. Kansake, B. A., Frimpong, S., Nyaaba, W., & Ateng, I. A. (2023). Three-dimensional finite element modeling of haul road response to ultra-large dump truck dynamic loading. Mining, Metallurgy & Exploration, 40(1), 315–335. https://doi.org/10.1007/s42461-022-00725-7
13. Kim, Y. R. (Ed.). (2014). Asphalt pavements. CRC Press.
14. Kim, N. H. (2026). Finite Element Analysis for Time-Dependent Problems. In *Introduction to Nonlinear Finite Element Analysis,* 449-487. Cham: Springer Nature Switzerland. https://doi.org/10.1007/978-3-032-09708-8_6
15. Khan, S., Nagabhushana, M. N., Tiwari, D., & Jain, P. K. (2016). Comparison of uni and bi-directional load induced rutting in flexible pavement with accelerated pavement testing facility (APTF). Transportation Research Procedia, 17, 521-528. https://doi.org/10.1016/j.trpro.2016.11.106
16. Kumar, Y. (2020). Dynamic analysis of constrained rigid pavement subjected to moving load (M. Tech dissertation). Delhi Technological University, Delhi, India.
17. Kumar, Y., Trivedi, A., & Shukla, S. K. (2024a). Damage evaluation in pavement-geomaterial system using finite element-scaled accelerated pavement testing. Transportation Infrastructure Geotechnology, 11(3), 922–933. https://doi.org/10.1007/s40515-023-00309-y

18. Kumar, Y., Trivedi, A., & Shukla, S. K. (2024b). Deflections governed by the cyclic strength of rigid pavement subjected to structural vibration due to high-velocity moving loads. Journal of Vibration Engineering & Technologies, 12(3), 3543–3562. https://doi.org/10.1007/s42417-023-01063-8

19. Kumar, Y., Trivedi, A., & Shukla, S. K. (2025). Impact of moving load vibrations on pavement damage supported by flow-controlled geomaterials. International Journal of Non-Linear Mechanics, 172, 105045. https://doi.org/10.1016/j.ijnonlinmec.2025.105045

20. Ling, H. I., & Liu, H. (2003). Finite element studies of asphalt concrete pavement reinforced with geogrid. Journal of Engineering Mechanics, 129(7), 801–811. https://doi.org/10.1061/(ASCE)0733-9399(2003)129:7(801)

21. Liu, Z., Niu, J., & Jia, R. (2021). Dynamic analysis of arbitrarily restrained stiffened plate under moving loads. International Journal of Mechanical Sciences, 200, 106414. https://doi.org/10.1016/j.ijmecsci.2021.106414

22. Lu, Z., Fang, R., Yao, H., Dong, C., & Xian, S. (2018). Dynamic responses of unsaturated half-space soil to a moving harmonic rectangular load. International Journal for Numerical and Analytical Methods in Geomechanics, 42(9), 1057–1077. https://doi.org/10.1002/nag.2780

23. Lytton, R. L., Uzan, J., Fernando, E. G., Roque, R., Hiltunen, D., & Stoffels, S. M. (1993). Development and validation of performance prediction models and specifications for asphalt binders and paving mixes, 357. Strategic Highway Research Program.

24. Ma, L., Nie, W., Zhang, X., Yan, J., & Wang, D. (2022). Experimental study of Poisson’s ratio in indirect tensile test mode for asphalt mixtures. Construction and Building Materials, 355, 129288. https://doi.org/10.1016/j.conbuildmat.2022.129288
25. Ministry of Road Transport and Highways. (n.d.). S.O. 1522(e): [F. No. RT-11028/07/2017-MVL].
26. Mercedes W11. (2020). F1 W14 E Performance – Mercedes-AMG PETRONAS F1 Team. https://www.mercedesamgf1.com/car/2023-car
27. Rith, M., Kim, Y. K., & Lee, S. W. (2021). Estimation of stress at interface of asphalt surface and rigid base of composite pavement. Proceedings of the Institution of Civil Engineers – Transport, 174(6), 345–353. https://doi.org/10.1680/jtran.17.00106
28. Snehasagar, G., Krishnanunni, C. G., & Rao, B. N. (2020). Dynamics of vehicle–pavement system based on a viscoelastic Euler–Bernoulli beam model. International Journal of Pavement Engineering, 21(13), 1669–1682. https://doi.org/10.1080/10298436.2018.1562189
29. Sun, L. (2016). Structural behavior of asphalt pavements: Integrated analysis and design of conventional and heavy-duty asphalt pavement. Butterworth-Heinemann.
30. Taheri, M. R., & Ting, E. C. (1989). Dynamic response of plate to moving loads: Structural impedance method. Computers & Structures, 33(6), 1379–1393. https://doi.org/10.1016/0045-7949(89)90478-1
31. Taheri, M. R., & Ting, E. C. (1990). Dynamic response of plates to moving loads: Finite element method. Computers & Structures, 34(3), 509–521. https://doi.org/10.1016/0045-7949(90)90276-8

32. Wang, B., & Yang, J. (2008). Effects of vehicle dynamic loading on CRCP by 3D finite element method. Journal of South-east University: Natural Science Edition, 38(5), 850–855.
33. Wang, Y. Z., & Fu, C. G. (2010). ABAQUS structural engineering analysis and example explanation. China Architecture and Building Press, Beijing, China.
34. Xu, Y., Yang, C., Zhang, W., Zhu, W., & Fan, W. (2022). A new moving Kirchhoff–Love plate element for dynamic analysis of vehicle–pavement interaction. Journal of Vibration and Acoustics, 144(4), 041007. https://doi.org/10.1115/1.4053474
35. Xu, Y., Yang, C. J., Zhu, W. D., & Zhang, W. H. (2023). A reduced-plate model transmission method for fast dynamic analysis of vehicle–pavement interaction. Journal of Sound and Vibration, 548, 117554. https://doi.org/10.1016/j.jsv.2023.117554
36. Yang, S., Li, S., & Lu, Y. (2010). Investigation on dynamical interaction between a heavy vehicle and road pavement. Vehicle System Dynamics, 48(8), 923–944. https://doi.org/10.1080/00423110903243166
37. Yang, S., Lu, Y., & Li, S. (2013). An overview on vehicle dynamics. International Journal of Dynamics and Control, 1(4), 385–395. https://doi.org/10.1007/s40435-013-0032-y
38. Yao, Z. Y., Zhou, L. J., Shang, Q. S., Guo, J. M., & Wang, N. (2012). Analysis of rutting change rule on asphalt pavement overlay. Advanced Materials Research, 368, 3131–3136. https://doi.org/10.4028/www.scientific.net/AMR.368-373.3131
39. Zhao, J., & Wang, H. (2020). Dynamic pavement response analysis under moving truck loads with random amplitudes. Journal of Transportation Engineering, Part B: Pavements, 146(2), 04020020. https://doi.org/10.1061/JPEODX.0000173

40. Zhuang, Z., You, X., Liao, J. H., Cen, S., Shen, X., & Liang, M. (2009). Finite element analysis and application based on ABAQUS. Beijing: Tsinghua University Press.

3

Chapter

Velocity-Induced Dynamic Response of Pavement–Soil System

Highlights

- In this chapter, A finite-element-based cyclic response model is proposed to evaluate velocity-induced stress ratios for rigid pavement design under high-velocity moving loads.
- The study identifies velocity-induced deflection zones and displacement contours, revealing displacement shifts and phase transformations in stress fields beyond critical conditions.
- The Vibrational Compounded Stress Transfer Mechanism (V-CSTM) is introduced, linking pavement thickness, load intensity, and vehicle velocity for dynamic pavement design.
- The cyclic strength of rigid pavement is quantified as 0.01–0.2% of the characteristic strength, indicating high endurance under repeated moving loads.
- The findings predict that rigid pavements can withstand 10^{15}–10^{9} load cycles, offering practical insights for engineers to estimate pavement lifespan over granular bases.

3.1 Background

The evaluation of cyclic strength due to structural vibrations caused by high-velocity moving loads on rigid pavements is a potential area of active research for scientists, engineers, and practitioners. Engineers and practitioners design pavements for a specific period (Bourdeau et al., 2021; Singh et al., 2020a). For effective design and durability consideration, a pavement must meet specific pavement performance parameters (Singh et al., 2020b). Cyclic strength is one of the parameters that can be used to estimate the life of a pavement (Singh et al., 2019). Hence, evaluating the cyclic strength of rigid pavements has a potential avenue for pavement design and construction practices (Kumar et al., 2024). In this direction, a non-uniform, bi-directionally functionally scaled beam was made to vibrate in a size-dependent mode while carrying a moving harmonic mass (Rajasekaran & Khaniki, 2019). Furthermore, in nanoscale studies, the effect of moving nanoparticles on nanobeams and nanoplates in a multi-layer viscoelastic medium has been investigated to understand the dynamics of a moving load on a nanoscale (Hashemi & Khaniki, 2018; Hosseini-Hashemi & Khaniki, 2018; Hashemi & Khaniki, 2017). Polygonal finite element and hybrid metaheuristic search algorithms, utilizing experimental data from wireless triaxial sensors, have been adopted in the literature to examine the two-dimensional lid-driven cavity flow and a multi-span bridge, respectively (Vu et al., 2022; Tran-Ngoc et al., 2021). Numerical prediction of microstructure & hardness and crack propagation in quasi-brittle materials by the fourth-order phase-field cohesive zone model was simulated in a finite element numerical programme, and reported the effectiveness of numerical modelling for better understanding of brittle material (Ling et al., 2023; Nguyen et al., 2022). The vehicle-pavement-soil interaction effects are crucially significant for the stability, durability, and strengthening or weakening of rigid pavements subjected to moving loads (Lewis & Harr, 1969; Taheri & Ting, 1990). The immense complexities of the pavement-soil interaction system remain to be adequately resolved and modelled for field applications. The transfer mechanism of stresses in layered media for a moving load has been a significant concern for engineers, scientists, and practitioners for many years (Burmister, 1945a, b, c; Chen, 1971; Hoskin & Lee, 1959). Timoshenko beam theory has been used in extensive pavement literature to obtain the analytical solution for an infinite beam subjected to moving load, assuming that the foundation soil is linearly viscoelastic (Achenbach & Sun, 1965). An improved two-dimensional finite element algorithm for analysing the transient response under arbitrary boundary conditions with the moving load was introduced by Taheri & Ting (1989; 1990).

Wu & Shen (1996) proposed an improved three-dimensional finite-element algorithm to analyse the behaviour of concrete pavements subjected to moving loads. The dynamic behaviour and interaction effects between moving load and pavement-subgrade-soil systems contain severe mathematical complexities. So, mathematical modelling for static loading alone cannot be adopted to study the dynamics of concrete pavement exposed to fast-moving vehicular loading (Wang & Yang, 2008; Yang et al., 2010; Eberle & Oberguggenberger, 2022). Using the classical approach, the mass-spring-dashpot system was adopted for modelling the moving load with constant velocity over concrete pavement (Ding et al., 2014). Further, Fourier Transform (FT) was adopted to obtain the solution for the problem of moving harmonic load on unsaturated half-space (Lu et al., 2018). Following the solution for the same problem, the variation of displacement and stress has been observed for varied saturation and permeability conditions. The investigations were carried out on plates supported by unsaturated poroelastic material (Kumar, 2020; Singh et al., 2022; Tang et al., 2020).

A 3D finite element creep model was established to investigate the rutting behaviour of pavement. The findings revealed that the pavement rutting under various loads and temperatures has a nonlinear development pattern (Zhao et al., 2015). Furthermore, ANSYS was utilized to investigate the deformation properties of the surface course and roadbed. Based on the Maxwell and Drucker-Prager model, it has been observed that load level and roadbed modulus have a substantial impact on rutting (Tang et al., 2008). The correlations were developed between rutting depth, load time, and surface course thickness. The creep and elastic models within ABAQUS were adopted to develop the aforesaid correlations (Yao et al., 2012). It was observed that the theoretical values and the actual measured values were consistent with each other. The relationship between the simulation results and the real measured indoor Asphalt Pavement Analyser (APA) results was developed using elastic and viscoplastic creep models (Pirabarooban et al., 2003). The anti-rutting characteristics of pavement structures were examined along with the influence of external factors. The temperature, tire contact pressure, and the number of loadings were considered as external factors for investigating the formation process of rutting. A 2D finite element model was developed based on the Bailey-Norton elasto-plastic and the Mohr-Coulomb plastic model (Li et al., 2015). Further, Hua & White (2002) demonstrated the critical congruence between the anticipated rutting values made by the 2D model and the 3D model using the time-hardening parameters. A 3D finite element model using ABAQUS was developed to examine the elastic viscoplastic behaviours of the road surface subjected to moving loads and provided numerous ways to prevent rutting (Cao et al., 2012). The anti-rutting performance of big-interspaced asphalt pavement under various rubber contents through static and repeated load tests was investigated (Imaninasab et al., 2016). The design criteria for concrete pavements in the literature are based on analytical solutions and empirical formulations and lack in calibrating the cyclic strength of pavement to the velocity inputs (BBK04, 2004; Eurocode 2 EC2, 2004; IRC 58, 2015). The solution to the central deflection (d_c) and stress response for moving load is very complex since they involve uncharacteristic end conditions (Tong et al., 2020). It has been observed that cyclic strength is a crucial parameter for pavement performance research and construction practices. A plastic strain as a function of the number of cycles was presented using a power law to estimate the cyclic strength of pavement (Monismith et al., 1975; VESYS, 1977). The power law mentioned in the literature could only relate plastic strain with the number of cycles with empirical fitting parameters. Hence, empirically driven semi-logarithmic and exponential functions were proposed to predict the plastic strain corresponding to the varied number of cycles (Barksdale, 1972; Lytton et al., 1993; Tseng & Lytton, 1989). Based on pavement performance research, standard codes of practice for different nations provided guidelines for estimating cyclic strength (AASTHO, 2002; IRC 58, 2015). The plastic strain corresponding to the number of cycles prescribing the cyclic strength of rigid pavements subjected to structural vibrations and codal provision relationships for stress and strain ratio corresponding to the number of cycles prescribing the cyclic strength of rigid pavements subjected to structural vibrations are tabulated in Table 3. 1 and 3.2.

Table 3.1 Plastic strain corresponding to the number of cycles prescribing cyclic strength of rigid pavements subjected to structural vibrations

Mathematical function	Constitutive relationship for plastic strains
Power law [p]	$\varepsilon_p = N^b$
Power law [q]	$\varepsilon_{pn} = \mu \varepsilon_r N^{-\alpha}$
Semi-logarithmic [r]	$\varepsilon_p = a + b\ logN$
Semi-logarithmic [s]	$\varepsilon_p = log\ \varepsilon_p(1) + S\ logN$
Exponential [t]	$\varepsilon_p = \varepsilon_0 e^{-(\rho/N)^{\beta}}$
Present Study	$\Delta\varepsilon^p = \dfrac{(1 - plogN)f_{ck}}{\sigma^{tr} - 2G}$

[p] Monismith et al., (1975), [q] VESYS (1977), [r] Barksdale (1972), [s] Lytton et al., (1993), [t] Tseng & Lytton (1989)

Table 3.2 Codal provision relationships for stress and strain ratio corresponding to the number of cycles prescribing cyclic strength of rigid pavements subjected to structural vibrations

Codal provisions	Constitutive relationship for stress and strain ratio
AASTHO[a]	$log\dfrac{\varepsilon_p}{\varepsilon_r} = -3.74938 + 0.4262 logN + 2.02755 \log T$
IRC[b]	$N = \infty, for\ S_r < 0.45$ $N = \left[\dfrac{4.2577}{S_r - 0.4325}\right]^{3.268}, for\ 0.45 \leq S_r \leq 0.55$ $log_{10}N = \dfrac{0.9718 - S_r}{0.0828}, for\ S_r > 0.55$
Cyclic response-based stress ratio model[c]	$\log N = \dfrac{1 - S_r}{p}$ $S_r = \dfrac{(\sigma_{CN:\,N=1})}{(f_{ck})} = \dfrac{\sigma^{tr} - 2G\Delta\varepsilon^p}{f_{ck}} = \lambda e^{\varphi \times v}$

[a] AASTHO (2002), [b] IRC 58 (2015), and [c] Present Study

The literature survey led to an observation that the aforementioned study demonstrates the widespread use of a numerical program like ABAQUS and ANSYS for estimating the deflection in the pavement at low velocities. Moreover, the experimental studies only estimate the rut depth with the number of cycles without giving due consideration to velocity. Very limited studies are available on the transfer mechanism of displacement in pavements. The empirical solutions provide displacement response of pavement in a limited scope of research. There is still a great need to study the displacement response of rigid pavement along with stress variation and cyclic strength under moving load conditions using numerical modelling. The cyclic strength in the literature is estimated without giving due consideration to the velocity of the moving load, stress transfer mechanism, pavement dynamics, and vibrations caused by the moving load. Hence, the present study is conducted with the following main objectives as presented below:

- To evaluate the effect of velocity on central deflection, stress, and stress ratio of pavement subjected to high velocity moving load.
- To identify the possible velocity-induced deflection concentrated zones for estimating the amplification caused by the action of the dynamic load of the wheel moving at high velocity.
- To determine the role of principal stresses and examine the compounded vibrational stress transfer mechanism.
- Finally, to develop a novel velocity-induced stress ratio for the design of highways supporting high-velocity moving loads.

In light of the aforementioned objectives, a novel finite-element-based cyclic response model has been developed to determine a velocity-induced stress ratio for rigid pavement design supported by granular bases. An attempt is made to develop a solution for the stress transfer, strength, and deformation characteristics of pavements subjected to moving loads in the commercial software package ABAQUS (2017). An implicit integration scheme has been employed to investigate the dynamic response of rigid pavements supported by granular bases. The moving load conditions were simulated using a DLOAD subroutine program. The stress variations have been studied using the concept of principal stress fields, and the velocity-based stress ratio (S_r) is calculated to overcome the limitations of available literature. The transfer of the stresses from pavement to granular bases, i.e., granular base (GB) and soil subgrade (SS), has been observed along the pavement length with one observation point at the centre, one at the near end (point towards which the vehicle is approaching), and one far end (point from which the vehicle started moving). The results are compared with the output obtained from numerically varied parameters utilizing codal specifications and American Concrete Institute (ACI 318-14, 2015) strength parameters.

3.2 Model Definition

The present study was conducted in terms of central deflection (d_c) and stress responses. The velocity-induced impact zones for moving loads on the pavement, in terms of central deflection (dc), are conceptualized as shown in Fig. 3.1. Based on these influence zones, engineers and practitioners can effectively make decisions for pavement design. The pavements are exposed to a varied magnitude of loading and velocity in a diverse pattern of geographical and demographic conditions. Traffic may be moving at low speeds (village roads, district roads), moderate speeds (state highways), or high speeds (National Highways and Expressways). Depending on the exposure conditions of the pavement, engineers and practitioners can decide on parameters for the design as presented in this study. A commercial finite element software package (ABAQUS, 2017) has been used to model the rigid pavement (P), granular base (GB), and soil subgrade (SS) assembly for the investigation of moving load problems (Wang & Fu, 2010).

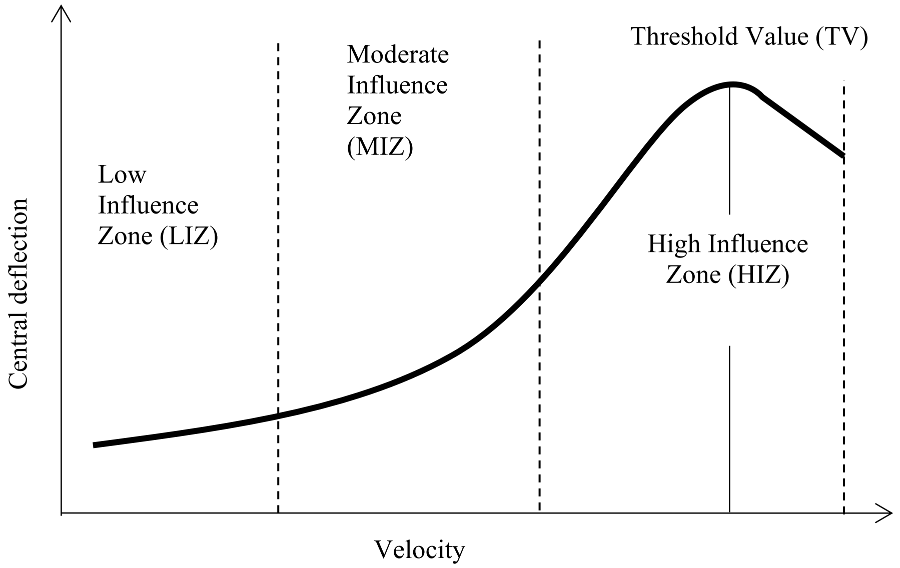

Figure 3.1 Conceptual visualization of velocity-induced impact zones for variation of central deflection

A few investigators preferred a reduced-dimensional analysis considering numerous tire models for modelling the quarter and half portions of the car (Yang et al., 2013). The half-model of symmetry has been considered to reduce computation time. Consequently, in the present investigative efforts, dimensions were reduced, and the analysis was performed. Fig. 3.2 shows the line diagram of the problem statement in the sectional and isometric views. The lengths of the pavement, granular base, and soil subgrade have been taken as 10 m for all three layers. Further, the width and thickness specifications of pavement, granular base, and soil subgrade have been shown in Fig. 3.2. Further, Fig. 3.3 shows the mesh profile of the pavement-granular base-soil subgrade system. The meshing has been done using the global seeding decrementing meshing approach. As shown in Fig. 3.3, the decrementing of elements has approached in the positive x-direction (i.e., below the loading section) with axisymmetric boundary conditions. The maximum and minimum sizes of the global seeding are set to 0.1 and 0.04, respectively, to address the issue of mesh convergence. A linear shape function of the 3D stress family with the C3D8R (Continuum Three-dimensional Eight Nodded with Reduced Integration), an 8-node linear brick element in a reduced integration scheme, has been adopted to examine the investigations performed in the present study.

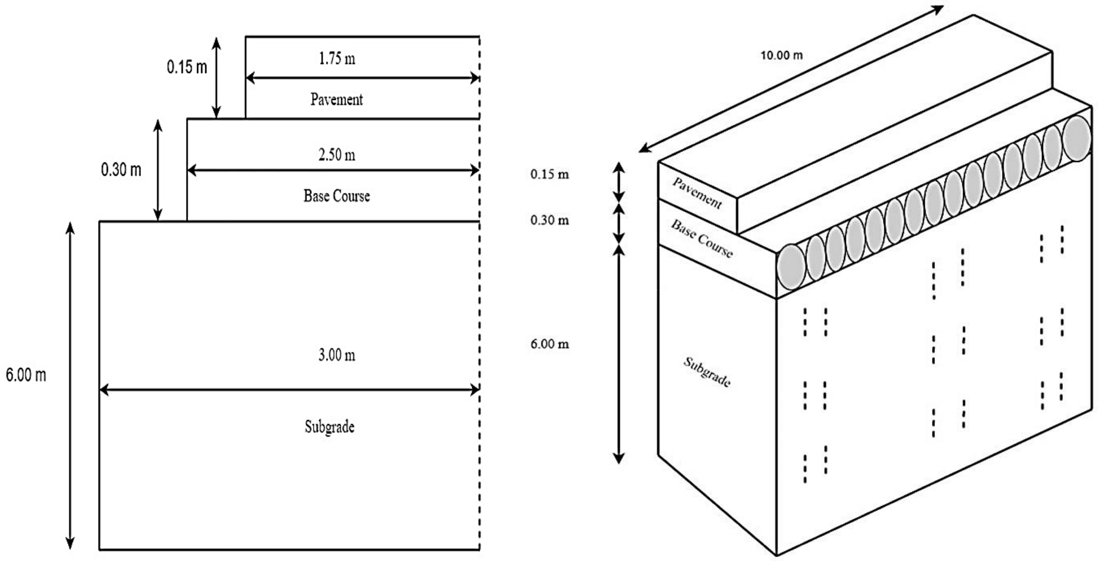

(a) (b)

Figure 3.2 Line diagram (not drawn to the scale) consisting of (a) a sectional front view of the rigid surface course-granular base course-soil subgrade system with boundary conditions and (b) an isometric view of a half-symmetric model of the rigid surface course-granular base course-soil subgrade system

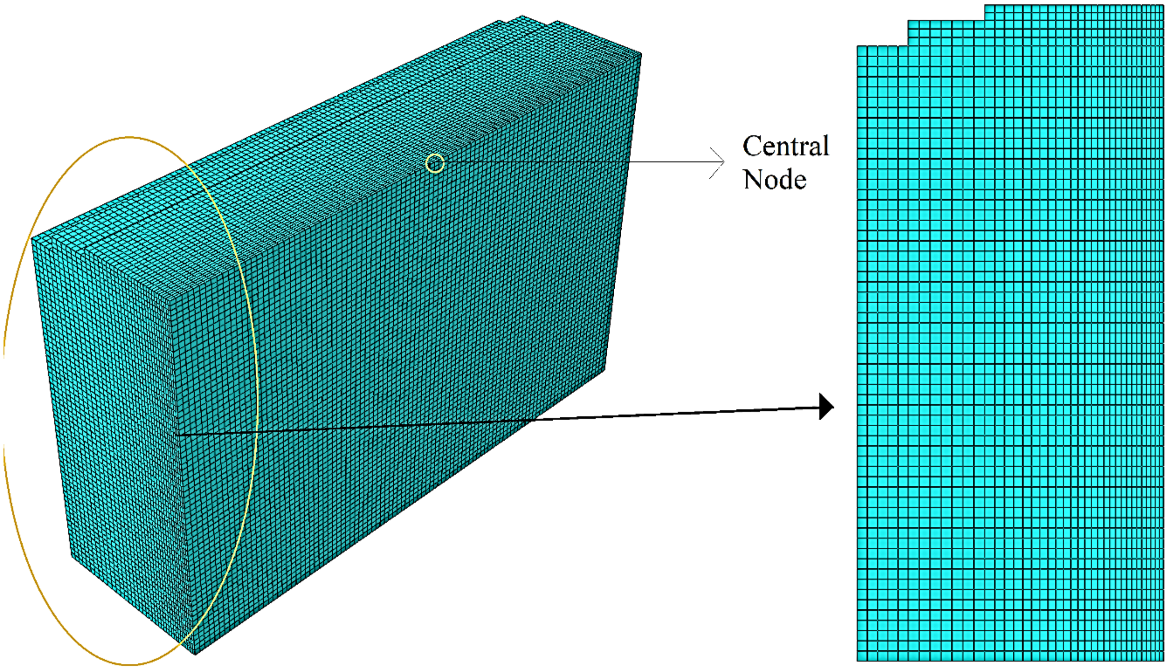

Figure 3.3 Mesh profile of the rigid surface course, granular-base course, and soil subgrade system with a mesh profile of global seeding from 0.1 to 0.04

The loading on the top surface of the pavement has been applied using a rectangle of size 0.24×0.16 m in a DLOADs subroutine program coded using FORTRAN (vs2013) with varied loading inputs as per the codal provision in IRC 58 (2015). Further, FORTRAN (vs2013) coding details are provided in the supplementary material. The specifications for properties of pavement, granular base, and soil subgrade are listed according to Young's modulus, Poisson's ratio, and unit weight, as presented in Table 3.3. The cyclic strength of the pavement has been calculated as,

$$f(N) = \frac{\sigma_{(CN:\,N=m)}}{f_{ck}} \tag{3.1}$$

where $\sigma_{(CN)}$ is the cyclic strength of the material;

if the material fails in the mth cycle, then cyclic strength is expressed as $\sigma_{(CN:\,N=m)}$ estimated using Eq. (3.1);

else if the material fails in one cycle of loading, then mathematically, it is equal to f_{ck} and calculated as per ACI (318-14) [38] as $f_{ck} = \left(\frac{E}{393}\right)^2$ Mpa.

Table 3.3: Input parameters for the present study

Material parameter	Layer	Magnitude
Young's modulus, E (Mpa)	Surface course	25×10^3
	Granular base course	276
	Soil subgrade	51.50
Poisson's ratio, v	Surface course	0.15
	Granular base course	0.30
	Soil subgrade	0.40
Unit weight, γ (kN/m^3)	Surface course	23.24
	Granular base course	17.60
	Soil subgrade	18.40

It is worth noting that this study is based on certain assumptions, as they are essentially required to make the solution presented possible. Key assumptions are the following:

- The joint is one of the important parameters considered for temperature variation in pavement. Temperature stress is a distinguished subject that is not considered in the present study.
- The numerical model is assumed to be symmetric about the length of the pavement to reduce computation time.
- The moving vehicular load is assumed as a rectangle of size 0.16 × 0.24 cm as prescribed in the literature.
- The damping effects in terms of mass and stiffness matrices are induced in the pavement-geomaterial model by numerical parameters.

Further, the details of the finite element numerical investigation model are provided in the supplementary material.

3.2.1 Numerical Modelling

The moving vehicular loading effects have been captured using the time-dependent implicit integration scheme. The displacement, depending on time, has been captured using the D'Alembert principle, and the motion equation is expressed as,

$$[M]\{\ddot{x}\} + [C]\{\dot{x}\} + [K]\{x\} = \{F_E\} \tag{3.2}$$

where $[M]$, $[C]$, and $[K]$ are the corresponding mass, damper, and stiffness matrices, respectively. $\{\ddot{x}\}$ is the acceleration vector associated with the mass matrix, $\{\dot{x}\}$ is the velocity vector associated with the damper matrix, $\{x\}$ is the displacement vector associated with the stiffness matrix, and $\{F_E\}$ is the externally prescribed force vector. The equation of motion in terms of externally prescribed force and body force related to elemental volume is expressed as,

$$\{Q_B\} + \{Q_I\} = \{Q_E\} \tag{1.3}$$

where, $\{Q_B\}$ is the body force, $\{Q_I\}$ is the inertial force, and $\{Q_E\}$ is the externally prescribed force.

The isoparametric solid elements used in the pavement, granular base, and soil subgrade system are solved numerically by a reduced integration scheme. The reduced integration scheme used in the present study is based on the uniform strain formulation. The first-order reduced integration elements pass the patch test and attain stability in the present context, ensuring precision for the moving loads. The interpolation function of the brick element used in the pavement system is expressed as:

$$x = N_{\epsilon}^{N}(g,h,r).\, X^{N} \tag{3.4}$$

and the shape function N_i^N can be expressed as

$$N_{\epsilon}^{N}(g,h,r) = \frac{1}{8}\Sigma^{I} + \frac{1}{4}g\Lambda_{1}^{I} + \frac{1}{4}h\Lambda_{2}^{I} + \frac{1}{4}r\Lambda_{3}^{I} + \frac{1}{2}hr\vartheta_{1}^{I} + \frac{1}{2}gr\vartheta_{2}^{I} + \frac{1}{2}gh\vartheta_{3}^{I} + \frac{1}{2}ghr\vartheta_{4}^{I} \tag{3.5}$$

where superscripted, I denote the node of the element. The vectors, $\vartheta_{\propto}^{I}$ are the hourglass base vectors. The uniform strain formulation calculates the average strain over the element volume for the first-order element used in the present study. Hence, the strain passed into the non-linear constitutive model is better convergent to the actual strain.

Further, the equation of virtual work done in terms of body force (Q_B) and externally applied force (Q_E) is expressed as,

$$\iiint W_B dv - \iiint W_I dv = \iiint W_E dv \tag{3.6}$$

where $W_B = Q_B\, \Delta v$ is the work done by body force, $W_I = (\rho\ddot{x})\, \Delta v$ is the work done by inertial force, and $W_E = Q_E\, \Delta v$ is the work done by externally prescribed force, respectively, on a small elemental volume Δv. Concerning the initial reference volume v_0 and initial reference density ρ_0, the D'Alembert force term can be rewritten as $\iiint W_I^i dv_0$ where $W_I^i = (\rho_0\ddot{x})\, \Delta\, v$ is the work done by initiating inertial force on small elemental volume Δv, and correspondingly equation of work done takes the form as,

$$\iiint W_B dv_0 - \iiint W_I^i dv_0 = \iiint W_E\, dv_0 \tag{3.7}$$

where $\ddot{x}$ is calculated using the time integration operator. The D'Allembert force term, assuming interpolation, can be written as $(\iiint \rho_0 N_i^N N_i^M\, dv_0)\, \ddot{x}^M$ and the corresponding equation of virtual work done is expressed as,

$$\iiint \rho_0 N_i^N N_i^M \, dv_0 \, \ddot{x}^M \; + \; \iiint \beta N{:}\sigma \, dv_0 \; = \iint N_i^N \, t \, ds \; + \; \iiint N_i^N \, Q_E \, dv \tag{3.8}$$

where ρ_0 is the initial reference density, v_0 is the initial reference volume, N_i^N and N_i^M are interpolation functions associated with the nth and mth nodes, and $\ddot{x}^M$ is the acceleration vector associated with the mth node. The body force term is calculated as the product of the mass matrix, formulated through consistent use of interpolation, and the nodal acceleration. The consistent use of interpolation helps maintain a constant mass value, thereby avoiding the violation of the law of conservation of mass. Finally, the equation of motion is expressed as,

$$[M_C^{NM}]\{\ddot{x}\} + \; [I_F^N] = \; [Q_F^N] \tag{3.9}$$

where

$M_C^{NM} \; = \; \iiint \rho_0 N_i^N N_i^M \; dv_0$ is the mass matrix obtained by consistent use of interpolation;

$I_F^N \; = \; \iiint \beta N{:}\sigma \; dv_0$ is inertial force vector, and

$Q_F^N \; = \; \iint N_i^N \; t \; ds + \iiint N_i^N \; Q_E \; dv$ is the external force vector

3.2.2 Cyclic Response Model

The constitutive stress-strain behaviour of the material for the total strain caused by the moving load can be expressed as,

$$\varepsilon \; = \; \varepsilon^p \; + \; \varepsilon^e \; = \; \varepsilon^p + \frac{\sigma}{E} \tag{3.10}$$

where, ε^p and ε^e represents elastic and plastic strain. Using Hooke's law, the stress tensor in terms of compliance matrix and strain can be expressed as,

$$\sigma = C\varepsilon^{e} = C\,(\varepsilon - \varepsilon^{p}) \tag{3.11}$$

Cyclic strength in the pavement material depends on deviatoric stress, which can be expressed as,

$$\acute{\sigma} = \sigma - PI \tag{3.12}$$

where, $P = \frac{1}{3}tr(\sigma)$

Further, the effective stress tensor can be expressed as,

$$\sigma_e = \sqrt{\frac{3}{2}\acute{\sigma}:\acute{\sigma}} \tag{3.13}$$

and an effective trial stress tensor can be expressed as,

$$\sigma_e^{tr} = \sqrt{\frac{3}{2}\acute{\sigma}^{tr}:\acute{\sigma}^{tr}} \tag{3.14}$$

where, $\acute{\sigma}:\acute{\sigma} = \sum_{i=1}^{3}\sum_{i=1}^{3}\acute{\sigma}_{ij}\acute{\sigma}_{ij}$, on two tensors is the double contracted product and has been obtained by multiplying two tensors component by component and summing the term to give the scalar quantity.

The effective stress tensor in terms of the second invariant can also be expressed as,

$$\sigma_e = \sqrt{3J_2} \tag{3.15}$$

where, $J_2 = \frac{1}{2}\acute{\sigma}:\acute{\sigma}$

For numerically implementing the cyclic response, the authors have considered that solving the behavior of a pavement subjected to a cyclic moving load is incremental. Hooke's law is used to predict the behaviour of pavement subjected to a moving load and can be expressed as,

$$\begin{bmatrix}\sigma_{11}\\ \sigma_{22}\\ \sigma_{33}\\ \sigma_{12}\\ \sigma_{13}\\ \sigma_{23}\end{bmatrix} = \begin{bmatrix}2G+\lambda & \lambda & \lambda & 0 & 0 & 0\\ \lambda & 2G+\lambda & \lambda & 0 & 0 & 0\\ \lambda & \lambda & 2G+\lambda & 0 & 0 & 0\\ 0 & 0 & 0 & G & 0 & 0\\ 0 & 0 & 0 & 0 & G & 0\\ 0 & 0 & 0 & 0 & 0 & G\end{bmatrix}\begin{bmatrix}\varepsilon_{11}\\ \varepsilon_{22}\\ \varepsilon_{33}\\ \varepsilon_{12}\\ \varepsilon_{13}\\ \varepsilon_{23}\end{bmatrix} \tag{3.16}$$

where G is the shear modulus, λ is Lame's parameter. Since, in all the diagonal components of the stiffness matrix G exist, we can relate the stress and strain components as follows,

$$\sigma_{ij} = 2G\varepsilon_{ij}^{e} + \lambda(\varepsilon_{11}^{e} + \varepsilon_{22}^{e} + \varepsilon_{33}^{e})\delta_{ij}\begin{cases}\delta_{ij} = 1\, for\ i = j\ (normal\ stresses)\\ \delta_{ij} = 0\, for\ i \neq j\ (shear\ stresses)\end{cases} \tag{3.17}$$

where, δ_{ij} is Kronecker delta and $\varepsilon_{11}^{e} + \varepsilon_{22}^{e} + \varepsilon_{33}^{e}$ can be written as $tr(\varepsilon^{e})I$ and hence Eq. (3.17) can be written as,

$$\sigma = 2G\varepsilon^{e} + \lambda tr(\varepsilon^{e})I \tag{3.18}$$

Eq. (3.18) is valid for all strains, and the equation is used at the end of the increment. For k+1 increment, Eq. (3.18) can be expressed as,

$$\sigma_{k+1} = 2G\varepsilon_{k+1}^{e} + \lambda tr(\varepsilon_{k+1}^{e})I \tag{3.19}$$

Now the elastic strain at the end of the increment is calculated based on the strain at the beginning of the increment. Total and plastic strain increments can be expressed as,

$$\varepsilon_{k+1}^{e} = \varepsilon_{k}^{e} + \Delta\varepsilon^{e} = \varepsilon_{k}^{e} + (\Delta\varepsilon - \Delta\varepsilon^{p}) \tag{3.20}$$

Substituting the value of ε_{k+1}^{e} in Eq. (3.19)

$$\sigma_{k+1} = 2G\left(\varepsilon_{k}^{e} + (\Delta\varepsilon - \Delta\varepsilon^{p})\right) + \lambda tr\left(\varepsilon_{k}^{e} + (\Delta\varepsilon - \Delta\varepsilon^{p})\right)I \tag{3.21}$$

As the material is incompressible therefore rearranging Eq. (3.21) as,

$$\sigma_{k+1} = 2G(\varepsilon_{k}^{e} + \Delta\varepsilon) + \lambda tr(\varepsilon_{k}^{e} + \Delta\varepsilon)I - 2G\Delta\varepsilon^{p} \tag{3.22}$$

The term $2G(\varepsilon_{k}^{e} + \Delta\varepsilon) + \lambda tr(\varepsilon_{k}^{e} + \Delta\varepsilon)I$ is equal to the strain at the beginning of the increment plus the stiffness matrix multiplied by the total strain increment

$$\sigma_{k+1} = \sigma_{k} + C\Delta\varepsilon - 2G\Delta\varepsilon^{p} \tag{3.33}$$

The stress at the end of the first increment has been calculated by assuming that the strain at the beginning of the increment is elastic and is known as elastic predictor trial stress expressed as

$$\sigma^{tr} = 2G(\varepsilon_{k}^{e} + \Delta\varepsilon) + \lambda tr(\varepsilon_{k}^{e} + \Delta\varepsilon)I = \sigma_{k} + C\Delta\varepsilon \tag{3.24}$$

Hence, Eq. (3.23) can be written as

$$\sigma_{k+1} = \sigma^{tr} - 2G\Delta\varepsilon^{p} \tag{3.25}$$

and the cyclic strength captured for one cycle of moving load over the pavement length is expressed as,

$$\left\{\sigma_{(CN:\,N=1)}\right\} = \sqrt{\frac{3}{2}(\,S\!:\!S\,)} \tag{3.26}$$

where $S = \sigma_{ij}^{n} + pI$ and $p = -\frac{1}{3}trace\left(\sigma_{ij}^{n}\right)$

Cyclic strength of the pavement subjected to moving load is captured using the above numerical formulation and codal recommendations as:

$$S_r = 1 - p\log N \tag{3.27}$$

$$p = \eta\chi \tag{3.28}$$

And, the novel S_r is the strength ratio given as:

$$S_r = \frac{Maximum\ stress\ applied\ by\ moving\ load\ in\ one\ cycle}{Characteristic\ strength\ of\ concrete\ calculated\ as\ per\ ACI} \tag{3.29}$$

$$S_r = \frac{\sigma_{CN:\,N=1}}{f_{ck}} \tag{3.30}$$

Where

$\chi = 0.0714$,

$\eta = 1 - r$ (Recommended by Swedish code),

$\eta = \sqrt{1 - r}$ (Recommended by section 6.8.7 of Eurocode, 2002),

$r = \frac{\sigma_{CD,min,equ}}{\sigma_{CD,max,equ}}$

and $\sigma_{CD,min,equ}$ and $\sigma_{CD,max,equ}$ are the lower and upper stress of the ultimate amplitude for N cycles. The cyclic response model is formulated using the output analysis of codal recommendations (section 6.8.7 of Eurocode) and ACI to predict the cyclic strength of pavement subjected to moving load conditions. The peak strength at varied velocities is a function of ε_{ij}^{n} i.e., $f_{peak} = f\left(\varepsilon_{ij}^{n}\right)$. The stress variation for pavements subjected to a moving load under various end conditions is found to be in the range of 10^2 to 10^4 kPa. The cyclic strength of concrete and stress ratio are calculated using a numerical formulation expressed in Eqs. (3.1) and (3.26) to (3.30).

3.3 Results and Discussion

The field monitoring results on the central deflection (d_c) of rigid pavement subjected to moving load in real time along the pavement length to predict stress and deformation characteristics are still elusive in the literature. Hence, the dependability of the present mathematical model is examined concerning the available solutions in the literature. The results obtained from the present three-dimensional numerical investigations are validated with the analytical and finite element numerical results available in the literature (Wu & Shen, 1996; Yang et al., 2010).

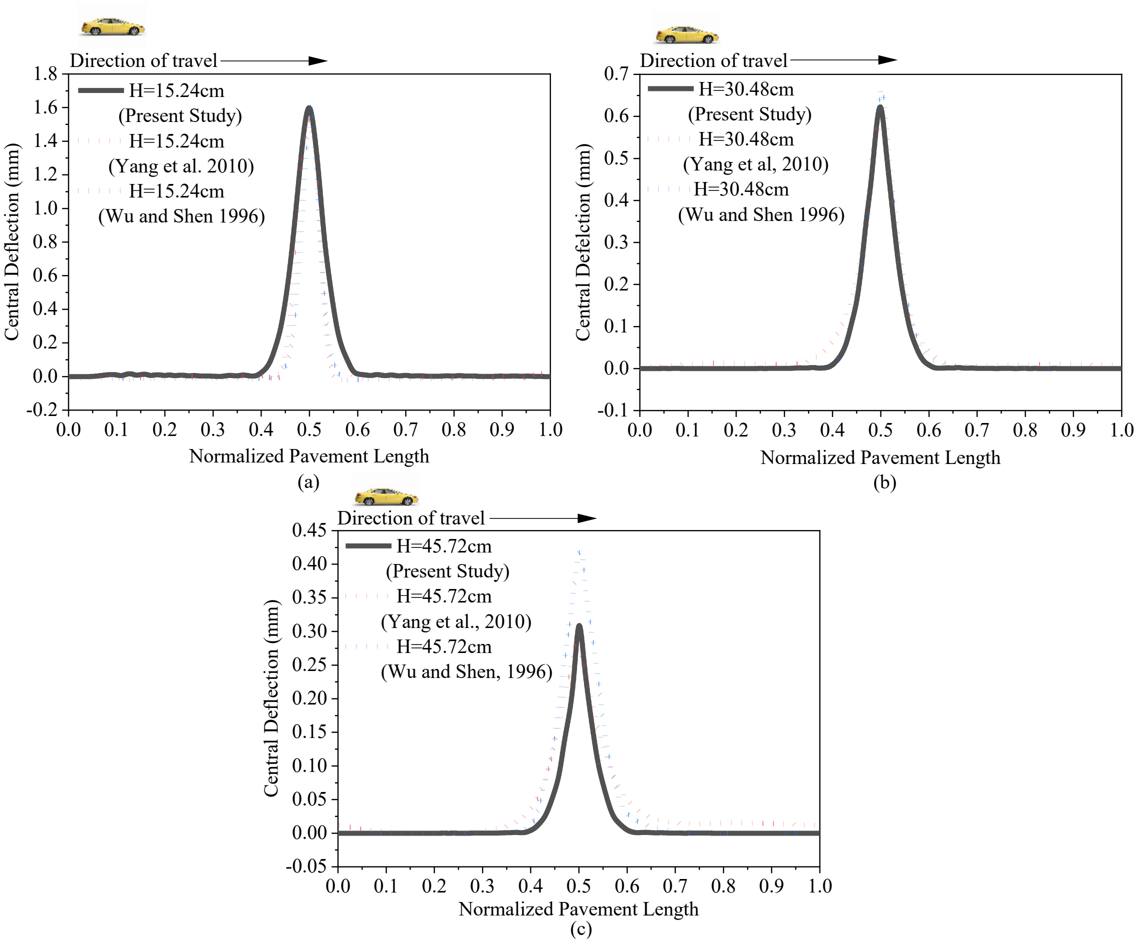

(a) (b) (c)

Figure 3.4 Central deflection for the position of the moving load along the normalized pavement length for varied pavement thicknesses

Wu and Shen (1996) considered the interaction between pavement and modelled soil as a spring beneath the pavement structure, and the investigation was performed using the 3D FEM technique. Yang et al. (2010) also conducted the same study using the quick, direct integral method, and the results were in close proximity. In the present study, the principle of virtual work, applied in conjunction with a 3D Finite Element model using dimensions and properties similar to those of Wu and Shen (1996) and Yang et al. (2010), is adopted to validate the dynamic response of the pavement subjected to a moving load. Fig. 3.4 shows the variation of central deflection (d_c) with the position of the moving load for varied pavement thickness. It is evident that the results of the present study align with those available in the literature.

3.3.1 Velocity-induced Displacement Response

To observe the displacement response, the central deflection (d_c) of the pavement is captured. The central deflection (d_c) is the displacement at the central node of the pavement surface when the moving load travels half the distance of pavement length. Fig. 3.5 shows the displacement contours for varied velocity values. The colour coding in the contour represents the magnitude of the area influenced by the rigid pavement supported by the granular base. The blue and red-coloured contours for the displacement profile indicate the minimum and maximum regions influenced by the moving load in terms of displacement. The displacement bulb contour is observed with lagging effects after reaching the threshold velocity of the moving load (120 m/s), simulating the advanced phase of rigid pavement dynamics. Figs. 3.6 and 3.7 show the variation of velocity-induced central deflection (d_c) for a range of moving load intensities, from 25 to 235 kN, and velocities, from 15 to 165 m/s. The loading values are taken from IRC 58 (2015), i.e., standard single axle load (100 kN), tandem axle load (186 kN), and tridem axle load (235 kN).

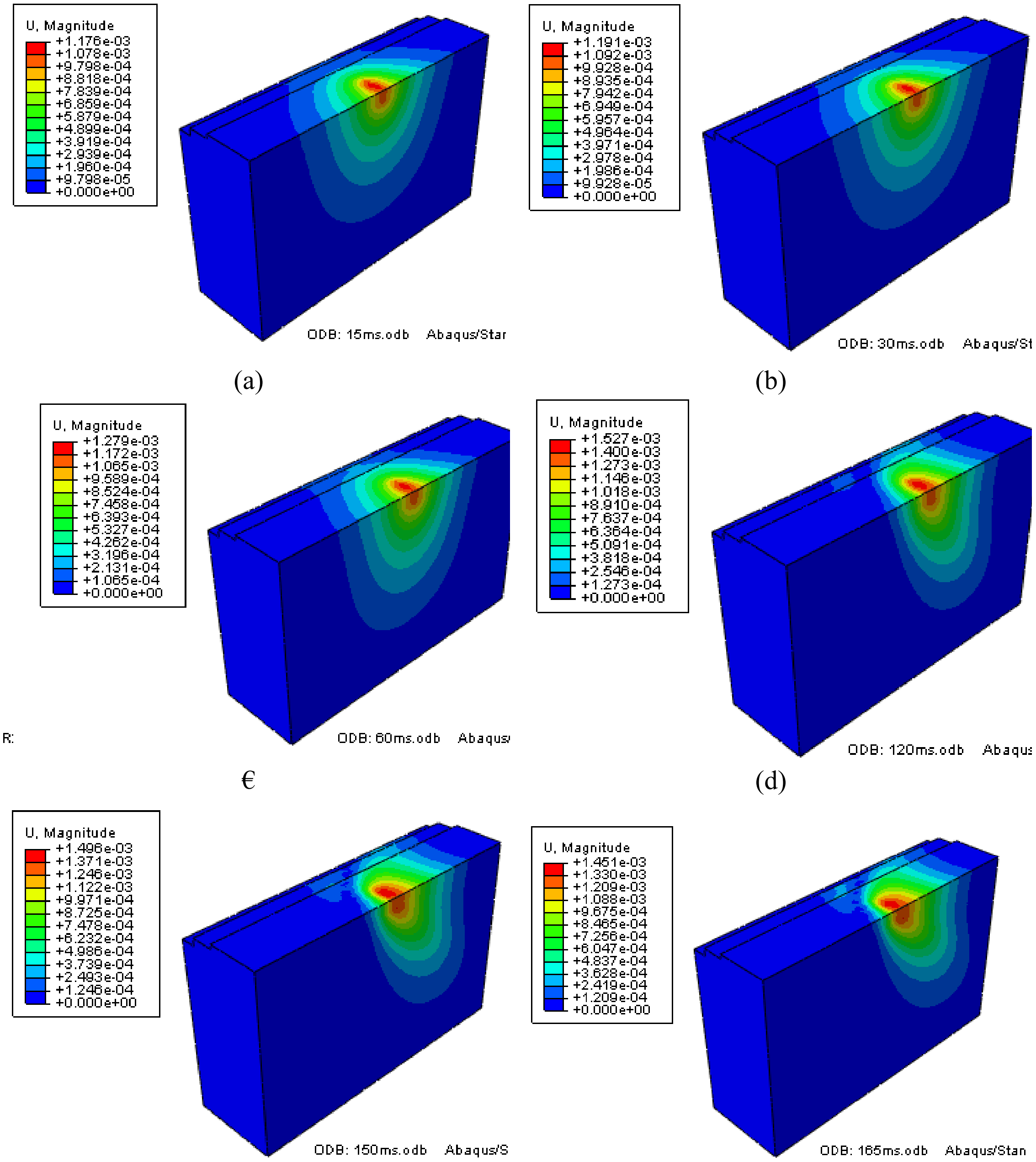

(a) (b)

€ (d)

€ (f)

Figure 3.5 Central deflection for moving load velocity of (a) 15 m/s, (b) 30 m/s, (c) 60 m/s, (d) 120 m/s, € 150 m/s, and (f) 165 m/s, at 100 kN loading, having displacement contour intervals shown in different colours (maximum displacement in red and negligible in blue)

Fig. 3.6 shows the variation of central deflection (d_c) with a velocity range of 15-165 m/s for pavement, subgrade, and subbase soil. Three influence zones, namely Low Influence Zone (LIZ), Moderate Influence Zone (MIZ), and High Impact Zone (HIZ), are separated by a vertical dotted line with a Threshold Value (TV) of central deflection (d_c) indicated by the solid line. An increasing response with increasing velocity is observed for the varied input parameters of velocity and loading magnitude up to a threshold value. Based on the findings, it has been confirmed that the deflection concentration on a pavement surface is directly proportional to the velocity of the moving load, which in turn affects the strength of the pavement exposed to varied inputs of the moving load velocity. It is observed that the maximum value of central deflection (d_c) for the pavement occurs at a velocity value of 120 m/s, whereas the available literature on the same input parameters indicates a threshold value of 120 m/s to 125 m/s. The value of central deflection (d_c) for the pavement and GB layer is observed to have identical values after attaining the threshold velocity of 120 m/s for the loads considered in the study.

Fig.3.7 shows the variation of central deflection along (d_c) the pavement length. A peak shift in the central deflection (d_c) is observed towards the near end of the pavement for the velocities of 120 m/s, 150 m/s, and 165 m/s. The maximum value of displacement for rigid pavement supported by granular bases has been reported in the range of 1.1 mm to 1.5 mm for pavement and granular base layer, and 0.9 mm to 1.3 mm for soil subgrade layer. The shifting of displacement for pavement and the granular base layer was observed at 60 m/s and 120 m/s for the soil subgrade layer. The deflection tends to lag for the higher velocity values.

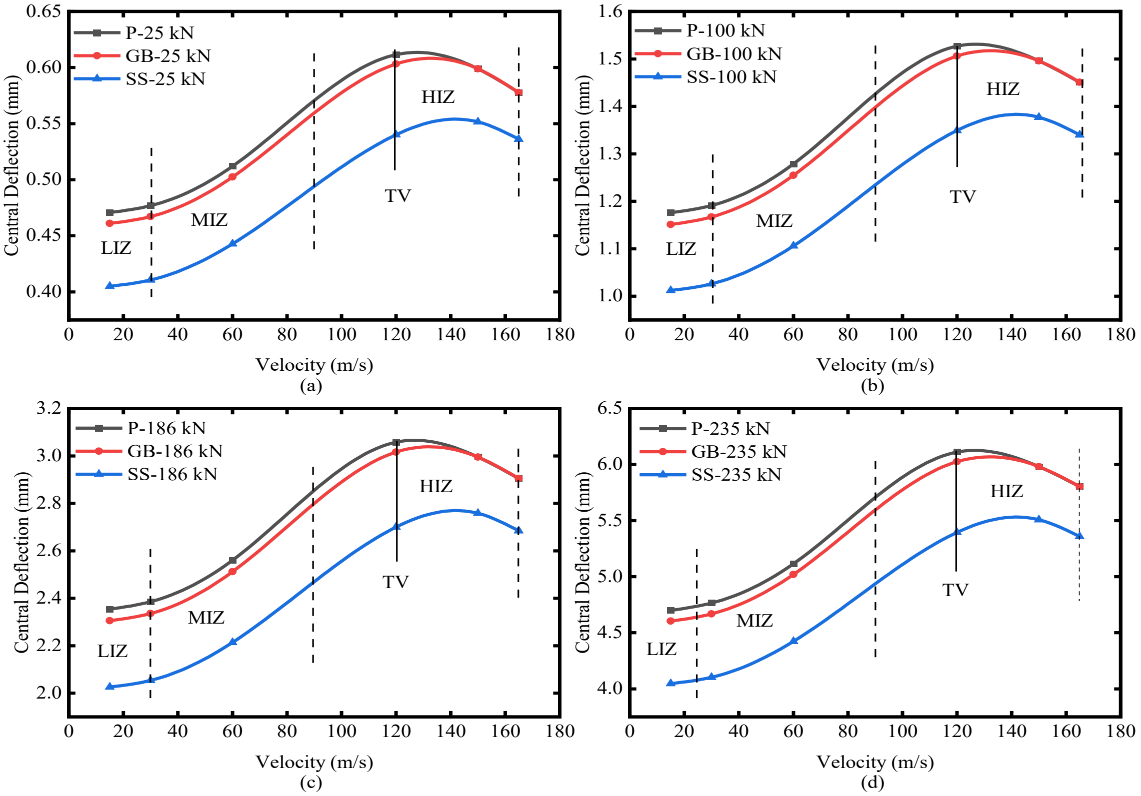

Figure 3.6 Variation of central deflection for (a) 25 kN (b) 100 kN, (c) 186 kN, and (d) 235 kN with a velocity range of 15-165 m/s for pavement, granular base, and subgrade soil and four influence zone separated by a vertical dotted line with the threshold value of central deflection indicated by the solid line

Corresponding amplification is recorded in the dynamic displacement factor (D_{df}).

$$D_{df} = \frac{Dynamic\ displacement}{Static\ displacement} \tag{3.31}$$

Using Eq. (3.31), the variation of the dynamic displacement factor in the vertical direction is calculated as listed in Table 3.4. For the lower ranges of velocities, the response observed was similar to that of static loading. For velocity values of 60 m/s to 150 m/s, the maximum difference in variation of displacement amplification was observed to be 11% to 62% in the vertical direction. It is observed from Fig. 3.4 and Table 3.4 that the solution presented for the problem of moving load is significantly improved compared to the solutions provided by other investigators. In the present study, the amplification of displacement at higher velocities ranges from 50% to 62% (Table 3.4). A significant displacement of 0.2% to 62.2% over static displacement is observed in the vertical direction. In contrast, the work of Wu and Shen (1996) showed an 18% increase in displacement in the vertical direction, similar to a study of a similar kind.

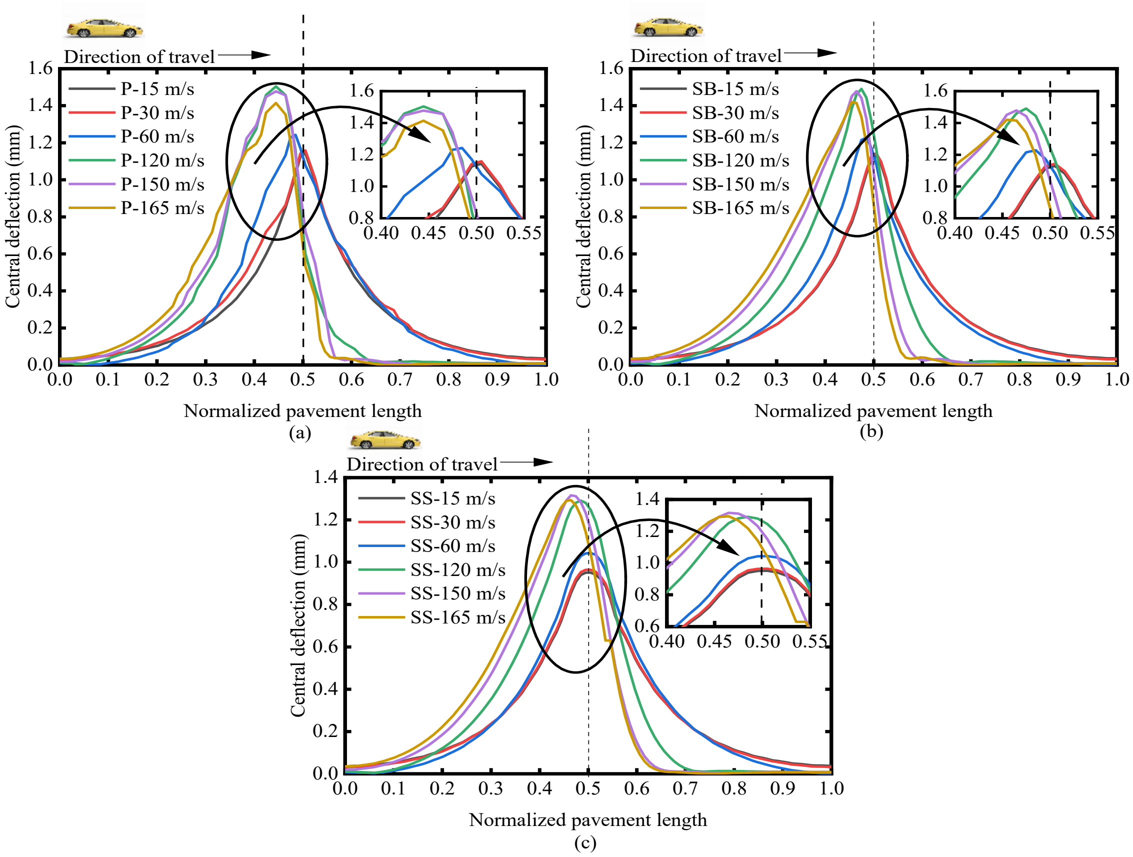

Figure 3.7 Velocity-induced Central deflection for the range of moving load velocities (15-165 m/s), having a shift of peak and displacement zone towards the near end of (a) pavement supported by the granular base, (b) subbase supported by subgrade soil, (c) subgrade soil

Table 3.4 Variation of dynamic displacement factor (D_{df}) in the vertical direction

Velocity (m/sec)	Dynamic displacement factor (D_{df}) on pavement top			
	Backward Euler method[a]	Present study		Newmark's β method[b]
		High precision	Low precision	
15	1.002	1.003	1.009	1.009
30	1.015	1.013	1.018	1.020
60	1.118	1.125	1.133	1.135
120	1.500	1.532	1.557	1.622
150	1.488	1.490	1.501	1.504
165	1.368	1.368	1.387	1.395

[a]Hilber et al. (1977); [b]ABAQUS (2017)

3.3.2 Velocity-induced Stress Response and Cyclic Strength

Fig. 3.8 shows findings in terms of the variation of principal stress fields for the pavement surface course subjected to the moving load. The stresses in the vertical (σ_{11}) and lateral direction (σ_{33}) show a zone of transition with a change in phase (transition of stress from the far end to near end of the pavement) around the centre for the stress caused by a moving load at a velocity of 120 m/s. The initiating transition and phase change are observed at a velocity of 120 m/s and continue for velocities of 150 m/s and 165 m/s. The transition and phase change of stress are observed in terms of principal stress fields, which is a potential reason for the shift in peak central deflection and equivalent stress, as well as an unusual stress-dominated zone.

Fig. 3.9 shows the velocity-induced stresses for a moving load velocity of 15 m/s applied on the pavement supported by the granular base and subgrade soil, and it is observed that more than one peak exists for σ_{CN}. The load is observed to produce a compounded effect in terms of stress waves with a vibrational compounded stress transfer mechanism (V-CSTM). The GB and soil subgrade layer exhibit stress wave generation in both GB and soil media due to the transfer of load from the pavement layer. The velocity-induced stress transfer from pavement to the GB and soil subgrade layer showed peak-to-peak mapping of cyclic strength. The rate of dissipation is such that it is likely to amplify the velocity-induced stress concentration, leading to damage.

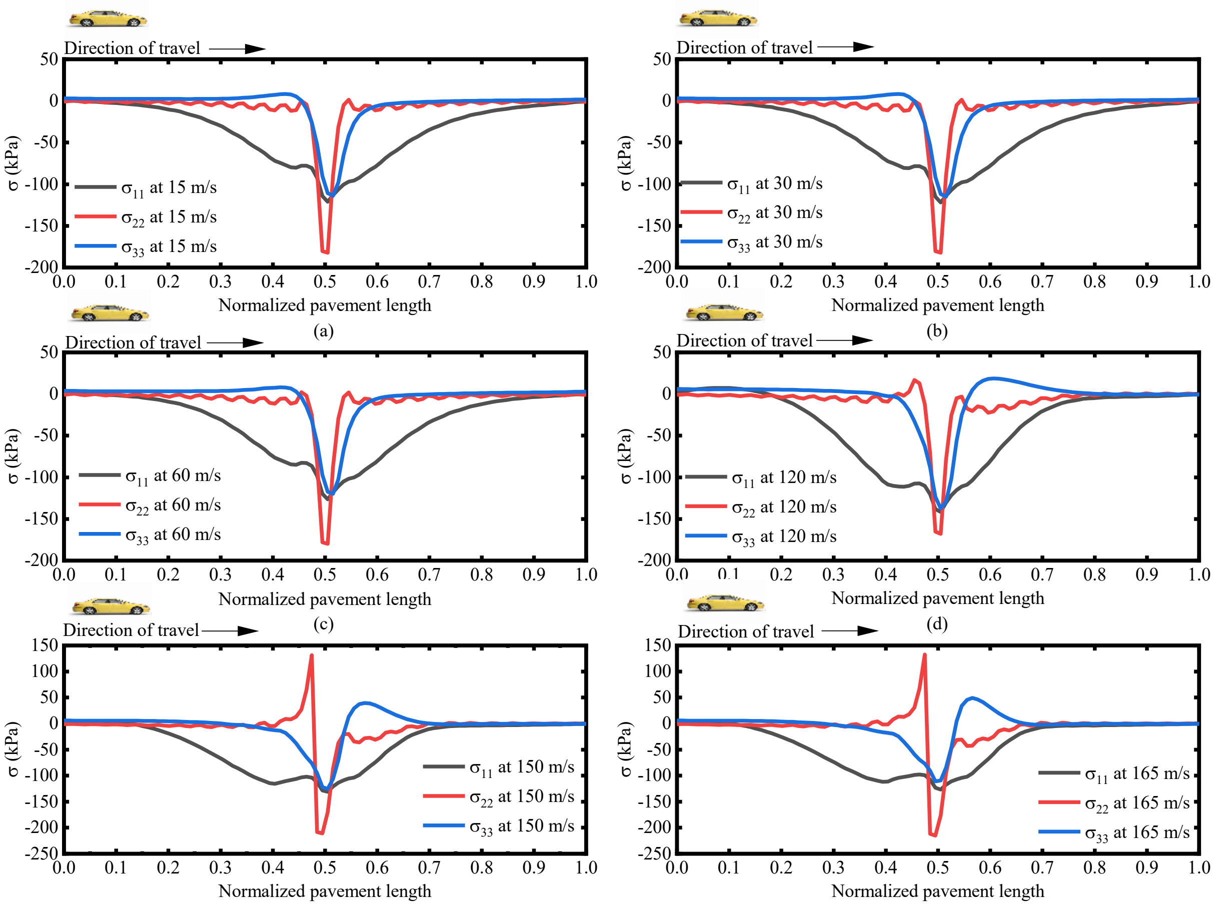

(a) (b)

(c) (d)

(e) (e)

Figure 3.8 Variation of normal stress along the normalized pavement length for the velocity of (a) 15 m/s, (b) 30 m/s, (c) 60 m/s, (d) 120 m/s, (c) 150 m/s, and (f) 165m/s; the cubical stress element of pavement representing σ_{11} is the stress in the lateral direction, σ_{22} is the stress in the vertical direction, and σ_{33} is the stress along the pavement length

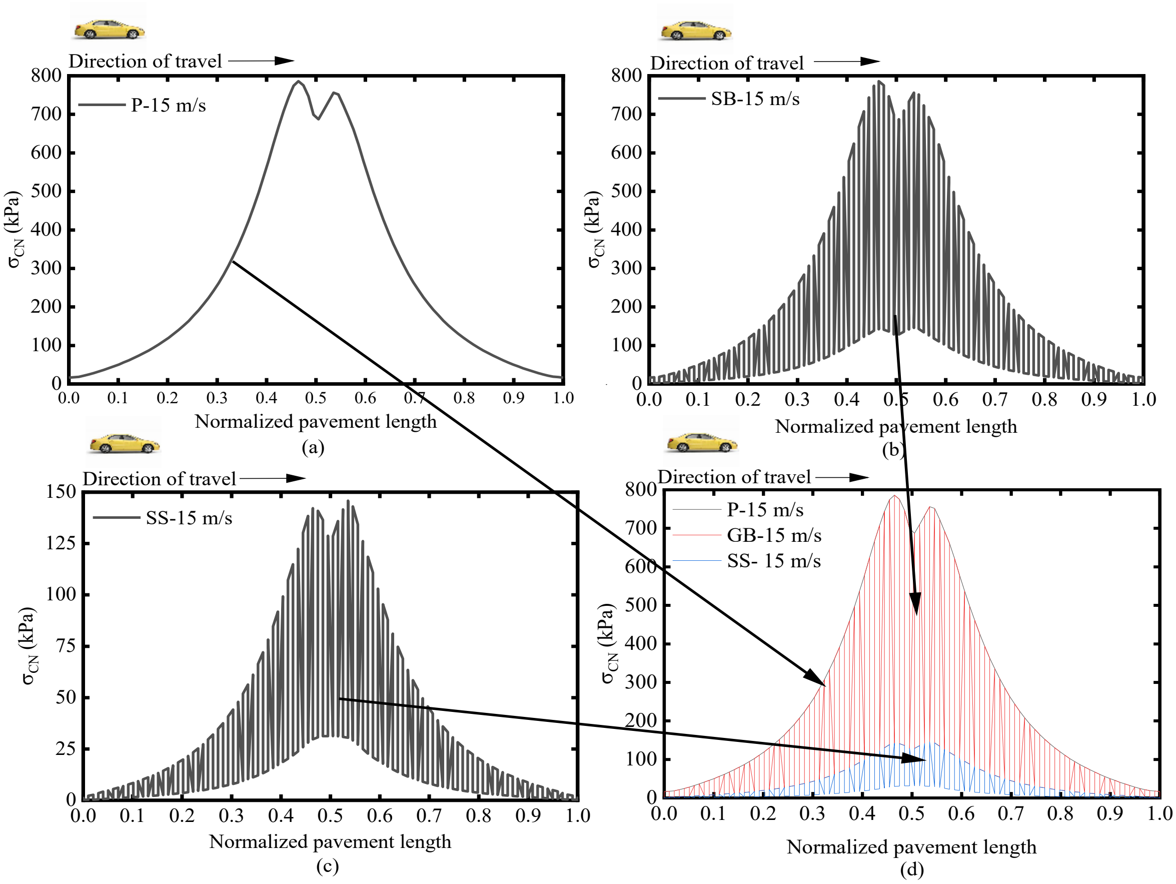

Figure 3.9 Variation of σ_{CN} along the normalized pavement length showing the vibrational compounded stress response for the velocity of 15 m/s in (a) pavement layer, (b) GB layer, (c) soil subgrade layer, and (d) combined system

Table 3.5 Peak shift ratio (η) for the layers of pavement supported by granular bases in the present work

Layer	η					
	15 m/s	30 m/s	60 m/s	120 m/s	150 m/s	165 m/s
Surface Course and Granular Base	0.962592	0.967064	0.972218	1.647658	2.358636	2.74758
Soil Subgrade	1.02542	1.028002	1.021895	1.740235	2.602292	3.026451

The stress response across the normalized pavement length for the pavement, granular base, and soil subgrade at varying velocities shows that it becomes distinct on peaks at higher velocities, with a peak shift ratio (η_s) as shown in Table 3.5. The peak shift ratio (η_s) consists of near-end, far-end stress, velocity, and empirical fitting parameter (η) of the pavement. The peak shift ratio (η_s) can be expressed as,

$$\eta_s = f\left(\sigma_{near\ end}^{peak}, \sigma_{far\ end}^{peak}, v, \eta\right) \tag{3.32}$$

$$\eta = \frac{\sigma_{near\ end}^{peak}}{\sigma_{far\ end}^{peak}} \tag{3.33}$$

In Fig. 3.10, η increase with the velocity at different rates, reaching their peaks at a normalized length. Further, Fig. 3.10 shows the variation of σ_{CN} along the normalized pavement length for the velocity of 15 m/s to 165 m/s. It is observed that up to a velocity of 60 m/s, the results are regularly compounded, i.e., without any lagging effect. After reaching a velocity value of 120 m/s, the peak toward the near end of the pavement starts to rise, and towards the far end starts to decline due to phase shift and transition in principal stress fields. The stresses are increased for higher velocities towards the near-end pavement, GB, and subgrade. The stress response for GB and soil subgrade is compounded compared to the stresses in pavement subjected to a moving load. The displacement and stress shift indicate significant displacement and stress concentration towards the near end of the rigid pavement. The effect is due to structural vibrations caused by a high-velocity moving load. It provides a suitable interpretation for the lagging displacement contours corresponding to velocities of 120 m/s to 165 m/s.

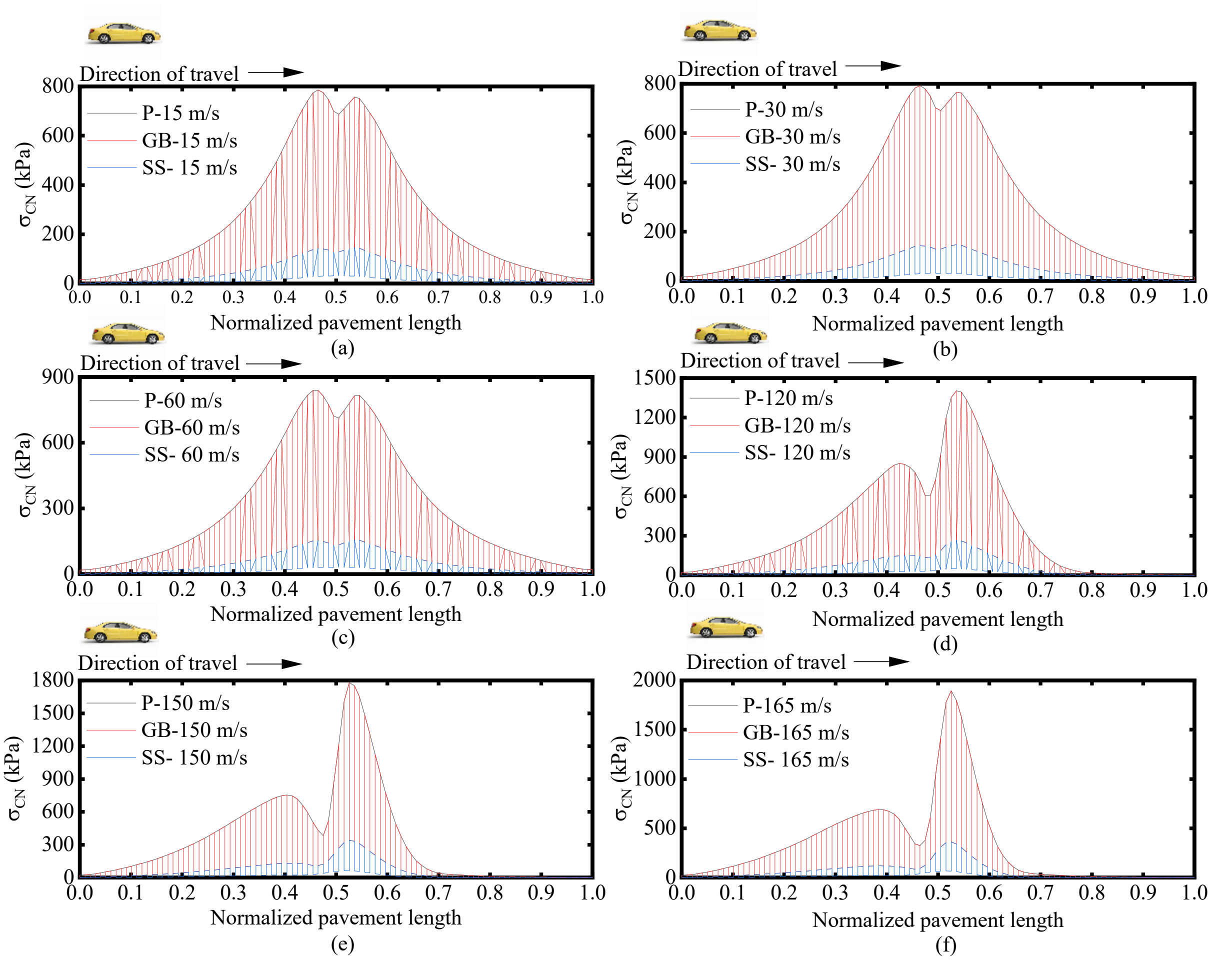

Figure 3.10 Variation of σ_{CN} along the normalized pavement length for the velocity of (a) 15 m/s, (b) 30 m/s, (c) 60 m/s, (d) 120 m/s, I 150 m/s, and (f) 165 m/s

The stress contours observed in the present study for varying velocity inputs are shown in Fig. 3.11. The color-coded contours indicate the maximum and minimum stress in red and blue, respectively. The transition in stress is observed beyond a threshold value of velocity (120 m/s), indicating the higher side of dynamics in rigid pavements. Due to the action of velocity, there is a stress wave distributed in outward and inward directions to the movement of the moving load, which are superimposed to give the Figs. 3.8-3.11.

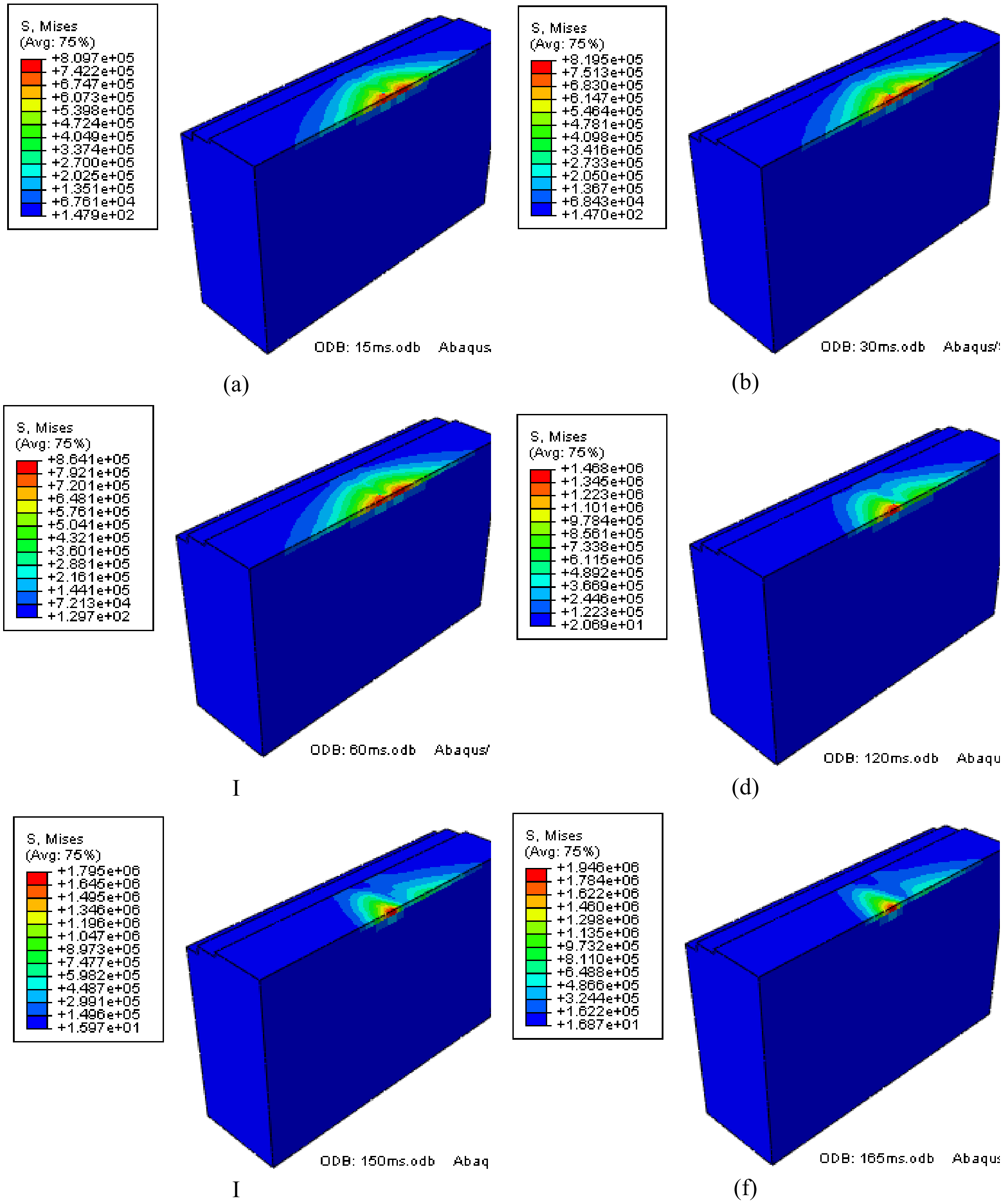

(a) (b)

I (d)

I (f)

Figure 3.11: Stress contours for moving load velocity of (a) 15 m/s, (b) 30 m/s, (c) 60 m/s, (d) 120 m/s, I 150 m/s, and (f) 165 m/s, respectively, with contour intervals shown in different colours (maximum stress in red and negligible in blue)

The difference in the intensity of stress wave magnitude is insignificant at lower velocities, while at higher velocities, it becomes greatly magnified for forward and backward peaks. Further, $\sigma_{(CN:\,N=1)}$ as a function of velocity can be expressed as,

$$\sigma_{(CN:\,N=1)} = f(v) \tag{3.34}$$

$\sigma_{(CN:\,N=1)}$ as a function of velocity-induced strength factors can be expressed as,

$$\sigma_{(CN:\,N=1)} = \lambda e^{\varphi \times v} \tag{3.35}$$

Putting the value of $\sigma_{(CN:\,N=1)}$ in Eq. (3.30) gives the following modified expression of *S_r*, which can further be utilised by field engineers to evaluate the number of cycles of moving load considering the velocity amplification effects as shown in Table 3.6.

$$S_r = \frac{\sigma_{CN:\,N=1}}{f_{ck}} = \frac{\lambda e^{\varphi \times v}}{f_{ck}} \tag{3.36}$$

Table 3.6 Velocity-induced strength factors obtained in the present study

Parameter	Load (kN)			
	10	25	50	100
λ	291.68	689.16	1372.1	2745.5
φ	0.006	0.0059	0.0058	0.0058

Fig. 3. 12 (a) shows the variation of the cyclic strength (σ_{CN}) and Fig. 3. 12 (b) stress ratio of the pavement with varied velocities. The σ_{CN} value for moving load for 15 m/s to 120 m/s is reported in the range of 3.2×10^{2} kPa to 5.86×10^{4} kPa with 10^{15} cycles to 10^{9} cycles interpreted using codal specification. The cyclic strength (σ_{CN}) of the pavement is interpreted for the set of selected parameters in terms of the stress ratio (S_r) is provided for the benefit of practitioners, engineers, and designers for evaluating the life of the pavement. Despite the assumptions, the results as presented compare well with the real-life observations, and applications to field engineers are presented in Appendix A. The

present study can also be expanded to explore avenues for further research based on its outcomes. The study's outcomes demonstrate that cyclic strength is a function of velocity, the number of cycle', the magnitude of loading, and pavement thickness, with numerically obtained damping factors. As there are no experimental facilities available to obtain velocity-induced deflection, stress, and cyclic strength parameters. Artificial intelligence and machine learning techniques can be effectively adopted for developing the instrumentation facility based on current findings.

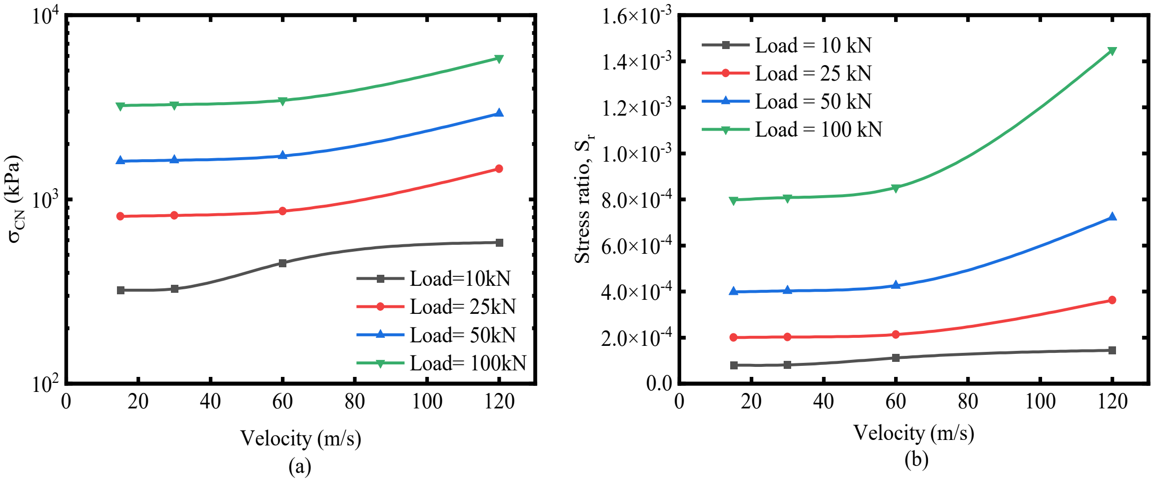

Figure 3.12 Variation (a) σ_{CN} for velocity ranging from 15-165 m/s and (b) stress ratio for velocity ranging from 15-120 m/s with varied loading intensity ranging from 10-100 kN

Under moving vehicular loading, the stress path beneath the wheel is non-proportional, leading to continuous rotation of principal stress axes. Due to which Principal Stress Rotation (PSR) phenomenon comes into the picture, which significantly influences shear strain accumulation and permanent deformation in unbound granular layers. The variation of σ_{11}, σ_{22}, and σ_{33} observed in Figures 3.8–3.12 reflects this stress redistribution mechanism. PSR enhances cyclic degradation and energy dissipation within the pavement-soil system under high-velocity loading.

3.3.3 Proposed Step-by-step Procedure for Estimating the Number of Cycles of Moving Load

Step 1: Calculate the characteristic strength f_{ck} of rigid pavement material using ACI clause 19.2.2.1(b) Building Code Requirements for Concrete and Commentary.

Step 2: Calculate the strength of pavement material for one cycle of moving load using Eq. (3.35) and Table 3.6.

Step 3: Estimated stress ratio (S_r) using Eq. (3.36).

Step 4: Finally, estimate the number of cycles for the pavement design.

3.4 Conclusions

In the present study, a novel finite element-based numerical model is presented to evaluate the deflections and cyclic strength of rigid pavements subjected to structural vibrations caused by a high-velocity moving load. It consists of velocity, characteristic strength, vibration-induced compounded stress transfer, and the number of cycles of the moving load. Based on the results and discussion as presented earlier, the following conclusions can be drawn:

- Velocity-induced zones, namely low, moderate, and high influence zones, have been identified, and a novel observation of displacement and stress shift in terms of central deflection (0.4-6.25 mm) and equivalent stress (10^2-10^4 kPa) has been observed for velocities more than 120 m/s.
- The displacement and stress shift indicate significant displacement and stress

concentration towards the near end of the rigid pavement. The effect is due to structural vibrations caused by a high-velocity moving load. It presents the importance of the critical threshold velocity (120 m/s) while designing the pavement soil system.

- The displacement is calculated as a function of velocity in the vertical direction using inputs of central deflection. It is observed that the central deflection increases with a decrease in the thickness of the pavement (15 cm to 60 cm) and velocity up to the optimum velocity of 120 m/s.
- The stress response across the normalized pavement length for the pavement, granular base, and soil subgrade at varying velocities shows that η_s become distinct on peaks at higher velocities (120-165 m/s) and are likely to amplify the velocity-induced stress concentration for damage.
- The Vibrational Compounder Stress Transfer Mechanism (V-CSTM) in the pavement, granular base, and soil subgrade layer shows a peak-to-peak mapping of cyclic strength. The strength of pavement is correlated with the number of cycles of moving load using a novel cyclic response model. The cyclic strength of the pavement material for the selected velocities (15-165 m/s) was found in a range of 0.01 to 0.2% of the characteristic strength corresponding to 10^{15} to 10^{9} cycles.

The amplification at higher velocities is very significant while designing the rigid pavements for future super expressways. The novel simulation results and new conclusions of the study demonstrate that the cyclic response model offers a reasonable interpretation for practitioners to evaluate the number of cycles of a moving load on rigid pavement. It would be helpful to restate the study’s main findings explicitly and discuss their implications for pavement design and constru’tion practices.

Appendix A: Application to Practical Field Engineering

A field engineer is required to obtain the number of cycles for the design of pavement with field conditions having a moving load of 100 kN with a velocity of 15 m/s, and the elastic modulus of concrete is 25×10^3 Mpa.

As per the outcomes of the following study following steps can be followed

Step 1: Calculate the characteristic strength f_{ck} of rigid pavement material using ACI clause 19.2.2.1(b) Building Code Requirements for Concrete and Commentary

$$E_c = 4700\sqrt{f_{ck}}$$

$$25 \times 10^3 = 4700\sqrt{f_{ck}}$$

$$f_{ck} = 28.29\ MPa$$

Step 2: Calculate the strength of pavement material for one cycle of moving load using Eq. (3.35) and Table 3.6

$$\sigma_{CN:\,N=1} = \lambda e^{\varphi \times v}$$

$$\sigma_{CN:\,N=1} = 0.0058 e^{2745.5 \times 15} kPa$$

$$\sigma_{CN:\,N=1} = 3220\ kPa = 3.22 MPa$$

Step 3: Using Eq. (3.36) stress ratio can be estimated as

$$S_r = \frac{\sigma_{CN:\,N=1}}{f_{ck}} = \frac{\lambda e^{\varphi \times v}}{f_{ck}}$$

$$S_r = \frac{3.22}{28.29} = 0.113$$

Step 4: Finally, the number of cycles can be estimated for the design of pavement using as,

$$\log N = \frac{1 - S_r}{p}$$

$$\log N = \frac{1 - 0.113}{0.0714}$$

$$\log N = 12.42$$

$N = 1.73 \times 10^{12}$ cycles

References

1. Abaqus. (2017). Abaqus Documentation: Dassault Systèmes.
2. Achenbach, J. D., & Sun, C. T. (1965). Moving load on a flexibly supported Timoshenko beam. International Journal of Solids and Structures, 1(4), 353-370. https://doi.org/10.1016/0020-7683(65)90001-6
3. American Association of State Highway and Transportation Officials (AASHTO). (2002). Guide for Pavement Design of Pavement Structures.
4. American Concrete Institute (ACI 318-14). (2015). Building Code Requirements for Structural Concrete and Commentary.
5. Barksdale, R. D. (1972). Laboratory evaluation of rutting in base course materials. Third International Conference on the Structural Design of Asphalt Pavements, 1, 11-15.
6. Bourdeau, P. L., Ashmawy, A. K., Trivedi, A., & Shukla, S. K. (2021). Unpaved roads. In ICE Handbook of Geosynthetic Engineering: Geosynthetics and their applications. ICE Publishing, London, UK.

7. Boverkets handbok om betongkonstruktioner, BBK 04. (2004). Boverkets handbok om betongkonstruktioner.
8. Burmister, D. M. (1945a). The general theory of stresses and displacements in layered soil systems-II. Journal of Applied Physics, 16(3) https://doi.org/10.1063/1.1707558
9. Burmister, D. M. (1945b). The general theory of stresses and displacements in layered soil systems-III. Journal of Applied Physics, 16(5). https://doi.org/10.1063/1.1707558
10. Burmister, D. M. (1945c). The general theory of stresses and displacements in layered systems-I. Journal of Applied Physics, 16(2). https://doi.org/10.1063/1.1707558
11. Cao, P., Feng, D. C., & Jing, R. X. (2012). Based on FE method to research resistant rutting ability of pavement structure in Heilongjiang province. Applied Mechanics and Materials. https://doi.org/10.4028/www.scientific.net/AMM.128-129.1349
12. Chen, W. T. (1971). Computation of stresses and displacements in a layered elastic medium. International Journal of Engineering Science, 9(9). https://doi.org/10.1016/0020-7225(71)90072-3
13. Ding, H., Yang, Y., Chen, L. Q., & Yang, S. P. (2014). Vibration of vehicle-pavement coupled system based on a Timoshenko beam on a nonlinear foundation. Journal of Sound and Vibration, 333(24). https://doi.org/10.1016/j.jsv.2014.07.016

14. Eberle, R., & Oberguggenberger, M. (2022). Vibrations of a bridge with random structural irregularities under random traffic load and a probabilistic structural degradation assessment approach. Journal of Vibration Engineering & Technologies. https://doi.org/10.1007/s42417-022-00675-w
15. Eurocode 2, EC2. (2004). Design of concrete structures – Part 1-1: General rules and rules for buildings.
16. Federal Highway Administration, VESYS. (1977). User’s manual: predictive design procedures.
17. Hashemi, S. H., & Khaniki, H. B. (2017). Dynamic behavior of multi-layered viscoelastic nanobeam system embedded in a viscoelastic medium with a moving nanoparticle. Journal of Mechanics, 33(5), 559-575. https://doi.org/10.1017/jmech.2016.91
18. Hashemi, S. H., & Khaniki, H. B. (2018). Dynamic response of multiple nanobeam system under a moving nanoparticle. Alexandria Engineering Journal, 57(1), 343-356. https://doi.org/10.1016/j.aej.2016.12.015
19. Hilber, H. M., Hughes, T. J. R., & Taylor, R. L. (1977). Improved numerical dissipation for time integration algorithms in structural dynamics. Earthquake Engineering and Structural Dynamics, 5(3), 283–292. https://doi.org/10.1002/eqe.4290050306
20. Hoskeini-Hashemi, S., & Khaniki, H. B. (2018). Three dimensional dynamic response of functionally graded nanoplates under a moving load. Structural Engineering and Mechanics: An International Journal, 66(2), 249-262.

21. Hoskin, B. C., & Lee, E. H. (1959). Flexible surfaces on viscoelastic subgrades. Journal of the Engineering Mechanics Division, 85(4). https://doi.org/10.1061/JMCEA3.0000101

22. Hua, J., & White, T. A. (2002). Study of nonlinear tire contact pressure effects on HMA rutting. International Journal of Geomechanics, 2(3). https://doi.org/10.1061/(ASCE)1532-3641(2002)2:3(353)

23. Imaninasab, R., Bakhshi, B., & Shirini, B. (2016). Rutting performance of rubberized porous asphalt using finite element method (FEM). Construction and Building Materials, 106. https://doi.org/10.1016/j.conbuildmat.2015.12.134

24. Indian Road Congress, IRC 58. (2015). Guidelines for the Design of Plain Jointed Rigid Pavements for Highways.

25. Kumar, Y. (2020). Dynamic analysis of constrained rigid pavement subjected to moving load. M. Tech dissertation, Delhi Technological University, Delhi, India.

26. Kumar, Y., Trivedi, A., & Shukla, S. K. (2023). Damage evaluation in pavement geomaterial system using finite element scaled accelerated pavement testing. Transportation Infrastructure Geotechnology. https://doi.org/10.1007/s40515-023-00309-y

27. Lewis, K. H., & Harr, M. (1969). Analysis of concrete slabs on ground subjected to warping and moving loads. Highway Research Record, 291(17), 194-211.

28. Li, S., Guo, Z., & Yang, Y. (2015). Rutting resistance ability analysis of heavy duty asphalt pavements based on consecutive temperature variation and finite element method. CICTP 2015 – Efficient, Safe, and Green Multimodal

Transportation – Proceedings of the 15th COTA International Conference of Transportation Professionals. https://doi.org/10.1061/9780784479292.0

29. Ling, Y., Ni, J., Antonissen, J., Hamouda, H. B., Voorde, J. V., & Wahab, M. A. (2023). Numerical prediction of microstructure and hardness for low carbon steel wire Arc additive manufacturing components. Simulation Modelling Practice and Theory, 122, 102664. https://doi.org/10.1016/j.simpat.2022.102664
30. Lu, Z., Fang, R., Yao, H., Dong, C., & Xian, S. (2018). Dynamic responses of unsaturated half-space soil to a moving harmonic rectangular load. International Journal for Numerical and Analytical Methods in Geomechanics, 42(9). https://doi.org/10.1002/nag.2780
31. Lytton, R. L., Uzan, J., Fernando, E. G., Roque, R., Hiltunen, D., & Stoffels, S. M. (1993). Development and validation of performance prediction models and specifications for asphalt binders and paving mixes. Strategic Highway Research Program. Washington, DC.
32. Monismith, C. L., Ogawa, N., & Freeme, C. R. (1975). Permanent deformation characteristics of subgrade soils due to repeated loading. Transportation Research Record, 537.
33. Nguyen, K. D., Thanh, C. L., Vogel, F., Nguyen-Xuan, H., & Abdel-Wahab, M. (2022). Crack propagation in quasi-brittle materials by fourth-order phase-field cohesive zone model. Theoretical and Applied Fracture Mechanics, 118, 103236. https://doi.org/10.1016/j.tafmec.2021.103236

34. Pirabarooban, S., Zaman, M., & Tarefder, R. A. (2003). Evaluation of rutting potential in asphalt mixes using finite element modeling. TAC/ATC Annual Conference and Exhibition of the Transportation Association of Canada: The Transportation Factor.
35. Rajasekaran, S., & Khaniki, H. B. (2019). Size-dependent forced vibration of non-uniform bi-directional functionally graded beams embedded in variable elastic environment carrying a moving harmonic mass. Applied Mathematical Modelling, 72, 129-154. https://doi.org/10.1016/j.apm.2019.03.021
36. Singh, M., Trivedi, A., & Shukla, S. K. (2019). Strength enhancement of the subgrade soil of unpaved road with geosynthetic reinforcement layers. Transportation Geotechnics, 19, 54-60. https://doi.org/10.1016/j.trgeo.2019.01.007
37. Singh, M., Trivedi, A., & Shukla, S. K. (2020a). Unpaved test sections reinforced with geotextile and geogrid. Materials Today: Proceedings, 32, 706-711. https://doi.org/10.1016/j.matpr.2020.03.260
38. Singh, M., Trivedi, A., & Shukla, S. K. (2020b). Fuzzy-based model for predicting strength of geogrid-reinforced subgrade soil with optimal depth of geogrid reinforcement. Transportation Infrastructure Geotechnology, 7(4), 664-683. https://doi.org/10.1007/s40515-020-00113-y
39. Singh, M., Trivedi, A., & Shukla, S. K. (2022). Evaluation of geosynthetic reinforcement in unpaved road using moving wheel load test. Geotextiles and Geomembranes, 50(4). https://doi.org/10.1016/j.geotexmem.2022.02.005

40. Taheri, M. R., & Ting, E. C. (1989). Dynamic response of plate to moving loads: Structural impedance method. Computers and Structures, 33(6). https://doi.org/10.1016/0045-7949(89)90478-1

41. Taheri, M. R., & Ting, E. C. (1990). Dynamic response of plates to moving loads: Finite element method. Computers and Structures, 34(3), 509-521. https://doi.org/10.1016/0045-7949(90)90276-8

42. Tang, C., Lu, Z., Duan, Y., & Yao, H. (2020). Dynamic responses of the pavement-unsaturated poroelastic ground system to a moving traffic load. Transportation Geotechnique, 25, 1-8. https://doi.org/10.1016/j.trgeo.2020.100404

43. Teng, X. Q., Li, X. Z., & Chou, K. (2008). Application of finite element analysis to access the rutting potential in asphalt pavements. Transportation and Development Innovative Best Practices 2008 – Proceedings of the 1st International Symposium on Transportation and Development Innovative Best Practices, 319. https://doi.org/10.1061/40961(319)79

44. Tong, L. H., Zeng, L., Geng, D. X., Hu, W., & Xu, C. J. (2020). Dynamic effect of a moving ring load on a cylindrical structure embedded in poroelastic space based on nonlocal Biot theory. Soil Dynamics and Earthquake Engineering, 128, 1-9. https://doi.org/10.1016/j.soildyn.2019.105897

45. Tran-Ngoc, H., Khatir, S., Le-Xuan, T., De Roeck, G., Bui-Tien, T., & Abdel Wahab, M. (2021). Finite element model updating of a multispan bridge with a hybrid metaheuristic search algorithm using experimental data from wireless

triaxial sensors. Engineering with Computers, 1-19. https://doi.org/10.1007/s00366-021-01307-9

46. Tseng, K. H., & Lytton, R. L. (1989). Prediction of permanent deformation in flexible pavement materials. Implication of Aggregates in the Design, Construction and Performance of Flexible Pavements, 1016, 154-172.
47. Vu, H. T., Le, T. C., Nguyen-Xuan, H., & Abdel Wahab, M. (2022). Polygonal finite element for two-dimensional lid-driven cavity flow. CMC-Computers Materials & Continua, 70(3), 4217-4239. https://doi.org/10.32604/cmc.2022.020889
48. Wang, B., & Yang, J. (2008). Effects of vehicle dynamic loading on CRCP by 3D finite element method. Journal of Southeast University: Natural Science Edition, 38(5), 850-855.
49. Wang, Y. S., & Fu, C. G. (2010). ABAQUS structural engineering analysis and example explanation. China Architecture and Building Press, Beijing, China.
50. Wu, C. P., & Shen, P. A. (1996). Dynamic analysis of concrete pavements subjected to moving loads. Journal of Transportation Engineering, 122(5). https://doi.org/10.1061/(ASCE)0733-947X(1996)122:5(36
51. Yang, S., Li, S., & Lu, Y. (2010). Investigation on dynamical interaction between a heavy vehicle and road pavement. Vehicle System Dynamics, 48(8). https://doi.org/10.1080/00423110903243166

52. Yang, S., Lu, Y., & Li, S. (2013). An overview on vehicle dynamics. International Journal of Dynamics and Control, 1(4), 385–395. https://doi.org/10.1007/s40435-013-0032-y

53. Yao, Z., Zhou, L., Shang, Q., Guo, J., & Wang, N. (2012). Analysis of rutting change rule on asphalt pavement overlay. Advanced Materials Research, 368–373. https://doi.org/10.4028/www.scientific.net/AMR.368-373.3131

54. Zhao, Y., Jiang, L., & Zhou, L. (2015). Ambient temperature and vehicle loading effects on asphalt concrete pavement rutting development. ICTE 2015 – Proceedings of the 5th International Conference on Transportation Engineering. https://doi.org/10.1061/9780784479384.136

4

Chapter

Dynamic Load-Induced Flow Characterization of Pavement–Soil System

Highlights

- In this chapter, a novel plastic damage model is developed to capture post-elastic, flow-controlled damage in pavement–soil systems subjected to vibrations from moving loads.
- This chapter aims to investigate the dynamics in single as well as multilayer pavement-soil systems using finite-element modelling, integrating a spring-dashpot soil system to simulate realistic pavement–soil interaction.
- Three mechanistic damage zones, elastic recoverable, transition, and post-elastic, are conceptualized to characterize the progressive failure behavior of geomaterials.
- The equivalent plastic strain varies between 10^{-16}–10^{-3}% in the granular base and 10^{-16}–10^{-4}% in the subgrade, revealing significant nonlinearity under varying velocities and load intensities.
- The chapter introduces a Vibrational Mechanism of Stress Transfer (VMST) in the post-elastic zone, explaining how nonlinear stress waves and plastic flow contribute to permanent deformation and design implications in pavement systems.

4.1 Background

The damage caused by the interaction between moving vehicular load, top pavement layer, and supporting geomaterials poses mathematical complexities that involve phenomena of dynamics, elasticity, and plastic flow control (Simões & Costa, 2019). Therefore, the solution to the problem of damage dynamics of pavement and supporting geomaterial has been attributed to be a compounded phenomenon consisting of various end conditions of soil dynamics and highway engineering (Sofi, 2024). In this direction, investigations have been performed to identify the role of geomaterials in surface deflections and rutting using field and finite element scaled accelerated pavement tests (Kumar et al., 2024a). The damage caused by moving loads in terms of rutting is mainly due to the non-recoverable plastic deformations and strains stored inside the pavement and supporting granular geomaterial. The response of pavement and supporting geomaterials can, therefore, be categorized as (a) elastic, (b) elastoplastic transition, and (c) post elastic, i.e., plastic zone. When the deformations and stress are in the elastic domain, a variety of modelling techniques can be adopted to model material behaviour. A few of them include linear, equivalent linear, quasi non-linear, and non-linear elastic models. Amongst these modelling techniques, the most realistic technique includes considering a stress dependent modulus of elasticity that varies with each increment of the loading cycle (Cho et al., 1996; Arnold et al., 2001; Korkiala-Tanttu et al., 2003; Kim & Tutumluer, 2006; Lee et al., 2009). In contrast to the elastic modelling techniques, post-elastic modelling techniques rely on the resilient modulus, tensorial strains, direction cosines, bulk stress, and stress invariants (Hicks & Monismith, 1971; Uzan, 1985; Hjelmstad & Taciroglu, 2000; Cortes et al., 2012). The most widely adopted techniques to model the material behaviour in post elastic domain are largely defined by the function of deviatoric and bulk stresses. In this regard, the finite element approach has been widely employed in the field of pavement-transportation research. The finite element numerical programs have been used in the literature to investigate the damage and dynamic response of pavements. The solution from 3D finite element creep model established that pavement damage under various loads and temperatures has a non-linear development pattern (Zhu et al., 2010). The numerical simulations for investigating the deformation characteristics of the wearing course and roadbed have been carried out using the Drucker-Prager and Maxwell model. It has been observed that the magnitude of loading and Young's modulus plays a vital role while investigating the damage behaviour and permanent deformation in the pavement (Teng et al., 2008). These studies developed some consistency in the results of theoretical and experimental investigations with varied numerical fitting parameters.

The experimental investigation using an asphalt pavement analyzer was numerically simulated using elastic and viscoplastic creep models (Cao et al., 2012). The contact model was then developed for analyzing the damage in the pavement, rutting, and fatigue caused by the dynamic interaction between the wheel and the pavement surface. Based on the results of finite element simulations, a response spectrum and damage profiles were proposed to understand the damage mechanism in pavements (Xia, 2010). The three-dimensional numerical models were proposed to understand the effects of moving load on the pavement. The elastic and viscoplastic models were considered to develop the solutions for anti-rutting pavements (Li et al., 2015; Imaninasab et al., 2016; Cheng et al., 2021a, b; Cheng et al., 2022) and the damage and permanent deformation were related to the density of layers and rutting characteristics (Hu et al., 2015). The time hardening model was developed to demonstrate the congruence between damage and rutting depths obtained by 2D and 3D models. It was shown in the study that 3D models were more precise than 2D models and could be adopted to evaluate the rutting and permanent deformation (Pi et., 2007). Kumar et al. (2024b) demonstrated the use of the numerical algorithm to simulate the finite element scaled accelerated pavement testing for damage evaluation in pavement-geomaterial systems. Numerous models, including empirical and mechanical constitutive models for damage and dynamic deflection, are as listed in Tables 4.1 and 4.2.

Table 4.1 Damage models and constitutive relationships relating flow-controlled strain to the number of moving load cycles

Model	Constitutive relationship
Semi-logarithmic model [p]	$\varepsilon_p = a + blogN$
Power function model [q]	$\varepsilon_p = N^b$
VESYS model [r]	$\varepsilon_{pn} = \mu\varepsilon_r N^{-\alpha}$
Superpave model[s]	$\varepsilon_p = log\varepsilon_p(1) + SlogN$
Exponential function model [t]	$\varepsilon_p = \varepsilon_0 e^{-(\rho/N)^\beta}$
Fatigue life models [u]	$N = A\left(\frac{1}{\varepsilon_t}\right)^B e^{CT+D\times RP}$
Stiffness modulus models [u]	$S = S_0\left\{1 - e^{-\left[\frac{a(RP+b)(T+c)\varepsilon^{-d}}{N}\right]^\beta}\right\}$
Plastic damage model [v]	$\varepsilon = \varepsilon^p + \varepsilon^e = \varepsilon^p + \frac{\sigma}{E}$ $f = \sigma_e - \sigma_y \begin{cases} f < 0; elastic\ zone \\ f = 0; post\ elastic\ zone \end{cases}$ $\sigma_y = f(d_t, d_c) \begin{cases} d_t = f\ (\tilde{\varepsilon}_t^{pl}, f_i); damage\ during\ tension \\ d_c = f\ (\tilde{\varepsilon}_c^{pl}, f_c); damage\ during\ compression \end{cases}$

[p]Barksdale (1972); [q]Monismith (1975); [r]VESYS (1977); [s]Lytton et al., (1993); [t]Tseng and Lytton (1989); Cheng et al. (2022); [v]Present study

Table 4.2 Dynamic models and governing equations for pavement deflection response

Model	Governing equation
Time variable model [a]	$x = \frac{1}{k_i}\left[Q + F - \left\{M_i\left(\vartheta_i a + \dot{\vartheta}_i v\right) + C_i(\vartheta_i v)\right\}\right]$
Direct integral model [b]	$x = \frac{1}{k_i}[R - \{M_i(a) + C_i(v)\}]$
Step integral model [c]	$\{x\,\lvert_{t+\Delta t}\} = \{x\,\lvert_t\} + \Delta t.\{v\,\lvert_t\} + \Delta t^2.(\psi).\{a\,\lvert_t\} + \left(\frac{1}{2} - \psi\right).\{a\,\lvert_{t+\Delta t}\}$

[a] Wu and Shen (1996); [b] Yang et al. (2010); [c] Present study

It has been analyzed that a variety of modelling techniques are available for investigating the geomaterials in elastic and post-elastic domains. However, modeling techniques for damage dynamics in pavement-soil systems due to moving loads remain elusive and are still one of the most problematic conditions affecting pavement life, even with low road traffic volumes. Due to the intrinsic post-elastic flow feature of the pavement material and numerous external factors, such as velocity and load, the investigation of pavement damage becomes a challenging topic. Considering the limitations prevailing in the literature, two key objectives have been set to conduct the research as follows:

1. To develop a numerical model for investigating the post-elastic flow-induced damage in coupled pavement-geomaterial assembly subjected to moving vehicular loads.
2. To investigate the role of moving load vibrations in damage dynamics of single and multilayer pavement supported by a spring-dashpot system and flow-controlled geomaterials.

4.2 Model Definition

The numerical modelling and investigations have been performed using a commercial finite element program (Abaqus) for examining the effects of moving load and its consequences in single and multilayer pavement systems as shown in Figs. 4.1(a) and (b).

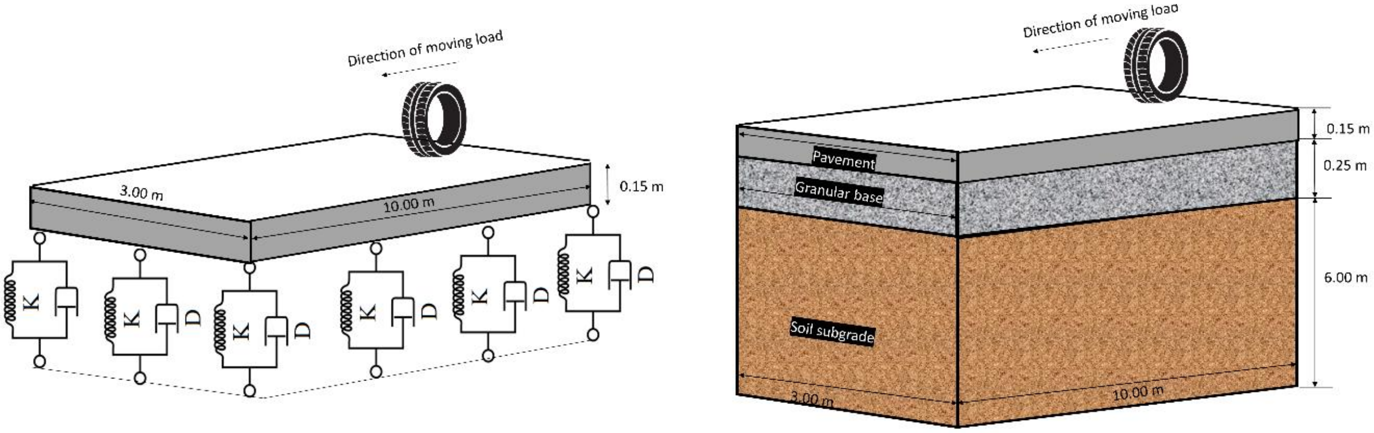

(a) Single layer pavement supported by spring dashpot system

(b) Pavement supported by multilayer geomaterial

Figure 4.1 Schematic representation of (a) single layer pavement supported by spring dashpot system and (b) pavement supported by multilayer geomaterial

Table 4.3 Input parameters adopted to conduct numerical investigations

Parameter	Top pavement layer	Base course	Subgrade
Young's modulus, E (MPa)$^{a, b}$	24	15	6
Poisson's ratio, v ^{c}	0.15	0.25	0.3
Unit weight, ρ (kN/m^{3}) $^{a, b}$	23.24	22	18
Friction angle, ϕ $^{b, d, e}$	-	45°	35°
Dilation angle, ψ $^{a\text{-}e}$	30°	10°	5°
Eccentricity, ê ^{f}	0.1	-	-
f_{b0}/f_{c0} ^{f}	1.16	-	-
K ^{f}	0.67	-	-

^{a}Kim, (2014); ^{b} Mehra and Trivedi (2021); ^{c}Ma et al., (2022); ^{d}Wosatko et al., (2019); ^{e}Schanz and Vermeer (1996); ^{f} Lubliner et al., (1989)

For a single layer system supported by spring and dashpot, the foundation soil has been modeled as a linear K-V model with a stiffness of 2.714×10^{4} kN/m^{3} and a damping ratio of 0.05. To model the impact of moving load vibration on pavement damage supported by flow-controlled geomaterials, the prerequisite parameters include Young's modulus, Poisson's ratio, unit weight, friction angle, dilation angle, eccentricity, stress ratio, the non-dimensional constant defining the yield surface (K), and layer dimensions. These properties for the pavement and geomaterial were sourced from various references (Lubliner, 1989; Schanz & Vermeer, 1996; Kim, 2014; Wosatko et al., 2019; Mehra & Trivedi, 2021; Ma et al., 2022). Further, the material properties adopted to model the pavement in single and multilayer were kept identical, and properties adopted to model multilayer geomaterial are listed in Table 4.3.

The unconditionally stable algorithm with a backward Euler operator in implicit integration has been used to investigate the response of pavement-geomaterial systems due to the moving action of vehicular loads and the motion equation can be written as:

$$[M]\{a\}+[C]\{v\}+[K]\{x\}=\{F_E(t)\} \tag{4.1}$$

The body force term has been derived using consistent interpolation, whereas the mass matrix uses consistent interpolation. Consistent interpolation helps maintain a constant mass value and prevents the violation of mass conservation law. The motion equation can be stated as:

$$[M_C]\{a\}+[b_f]=[q_f] \tag{4.2}$$

where,

$\boldsymbol{M_C}$ is the consistent mass matrix, $\boldsymbol{b_f}$ is the body force, and $\boldsymbol{q_f}$ is the externally prescribed force.

The issue of a moving load on the assembly of pavement, granular base, and soil subgrade is solved using a modified version of Newmark's β approach to produce a numerical solution. During the temporal integration procedure, a small quantity of undesirable high-frequency noise is inadvertently introduced. The noise was eliminated by the use of damping factors. The operator substitutes the current equilibrium equation of motion with equilibrated D'Allembert forces. A weighted average was calculated for the static forces at the beginning and end of each time step. The equation of motion is now given as:

$$[M_D^*]\{a\,|_{t+\Delta t}\} + \left\{b_F^*\,|_{t+\Delta t}\right\} - \Phi\left\{b_F^*\,|_t\right\} = 0 \tag{4.3}$$

where $[M_D^*]$ represents the damped consistent mass matrix,

$b_F^*\,|_{t+\Delta t} = \frac{\{I_F^N\,|_{t+\Delta t}\} - \{q_F^N\,|_{t+\Delta t}\}}{L^N\,|_{t+\Delta t}}$ and $b_F^*\,|_t = \frac{\{I_F^N\,|_t\} - \{q_F^N\,|_t\}}{L^N\,|_{t+\Delta t}}$ are the resultant force vector at $t + \Delta t$ and t time in which Lagrange multiplier is denoted by $L^N\,|_{t+\Delta t}$ and modified formula for deflection can be expressed as,

$$\{x\,|_{t+\Delta t}\} = \{x\,|_t\} + \Delta t.\{v\,|_t\} + \Delta t^2.(\psi).\{a\,|_t\} + \left(\frac{1}{2} - \psi\right).\,\{a\,|_{t+\Delta t}\} \tag{4.4}$$

where $\ddot{x}\,|_{t+\Delta t}$, $\dot{x}\,|_{t+\Delta t}$, and $x\,|_{t+\Delta t}$ are the acceleration, velocity, and displacement vector at time $t + \Delta t$ and $\ddot{x}\,|_t$, $\dot{x}\,|_t$, and $x\,|_t$ are the acceleration, velocity, and displacement vector at time t. The limits of damping factors are as below:

$-0.5 \leq \Phi \leq 0$, $4\psi = (1-\Phi)^2$, and $2\Gamma = 1 - \Phi$.

4.2.1 Plastic Flow-induced Damage in the Pavement

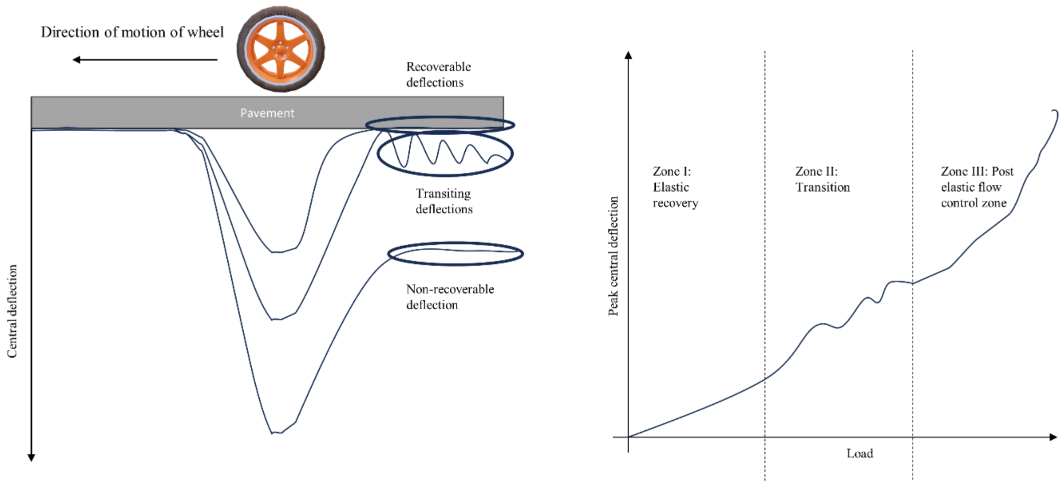

Figure 4.2 Conceptualization of the flow-controlled damage from recoverable, transiting, and non-recoverable deformations corresponding to the three zones of mechanistic analysis, namely, zone of elastic recovery, transition zone, and zone of flow control

Numerical simulations have been performed to investigate flow-induced pavement damage that considers compressive and tensile damages due to plastic deformations caused by the movement of vehicular load. The governing mechanism for the failure of the paving material in the pavement-soil system is controlled by flow control and yielding. Tensile and compressive equivalent plastic strains govern the yielding in the pavement under tension and compression ($\tilde{\varepsilon}_t^{pl}$ and $\tilde{\varepsilon}_c^{pl}$). The stress-strain response for the uniaxial tension mechanism of failure follows a straight-line path till the failure stress (σ_t). The beginning of the micro-cracks in the pavement is marked by achieving the failure stress (σ_t). Further, a softening stress-strain curve onset the macroscopic failure with strain localization in the pavement. Under uniaxial compression, the response is linear until the value of the initial yield, σ_{c0}. The post-elastic zone has been identified by stress hardening and strain softening after the ultimate stress. Based on this hypothesis recoverable, transiting, and non-recoverable deformations have been conceptualized which corresponds to the three zones of mechanistic analysis, namely, zone of elastic recovery, transition zone, and zone of flow control as shown in Fig. 4.2.

To make the study as presented, the following assumptions have been made:

(1) The flow-controlled material is governed by a plastic dislocation and movement of particles referred in the manuscript as flow. The flow potential function (G) grows closer to the asymptote at a rate determined by the eccentricity (ê); as the eccentricity gets closer to zero, the flow potential tends to follow a straight line.

(2) The uniaxial σ-ε curves were modified into stress vs. plastic-strain curves.

(3) The plastic rate is a function of instantaneous stress ($\sigma : \dot{\varepsilon}^{pl}$) and a compliance factor C. Hence, it has been assumed that a non-associated potential plastic flow governs the damage in the pavement supported by spring-dashpot and flow-controlled geomaterial.

Considering these assumptions, the damage model can be expressed as,

$$\sigma_t = f\left(\tilde{\varepsilon}_t^{pl}, \dot{\tilde{\varepsilon}}_t^{pl}, f_i\right) \tag{4.5}$$

$$\sigma_c = f\left(\tilde{\varepsilon}_c^{pl}, \dot{\tilde{\varepsilon}}_c^{pl}, f_i\right) \tag{4.6}$$

The subscripted letters *c* and *t* account for the compression and tension. Further, the accented dot accounts for the plastic strain rates. The variables have calculated the loss in the stiffness to account for damage as a function of the plastic strains expressed as,

$$d_t = f\left(\tilde{\varepsilon}_t^{pl}, f_i\right) \tag{4.7}$$

$$d_c = f(\tilde{\varepsilon}_c^{pl}, f_i) \tag{4.8}$$

The variables to incorporate damage (*d*) stretches from zero to one, showing the undamaged material at zero to complete loss in strength at one.

The constitutive equation for the tensile and compressive stress for the moving load action of the wheel over pavement can be expressed as,

$$\sigma_t = (1 - d_t)E_0\left(\varepsilon_t - \tilde{\varepsilon}_t^{pl}\right) \tag{4.9}$$

and

$$\sigma_c = (1 - d_c)E_0\left(\varepsilon_c - \tilde{\varepsilon}_c^{pl}\right) \tag{4.10}$$

Further, effective tensile and compressive stress for moving load action of the wheel over pavement can be expressed as,

$$\bar{\sigma_t} = \frac{\sigma_t}{1 - d_t} = E_0\left(\varepsilon_t - \tilde{\varepsilon}_t^{pl}\right) \tag{4.11}$$

and

$$\bar{\sigma_c} = \frac{\sigma_c}{1 - d_c} = E_0\left(\varepsilon_c - \tilde{\varepsilon}_c^{pl}\right) \tag{4.12}$$

The effective stress stated above in Eq. (4.11) and (4.12) governs the yield surface and, on simplification, can be expressed as,

$$\bar{\sigma} = D_0^{el}: (\varepsilon - \varepsilon^{pl}) \tag{4.13}$$

The effective stress tensor comprises the potential function for plastic flow control and the failure (yield) surface and the hydrostatic state of stress can be expressed as,

$$\bar{p} = -\frac{1}{3}\, Tr\, (\bar{\sigma}) \tag{4.14}$$

and the equivalent stress can be expressed as,

$$\bar{q} = \sqrt{\frac{3}{2}(\bar{S}{:}\bar{S})} \tag{4.15}$$

where $\bar{S} = \bar{\sigma} + \bar{p}I$

The flow potential G can be expressed as,

$$G = \sqrt{\hat{e}\sigma_{to} \tan\psi^2 + \bar{q}^2} - \bar{p}\tan\psi \tag{4.16}$$

where,

ψ is the dilation angle

σ_{to} is the tensile stress

ê is the eccentricity

4.2.2 Framework for Flow-controlled Geomaterial

The elastic analysis conventionally assumes that the geomaterial supporting the paving layers remains continuously in contact to the pavement. However, geomaterial undergoes a significant deformation, particularly near the bottom surface of pavement layer. This deformation coupled with local yielding is primarily responsible for the non-linear behavior observed in geomaterial, even under low load traffic conditions, inducing ruts and permanent deformation in the pavement and supporting geomaterial layers.

In the present study, it has also been assumed that yielding can be considered if shear stress at any spatial coordinate in the geomaterial attains a value linearly dependent on the normal stress in the same stress-strain plane. Therefore, the flow control (FC) modelling technique has been adopted to investigate plastic flow-induced damage in the geomaterials where shearing stresses are a function of strain rate at elastic and post elastic levels. To develop the robust model for flow-controlled geomaterial interaction in pavement-geomaterial system subjected to moving load, following assumptions have been considered;

(1) The behaviour of geomaterial is elastic within the yield surface. Nonlinear hardening (Fig. 4.3) is assumed for the initial behaviour of the plastic yield surface.

(2) The flow controlled geomaterial follows a law for the stress-strain relation as a function of I_1, J_2, and J_3 and has onset of non-linearity at $\varepsilon_{ij}^{p} > 0$.

(3) The shear criterion has an onset of controlled granular flow, which intersects the yield surface as a special case, having a smooth yield surface such that, $f = 0$.

(4) The flow controlled geomaterial follows a plastic stress-strain relation defined by a chain rule such that $\left(\delta f / \sigma_{ij}\right) \delta \sigma_{ij} > 0$.

(5) The smooth flow potential for the geomaterial has a hyperbolic shape with a constant eccentricity in the meridional stress plane and a piecewise elliptic shape in the deviatoric stress plane.

Considering these assumptions, the yield function can be expressed as:

$$f = \sigma_e - \sigma_y \begin{cases} f < 0; elastic\ zone \\ f = 0; plastic\ zone \end{cases} and\ \frac{\partial f}{\partial \sigma_{ij}} \partial \sigma_{ij} > 0 \tag{4.17}$$

where, $\sigma_e = \sqrt{\frac{3}{2} \acute{\sigma} : \acute{\sigma}}$ and $\sigma_y = f(p)$ which can be expressed as:

$$\sigma_y = f(p) = \sigma_{y0} + H\varepsilon^p \; , (\varepsilon^p = p + \Delta p) \tag{4.18}$$

In the present research, H is considered as a function of principal stresses, friction angle, dilation angle, and yield stresses. This can be conceptualized through Fig. 4.3.

The total strain (ε_{ij}) is varied with loading such that $\partial\varepsilon_{ij}^p \neq 0$, and the consistency conditions guarantee that the yield surface is carried along with the stress point such that,

$$\partial f = \frac{\partial f}{\partial\sigma_{ij}}\partial\sigma_{ij} + \frac{\partial f}{\partial\varepsilon_{ij}^p}\partial\varepsilon_{ij}^p \; = 0 \tag{4.19}$$

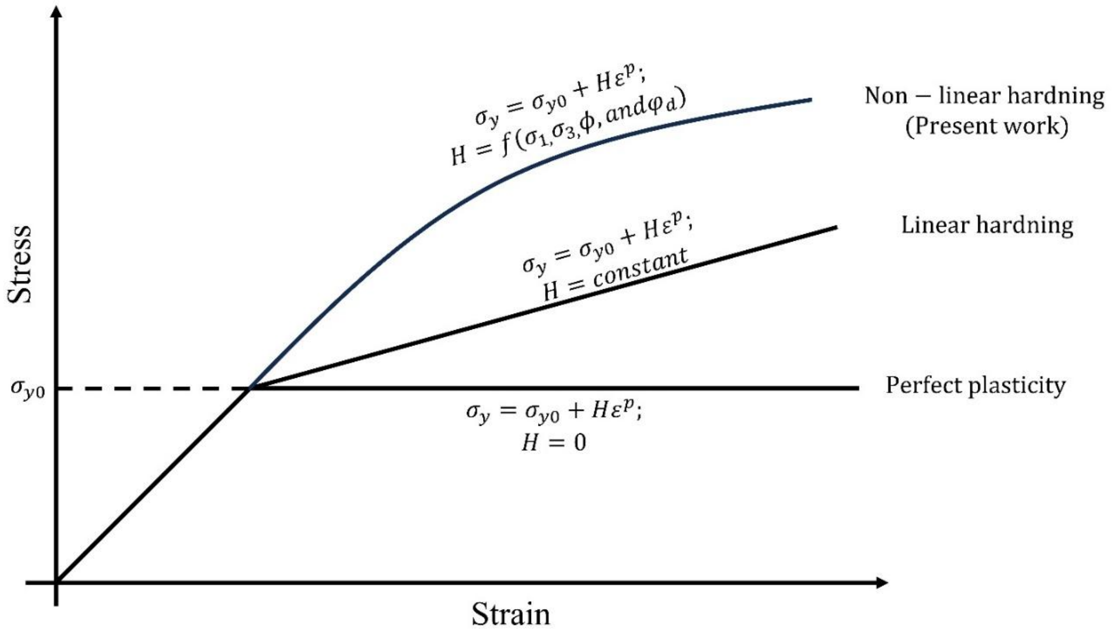

Figure 4.3 Conceptualization of nonlinear hardening adopted in the present work as compared to perfect plasticity and linear hardening

The direction of plastic strain increment, ε_{ij}^p, is expressed as:

$$d\varepsilon_{ij}^p = \partial\lambda \frac{\partial g}{\partial\sigma_{ij}} \tag{4.20}$$

Therefore, total incremental strain can be expressed as:

$$d\varepsilon = d\varepsilon_{ij}^{e} + d\varepsilon_{ij}^{p} \tag{4.21}$$

The modified yield criteria for any frictional material would be a function of first stress invariant. If the stress state lies on the single yield surface, the yield criteria for the geomaterial can be expressed as:

$$f = \sigma_3 - \sigma_1 + (\sigma_3 + \sigma_1)\sin\phi \tag{4.22}$$

The plastic potential is obtained using the dilation angle φ_d, and can be expressed as:

$$g = \sigma_3 - \sigma_1 + (\sigma_3 + \sigma_1)\sin\varphi_d \tag{4.23}$$

Frictional geomaterials are generally assumed to follow the Mohr-Coulomb (MC) failure criterion. However, the MC plasticity has certain discontinuity on the yield surface with edges at which the yield criterion is not with the flow. Therefore, in the present research, the flow potential, *g*, for the yield surface was chosen to be geometrically continuous function in the meridional stress plane and smooth elliptic function in the deviatoric stress plane which can be expressed as:

$$g = \sqrt{(\varepsilon c \tan\varphi_d)^2 + (R_{mw} q)^2} - \ p \tan\varphi_d \tag{4.24}$$

where

$$R_{mw}(\Theta, e) = \frac{4(1-e^2)\cos^2\Theta + (2e-1)^2}{2(e-1)^2\cos\Theta + (2e-1)\sqrt{4(e-1)^2\cos^2\Theta + 5e^2 - 4e}} R_{mc}\left(\frac{\pi}{3}, \phi\right)$$

$$R_{mc}\left(\frac{\pi}{3}, \phi\right) = \frac{3 - \sin\phi}{6\cos\phi}$$

$$e = \frac{3 - \sin\phi}{3 + \sin\phi}$$

where, φ_d = angle of dilation, c = initial cohesion yield stress, Θ = deviatoric polar angle, ε = meridional eccentricity, and *e* = deviatoric eccentricity

4.2.3 Numerical Implementation of Flow-control Model

For numerically implementing the flow control response, it has been considered that solving the flow control behaviour of pavement-geomaterial system subjected to moving load is incremental. The material is assumed to obey Hoek's law, and mathematically expressed as:

$$\begin{bmatrix}\sigma_{11}\\\sigma_{22}\\\sigma_{33}\\\sigma_{12}\\\sigma_{13}\\\sigma_{23}\end{bmatrix}=\begin{bmatrix}2G+\lambda & \lambda & \lambda & 0 & 0 & 0\\ \lambda & 2G+\lambda & \lambda & 0 & 0 & 0\\ \lambda & \lambda & 2G+\lambda & 0 & 0 & 0\\ 0 & 0 & 0 & G & 0 & 0\\ 0 & 0 & 0 & 0 & G & 0\\ 0 & 0 & 0 & 0 & 0 & G\end{bmatrix}\begin{bmatrix}\varepsilon_{11}\\\varepsilon_{22}\\\varepsilon_{33}\\\varepsilon_{12}\\\varepsilon_{13}\\\varepsilon_{23}\end{bmatrix} \tag{4.25}$$

where, $\boldsymbol{G}$ is shear modulus, $\boldsymbol{\lambda}$ is Lame's parameter. Since in the all-diagonal components of the stiffness matrix *G* exists, we can relate the stress and strain components as:

$$\sigma_{ij} = 2G\varepsilon_{ij}^{e} + \lambda(\varepsilon_{11}^{e} + \varepsilon_{22}^{e} + \varepsilon_{33}^{e})\delta_{ij}\begin{cases}\delta_{ij} = 1\, for\ i = j\ (normal\ stresses)\\ \delta_{ij} = 0\, for\ i \neq j\ (shear\ stresses)\end{cases} \tag{4.26}$$

where, $\boldsymbol{\delta_{ij}}$ is Kronecker delta and $\boldsymbol{\varepsilon_{11}^{e} + \varepsilon_{22}^{e} + \varepsilon_{33}^{e}}$ can be written as $\boldsymbol{tr(\varepsilon^{e})I}$ and hence Eq. (4.26) can be written as:

$$\sigma = 2G\varepsilon^{e} + \lambda tr(\varepsilon^{e})I \tag{4.27}$$

Equation (4.26) is valid for all strains so the equation is used at the end of the increment. For k+1 increment, Eq. (4.27) can be expressed as:

$$\sigma_{k+1} = 2G\varepsilon_{k+1}^{e} + \lambda tr(\varepsilon_{k+1}^{e})I \tag{4.28}$$

Now the elastic strain at the end of the increment is calculated based on the strain at the beginning of the increment. Total and plastic strain increment can be expressed as:

$$\varepsilon_{k+1}^{e} = \varepsilon_{k}^{e} + \Delta\varepsilon^{e} = \varepsilon_{k}^{e} + (\Delta\varepsilon - \Delta\varepsilon^{p}) \tag{4.29}$$

Substituting the value of $\boldsymbol{\varepsilon_{k+1}^{e}}$ in Eq. (4.28),

$$\sigma_{k+1} = 2G\big(\varepsilon_{k}^{e} + (\Delta\varepsilon - \Delta\varepsilon^{p})\big) + \lambda tr\big(\varepsilon_{k}^{e} + (\Delta\varepsilon - \Delta\varepsilon^{p})\big)I \tag{4.30}$$

As the geomaterial is incompressible, rearrangement of the Eq. (4.30) can be expressed as:

$$\sigma_{k+1} = 2G(\varepsilon_{k}^{e} + \Delta\varepsilon) + \lambda tr(\varepsilon_{k}^{e} + \Delta\varepsilon)I - 2G\Delta\varepsilon^{p} \tag{4.31}$$

The term $\boldsymbol{2G(\varepsilon_{k}^{e} + \Delta\varepsilon) + \lambda tr(\varepsilon_{k}^{e} + \Delta\varepsilon)I}$ is equal to the strain at the beginning of the increment plus stiffness matrix multiplied by the total strain increment. Hence,

$$\sigma_{k+1} = \sigma_{k} + C\Delta\varepsilon - 2G\Delta\varepsilon^{p} \tag{4.32}$$

The stress at the end of the first increment has been calculated assuming that the strain at the beginning of increment is elastic and is known as elastic predictor trial stress expressed as:

$$\sigma^{tr} = 2G(\varepsilon_{k}^{e} + \Delta\varepsilon) + \lambda tr(\varepsilon_{k}^{e} + \Delta\varepsilon)I = \sigma_{k} + C\Delta\varepsilon \tag{4.33}$$

Hence, Eq. (4.32) can be written as:

$$\sigma_{k+1} = \sigma^{tr} - 2G\Delta\varepsilon^{p} \tag{4.34}$$

The plastic strain increment $\boldsymbol{\Delta\varepsilon^{p}}$ is obtained by the normality hypothesis as:

$$\Delta\varepsilon^{p} = \Delta p \frac{\acute{\sigma}}{\sigma_{e}} \tag{4.35}$$

So, $\boldsymbol{\sigma_{k+1}}$ can be written as:

$$\sigma_{k+1} = \sigma^{tr} - 2G\Delta p \frac{\acute{\sigma}}{\sigma_{e}} \tag{4.36}$$

To obtain $\boldsymbol{\Delta p}$, replacing $\boldsymbol{\sigma_{k+1}}$ with the deviatoric stress ($\boldsymbol{\acute{\sigma} + PI}$) in Eq. (4.36),

$$\acute{\sigma} + PI = \sigma^{tr} - 2G\Delta p \frac{\acute{\sigma}}{\sigma_{e}} \tag{4.37}$$

Rearranging Eq. (4.36) and replacing the RHS of the equation by deviatoric trial stress,

$$\left(1 + 3G\frac{\Delta p}{\sigma_{e}}\right)\acute{\sigma} = \sigma^{tr} - PI = \acute{\sigma}^{tr} \tag{4.38}$$

The double contracted product of both sides can be expressed as:

$$\left(1 + 3G\frac{\Delta p}{\sigma_{e}}\right)^{2}\acute{\sigma}:\acute{\sigma} = \acute{\sigma}^{tr}:\acute{\sigma}^{tr} \tag{4.39}$$

Calculate the square root of Eq. (4.39),

$$\left(1 + 3G\frac{\Delta p}{\sigma_e}\right)\sigma_e = \sigma_e^{tr} = \sigma_e + 3G\Delta p \tag{4.40}$$

Further, yield function is obtained by replacing the effective stress by trial stress and can be expressed as:

$$f = \sigma_e^{tr} - 3G\Delta p - \sigma_y \tag{4.41}$$

The newton iteration method is adopted to solve the above equation to find $\boldsymbol{\Delta p}$ as:

$$f = \frac{\partial f}{\partial \Delta p} d\Delta p + \cdots \ldots \ldots \ldots \ldots . = 0 \tag{4.42}$$

Solving Eq. (4.42) by putting value of yield function and differentiating gives

$$\sigma_e^{tr} - 3G\Delta p - \sigma_y + (-3G - H)d\Delta p = 0 \tag{4.43}$$

Therefor the correction of $\boldsymbol{\Delta p}$ is

$$d\Delta p = \frac{\sigma_e^{tr} - 3G\Delta p - \sigma_y}{(3G + H)} \tag{4.44}$$

Eq. (4.44) in iterative loop is used to calculate the $\Delta \boldsymbol{p}$ and applied as shown in Fig. 4.4.

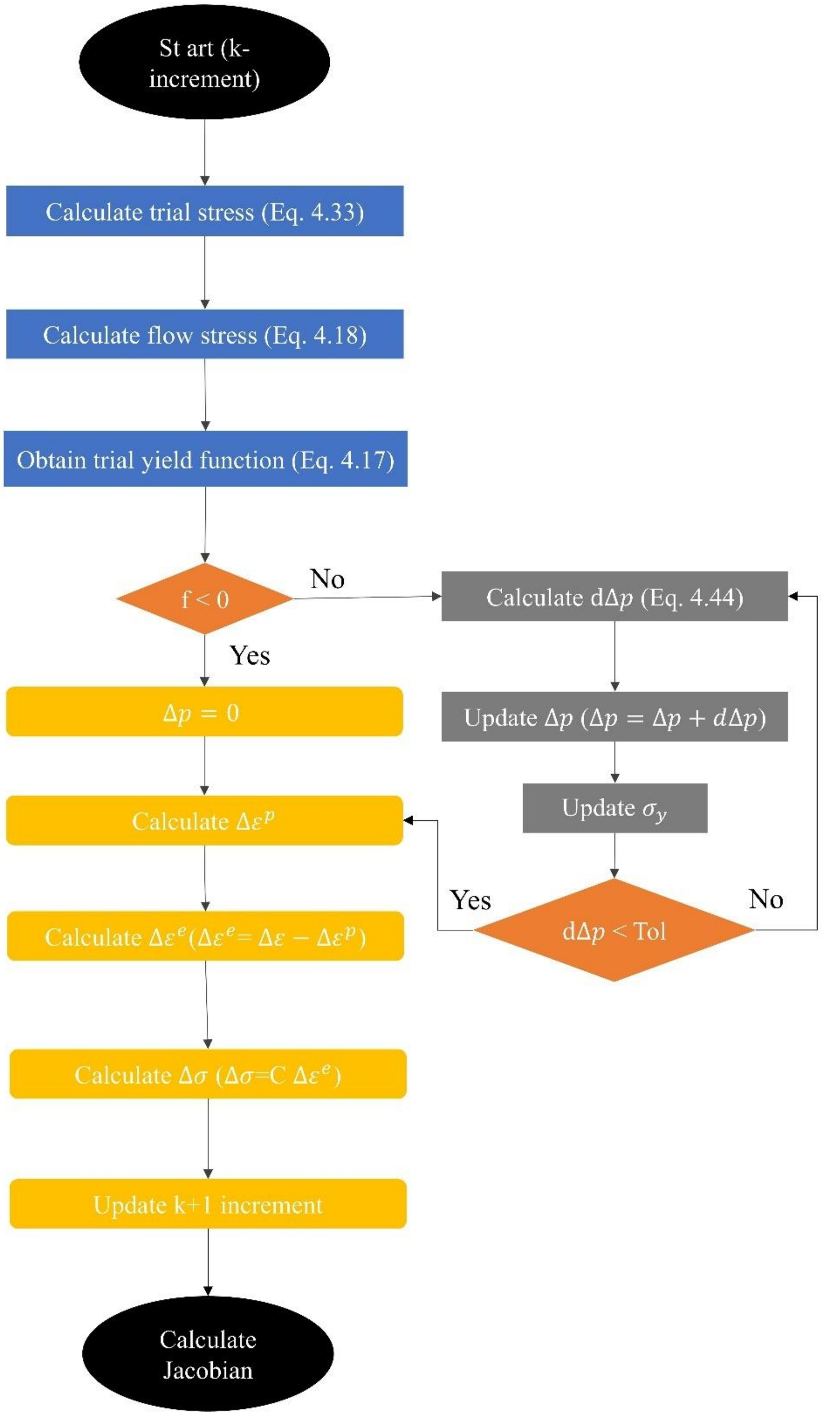

Figure 4.4 Flow chart for numerical implementation of the flow response

4.3 Results and Discussion

4.3.1 Model Validation and Feasibility

The feasibility of the model has been confirmed by (a) mesh convergence, and (b) comparison of results as reported in the available literature.

4.3.1.1 Mesh Convergence

After conducting a thorough examination of mesh convergence as described in the Table 4.4, it has been determined that a global seeding parameter consisting of a biased mesh (0.1-0.04) is the most appropriate value for this research. This parameter selection ensures an optimal equilibrium between computational efficiency and result accuracy. Moreover, the numerical study findings have been systematically validated to match the reference outcomes documented in the current literature, thereby confirming the accuracy.

Table 4.4 Mesh convergence performed to optimize the numerical simulation

Part/Instance	Global seeding	Number of elements	Size of element (mm)	Isometric view of meshed geometry	Computation time for one simulation (hours)	Magnitude of displacement on pavement top (mm)
Pavement	0.5	1620	437 × 500 × 150	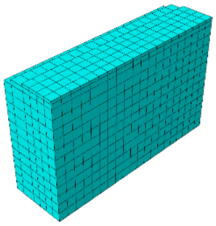	0.25	0.8803~0.88
Granular base			437× 500 × 250			
Subgrade			437 × 500 × 500			
Pavement	0.4	2875	437× 400 × 150	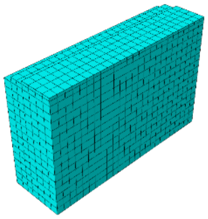	0.65	0.7412~0.74
Granular base			437× 400 × 250			
Subgrade			437 × 400 × 400			

Pavement	0.3	7062	291 × 303× 150	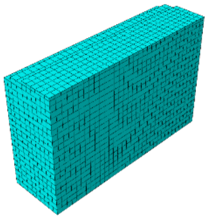	3.00	0.5777~0.57
Granular base			291 × 303× 250			
Subgrade			291 × 303 × 300			
Pavement	0.2	25100	194 × 200 × 150	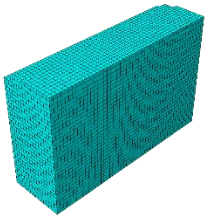	15.25	0.5076~0.51
Granular base			194 × 200 × 250			
Subgrade			194 × 200 × 200			
Pavement	0.1	191100	97 × 100 × 75	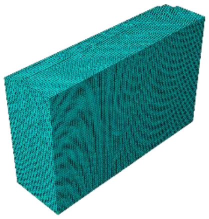	40.00	0.4746~0.47
Granular base			97 × 100 × 83			
Subgrade			97 × 100 × 100			
Pavement	0.08	364000	79 × 80 × 75	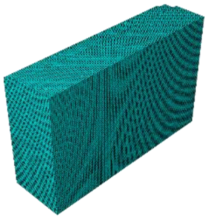	98.75	0.4698~0.47
Granular base			79 × 80 × 83			
Subgrade			79 × 80 × 80			
Pavement	0.04	2988500	40 × 40 × 37.5	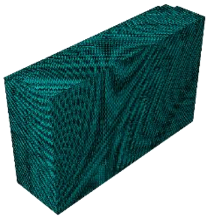	Unable to simulate (System limitations)	-
Granular base			40 × 40 × 41			
Subgrade			40 × 40 × 40			
Pavement	Biased mesh (0.1-0.04)	249600	40 × 100 × 75	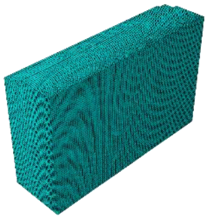	54.00	0.4708~0.47
Granular base			40 × 100 × 83			
Subgrade			40 × 100 × 100			

4.3.1.2 Comparison of Results as Reported in the Available Literature

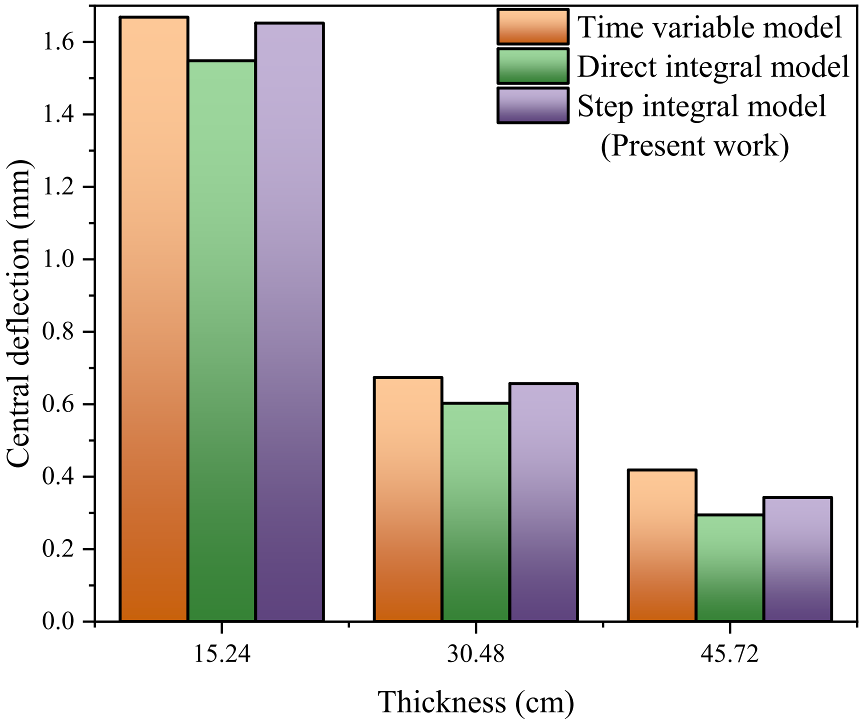

Figure 4.5 Comparison of peak central deflection obtained in the step integral model (present work) with the results obtained by time variable and direct integral model by the researchers for varied thicknesses of pavement ranging from 15 to 45 cm

Fig. 4.5 shows a comparison of peak central deflection obtained in the step integral model (present work) with the results obtained by time variable and direct integral model by the researchers for varied thicknesses of pavement ranging from 15 to 45 cm. This research demonstrates a noticeable pattern in peak deflections in pavement due to the moving load vibrations over the pavement length. The measured peak displacements decrease in proportion to the increase in pavement thickness. The correlation between pavement thickness and displacement magnitude shown in previous investigations supports the validity of the present numerical findings.

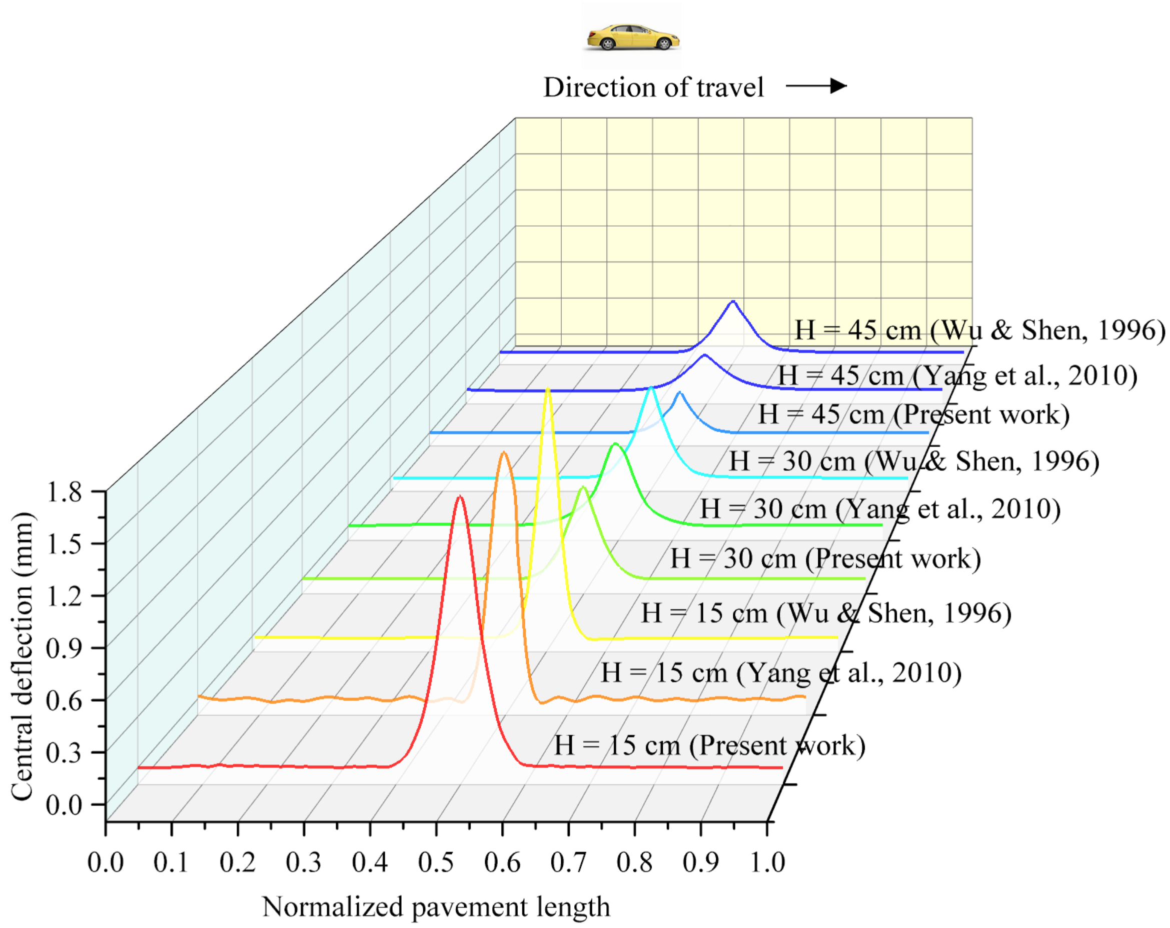

Figure 4.6 Central deflection for the position of moving load along the normalized pavement length for varied pavement thicknesses compared to the results available in literature

Further, Fig. 4.6 shows the response of pavement to the moving load vibrations has been analyzed over the pavement length in comparison to the results available in literature (Wu & Shen, 1996; Yang et al., 2010). Wu & Shen (1996) considered the direct dynamic interaction between pavement and moving load, and modelled soil as a spring beneath the pavement structure. The investigations were performed using the 3D FEM technique. Yang et al. (2010) also conducted the similar study using the quick, direct integral method, and the results were in close proximity. In the present study, the principle of virtual work done in conjunction with the 3D Finite Element model using the similar dimension and properties to that of Wu & Shen (1996) and Yang et al. (2010) is adopted to validate the dynamic response of the pavement subjected to moving load. It is evident from Figs. 4.5 and 4.6 the results of the present study are well in conjunction with the results available in the literature of Wu & Shen (1996) and Yang et al. (2010).

4.3.2 Single Layer Modelling

Fig. 4.7(a-d) illustrate the variation in the magnitude of dynamic displacement as a function of the application point of a moving load positioned at the center. The investigation covers a spectrum of velocities ranging from 10 to 40 m/s and load magnitudes ranging from 50 to 200 kN. The displacement response shows comparable patterns for velocities of 10 m/s and 20 m/s until it reaches a loading threshold of 150 kN. It has been noted that the displacement after reaching the elastic limit is inversely proportional to the intensity of the load applied at various velocities. More precisely, for velocities of 10, 20, 30, and 40 m/s, the displacement after the elastic phase is seen when the loading intensities are 200, 175, 150, and 125 kN,135onceptively. The inverse connection between velocity and threshold loading intensity suggests that as velocity rises, the point at which post-elastic displacement occurs decreases.

$$D^{pe} \propto \frac{1}{l_v} \tag{4.45}$$

where D^{pe} is the post elastic displacement, and l_v is loading at incremental velocity. The surface region affected by the dynamic load exhibits plastic deformation characterized by non-recoverable displacements. This plastic deformation arises due to variations in both the intensity and velocity of the applied load.

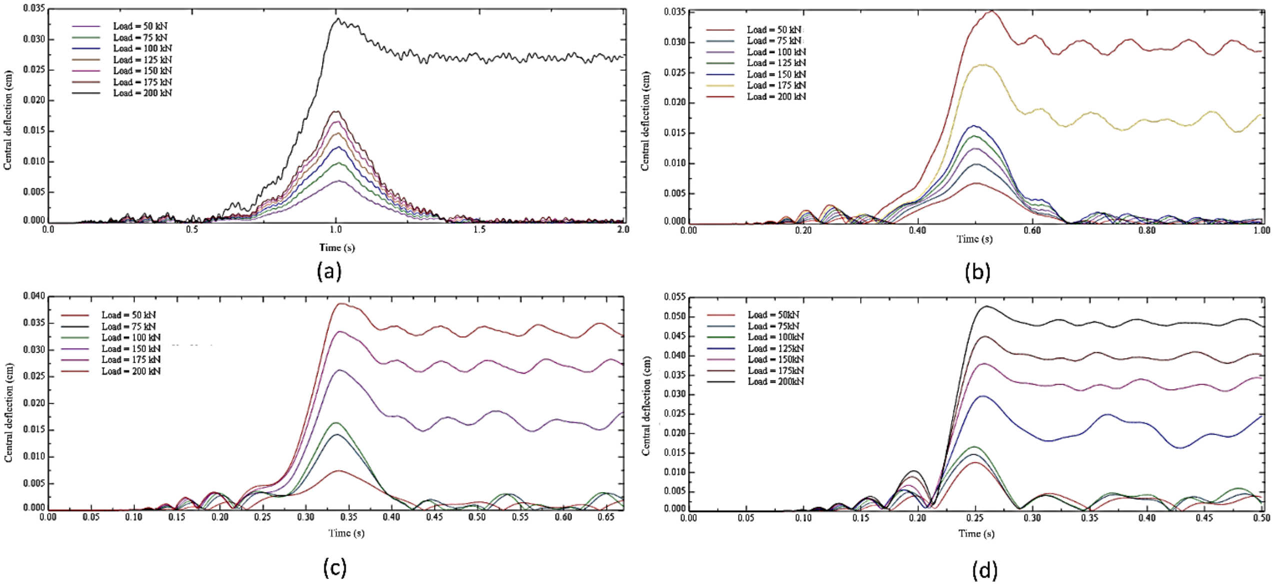

(a) (b)

(c) (d)

Figure 4.7 Variation of displacement for a moving load velocity of (a) 10 m/s, (b) 20 m/s, (c) 30 m/s, and (d) 40 m/s

Fig 4.8(a-d) illustrates the contour images of the plastically stored, non-recoverable displacement field corresponding to a range of moving load velocities between 10 to 40 m/s. In this contour image, areas highlighted in red represent zones of maximum displacement, indicating the highest degree of plastic deformation. Conversely, areas shaded in blue denote regions of minimal displacement, reflecting the lowest levels of plastic deformation. The arrows within the figure indicate towards plastically stored, post-elastic displacements, thereby providing a comprehensive visualization of the deformation field induced by the moving load.

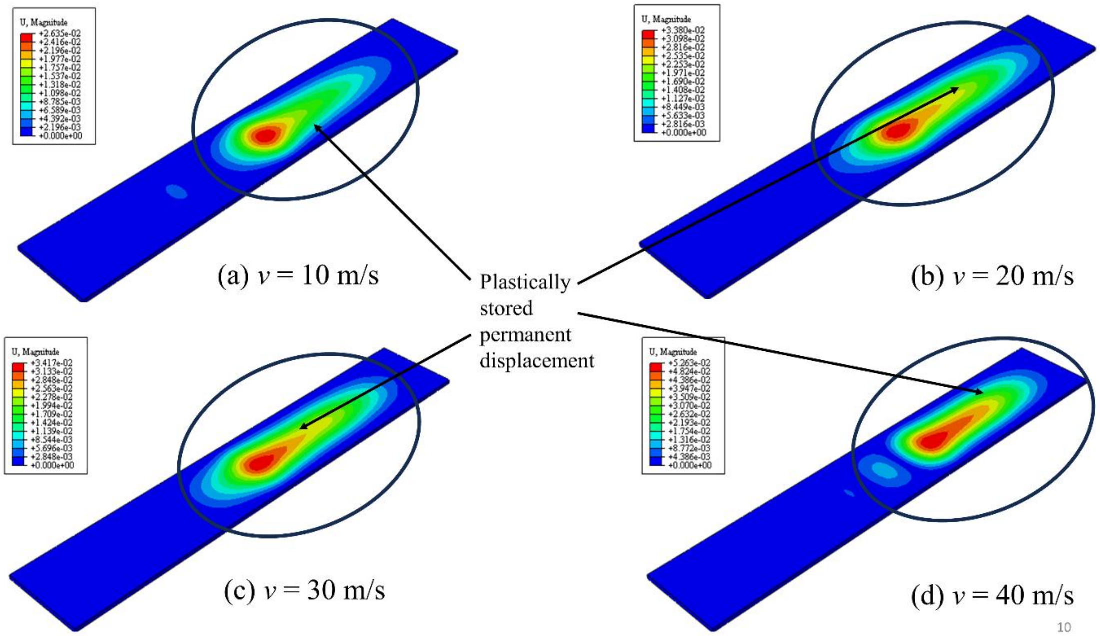

Figure 4.8 Displacement contours for a moving load velocity of (a-d) 10 to 40 m/s

Fig. 4.9 shows the reason for variation of the resultant central deflection in response to the deflections in the x, y, and z directions for a centralized reference position of a moving load along a normalized pavement length. In Fig. 4.9(a), the deflection in the x-direction for a load range of 50-150 kN demonstrates that the pavement material remains in the elastic region, with recoverable deflections across the normalized pavement length. Fig. 4.9(b) shows deflection in the x-direction for a 175 kN load, where the results are comparable to the 50-150 kN range near the starting point of the moving load, but transition into a post-elastic response towards the far end of the pavement. The far end is where the moving load is approaching, indicating the onset of non-recoverable deformation.

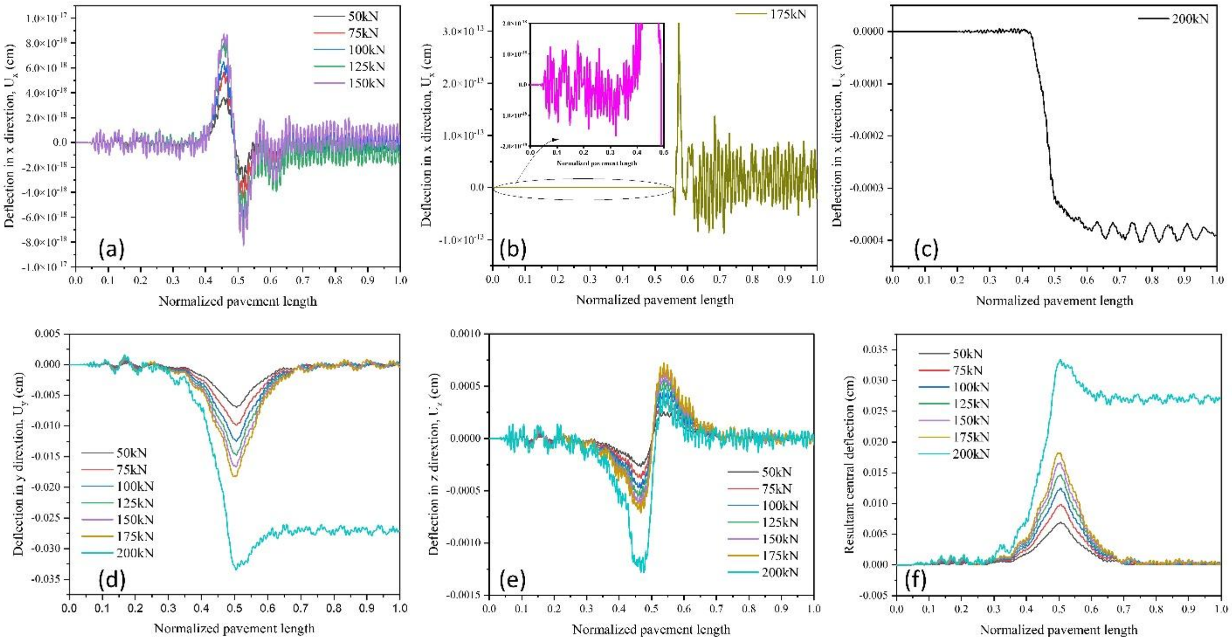

Figure 4.9 Variation of resultant central deflection due to deflection in x, y, and z directions for a conceptulised reference position of moving load along the normalized pavement length where (a) deflections in x direction observed in elastic range corresponding to a loading magnitude ranging from 50-150kN, (b) deflections in x direction observed in transition zone corresponding to a loading magnitude of 175kN, (c) deflections in x direction observed in post-elastic zone corresponding to a loading magnitude of 200kN, (d) deflections in y direction corresponding to a loading magnitude ranging from 50-200kN, I deflections in z direction corresponding to a loading magnitude ranging from 50-200kN, (f) resultant central deflection corresponding to a loading magnitude ranging from 50-200kN

In Fig. 4.9I, with a 200 kN load, deflections in the x-direction reflect a complete transition to the post-elastic region, with non-recoverable deformation observed at the far side of the pavement. Fig. 4.9(d) depicts deflections in the y-direction, confirming elastic recoverable behavior for loads of 50-150 kN, a transition at 175 kN, and post-elastic behavior at 200 kN. Finally, Fig. 4.9I shows deflections in the z-direction, where the material undergoes a phase change between compressive and tensile symmetries. Compressive deflections remain recoverable up to 150 kN, while a shift towards compressive deflections at the near end is noted for the 200 kN load, confirming a transition from elastic to post-elastic behavior. The findings of resultant central deflection shown in 4.9(f), reveal the overall elastic, transitional, and post-elastic responses of the pavement subjected to a moving load of 50-200 kN at 10 m/s.

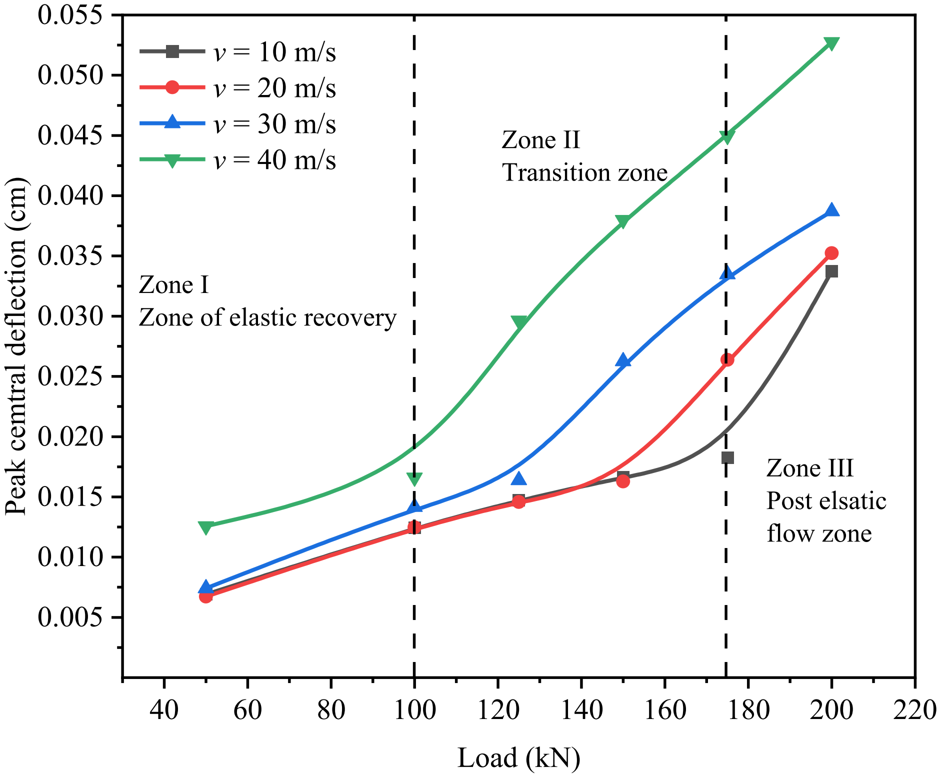

Figure 4.10 Load versus displacement graph showing the response and zonal classification for elastic recovery and post-elastic flow control

Fig. 4.10 illustrates the variation in peak central deflection in response to an applied load ranging from 50 to 200 kN, with increments of 25 kN, under a velocity input of 10-40 m/s. As hypothesized, the deflection was found to be elastic and fully recoverable up to an applied load of 100 kN, corroborating the observations depicted in Figs. 4.7 to 4.10. Within the load range of 100 kN to 150 kN, the deflections exhibited characteristics of the transition zone, indicating a shift from elastic to plastic behavior. Beyond 150 kN, up to 200 kN, the deflections were plastically stored and thus non-recoverable.

4.3.3 Multilayer Modelling: Displacement and Stress-strain Response

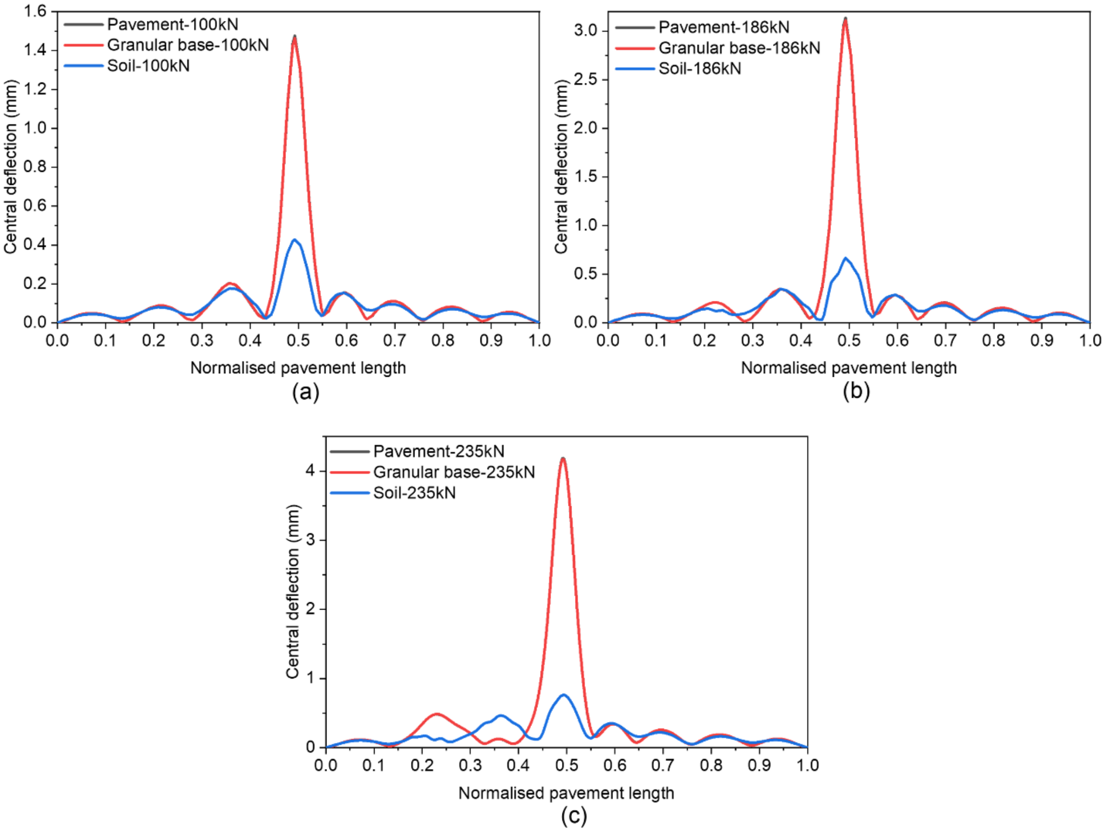

(a) (b) (c)

Figure 4.11 Central deflection variation in (a) pavement, (b) granular base, and (c) subgrade soil along the normalized length of pavement for the load (100 to 235 kN) moving at 10 m/s

The displacement response of the pavement-geomaterial system under the action of a moving vehicular load has been assessed through the measurement of central deflection. The central deflection is defined as the displacement observed at the center of the top surface of the pavement-geomaterial system, provided that the moving load has traversed fifty percent distance, i.e., half of the pavement length. The central deflection is a crucial parameter for the dynamic investigations of pavement-geomaterial interaction with moving vehicular loading conditions. Fig. 4.11 shows the central deflection for the load intensities prescribed by IRC 58:2015, i.e., 100 to 235 kN. It has been found that the central deflection is identical in pavement and granular base, whereas a significant difference is observed in the central deflection of the subgrade layer. The peak deflection for pavement, granular base, and subgrade soil layer has been observed in the range of 0.4 mm to 4.5 mm, for the selected set of loading inputs.

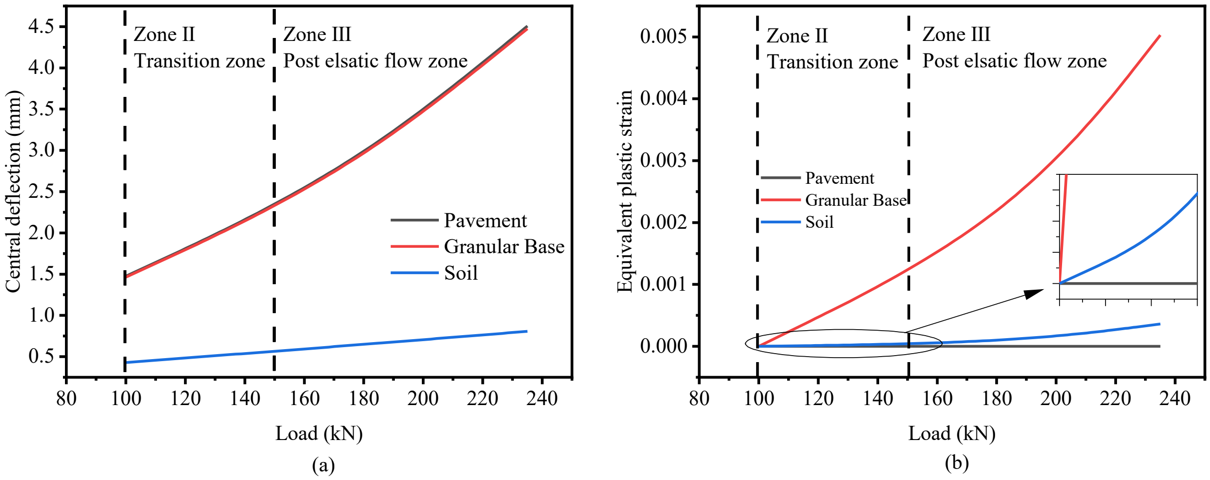

Figure 4.12 Variation of (a) load versus central deflection and (b) load versus plastic strain (PEEQ)

Fig. 4.12 illustrates the impact of varying moving load intensities on central deflection and equivalent plastic strain (EPS) within the pavement structure, the granular base course, and the soil subgrade layer. From Fig. 4.12(a), it is evident that the central deflection values for the pavement and granular base range from 1.4 mm to 4.5 mm, while the deflection values for the soil subgrade layer range from 0.4 mm to 0.8 mm. Fig. 4.12(b) details the EPS variations for the pavement and granular base. The analysis reveals that no plastic strain develops within the pavement layer under the selected loading conditions of this study. The EPS for the granular base course and the soil subgrade layer is observed to range from 2.2×10^{-16} to 0.362 % and 2.2×10^{-16} to 0.5 %, respectively. Furthermore, a magnified view in Fig. 4.12(b) indicates the initiation of plasticity in the granular base at a loading intensity of 100 kN. Hence, addressing the mechanistic reason for damage due to dynamic deflections prescribed by moving loads at varied velocities.

Fig. 4.13 illustrates the variation of stress and plastic strain along the normalized length of the pavement under moving loads prescribed by codal provision and falling in transition zone i.e., 100 kN and 186 kN. As also depicted in Figs. 4.13(a) and 4.13(b), the variation in stress magnitude and equivalent plastic strain within the layers of the pavement-geomaterial system supporting moving vehicular loads reveals a complex mechanism of stress transfer. The stress response of the pavement can be characterized by connecting the peak-to-peak responses of the granular base layer, and this approach can similarly be applied to the granular base and soil subgrade layers. Further analysis indicates that plastic deformation in the geomaterial initiates at a loading of 100 kN, with an observed plastic strain of 2.2×10^{-16} %. No plastic strain is observed in the pavement layer, as also confirmed by the data presented in Fig. 4.12(b). This detailed observation underscores the significance of the load threshold in triggering plastic behavior in the geomaterial, while the pavement layer remains unaffected under the same conditions.

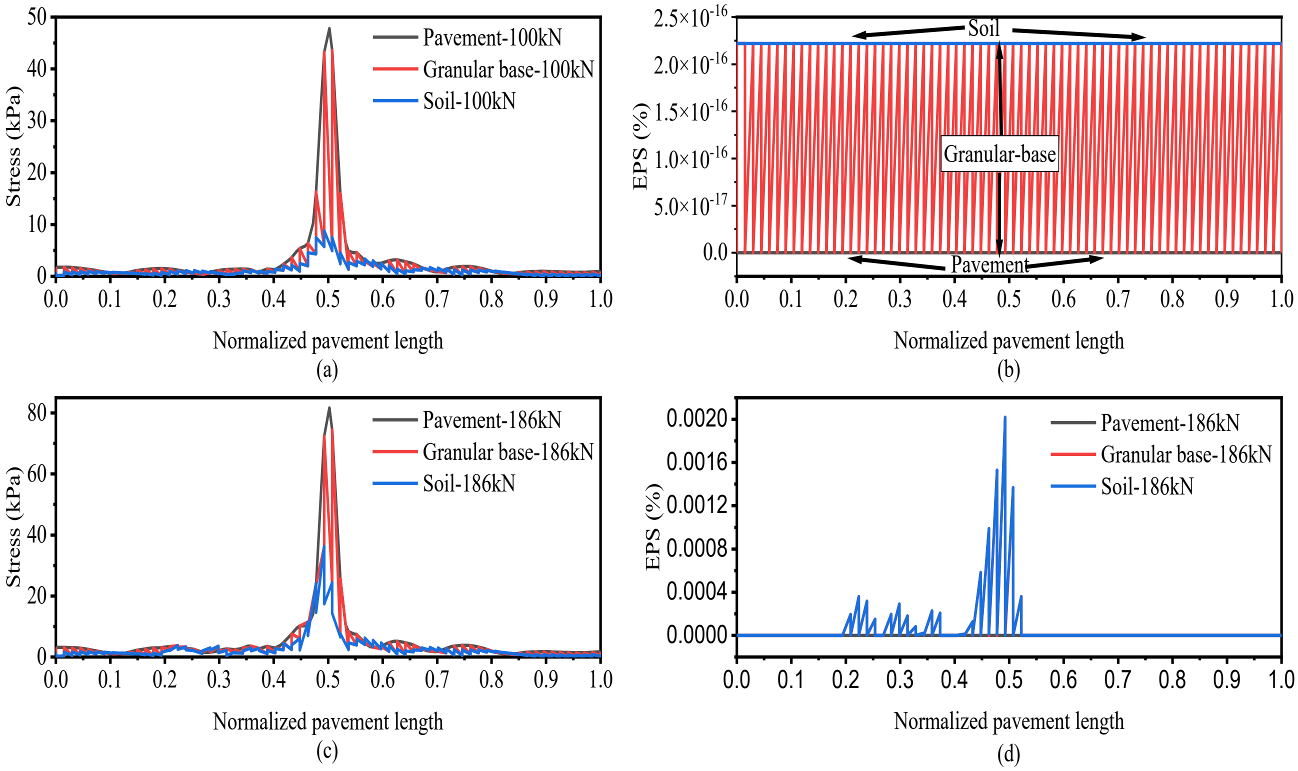
(a) (b) (c) (d)

Figure 4.13 Variation of (a) stress, (b) equivalent plastic strain at 100 kN, and (c) stress (d) equivalent plastic strain at 186 kN along the normalized length of pavement

Fig. 4.14 shows the graphical comparison of the elastic linear transfer of vibrations (Kumar et al., 2024b) and post-elastic non-linear transfer of vibrations in pavement structure and supporting layers of geomaterial. The vibration-induced stresses for a moving load velocity were observed on the pavement supported by the granular base and subgrade soil, and it was observed that more than two wide peaks exist for stress in elastic domain and one narrow peak exists for stress in post-elastic domain. This behaviour is attributed to the superimposition without decay in elastic regime whereas post elastic region dissipates vibrations through plastic flow control i.e., plastic dissipation of strain, which mathematically can be expressed as:

$$\dot{\varepsilon}^{pl} = \frac{d\varepsilon^{pl}}{dt} = \frac{d}{dt}\left(\frac{u_n - u_{n-1}}{u_n}\right)^{pl} = \frac{d}{dt}\left(1 - \frac{u_{n-1}}{u_n}\right)^{pl}$$
$$= \frac{d}{dt}(1)^{pl} - \frac{d}{dt}\left(\frac{u_{n-1}}{u_n}\right)^{pl} \tag{4.46}$$

$$\dot{\varepsilon}^{pl} = -\frac{d}{dt}\left(\frac{u_{n-1}}{u_n}\right)^{pl} = -\left(\frac{u_n \frac{du_{n-1}}{dt} - u_{n-1}\frac{du_n}{dt}}{{u_n}^2}\right)^{pl} \quad or\ \dot{\varepsilon}^{pl}$$
$$= \left(\frac{u_{n-1}\frac{du_n}{dt} - u_n \frac{du_{n-1}}{dt}}{{u_n}^2}\right)^{pl} \tag{4.47}$$

$$\dot{\varepsilon}^{pl} = v_n^{pl}\left(\frac{u_{n-1} - u_n \frac{v_{n-1}}{v_n}}{{u_n}^2}\right)^{pl} \quad or\ \dot{\varepsilon}^{pl} = \xi^{pl} v_n^{pl} \tag{4.48}$$

where, $\xi^{pl} = \left(\frac{u_{n-1} - u_n \frac{v_{n-1}}{v_n}}{{u_n}^2}\right)^{pl}$, plastic nonlinearity of flow control in damper force related to coefficient to velocity (v); Damper force, $F_d = v.\ c$; $v_n^{pl} = \frac{du_n}{dt}$ and $v_{n-1}^{pl} = \frac{du_{n-1}}{dt}$

The transmission of moving load vibrations from the top pavement layer causes stress wave creation between different sub-media of geomaterial. Therefore, the observed phenomenon results in the production of stress waves resulting from a vibrational mechanism of stress transfer (VMST).

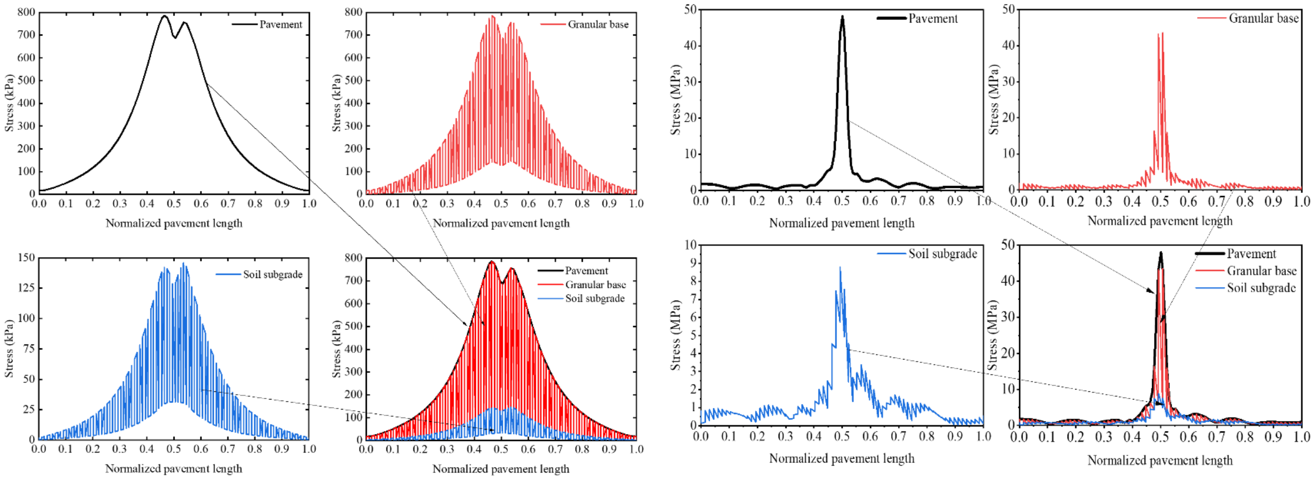

(a) Elastic linear transfer of vibrations

(a) Post elastic non linear transfer of vibrations

Figure 4.14 Graphical comparison of (a) elastic linear transfer of vibrations (Kumar et al., 2024b) and (b) post-elastic non-linear transfer of vibrations in pavement structure and supporting layers of geomaterial as studied in this work

4.4 Conclusions

This study utilized a finite element-based numerical program to analyse the damage dynamics of a pavement-geomaterial system within both the elastic and post-elastic domains. Three distinct influence zones were identified: the elastic zone, the transition zone, and the post-elastic zone. The pavement response was examined across these zones under varying loading intensities and velocities. Based on the results and discussion as presented earlier, the following conclusions have been made:

- **Central Deflection Response:** The study reveals that both the load intensity (ranging from 50 to 200 kN) and the velocity (from 10 to 40 m/s) of moving vehicular loads significantly influence the central deflection on the pavement surface and its supporting geomaterial layers. The maximum elastic deflection observed in a single-layer system was 1.55 mm for a 125 kN load at 40 m/s. In a multilayer system, deflections ranged from 1.4 mm to 4.5 mm in the pavement and granular base layers, while the subgrade soil experienced deflections between 0.4 mm and 0.8 mm. These results underline the critical role of load intensity and velocity in the deformation response of pavements, providing valuable detail for the design and maintenance of pavement structures under dynamic loading conditions.

- **Post-Elastic Displacement Dynamics:** As velocity increased from 10 to 40 m/s, the post-elastic displacement decreased for loading values ranging from 200 kN to 125 kN. This counterintuitive result suggests that higher speeds may reduce the loading extent of plastic deformation within the pavement system. This insight can inform future studies on the optimization of pavement materials and construction techniques to better withstand high-velocity traffic conditions, particularly in regions where high-speed vehicles are common.
- **Incremental Load Impact on Post-Elastic Displacement:** The analysis demonstrates that the post-elastic displacement accumulates along the pavement length with increasing load intensities. Notably, plasticity in the geomaterial was first observed at a moving load intensity of 100 kN, corresponding to a very small plastic strain of 2.2×10^{-16} %. This finding provides critical insight into the threshold at which materials begin to exhibit irreversible deformation under dynamic loading, which is essential for determining load limits and designing pavements that can tolerate repeated heavy traffic.

- **Stress Response:** The study demonstrates that the stress response of pavement systems can be effectively predicted by analyzing the peak-to-peak responses within the granular base layer, with similar methodologies applicable to both the base course and subgrade soil layers. The maximum plastic strains in these layers were recorded at 3.6×10^{-4} % for the base course and 5×10^{-3} % for the subgrade soil. These results emphasize the importance of considering not only the elastic but also the plastic behavior of geomaterials under dynamic loading, which can influence the long-term durability of pavements.
- **Vibrational Mechanism of Stress Transfer (VMST):** The research introduces a novel understanding of how dynamic load vibrations propagate through the pavement structure, inducing stress waves in the sub-layers of the geomaterials. This vibrational mechanism of stress transfer (VMST) suggests that dynamic loading not only causes immediate deformation but also triggers a complex wave propagation within the pavement system. This insight opens up new avenues for research into vibration-based monitoring techniques and non-destructive testing methods to assess the condition of pavements.

The observed displacements, which lead to permanent deformations, are crucial parameters that influence the mechanics of pavement damage and the overall lifespan of the pavement. Accurately evaluating these deformations is essential for engineers to identify the rutting mechanism, the depth of deformations, and potential failures within the pavement structure. The findings and numerical methodologies presented in this research provide a valuable framework for engineers and practitioners. These can be utilized to estimate the damage dynamics and post-elastic responses of pavement-geomaterial systems, thereby enhancing the design and resilience of pavement infrastructure. Future work could explore the effects of varying material properties and layer configurations on deflection behavior, enhancing predictive models for pavement performance. The researchers can focus on identifying the precise thresholds for different material types and investigating how environmental factors like temperature and moisture influence plasticity initiation.

References

1. Arnold, G., Alabaster, D., & Steven, B. (2001). Prediction of pavement performance from repeat load tri-axial (RLT) tests on granular materials. Transfund New Zealand research report 214. Wellington: Transfund New Zealand.
2. Barksdale, R. D. (1972). Laboratory evaluation of rutting in base course materials. In Third International Conference on the Structural Design of Asphalt Pavements (pp. 11-15). Grosvenor House, Park Lane, London, England.
3. Cao, P., Feng, D. C., & Jing, R. X. (2012). Based on FE method to research resistant rutting ability of pavement structure in Heilongjiang province. Applied Mechanics and Materials, 128, 1349-1354. https://doi.org/10.4028/www.scientific.net/AMM.128-129.1349
4. Cho, Y. H., McCullough, B. F., & Weissmann, J. (1996). Considerations on finite-element method application in pavement structural analysis. Transportation

Research Record, 1539(1), 96-101. https://doi.org/10.1177/0361198196153900011

5. Cheng, H., Liu, J., Sun, L., Liu, L., & Zhang, Y. (2021a). Fatigue behaviours of asphalt mixture at different temperatures in four-point bending and indirect tensile fatigue tests. Construction and Building Materials, 273, 121675. https://doi.org/10.1016/j.conbuildmat.2020.121675
6. Cheng, H., Liu, J., Sun, L., & Liu, L. (2021b). Critical position of fatigue damage within asphalt pavement considering temperature and strain distribution. International Journal of Pavement Engineering, 22(14), 1773-1784. https://doi.org/10.1080/10298436.2020.1724288
7. Cheng, H., Liu, J., & Sun, L. (2022). Bridging the gap between laboratory and field moduli of asphalt layer for pavement design and assessment: A comprehensive loading frequency-based approach. Frontiers of Structural and Civil Engineering, 16(3), 267-280. https://doi.org/10.1007/s11709-022-0811-7
8. Cheng, H., Sun, L., Wang, Y., Liu, L., & Chen, X. (2022). Fatigue test setups and analysis methods for asphalt mixture: A state-of-the-art review. Journal of Road Engineering, 2(4), 279-308. https://doi.org/10.1016/j.jreng.2022.11.002
9. Cortes, D. D., Shin, H., & Santamarina, J. C. (2012). Numerical simulation of inverted pavement systems. Journal of Transportation Engineering, 138(12), 1507-1519. https://doi.org/10.1061/(ASCE)TE.1943-5436.0000472
10. Federal Highway Administration, VESYS. (1977). User’s manual: predictive design procedures. Washington, DC.

11. Hicks, R. G., & Monismith, C. L. (1971). Factors influencing the resilient response of granular materials. Highway Research Record, 345, 15-31.
12. Hjelmstad, K. D., & Taciroglu, E. (2000). Analysis and implementation of resilient modulus models for granular solids. Journal of Engineering Mechanics, 126(8), 821-830. https://doi.org/10.1061/(ASCE)0733-9399(2000)126:8(821
13. Hu, X., Zhong, S., & Walubita, L. F. (2015). Three-dimensional modelling of multilayered asphalt concrete pavement structures: strain responses and permanent deformation. Road Materials and Pavement Design, 16(3), 727-740. https://doi.org/10.1080/14680629.2015.1028968
14. Imaninasab, R., Bakhshi, B., & Shirini, B. (2016). Rutting performance of rubberized porous asphalt using finite element method (FEM). Construction and Building Materials, 106, 382-391. https://doi.org/10.1016/j.conbuildmat.2015.12.134
15. Kim, M., & Tutumluer, E. (2006). Modeling non-linear, stress-dependent pavement foundation behavior using a general-purpose finite element program. In Pavement Mechanics and Performance (pp. 29-36). https://doi.org/10.1061/9780784408667
16. Korkiala-Tanttu, L., Laaksonen, R., & Törnqvist, J. (2003). Effect of spring and overload to the rutting of a low-volume road. Finnra Reports 22/2003. Helsinki: HVS-Nordic-research, Finnish Road Administration.
17. Kumar, Y., Trivedi, A., & Shukla, S. K. (2024a). Damage evaluation in pavement-geomaterial system using finite element-scaled accelerated pavement

testing. Transportation Infrastructure Geotechnology. https://doi.org/10.1007/s40515-023-00309-y

18. Kumar, Y., Trivedi, A., & Shukla, S. K. (2024b). Deflections governed by the cyclic strength of rigid pavement subjected to structural vibration due to high-velocity moving loads. Journal of Vibration Engineering and Technologies. https://doi.org/10.1007/s42417-023-01063-8
19. Lee, J., Kim, J., & Kang, B. (2009). Normalized resilient modulus model for subbase and subgrade based on stress-dependent modulus degradation. Journal of Transportation Engineering, 135(9), 600-610. https://doi.org/10.1061/(ASCE)TE.1943-5436.0000019
20. Li, S., Guo, Z., & Yang, Y. (2015). Rutting resistance ability analysis of heavy-duty asphalt pavements based on consecutive temperature variation and finite element method. In CICTP (pp. 992-1008). https://doi.org/10.1061/9780784479292.094
21. Lubliner, J., Oliver, J., Oller, S., & Onate, E. (1989). A plastic-damage model for concrete. International Journal of Solids and Structures, 25(3), 299-326. https://doi.org/10.1016/0020-7683(89)90050-4
22. Lytton, R. L., Uzan, J., Fernando, E. G., Roque, R., Hiltunen, D., & Stoffels, S. M. (1993). Development and validation of performance prediction models and specifications for asphalt binders and paving mixes. Washington, DC: Strategic Highway Research Program 357.
23. Ma, L., Nie, W., Zhang, X., Yan, J., & Wang, D. (2022). Experimental study of

Poisson's ratio in indirect tensile test mode for asphalt mixtures. Construction and Building Materials, 355, 129288. https://doi.org/10.1016/j.conbuildmat.2022.129288

24. Mehra, S., & Trivedi, A. (2021). Pile groups subjected to axial and torsional loads in flow-controlled geomaterial. International Journal of Geomechanics, 21(3), 04021002. https://doi.org/10.1061/(ASCE)GM.1943-5622.0001928
25. Monismith, C. L., Ogawa, N., & Freeme, C. R. (1975). Permanent deformation characteristics of subgrade soils due to repeated loading. Transportation Research Record, 537, 1-17.
26. Pi, Y., Zhang, J., Huang, X., & Li, H. (2007). Numerical simulation of indirect tensile tests of asphalt mixture. Journal of Highway and Transportation Research and Development, 24(8), 1-6.
27. R, Y., & Kim. (2014). Asphalt pavements. 1st ed. CRC Press.
28. Schanz, T., & Vermeer, P. A. (1996). Angles of friction and dilatancy of sand. Géotechnique, 46(1), 145-151. https://doi.org/10.1680/geot.1996.46.1.145
29. Simões, F. M. F., & Pinto da Costa, A. (2019). Finite element steady state solution of a beam on a frictionally damped foundation under a moving load. International Journal of Non-Linear Mechanics, 117, 103247. https://doi.org/10.1016/j.ijnonlinmec.2019.103247
30. Sofi, A. (2024). Nonlinear vibrations of beams with fractional derivative elements crossed by moving loads. International Journal of Non-Linear Mechanics, 159, 104567. https://doi.org/10.1016/j.ijnonlinmec.2023.104567

31. Teng, X., Li, X., & Chou, K. (2008). Application of finite element analysis to access the rutting potential in asphalt pavements. In Transportation and Development Innovative Best Practices (pp. 480-485). https://doi.org/10.1061/40961(319)79
32. Tseng, K., & Lytton, R. L. (1989). Prediction of permanent deformation in flexible pavement materials. Implication of Aggregates in the Design, Construction and Performance of Flexible Pavements, ASTM STP 1016, 154-172.
33. Uzan, J. (1985). Characterization of granular material. Transportation Research Record, 1022(1), 52-59.
34. Wosatko, A., Andrzej, W., Maria, A. P., & Jerzy, P. (2019). Role of dilatancy angle in plasticity-based models of concrete. Archives of Civil and Mechanical Engineering, 19, 1268-1283. https://doi.org/10.1016/j.acme.2019.07.003
35. Wu, C. P., & Shen, P. A. (1996). Dynamic analysis of concrete pavements subjected to moving loads. Journal of Transportation Engineering, 122(5). https://doi.org/10.1061/(ASCE)0733-947X(1996)122:5(367)
36. Xia, K. (2010). Finite element modeling of dynamic tire/pavement interaction. In Pavements and Materials: Testing and Modeling in Multiple Length Scales (pp. 204-214). https://doi.org/10.1061/41129(385)18
37. Yang, S., Li, S., & Lu, Y. (2010). Investigation on dynamical interaction between a heavy vehicle and road pavement. Vehicle System Dynamics, 48(8), 923-944. https://doi.org/10.1061/41127(382)390

38. Zhu, J., Zhang, M., Liu, Y., & Ming-Gao. (2010). Mechanical analysis on rutting resistance in asphalt pavement. In ICCTP 2010: Integrated Transportation Systems: Green, Intelligent, Reliable (3611-3617). https://doi.org/10.1080/00423110903243166

5

Chapter

Dynamic Characteristics Evaluation of Foundation Geomaterial Supporting Pavement Infrastructures

Highlights

- In this chapter, the influence of PVDF film thickness and excitation frequency on its dynamic response and vibration sensitivity under vibratory loading is investigated.
- Pristine PVDF films (0.02–0.1 mm thick) were synthesized via the drop-casting method and tested within confined geomaterials excited at 3–12 Hz, generating voltages between 1 to 8 V.
- A novel numerical model based on a second-degree non-homogeneous differential equation was developed to predict the dynamic behavior of PVDF films.
- The model predicted deflections of 0.001–0.01 mm and stresses of 0.9–12 kPa, demonstrating strong correlation with experimental observations.
- The findings lay the groundwork for developing advanced piezoelectric sensors, energy harvesters, and smart materials for vibration monitoring and control in engineering systems.

5.1 Background

Investigations into the piezoelectric, pyroelectric, and ferroelectric capabilities of polymer piezoelectric materials have been sparked by the expanding applications of polyvinylidene fluoride (PVDF) and its copolymers. The PVDF has been identified as an artificial semi-crystalline polymer of long-chain (—CF_2—CH_2—) units that repeat in chemical configuration (Kepler & Anderson, 1978; Vinogradov & Holloway, 1999). The PVDF is intrinsically polar as the fluoride atoms possess a negative electrical charge compared to the carbon atoms, and the hydrogen atoms have a positive electrical charge with respect to the carbon atoms. However, due to the arbitrary arrangement of the crystals, the material initial state net polar moment is zero (Dunn & Carr, 1989). The PVDF has been confirmed to have significantly better piezoelectric characteristics than organic materials. In addition, PVDF components seem to have a distinct edge over the piezoceramics in terms of piezoelectric output (Cross, 1995; Gandhi & Thompson, 1992). Therefore, the PVDF can also be adopted as a potential sensor and energy harvester. Considerable investigations have been performed to determine the effectiveness of piezoelectric nanogenerators (PENGs) like PVDF in view of energy conversion using mechanical vibration (Beeby et al., 2006). PENGs are highly advantageous for energy harvesting and vibration detection, employing accelerometers, piezo devices, geophones, etc., compared to electromagnetic and electrostatic components during the investigation of geomaterials subjected to mechanical vibrations. The piezoelectric material offers an increased energy concentration and manoeuvrability in system integration for geomaterial investigation subjected to dynamic load (Anton & Sodano, 2007). The Hamiltonian principle has been adopted to analyse the frequency-dependent surface strains and vibration modes. The voltage efficiency has been demonstrated as a function of surface vibration induced by the dynamic load (Erturk, 2011). Further, the electrical energy in terms of voltage output has been examined for the tuneable piezoelectric energy harvester under prestressed conditions (Rhimi & Lajnef, 2012). The numerical model was validated by a laboratory environment, which was created to experimentally harvest the energy from random vibration caused by dynamic load over the rail bridge to overcome the accuracy limitation of the numerical simulations (Cahill et al., 2018). The optimized design and elementary structural behaviour of the pavement coupled with an embedded PZT have been investigated for varied inputs of the dynamic load (Roshani et al., 2018; Chen et al., 2019; Liu et al., 2019). Further, the voltage output of the cantilever PZT has been investigated from surface installation to varied pavement depths (Guo & Lu, 2017). The magnitude of dynamic loading significantly influences the power output of the PENGs as compared to the thickness of the pavement (Roshani & Dessouky, 2015). Moreover, the force of excitation, material properties, and electromechanical coupling of PENGs have significantly influenced output charge efficiency (Singh et al., 2013; Petroff et al., 2019). The input vibrations, loading frequency, and amplitude are key parameters governing energy harvesting and power generation from PENGs (Erturk, 2011; Kumari & Trivedi, 2019). The effect of vibrations induced by the dynamic action of moving load on the piezoelectric performance of PENGs in transportation networks has been studied. It has been observed that the excitation frequency of load governs the power generation from roadways (Roshani et al., 2016; Ding et al., 2018). Kumari and Trivedi (2022a, b) investigated the role of excitation frequency on the vertical and horizontal embedded PENG in confined geomaterial subjected to vibratory loads. The dynamic analysis of geomaterial supporting pavements depends on deflections prescribed by the intensity of loading and frequency (Kumar et al., 2024a, b).

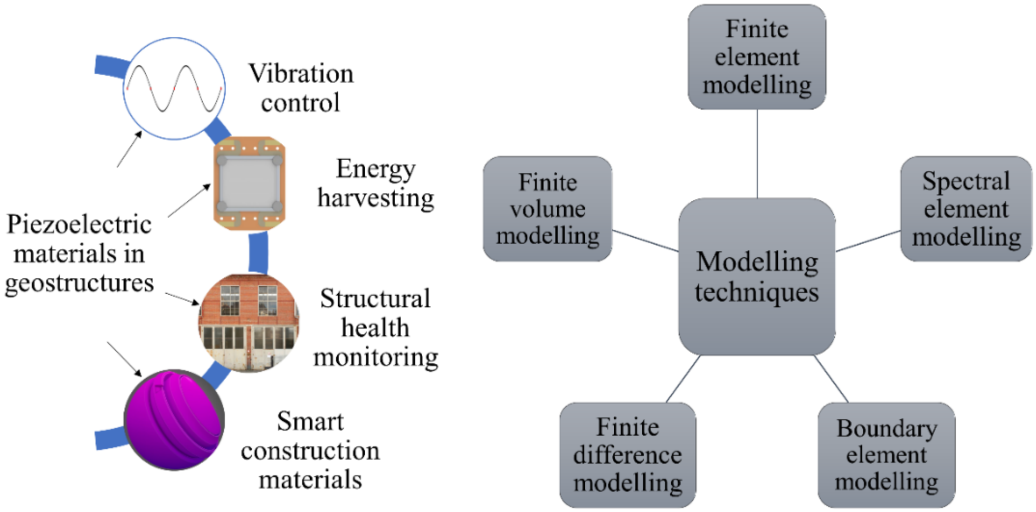

(a) (b)

Figure 5.1 Schematic representation of (a) piezoelectric material in geostructures and (b) modelling techniques

The role of piezoelectric materials and modelling techniques adds significant importance to determining the deflection and stress of piezoelectric nanogenerators embedded in confined geostructures subjected to dynamic loads (Kumari & Trivedi, 2022; Wei & Jing, 2017). It is found in the literature that there are primarily four uses of piezoelectric material in geostructures, namely, vibration control (Xin et al., 2017), energy harvesting (Sezer & Koç, 2021), structural health monitoring (Jiao et al., 2020), and smart construction material (Mahapatra et al., 2021). There are five basic numerical modelling techniques to achieve and implement these four piezoelectric uses in the real-world situation, namely, finite element modelling (Wang et al., 2006), spectral element modelling (Lee et al., 2013), boundary element modelling (Zou et al., 2013), finite difference modelling (Filoux et al., 2008), and finite volume modelling (Bolborici et al., 2012) as shown in Fig. 5.1. Moreover, the existing numerical models and their basic governing equation for stress and deflection are presented in Table 5.1.

Table 5.1 The numerical models existing in the literature with governing equations and their applications

Model	Governing equations	Application
Finite element model [a, b]	$\sigma_{ij} = D^{E}_{ijkl}\varepsilon_{kl} - e^{\varphi}_{mij}E_m$ $u(t) = N_i^N u_n(t)$	Vibration control, smart construction material, and energy harvesting
Spectral element Model [c]	$\sigma = D^E\left(\varepsilon - \frac{e^{\varphi}E}{D}\right)$ $\{u_{b0}(x,t)w_{b0}(x,t)\theta_b(x,t)\varphi_b(x,t)\theta_b(x,t)\} = \frac{1}{N}\sum_{n=0}^{N-1}\{U_n(x)W_n(x)\Theta_{bn}(x)\Psi_n(x)\Theta_{pn}(x)\}\,e^{i\omega_n t}$	Vibration control
Boundary element model [d]	$\frac{\sigma}{D^E\varepsilon} = \left(1 - \frac{e^{\varphi}E}{\varepsilon D}\right)$ $U = [u_1, u_2, u_3, V]^T$	Structural health monitoring
Finite difference model [e]	$\sigma = D^E e^{\varphi}\left(\frac{\varepsilon}{e^{\varphi}} - \frac{E}{D^E}\right)$ $u(t\text{-}\Delta t) = u(t) + \frac{\Delta t}{24}.\left[26.\frac{\partial y}{\partial t}\left(t + \frac{\Delta t}{2}\right) - 5\frac{\partial y}{\partial t}\left(t + \frac{\Delta t}{2}\right) + 4.\frac{\partial y}{\partial t}\left(t + \frac{3\Delta t}{2}\right) - \frac{\partial y}{\partial t}\left(t + \frac{5\Delta t}{2}\right)\right]$	Vibration control and structural health monitoring
Finite volume model [f]	$\frac{\sigma}{D^E e^{\varphi}} = \frac{\varepsilon}{e^{\varphi}}\left(1 - \frac{e^{\varphi}E}{\varepsilon D^E}\right)$ $\rho\frac{\partial^2 u}{\partial t^2} = \rho_{tt} = \Delta.\mathbf{T}$	Vibration control and structural health monitoring

[a] Present study; [b] Wang et al. (2006); [c] Lee et al. (2013); [d] Zou et al. (2013); [e] Filoux et al. (2008); [f] Bolborici et al. (2012)

The abovementioned research proposes a wide-ranging use of piezoelectric nanogenerators synthesized by inorganic materials with high piezoelectric coefficients. However, the studies mentioned above cannot be suitably accepted because of their toxic lead constituent, cost-prohibitive processability, and brittle nature (Guan et al., 2013). To overcome these limitations, researchers have developed a non-toxic, highly flexible, and cost-efficient piezoelectric polymer (PVDF) (Fukada, 2000). Further, as per the Scopus database, there is very limited study on the stress, deflection, and voltage output of PVDF embedded in confined geomaterial subjected to vibratory loads, and its use in geotechnical engineering is still elusive. The PVDF films have the potential to produce renewable green energy. The energy harvesting and sensing industry can use this technology to develop energy harvesters and sensors from the vibration inputs of geostructures. Several uses of such composite films are found in structural health monitoring using lead-based elements only. Hence, this work aims to explore the PVDF for renewable energy and possible sensor application from geostructures for vibration control, energy harvesting, and structural health monitoring.

As per the literature surveyed, investigations are required for the dynamic analysis of PVDF film embedded in geomaterial. Considering the gaps prevailing in the literature, the following objectives have been set for this study:

- To synthesize the pristine films of polyvinylidene difluoride (PVDF).
- To find the effect of mechanical vibration on the performance of pristine PVDF films.

- To examine the validity of a finite element-based numerical program in light of experimental outcomes for investigating the performance of the PVDF embedded in geomaterial subjected to vibratory loads.
- To find the effect of vibration on stress and deflection characteristics of PVDF embedded in geomaterial.
- To develop the mathematical co-relations between vibration frequency, voltage output, stress, and deflection of pristine PVDF embedded in geomaterial subjected to vibratory loads.

5.2 Materials and Methods

5.2.1 Materials

The geomaterial, N, N Dimethyl Formamide (DMF), Ethanol, 161onceptua (DI) water, and PVDF powder were commercially procured and used without any treatment or processing. The geomaterial was washed and sundried for 24 hours without any chemical treatment.

5.2.2 Geomaterial Characterization

The grain size distribution, compaction, and shear parameters have been plotted as shown in Fig. 5.2 (a-c), conforming to *IS 2720-Part 4, Part 7, and Part 13*. The D_{10} value indicates that the effective grain size is 0.145 mm in the bulk geomaterial. The C_u and C_c values indicated in the graph characterize the geomaterial as poorly graded sand (SP), as shown in Fig 5.2 (a). The variation of shear stress with normal stress for the geomaterial is demonstrated in Fig. 5.2 (b). The values of cohesion (*c*) and angle of internal friction

(ϕ) from Fig. 5.2 (b) indicate that the shear strength parameters of the geomaterial, namely, c and ϕ, are 4.4 kPa and 36.6°, respectively. Fig. 5.2 (c) shows the variation of dry unit weight with moisture content for the soil specimen. The dry unit weight and moisture content from Fig. 5.2 (c) indicate that the geomaterial's optimum moisture content and maximum dry unit weight are 10.4% and 17.00 $\mathrm{kNm^{-3}}$, respectively. These properties, along with Young's modulus and Poisson's ratio, were used as input for conducting the numerical simulations (Sezer & Koç, 2021), as reported in Table 5.2.

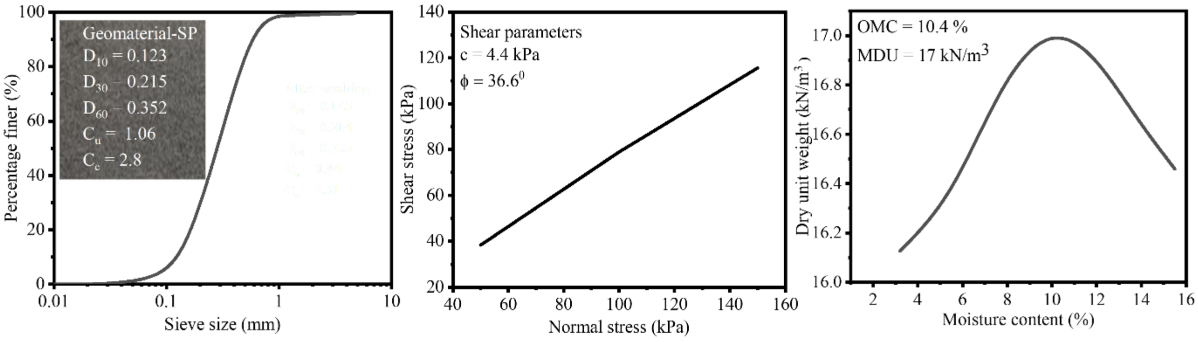

(a) (b) (c)

Figure 5.2 Basic properties of the geomaterial adopted to conduct this research (Note: D_{10} value indicates that the effective grain size is 0.145 mm, *OMC* and *MDU* are 10.4% and 17 $\mathrm{kN/m^3}$, and c and ϕ values are 4.4 kPa and 36.6°, respectively)

Table 5.2 Input properties of PVDF for conducting numerical simulation

Parameter	Magnitude	`Unit
Unit weight [a]	17.00	$\mathrm{kN/m^3}$
Cohesion [a]	4.4	kPa
Friction angle [a]	36.6	Degree
Poisson's ratio [b]	0.3	Dimensionless
Young's modulus [b]	0.15	Gpa
Frequency of vibratory load	3-12	Hz

[a] Properties obtained from the conceptualization performed in this work, as also shown in Fig. 5.2

[b] Range of Young's modulus (5 to 150 MPa) and Poisson's ratio (0.1 to 0.5) for Geomaterial (Sezer & Koç, 2021)

5.2.3 Synthesis and Characterization of Pristine PVDF Film

A line sketch flow diagram and real-time fabrication process of the drop-casting method have been adopted to synthesize the pristine PVDF piezoelectric films, as shown in Fig. 5.3 (a and b).

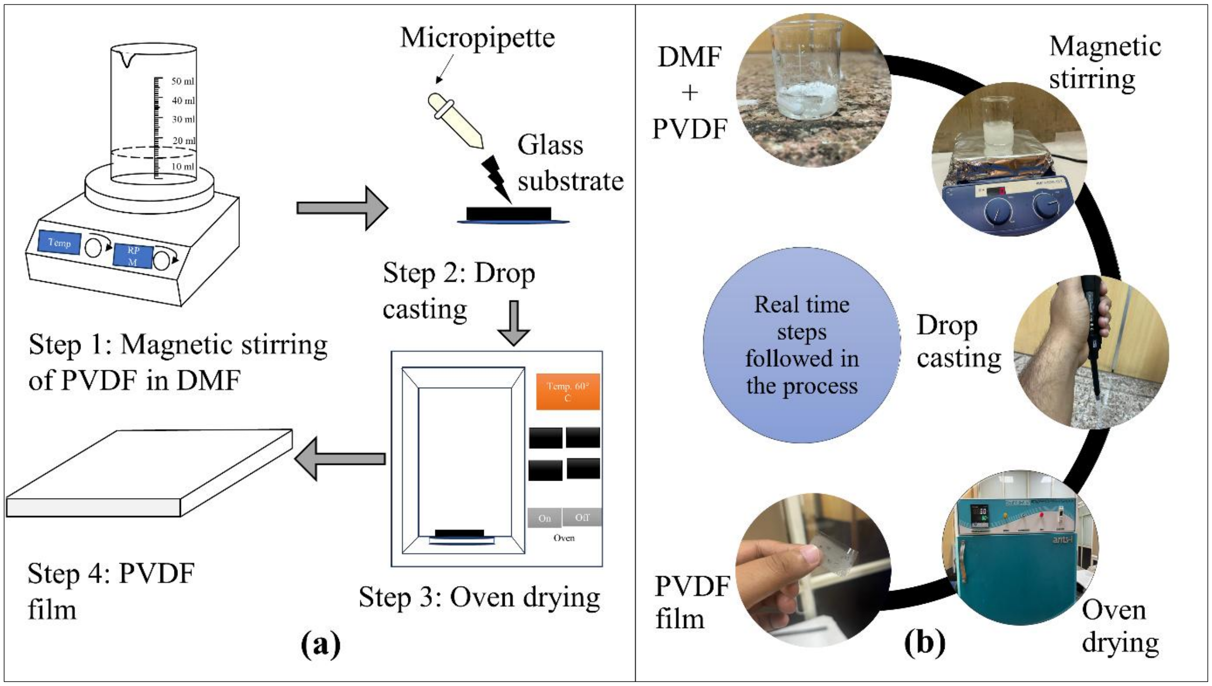

Figure 5.3 (a) Flow diagram and (b) real-time fabrication process of PVDF

Following are the steps to synthesize the pristine PVDF piezoelectric films:

- To synthesize the PVDF film, one gram of PVDF was dissolved in a 10 mL DMF solution.
- The solution was then placed on a magnetic stirrer for homogeneous mixing. The stirring was operated for 45 minutes at room temperature for the homogenous mixing of PVDF-DMF solution.
- The solution was then drop-cast on sterilized glass substrates using a micropipette.

- The drop casted solution on a glass substrate was then placed in an oven at 60° C for 2 hours.
- Finally, the PVDF films were extracted using DI water.

In the present study, XRD and SEM tests were conducted to confirm the synthesis of PVDF and its morphology. As stated above, XRD was performed to investigate the presence of α and β-phase, as shown in Fig. 5.4 (a). The peaks at 18.5° show the non-electroactive α-phase and 20.2° shows the electroactive β-phase in PVDF film. The XRD analysis confirms the successful synthesis of PVDF film. The morphological analysis conducted using SEM revealed the uniform distribution of PVDF with nano-cavities, as shown in Fig. 5.4 (b). Hence, the dynamic response of PVDF films with varied thicknesses has been investigated for sensing and energy harvesting engineering applications. To model the PVDF embedded in confined geomaterial on a finite element scale, the pre-requisite parameters are elastic modulus, Poisson's ratio, dielectric constant, and piezoelectric constant of PVDF. There have been very limited studies on the determination and effect of these properties on confined geomaterial testing. Unfortunately, these parameters altogether are not available in a single article. The material adopted in the present study has the following possible range of values for PVDF. The elastic modulus, Poisson's ratio, dielectric constant, and piezoelectric constant typically varies from 1.3 to 2.0 Gpa, 0.2 to 0.4, 7.5 to 13.2, and d_{11}= 3 to 35 pC/N; d_{33} = -5 to 5 pC/N, respectively, for PVDF films. So, considering the above fact, the properties of PVDF were obtained from different sources (Tasaka & Miyata, 1981; Tasaka et al., 1984; Roopa et al., 2021;

Saxena & Shukla, 2021). The material properties adopted to model the PVFG embedded in confined geomaterial are listed in Table 5.3.

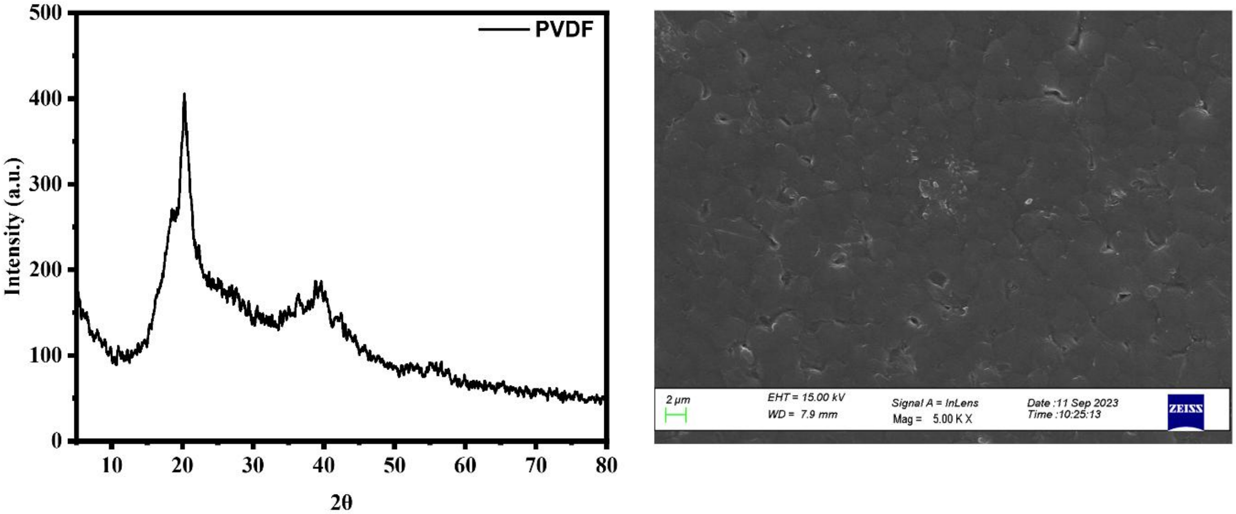

(a) XRD of PVDF Film **(b) FESEM image of PVDF**

Figure 5.4 (a) XRD and (b) FESEM characterization of the pristine PVDF film

Table 5.3 Input properties of PVDF for conducting numerical simulation

Parameter		Magnitude	Unit
Poisson's ratio [a]		0.33	Dimensionless
Young's modulus [b]		1.63	Gpa
Dielectric constant [b]		11.4	Dimensionless
Piezoelectric constant [c]	D_{11}	2.0	pC/N
	D_{33}	-5	pC/N

[a] Range of Poisson's ratio (0.1 to 0.5) (Tasaka & Miyata, 1981)

[b] Range of Young's modulus (1.3 to 2.0 Gpa) and Dielectric constant (7.5 to 13.2) (Tasaka et al., 1984; Roopa et al., 2021)

[c] Range of dielectric constants (d_{11}= 3 to 35 pC/N; d_{33} = -5 to 5 pC/N) (Saxena & Shukla, 2021)

5.2.4 Experimental Program and Numerical Modelling

Figure 5.5 shows the line sketch of the experimental facility at the Soil Dynamics Lab of the Department of Civil Engineering, Delhi Technological University, Delhi, India. The experimental setup consists of a dynamic shaker (max peak-to-peak armature displacement of 14 mm), digital storage oscilloscope, steel tank, and power amplifier cum signal generator. The numerical analysis of PVDF embedded in confined geomaterial has been performed using the commercialized software package Abaqus. The finite elements adopted to conduct the presented research pose deflection-based degrees of freedom and voltage as variables on the nodes of meshed geometry.

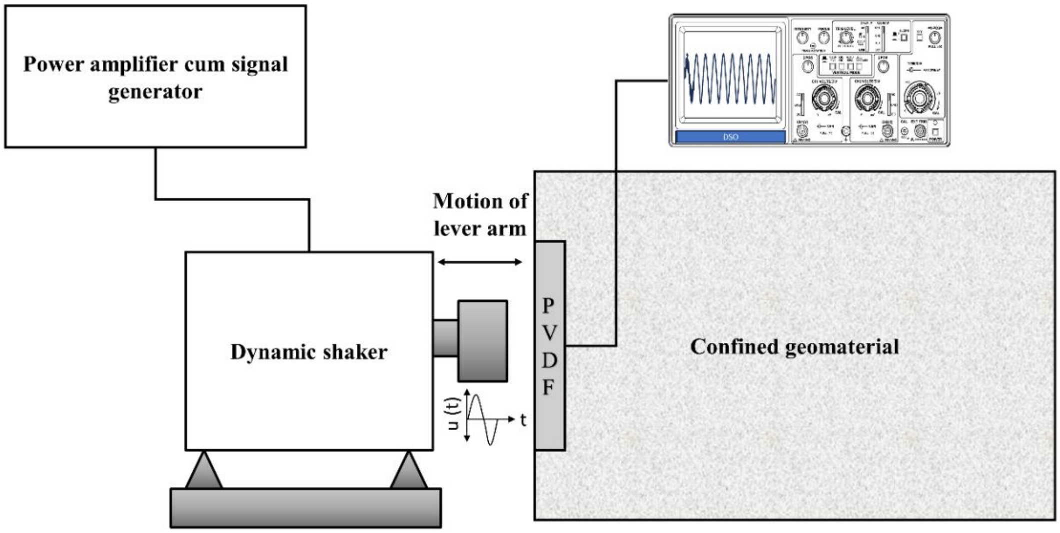

Figure 5.5 Diagrammatic representation of the experimental setup

5.2.4.1 Step-by-step Procedure to Model PVDF-geomaterial System

The step-by-step procedure to conduct numerical simulation is detailed below and supplemented by a flow diagram, as represented in Fig. 5.6.

a) Firstly, the geometry of the numerical model was sketched and extruded in the graphic user interface of the Abaqus. After that, the material properties, as specified in Tables 5.2 and 5.3, were assigned to the extruded numerical model.

b) The dynamic implicit step in the Abaqus standard module was adopted to provide a surface-to-surface interaction with a tie constraint. After defining interactions, the encaster boundary condition was assigned to the bottom face of the geomaterial, and the electric potential at a tied face of PVDF was prescribed using an electric potential boundary condition.

c) The loading amplitudes, i.e., input frequencies as that of the experiment performed, were defined using the “amplitude manager” option from the “Tool” drop-down menu.

d) The meshing to the extruded geometry was assigned using the global seeding tool. A C3D8 (Continuum three dimensional eight nodded) element in the global seeding value of 0.01 to 0.05 (number of elements = 960 to 110400) was assigned to geomaterial, and 0.001-0.005 (75 to 1875) was assigned to PVDF for mesh convergence testing. The relevant GUI images of boundary conditions, loading, and meshing are provided in the supplementary document.

e) Finally, the converged results were tested with the experimental results for numerical validation.

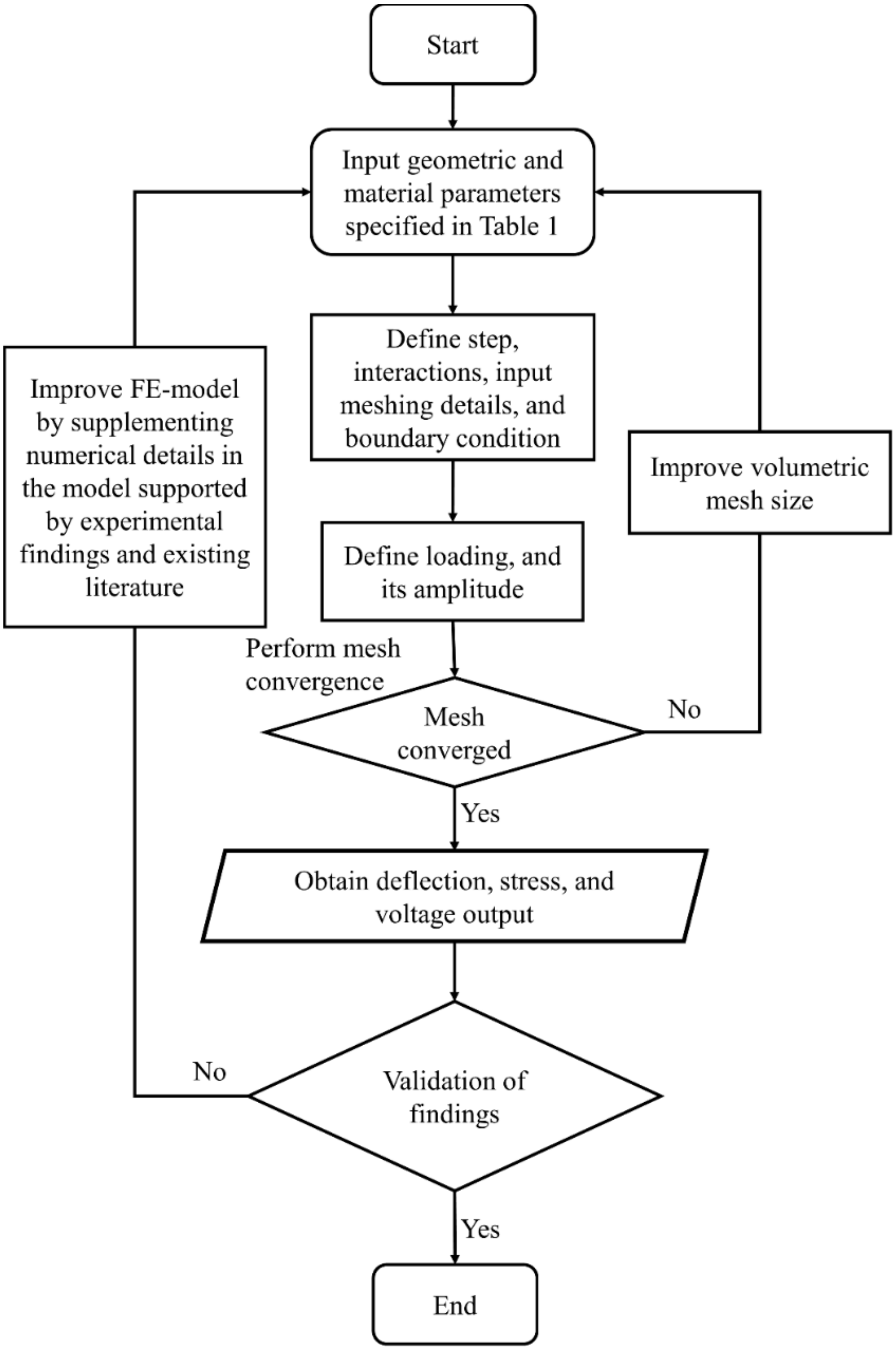

Figure 5.6 Flow diagram representing the modelling procedure adopted in the Abaqus to conduct presented research

The time-dependent direct integration scheme has been adopted in the present work to investigate the effect of vibrations caused by the periodic tapping of armature on PVDF. The dynamic response depending on the inertial frame has been simulated using the equation of motion (Braun & Golubitsky, 1983; Mario & Young, 2019) and can be expressed as:

$$m\ddot{u} + c\dot{u} + ku = f_e \tag{5.1}$$

where m is the mass matrix, c is the damper matrix, k is the stiffness matrix, $\ddot{u}$ is the acceleration vector, $\dot{u}$ is the velocity vector, u is the displacement vector, and f_e is the externally prescribed force vector. The exciting force by the mechanical shaker is harmonic in nature; hence, it can be presented as:

$$f_e = p \cos \lambda t \tag{5.2}$$

Therefore, the equation can be expressed as:

$$m\ddot{u} + c\dot{u} + ku = p \cos \lambda t \tag{5.3}$$

Dividing Eq. (5.3) by *m,* we get:

$$\ddot{u} + \frac{c}{m}\dot{u} + \frac{k}{m}u = \frac{p}{m} \cos \lambda t \tag{5.4}$$

From the basic definitions of dynamics, the Eq (5.4) can be written as:

$$\ddot{u} + 2\eta\omega_n\dot{u} + {\omega_n}^2 u = \frac{p}{m} \cos \lambda t \tag{5.5}$$

The above equation is a second-order, non-homogenous differential equation. Solution of which could be obtained as follows:

$$u(t) = u(t)_{CF} + u(t)_{PI} \tag{5.6}$$

Here, subscripted CF denotes solution in terms of complementary function, and PI denotes solution in terms of a particular integral. In solving non-homogeneous differential equations, the method of undetermined coefficients or variation of parameters is often used. Both methods require finding a particular solution to the non-homogeneous equation. While using the method of undetermined coefficients, a particular form for the solution is assumed based on the form of the non-homogeneous term. To avoid redundancy, any term in the assumed solution that already exists in the complementary function is excluded (the solution to the corresponding homogeneous equation). The complementary function already accounts for the homogeneous part of the solution, and if those terms appear again in the particular solution, it will lead to overcounting. So, setting the complementary function equal to zero avoids the duplicacy of any terms in the particular solution (Braun & Golubitsky, 1983).

This approach helps streamline the process of finding a particular solution and ensures that there are no redundancies in the solution (Das, 1983; Verruijt, 2009; Mario & Young, 2019). Hence, to find out CF, it is assumed that the system of forces would behave the same as that for underdamped free vibration. Hence, CF can be calculated using the below equation:

$$\{\ddot{u}\} + [2\eta\omega]\{\dot{u}\} + [\omega^2]\{u\} = 0 \tag{5.7}$$

$$u(t)_{CF} = e^{-\omega t}[A\cos\omega_d t + B\sin\omega_d t] \tag{5.8}$$

Let

$$u(t)_{PI} = E\cos\lambda t + D\sin\lambda t \tag{5.9}$$

$$\dot{u}(t)_{PI} = -E\lambda\sin\lambda t + D\lambda\sin\lambda t \tag{5.10}$$

$$\ddot{u}(t)_{PI} = -E\lambda^2 \cos\lambda t + D \sin\lambda t \tag{5.11}$$

Putting $u(t)_{PI}$, $\dot{u}(t)_{PI}$, and $\ddot{u}(t)_{PI}$ in equation in eq. (5.5) we get:

$$\begin{aligned}\{-E\lambda^2 \cos\lambda t + D \sin\lambda t\} + [2\eta\omega]\{-E\lambda \sin\lambda t + D\lambda \cos\lambda t\} \\ + [\omega^2]\{E \cos\lambda t + D \sin\lambda t\} = \frac{P}{M} \cos\lambda t\end{aligned} \tag{5.12}$$

Using the concept that if $a\cos\theta + b\sin\theta = c\cos\theta + d\sin\theta$, coefficient of sine and cosine terms hold equality, we get $a = b \; and \; c = d$. The coefficient of the equation using this concept (5.12) can be obtained as:

$$-E\lambda^2 + 2\eta\omega D\lambda + \omega^2 E - \frac{P}{M} = 0 \qquad \text{(Equating Cosine terms)} \tag{5.13}$$

$$-D\lambda^2 - 2\eta\omega E\lambda + \omega^2 D = 0 \qquad \text{(Equating Sine terms)} \tag{5.14}$$

Solving the above two equations, we get:

$$E = \frac{\frac{P}{M}(\omega^2 - \lambda^2)}{(\omega^2 - \lambda^2)^2 + (2\eta\omega\lambda)^2} \tag{5.15}$$

and

$$D = \frac{\frac{P}{M}(2\eta\omega\lambda)}{(\omega^2 - \lambda^2)^2 + (2\eta\omega\lambda)^2} \tag{5.16}$$

Let $\omega^2 - \lambda^2 = R\cos\theta$

$2\eta\omega\lambda = R\sin\theta$

$\therefore R = \sqrt{(\omega^2 - \lambda^2)^2 + (2\eta\omega\lambda)^2}$

$\theta = \tan^{-1}\left(\frac{2\eta\omega\lambda}{\omega^2 - \lambda^2}\right)$

Putting the value of E and D and resolving in Eq. (5.9), we get:

$$u(t)_{PI} = \frac{\frac{P}{M}\cos(\lambda t-\theta)}{R} = \frac{\frac{P}{M}\cos(\lambda t-\theta)}{\sqrt{(\omega^2-\lambda^2)^2+(2\eta\omega\lambda)^2}} \tag{5.17}$$

It can be seen that Eq. (5.17) is not affected by initial conditions. Hence, initial conditions have no effect on the particular integral. So, putting the value of Eq. (5.8) and Eq. (5.17) in Eq. (5.6), the complete solution can be expressed as:

$$u(t) = e^{-\eta\omega t}[A\cos\omega_d t + B\sin\omega_d t] + \frac{\frac{P}{M}\cos(\lambda t-\theta)}{\sqrt{(\omega^2-\lambda^2)^2+(2\eta\omega\lambda)^2}} \tag{5.18}$$

$$\begin{aligned}\dot{u}(t) = &-\eta\omega e^{-\eta\omega t}[A\cos\omega_d t + B\sin\omega_d t] \\ &+ e^{-\eta\omega t}[-A\omega_d\sin\omega_d t + B\omega_d\cos\omega_d t] \\ &- \frac{\frac{P}{M}\lambda\sin(\lambda t-\theta)}{\sqrt{(\omega^2-\lambda^2)^2+(2\eta\omega\lambda)^2}}\end{aligned} \tag{5.19}$$

Let the initial conditions are:

$u(t=0) = u_0$

$\dot{u}(t=0) = \dot{u}_0$

Using initial condition $u(t=0)$ in Eq. (5.18), we get:

$$u_0 = A + \frac{\frac{P}{M}\cos\theta}{\sqrt{(\omega^2-\lambda^2)^2+(2\eta\omega\lambda)^2}} \tag{5.20}$$

Rearranging Eq. (5.20), we get:

$$A = u_0 - \frac{\frac{P}{M}\cos\theta}{\sqrt{(\omega^2 - \lambda^2)^2 + (2\eta\omega\lambda)^2}} \tag{5.21}$$

Using initial condition $\dot{u}(t = 0)$ in Eq. (5.19), we get:

$$\dot{u}_0 = -\eta\omega A + B\omega_d - \frac{\frac{P}{M}\lambda\sin\theta}{\sqrt{(\omega^2 - \lambda^2)^2 + (2\eta\omega\lambda)^2}} \tag{5.22}$$

Rearranging Eq. (5.22), we get:

$$B = \left[\dot{u}_0 + \eta\omega A - \frac{\frac{P}{M}\lambda\sin\theta}{\sqrt{(\omega^2 - \lambda^2)^2 + (2\eta\omega\lambda)^2}}\right] \times \frac{1}{\omega_d} \tag{5.23}$$

Putting the value of A in Eq. (5.23), we get:

$$\begin{aligned} B = \Bigg[\dot{u}_0 + \eta\omega\left(u_0 - \frac{\frac{P}{M}\cos\theta}{\sqrt{(\omega^2 - \lambda^2)^2 + (2\eta\omega\lambda)^2}}\right) \\ - \frac{\frac{P}{M}\lambda\sin\theta}{\sqrt{(\omega^2 - \lambda^2)^2 + (2\eta\omega\lambda)^2}}\Bigg] \times \frac{1}{\omega_d} \end{aligned} \tag{5.24}$$

Putting the value of the coefficient, A and B in Eq. (5.18), we get:

$$
\begin{aligned}
u(t) = e^{-\eta\omega t}\Bigg[\left(u_0 - \frac{\frac{P}{M}\cos\theta}{\sqrt{(\omega^2-\lambda^2)^2+(2\eta\omega\lambda)^2}}\right)\cos\omega_d t \\
+\left(\left[\dot{u}_0 + \eta\omega\left(u_0 - \frac{\frac{P}{M}\cos\theta}{\sqrt{(\omega^2-\lambda^2)^2+(2\eta\omega\lambda)^2}}\right)\right.\right. \\
\left.\left. - \frac{\frac{P}{M}\lambda\sin\theta}{\sqrt{(\omega^2-\lambda^2)^2+(2\eta\omega\lambda)^2}}\right]\times\frac{1}{\omega_d}\right)\sin\omega_d t\Bigg] \\
+\frac{\frac{P}{M}\cos(\lambda t-\theta)}{\sqrt{(\omega^2-\lambda^2)^2+(2\eta\omega\lambda)^2}}
\end{aligned}
\tag{5.25}
$$

The above equation shows that CF is an exponential decay function, and the particular integral is a harmonic function. Conceptually, it can be understood by the Fig. 5.7 as depicted below:

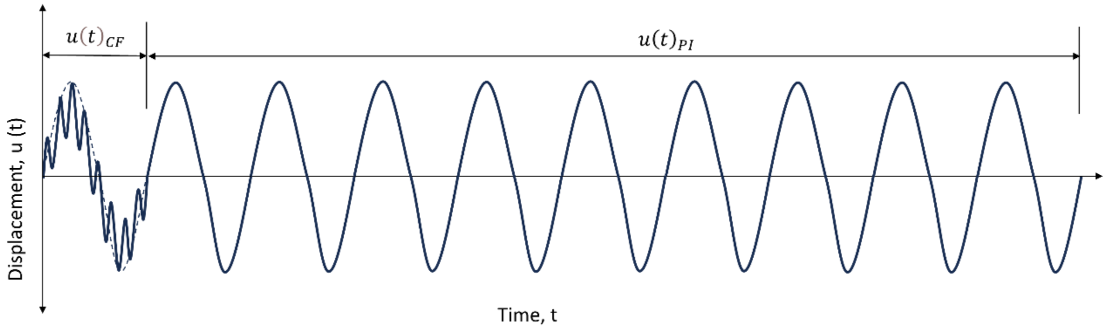

Figure 5.7 Diagrammatic conceptualization of the complementary function and particular integral assumed in the present work

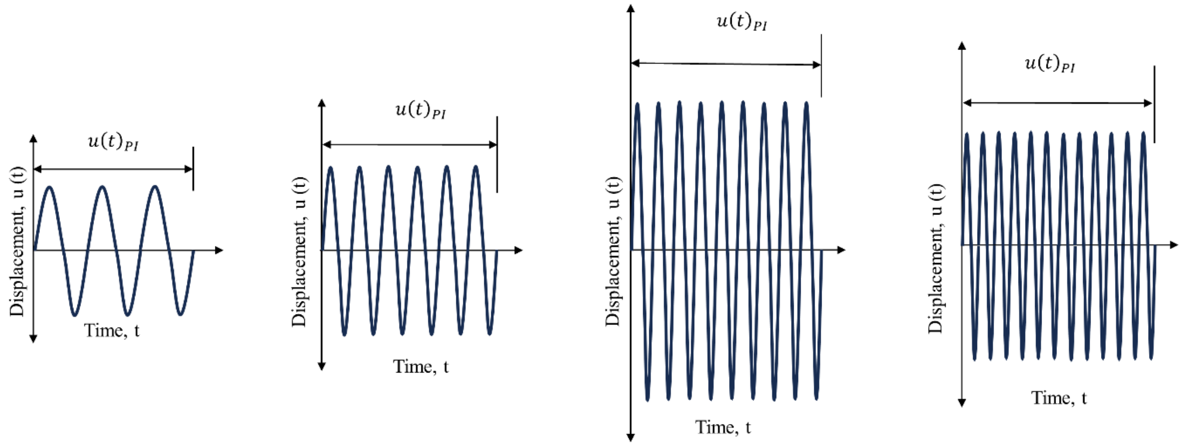

(a) Frequency $= f_1$ (b) Frequency $= f_2$ (c) Frequency $= f_3$ (d) Frequency $= f_4$

Figure 5.8 Diagrammatic conceptualization of the particular integral with increasing frequency as conceptualized in the present numerical framework

As the complementary function is an exponential decay function that produces a transient response decaying very fast in time, it is assumed that the displacement response can be best explained by a particular integral, i.e., a harmonic function that shall last till the load is applied by the lever arm of the mechanical shaker. Based on this assumption, it has been conceptualized that the particular integral will increase till a threshold value of frequency, say f_3, as depicted in Fig. 5.8. Therefore, the nodal displacement distributions of the PVDF-geomaterial system are given by:

$$u(t) = N_i^N u_n(t) \tag{5.28}$$

$$N_i^N(u, v, w) = \frac{1}{8}(1+u_i u)(1+v_i v)(1+w_i w) \tag{5.29}$$

where N_i^N is the interpolation shape factor for calculating nodal displacements.

It has been considered in the present study that the piezoelectric effect in the PVDF matrix has been governed by vibration-induced mechanical equilibrium and electric field-based flux conservation, which can be expressed as:

$$\iiint \sigma : \delta\varepsilon \, dV = \iint t . \delta u \, dS + \iiint f . \delta u \, dV \tag{5.30}$$

where σ is the “true” (Cauchy) stress,

t is the traction,

f is the body force per unit volume and

$$\delta\varepsilon \overset{\text{def}}{=} sym \left(\partial \, \delta u / \delta x\right) \tag{5.31}$$

where δu is a virtual vector field, and the equation for the conservation of electrical flux can be expressed as:

$$\iiint q . \delta E \, dV = \iint q_s . \delta\varphi \, dS + \iiint q_v . \delta\varphi \, dV \tag{5.32}$$

where

q is the electric flux,

q_s is the flux per unit area,

q_v is the flux per unit volume

$$\delta E \overset{\text{def}}{=} \partial \, \delta\varphi / \delta x \tag{5.33}$$

where δx is a virtual scalar field, the basic equations to investigate the stress and charge can be presented as follows (Ragab et al., 2021; Abouelregal et al., 2023a; 2023b):

$$\sigma_{ij} = D^{E}_{ijkl}\varepsilon_{kl} - e^{\varphi}_{mij}E_m \tag{5.34}$$

$$q_i = e^{\varphi}_{ijk}\varepsilon_{jk} - e^{\varphi}_{mij}E_m \quad (5.35)$$

These equations offer a practical means of interpreting and validating the outcomes of piezoelectric analyses. At the nodal positions of the piezoelectric elements, displacements, and electric potentials are present. These displacements and electric potentials are estimated within the element as follows:

$$u(t) = N_i^N u_n(t) \quad (5.36)$$

$$\varphi(t) = N_i^N \varphi_n(t) \quad (5.37)$$

where N_i^N is the interpolating shape function, and $u(t)$ and $\varphi(t)$ are nodal displacements and electric potential quantities. Similarly, the strain and electric potential gradient can be expressed as:

$$\varepsilon(t) = B_u^N u_n(t) \quad (5.38)$$

$$E(t) = -B_\varphi^N \varphi_n(t) \quad (5.39)$$

where B_{u}^N and $-B_\varphi^N$ are the spatial derivatives of N_I^N. Based on the above numerical model, it has been conceptualized that the response of displacement, stress, and voltage output will increase till the threshold value of frequency for varied input thicknesses of PVDF films.

5.3 Results and Discussion

5.3.1 Mesh Convergence and Validation

The numerical model has been studied and tested for mesh convergence, and the findings have been analysed and compared to the experimental results. The mesh convergence has been performed from coarser to relatively finer mesh size to remove any noise that may arise due to inappropriate mesh size.

Table 5.4 Mesh convergence test conducted in the present study to assess the numerical accuracy of the model

Instance	Global seeding	Number of elements	Volumetric size of instance (mm) $(x \times y \times z)$	Isometric view of meshed geometry	Computation time for one simulation (in hours)	Magnitude of deflection (mm)
Geomaterial	0.05	960	8 × 10 × 12	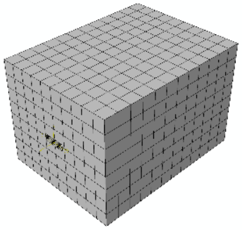	~1.00	0.00174507~0.0017
PVDF film	0.005	75	15× 5 × 1			
Geomaterial	0.04	1800	10 × 12 × 15	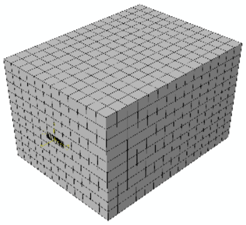	~4.00	0.001396056~0.0014
PVDF film	0.004	114	19× 6 × 1			
Geomaterial	0.03	4160	13 × 16 × 20	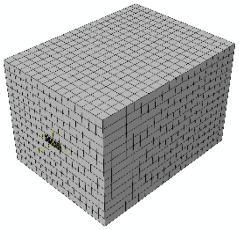	~9.00	0.001259718~0.0012
PVDF film	0.003	200	25× 8 × 1			
Geomaterial	0.02	13200	20 × 22 × 30	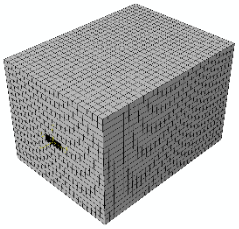	~22.00	0.00114338~0.0011
PVDF film	0.002	494	38×13 × 1			
Geomaterial	0.01	110400	40 × 46 × 60	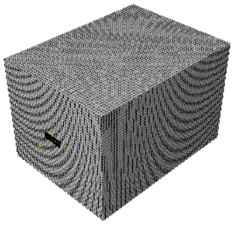	~34.00	0.0011284786~0.0011
PVDF film	0.001	1875	75× 25 × 1			

An increasing magnitude of global seeding points toward a coarser mesh and vice versa.

The number of elements exponentially increases with a decrease in the magnitude of global seeding. The mesh convergence was conducted for a global seeding value ranging from 0.05 to 0.01 for geomaterial and 0.005 to 0.001 for PVDF film, representing coarser to finer mesh size, as shown in Table 5.4. The percentage variation in deflection value was observed to be less than 1% for a global seeding value of 0.02 to 0.01 for geomaterial and 0.002 to 0.001 for PVDF film. Hence, to save the computation time, a global seeding of 0.02 for geomaterial and 0.002 for PVDF film was adopted to conduct the numerical simulation.

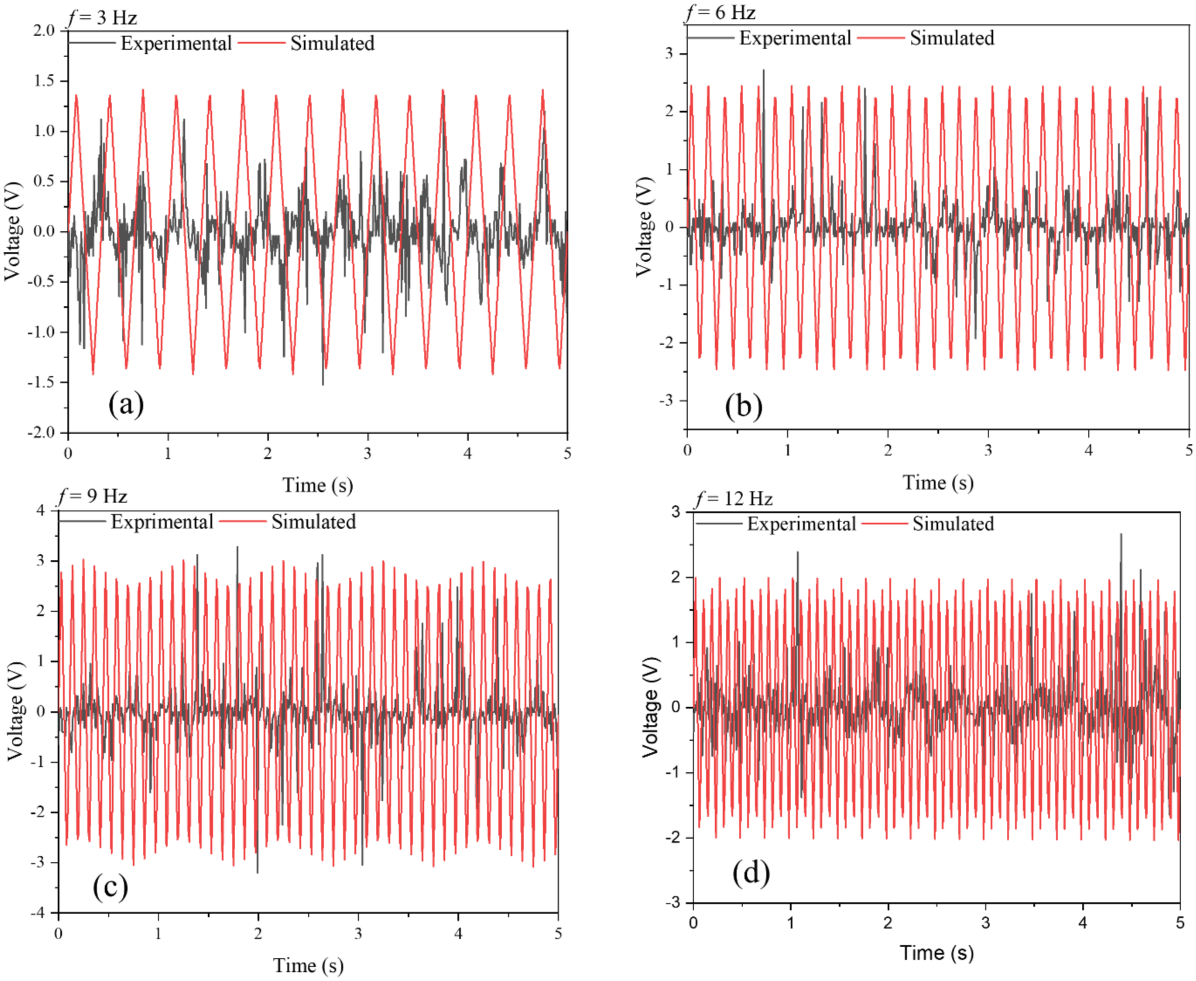

Figure 5.9 Experimental and numerical observations of voltage with time for pristine

PVDF embedded in confined geomaterial subjected to a dynamic load with varied frequencies, namely, (a) *f* = 3Hz, (b) *f* = 6 Hz, (c) *f* = 9 Hz, and (d) *f* = 12 Hz

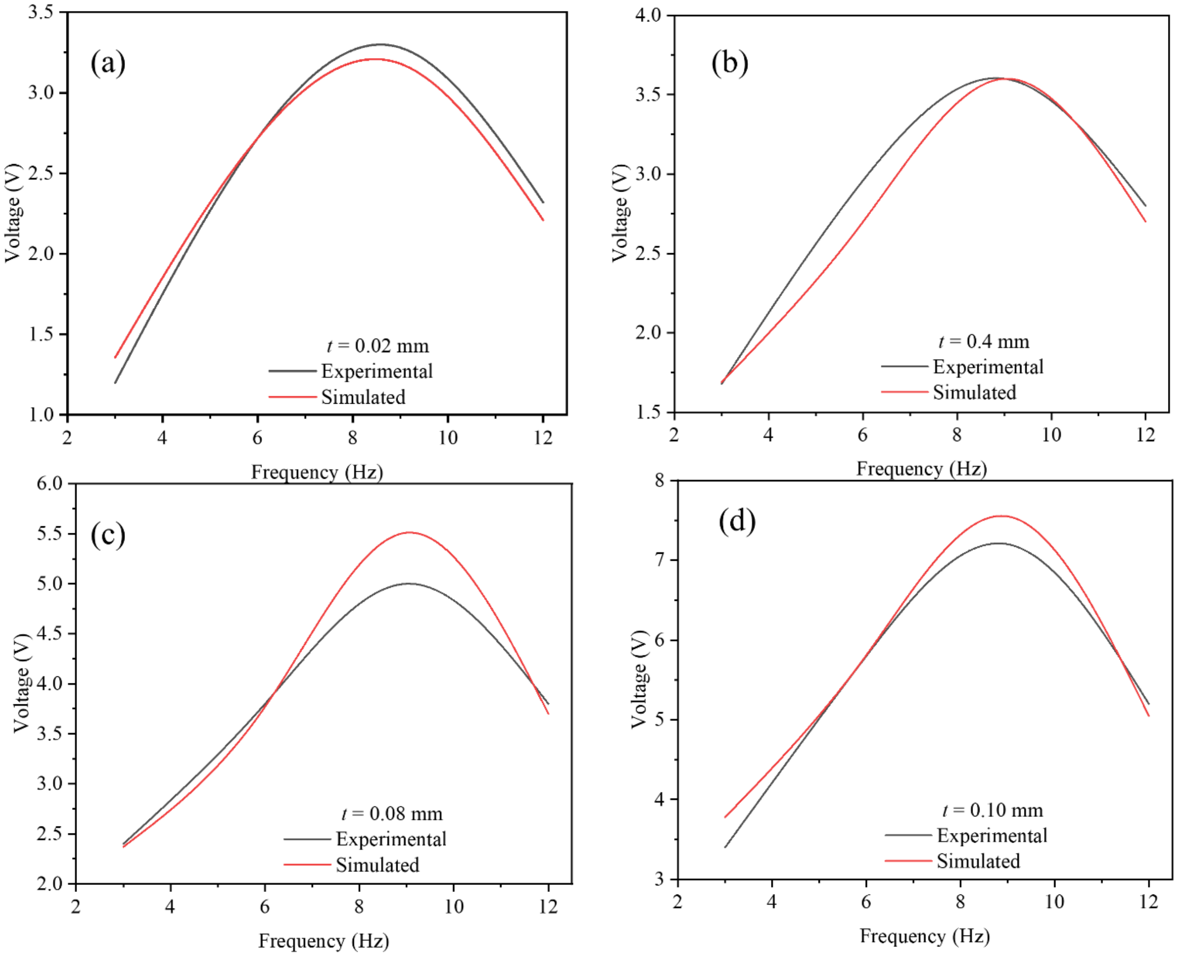

Figure 5.10 Experimental and numerical observations of voltage with frequency for pristine PVDF embedded in confined geomaterial subjected to a dynamic load with varied thicknesses, namely, (a) *t* = 0.02 mm, (b) *t* = 0.04 mm, (c) *t* = 0.08 mm, and (d) *t* = 0.10 mm

The performance of the PVDF film subjected to a dynamic load has been captured by giving periodic vibrations. The input parameters, namely, the dimensions, material properties, and loading conditions, are kept identical to experimental investigations. In comparison with the experimental voltage findings, the open circuit voltage of numerically simulated PVDF films has been studied, as shown in Figs. 5.9 and 5.10. In compliance with the experimental findings, the numerical results vary from 1.2 to 7.25 V for the selected set of input frequencies. It may be noted that the variation of input property from various sources has some deviation from experimental results (Figs. 5.9 and 5.10). Despite this consideration, the results as presented map well with the real-time experimental observations.

Numerical simulations corresponding to the maximum open circuit voltage have also confirmed a threshold frequency (f_{th}) of 9 Hz, as shown in Fig. 5.10. Hence, it can be stated that numerical results in terms of peak voltage are in good agreement with the variation in experimental findings. The variation in voltage with time for varied thicknesses of PVDF film has been studied using numerically varied algorithms.

5.3.2 Dynamic Response of PVDF Film

Fig. 5.11 shows the numerically observed variation of deflection, stress, and voltage with time for the varied thickness of the PVDF film. The distributed load (DLOAD) subroutine in the commercialized software package Abaqus has been selected to apply the dynamic load in numerical simulations. A time interval of 5 seconds, along with a frequency range of 3-12 Hz, has been adopted to conduct the presented numerical investigations. The compounded variation has been observed for deflection, stress, and voltage response on the numerical time window of 5 seconds.

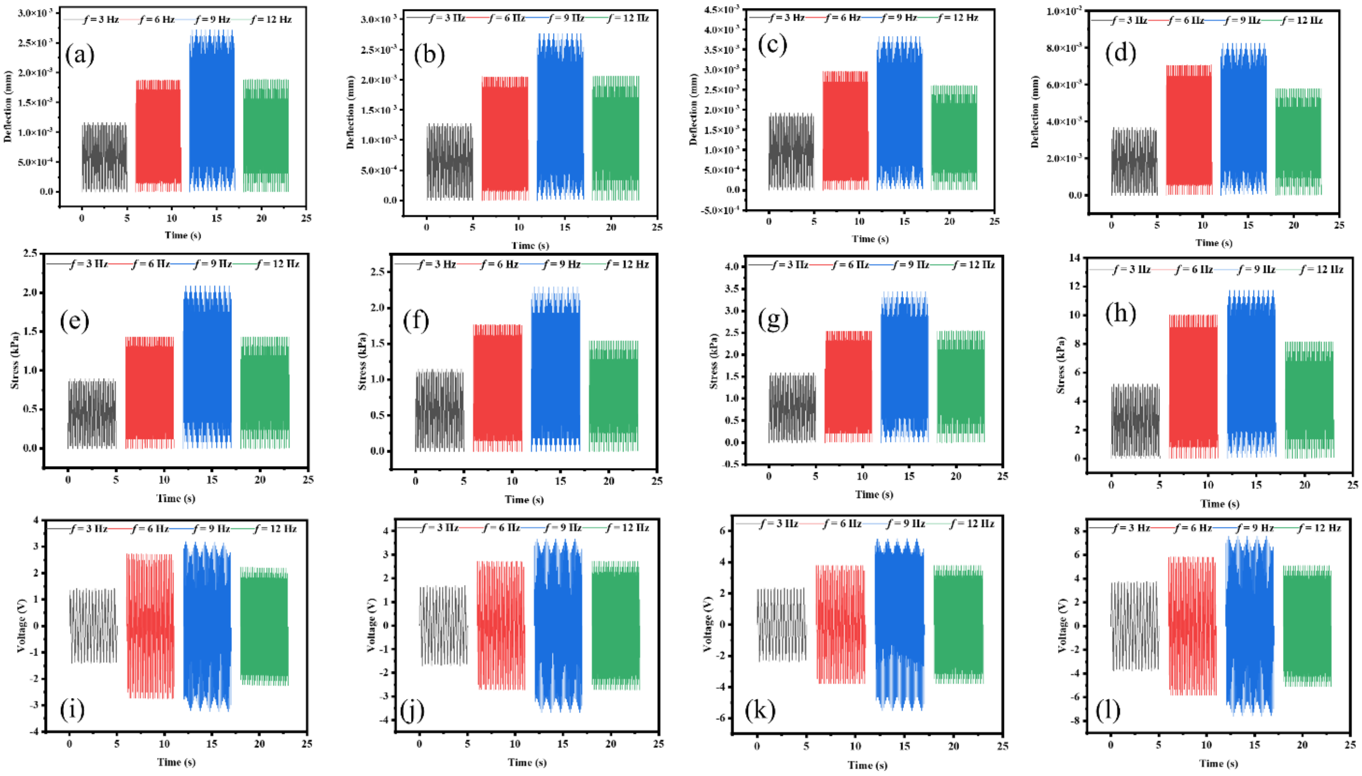

Figure 5.11 Numerical observations of the variation in (a-d) deflection, (e-h) stress, and (i-l) voltage with time for 0.02 mm, 0.04 mm, 0.08 mm, and 0.10 mm thick PVDF films subjected to varied loading frequencies ranging from 3-12 Hz with an interval of 3 Hz

The influence of frequency on stress-voltage and deflection-voltage response has been observed, as shown in Fig. 5.12 (a) and (b). Fig. 5.12 (a) depicts the variation of stress voltage in PVDF film prescribed by the input frequencies of periodical vibrations. The variation of peak stress and voltage from the compounded plot (Fig. 5.11) has been extracted for a 3-12 Hz set of frequency range. It has been observed that peak stress varies from 1 to 12 kPa for the selected set of input frequencies. The maximum stress in PVDF films has been observed for an input of 9 Hz frequency. Fig. 5.12(b) shows the peak deflection voltage with varied input frequencies ranging from 3-12 Hz. The deflection varies from 0.0002 to 0.0082 mm in 0.02-0.10 mm thick, pristine PVDF films for the selected set of frequencies considered in this research. The threshold frequency produces a maximum of 0.0082 mm deflection in a 0.10 mm thick PVDF film with a voltage magnitude of 7.2 V.

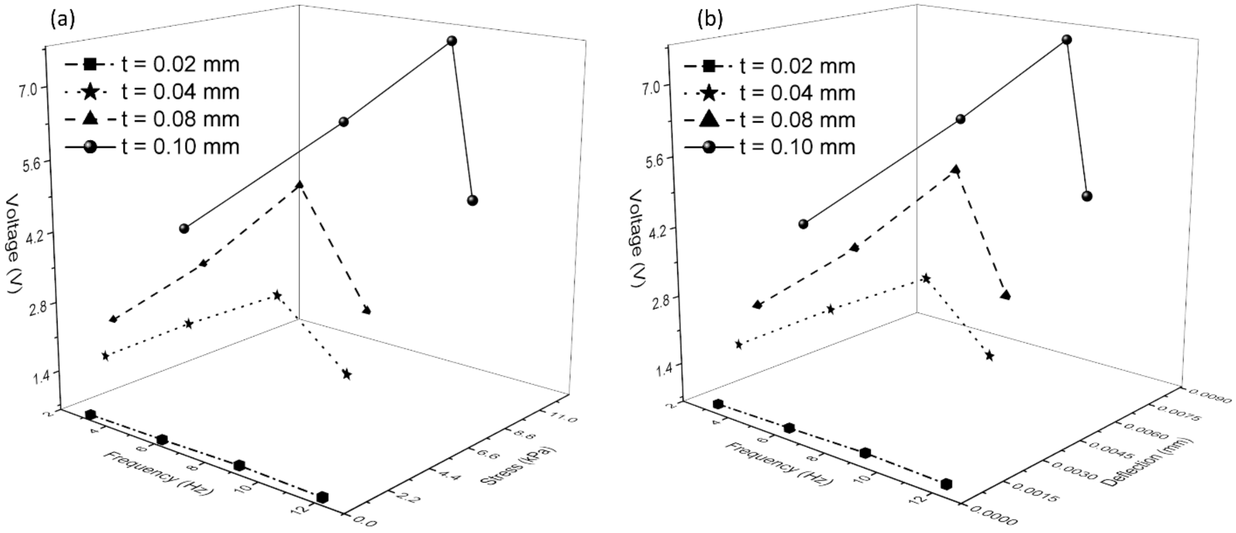

Figure 5.12 Variation of (a) stress-voltage and (b) deflection-voltage with frequency for the varied thickness of PVDF film

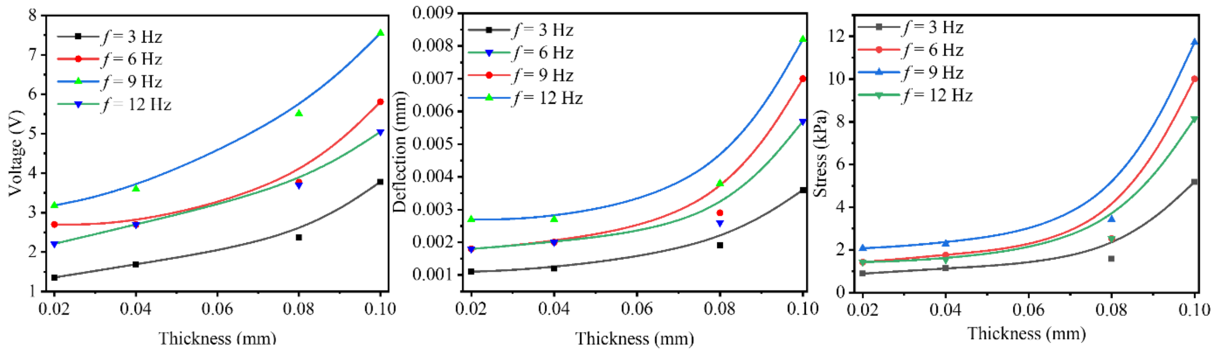

(a) (b) (c)

Figure 5.13 (a to c) Variation of voltage, deflection, and stress with thickness for the varied input frequencies

The influence of frequency on voltage, deflection, and stress response with increasing thickness has been investigated, as shown in Figs. 5.13 (a), (b), and (c). These observations showed that the deflections exhibited a corresponding rise as both frequency and thickness increased. This behavior suggests a direct relationship between these parameters, where higher frequencies and thicker PVDF films lead to increased deflection and stress. However, in the case of voltage, a notable trend was observed. The voltage increased proportionally with frequency and thickness until it reached a threshold value at 9 Hz frequency. Beyond this frequency threshold, further increases in frequency did not result in corresponding increases in voltage. This phenomenon may be attributed to material properties and their inherent limitations at limiting threshold frequencies, leading to a saturation effect in voltage response beyond the critical frequency point. These findings highlight the complex interplay between frequency, thickness, and PVDF material response.

The deflections, stress, and voltage magnification factors (D_{mf}, S_{mf}, V_{mf}) have been evaluated for pristine PVDF films to understand the compounded vibrational effect. The peak deflection, stress, and voltage prescribed by 9 Hz frequency on a 0.02 mm thick PVDF film have been selected as the critical offset value. The deflection, stress, and voltage magnification have been captured correspondingly to this offset value.

Mathematically, these magnification factors can be calculated as follows;

$$D_{mf} = \frac{D_{(t=\sum_{i=0.02}^{0.10} t_i)}}{D_{t_c}} \tag{5.40}$$

$$S_{mf} = \frac{S_{(t=\sum_{i=0.02}^{0.10} t_i)}}{S_{t_c}} \tag{5.41}$$

$$V_{mf} = \frac{V_{(t=\sum_{i=0.02}^{0.10} t_i)}}{V_{t_c}} \tag{5.42}$$

Where

$D_{(t=\sum_{i=0.02}^{0.10} t_i)}$ = maximum deflection observed in 0.02 – 0.10 mm thick PVDF film

D_{t_c} = critical offset value of deflection observed in a 0.02 mm thick PVDF film

$S_{(t=\sum_{i=0.02}^{0.10} t_i)}$ = maximum output of stress observed in 0.02 – 0.10 mm thick PVDF film

S_{t_c} = critical offset value of stress observed in a 0.02 mm thick PVDF film

$V_{(t=\sum_{i=0.02}^{0.10} t_i)}$ = maximum output of voltage observed in 0.02 – 0.10 mm thick PVDF film

V_{t_c} = critical offset value of voltage observed in a 0.02 mm thick PVDF film

An exponential amplification in deflection, stress, and voltage has been observed with an increase in the thickness of the PVDF film, as shown in Fig. 5.14 (a), (b), and (c). A 0 % to 203 % magnification in deflection, 0 % to 411 % magnification in the stress, and 0 % to 119 % magnification in voltage, respectively, has been observed for 0.02-0.10 mm thick

PVDF films. The increased vibration on varied thicknesses of PVDF films greatly amplifies the charge concentration in the PVDF films. This indicates that an increase in periodic vibrations on the PVDF film significantly increases the deflection, stress, and voltage in the PVDF film.

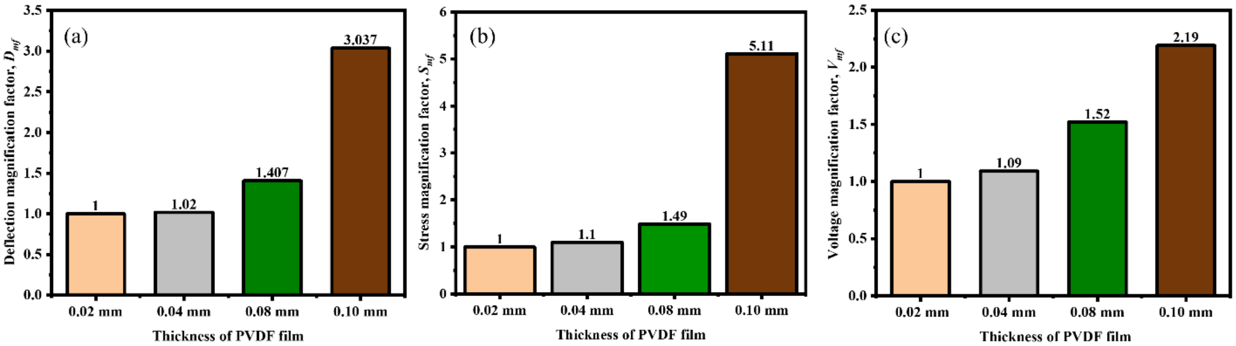

Figure 5.14 Numerical observations of the amplification in (a) deflection, (b) stress, and (c) voltage

Fig. 5.10 to 5.14 show the frequency-induced voltage, deflection, and stress, along with their magnification factors. The piezoelectric response in PVDF films has been observed to be a function of frequency and the thickness of the PVDF film as the thickness of PVDF increases, voltage output increases, and vice-versa. The thickness of the PVDF film from 0.02 mm to 0.10 mm increased the voltage output by 119%, producing an open circuit voltage of 7.2 V. Also, an increase in the magnitude of frequency increases the deflection and stress on the PVDF film. The minuscule deflection of 0.001 mm in the PVDF film due to a periodic vibration of 3 Hz imparts a stress of 0.9 kPa, producing an open circuit voltage of 1.2 V. The maximum deflection observed in the pristine PVDF film was 0.0082 mm, caused by a frequency of 9 Hz that stressed the PVDF matrix to 11.72 kPa, which produced an open circuit voltage of 7.2 V, as shown in Fig. 5.15.

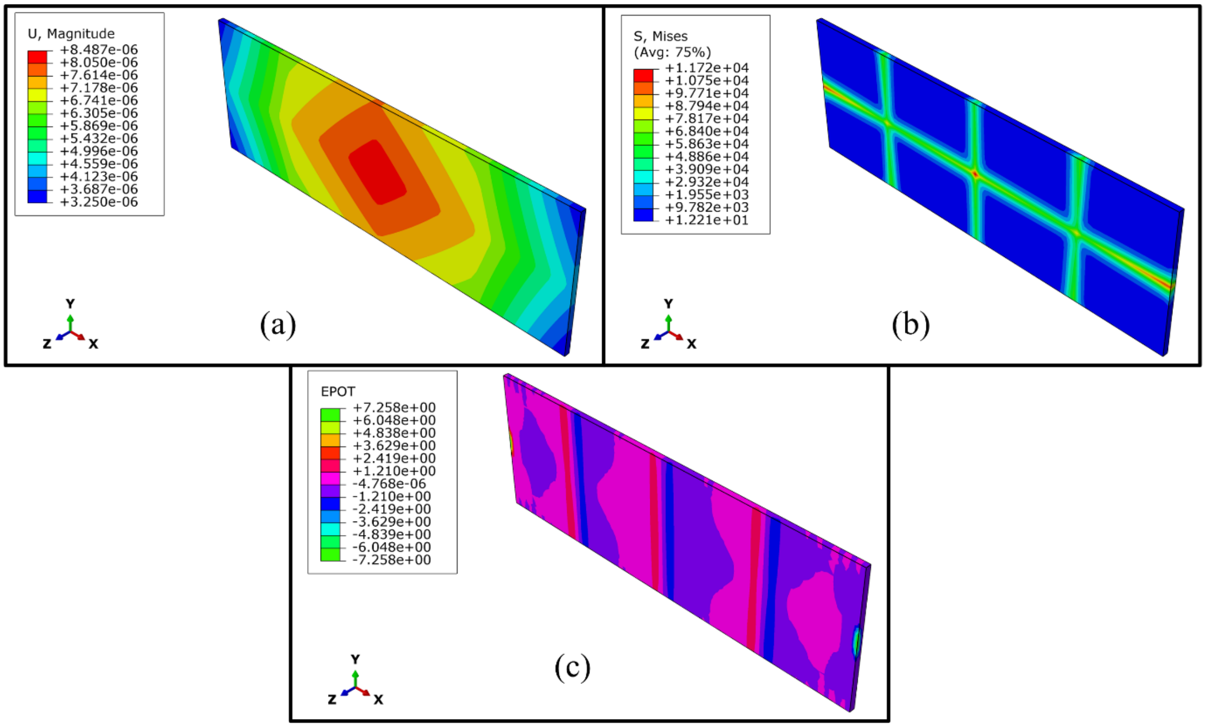

Figure 5.15 Contour representation of (a) deflection, (b) stress, and (c) voltage profile in PVDF film

Hence, from the outcomes of the presented study, the performance of pristine PVDF embedded in confined geomaterial can be conceptualized as a function of voltage (v), stress (σ), deflection (δ), and frequency of excitation (f) expressed as $g\,(v, \sigma, \delta, f)$. A set of novel second-degree polynomial co-relations have been proposed in the present study to relate the tapping frequency with voltage, deflection, and stress, as presented by the equation below:

$$g(v,\sigma,\delta,f)=\begin{cases} v = a_v f^2 + b_v f + c_v \\ \delta = a_\delta f^2 + b_\delta f + c_\delta \\ \sigma = a_\sigma f^2 + b_\sigma f + c_\sigma \end{cases} \tag{5.43}$$

Alternatively, the above equation can be written as:

$$\begin{bmatrix} v \\ \delta \\ \sigma \end{bmatrix} = \begin{bmatrix} a_v & b_v & c_v \\ a_\delta & b_\delta & c_\delta \\ a_\sigma & b_\sigma & c_\sigma \end{bmatrix} \begin{bmatrix} f^2 \\ f \\ 1 \end{bmatrix} \tag{5.44}$$

The numerical values for these non-dimensional stress, deflection, and voltage have been appended in the appendix. The equation above can be effectively adopted to evaluate the performance of a PVDF-based piezoelectric nanogenerator. The evaluation of the voltage response of the PVDF embedded in a confined geomaterial system subjected to dynamic load has potential use for engineers, practitioners, and scientists for strain sensing and energy harvesting in the context of green and renewable energy. Furthermore, PZT is one of the most widely adopted materials in civil engineering, renewable energy aspects, structural health monitoring, and sensing technology. However, the lead (Pb) in PZT has been established to be toxic and hazardous to human health. Hence, this study provides a suitable alternative for toxic PZT by removing it with a non-toxic PVDF for developing sensors and harvesting renewable energy. The results showed an incremental voltage, deflection, and stress with an increased frequency up to a threshold limit (9 V).

Table 5.5 compares engineering application, thickness (mm), output voltage, deflection, and stress in the synthesized PVDF films and piezoelectric nanogenerators available in the literature. It can be observed in Table 5.5 that 0.02-0.10 mm thick PVDF film produces 1.20-7.20 V due to 0.0036-0.0082 mm deflection prescribed by 5.19-11.72 kPa of stress, which is significantly higher than the voltage produced by the PENG conceptualized using lead (Pb, output voltage = 0.56 V) and reduced graphene oxide (rGO, output voltage = 0.736 V) based nanogenerators. One more important observation is that the inclusion of molybdenum disulphide (MoS_2) enhanced the output voltage of the piezoelectric nanogenerator. Hence, the present study paves a new path to establish a PVDF and PVDF doped with other non-toxic element-based piezoelectric nanogenerators in geostructures for energy harvesting and sensor technology applications.

Table 5.5 Comparison of engineering application, thickness (mm), output voltage (V), deflection, and stress in synthesized PVDF and piezoelectric nanogenerators as reported in the literature

PENG	Engineering application	Thickness (mm)	Voltage (V)	Deflection (mm)	Stress (kPa)
PZT [a,b,c]	Functionally graded piezoelectric (FGP) structure	-	0.40	0.13	0.5
PZT [d]	Confined geostructures (indirect loading conditions)	-	0.56	0.002	20
PVDF [e]	Prismatic member	-	1.0	-	-
PVDF/rGO [f]	Prismatic member	-	0.756	-	-
PVDF/MoS_2 [g]	Prismatic member	-	14.00	-	-
PVDF [h]	Pavements/confined geostructures	0.02-0.10	3.10-7.20	0.0036-0.0082	5.19-11.72

[a] Abouelregal et al. (2023a); [b] Abouelregal et al. (2023b); [c] Ragab et al. (2021); [d] Kumari & Trivedi (2022), [e] Aanand et al. (2020), [f] Singh et al. (2017), [g] Maity et al. (2017), [h] Present Work

The performance of PVDF films presented in this research has the potential to produce renewable energy. Moreover, the sensing industry can use this technology to develop sensors. Often, vibratory loads on geomaterials are utilized in energy harvesting using thin films consisting of PVDF embedded in geomaterials. Several uses of such composite films are found in structural health monitoring. Hence, based on the presented research findings, a future direction has been established for investigating the PVDF for renewable energy and geo-structure sensing technologies.

5.4 Conclusions

In the present study, experimental investigation and a finite element-based numerical program have been considered to investigate the performance of PVDF films embedded in confined geomaterials subjected to vibratory loads. This study explores the performance of PVDF in terms of stress, deflection, and voltage as a function of frequency and non-dimensional numerical parameters. The non-dimensional parameters obtained in the study are for the selected set of thicknesses adopted in the present work. Based on the results and discussion, the following conclusions have been drawn:

- Influence of PVDF thickness on voltage output: The thickness of PVDF films within the range of 0.02-0.10 mm correlates well with the voltage output of the tested configurations, with the 0.10 mm thick PVDF film exhibiting the maximum open circuit voltage of 7.2 V.
- Impact of frequency on magnification factors: A significant magnification of stress and deflection has been observed in pristine PVDF film due to a varied set of input frequencies (3-12 Hz), with stress amplifying by 411% and deflection by 203%, subsequently amplifying the voltage output by 119%.
- Stress and Deflection Relationship: The armature displacement limit (1 mm) of load vibrating at 3-12 Hz deflected the PVDF films from 0.001 to 0.0082 mm with a stress concentration varying from 0.9 to 11.72 kPa within the PVDF film. It establishes that the deflection and stress are direct functions of the input frequency and thickness of PVDF films.
- Relationship with Open Circuit Voltage: The observed deflections and stress concentrations directly influence the open circuit voltage output (1.2 to 7.2 V)

across the investigated conditions, which play a vital role in the electrical performance of PVDF films.

The findings pave a new path for the potential engineering applications of PVDF films in sensor development and energy harvesting, driven by their ability to convert mechanical vibrations into electrical energy. The observations and findings in the study conclude that the study provides a comprehensive display of PVDF film thickness, stress distribution, deflections, and resultant voltage output under vibratory loading conditions, thereby offering valuable insights for the design and optimization of PVDF-based sensors and energy harvesting systems.

Appendix A: Non-Dimensional Factors

Table A.1 Non-dimensional voltage, deflection, and stress parameters extracted from the results obtained from non-dimensional voltage, deflection, and stress parameters

Thickness of PVDF patch (mm)	Non-dimensional voltage, deflection, and stress parameters								
	a_v	a_δ	a_σ	b_v	b_δ	b_σ	c_v	c_δ	c_σ
0.02	0.0089	0.0002	0.1628	0.6444	-0.0011	-0.07367	-0.72	0.0026	1.87
0.04	0.0533	0.0001	0.1272	0.2578	-0.0005	-0.04756	0.56	0.0016	1.62
0.08	0.2333	0.0002	0.1906	-0.7778	-0.0008	-0.7217	3	0.0028	2.32
0.10	0.2111	0.00004	0.0683	-0.1667	0.0013	1.8356	2.4	-0.0005	-0.57

Appendix B: Field Application

Illustrative Example B#1 (Sensor): An engineer is required to design a sensor to capture the vibration sensitivity coming from the idling of an engine on an unpaved road. He has opted for PVDF film, looking at the advantages of films being flexible (manoeuvrability) and non-toxic (environment friendly). The engine is idling at a 9 Hz frequency. Estimate the deflection and stress produced by the idling of the engine in 0.04 mm and 0.08 mm thick PVDF films along with their voltage output so that he can use PVDF as a sensor to capture the vibration sensitivity. The vendor who supplied the PVDF films provided the engineer with the properties of PVDF, as given in Table 5.2 and 5.3.

Solution:

As per the research conducted in the present study, the following steps can be followed:

Step 1: Use Eq. (B.1) to estimate the deflection, stress, and voltage output.

$$\begin{bmatrix} v \\ \delta \\ \sigma \end{bmatrix} = \begin{bmatrix} a_v & b_v & c_v \\ a_\delta & b_\delta & c_\delta \\ a_\sigma & b_\sigma & c_\sigma \end{bmatrix} \begin{bmatrix} f^2 \\ f \\ 1 \end{bmatrix} \tag{B.1}$$

Step 2: Obtain values of non-dimensional factor from Table 6 for 0.04 mm and 0.08 mm thick PVDF film.

Thickness of PVDF patch (mm)	Non-dimensional voltage, deflection, and stress parameters								
	a_v	a_δ	a_σ	b_v	b_δ	b_σ	c_v	c_δ	c_σ
0.04	0.0533	0.0001	0.1272	0.2578	-0.0005	-0.04756	0.56	0.0016	1.62
0.08	0.2333	0.0002	0.1906	-0.7778	-0.0008	-0.7217	3	0.0028	2.32

Step 3: Put the values of non-dimensional factors from Table A.1 to Eq. (B.1) and calculate deflection, stress, and voltage output.

Thickness (mm)	Deflection (mm)	Stress (kPa)	Voltage (V)
0.04	0.0012	1.14	1.69
0.08	0.0019	1.58	2.37

Illustrative Example B#2 (***Energy Harvester):*** Considering the data as per illustrative example B.1, discuss the potential of PVDF as an energy harvester.

Solution:

Repeat steps 1 to 3, mentioned in illustrative example B#1, to discuss the potential of PVDF as an energy harvester; we need to obtain amplification in PVDF films.

Step 4: Obtain deflection, stress, and voltage magnification factors using Eq. C.1, C.2, and C.3.

$$D_{mf} = \frac{D_{(t=\sum_{i=0.02}^{0.10} t_i)}}{D_{t_c}} \tag{C.1}$$

$$S_{mf} = \frac{S_{(t=\sum_{i=0.02}^{0.10} t_i)}}{S_{t_c}} \tag{C.2}$$

$$V_{mf} = \frac{V_{(t=\sum_{i=0.02}^{0.10} t_i)}}{V_{t_c}} \tag{C.3}$$

Thickness (mm)	D_{mf}	S_{mf}	V_{mf}
0.04	1	1	1
0.08	1.58	1.38	1.42

Note: D_{tc}, S_{tc}, and V_{tc} are taken for 0.04 mm thick PVDF film

The magnification factors show that the values of deflection, stress, and voltage are magnified by 1.58, 1.38, and 1.42 times than 0.04 mm thick PVDF film in 0.08 mm thick

PVDF film as compared to 0.04 mm thick PVDF film. Hence, in the situation considered in illustrative example B.1, a 0.08 mm thick PVDF film can be used for energy harvesting from the mechanical vibration input of engine idling.

References

1. Abouelregal, A. E., Askar, S. S., Marin, M., & Mohamed, B. (2023a). The theory of thermoelasticity with a memory-dependent dynamic response for a concept-piezoelectric functionally graded rotating rod. Scientific Reports, 13(1), 9052. https://doi.org/10.1038/s41598-023-36371-2
2. Abouelregal, A. E., Marin, M., & Abusalim, S. M. (2023b). An investigation into thermal vibrations caused by a moving heat supply on a spinning functionally graded isotropic piezoelectric bounded rod. Mathematics, 11(7), 1739. https://doi.org/10.3390/math11071739
3. Anand, A., Meena, D., Dey, K. K., & Bhatnagar, M. C. (2020). Enhanced piezoelectricity properties of reduced graphene oxide (RGO) loaded polyvinylidene fluoride (PVDF) nanocomposite films for nanogenerator application. Journal of Polymer Research, 27, 1-11. https://doi.org/10.1007/s10965-020-02323-x
4. Anton, S. R., & Sodano, H. A. (2007). A review of power harvesting using piezoelectric materials (2003–2006). Smart Materials and Structures, 16(3), R1. https://doi.org/10.1088/0964-1726/16/3/R01
5. Beeby, S. P., Tudor, M. J., & White, N. M. (2006). Energy harvesting vibration sources for microsystems applications. Measurement Science and

Technology, 17(12), R175. https://doi.org/10.1088/0957-0233/17/12/R01

6. Bolborici, V., Dawson, F. P., & Pugh, M. C. (2012). Modeling of composite piezoelectric structures with the finite volume method. IEEE Transactions on Ultrasonics, Ferroelectrics, and Frequency Control, 59(1), 156-162.
7. Braun, M., & Golubitsky, M. (1983). Differential equations and their applications, 2. New York: Springer-Verlag. https://doi.org/10.1007/978-1-4684-0053-3
8. Cahill, P., Mathewson, A., & Pakrashi, V. (2018). Experimental validation of piezoelectric energy-harvesting device for built infrastructure applications. Journal of Bridge Engineering, 23(8), 04018056. https://doi.org/10.1061/(ASCE)BE.1943-5592.000126
9. Chen, F., Balieu, R., Córdoba, E., & Kringos, N. (2019). Towards an understanding of the structural performance of future electrified roads: A finite element simulation study. International Journal of Pavement Engineering, 20(2), 204-215. https://doi.org/10.1080/10298436.2017.1279487
10. Cross, L. E. (1995). Ferroelectric materials for electromechanical transducer applications. Japanese Journal of Applied Physics, 34(5S), 2525. https://doi.org/10.1016/0254-0584(95)01617-4
11. Das, B. M. (1983). Fundamentals of soil dynamics. Elsevier, Gainesville, USA.
12. Ding, G., Zhao, X., Sun, F., & Wang, J. (2018). Effect of subgrade on

piezoelectric energy harvesting under traffic loads. International Journal of Pavement Engineering, 19(8), 661-674. https://doi.org/10.1080/10298436.2017.1413241

13. Dunn, P. E., & Carr, S. H. (1989). A historical perspective on the occurrence of piezoelectricity in materials. MRS Bulletin, 14(2), 22-31. https://doi.org/10.1557/S0883769400063405
14. Erturk, A. (2011). Piezoelectric energy harvesting for civil infrastructure system applications: Moving loads and surface strain fluctuations. Journal of Intelligent Material Systems and Structures, 22(17), 1959-1973. https://doi.org/10.1177/1045389X11420593
15. Filoux, E., Callé, S., Certon, D., Lethiecq, M., & Levassort, F. (2008). Modeling of piezoelectric transducers with combined pseudospectral and finite-difference methods. Journal of the Acoustical Society of America, 123(6), 4165-4173. https://doi.org/10.1121/1.2903876
16. Fukada, E. (2000). History and recent progress in piezoelectric polymers. IEEE Transactions on Ultrasonics, Ferroelectrics, and Frequency Control, 47(6), 1277-1290. https://doi.org/10.1109/58.883516
17. Gandhi, M. V., & Thompson, B. D. (1992). Smart materials and structures. Springer Science & Business Media, NY, USA.
18. Guan, X., Zhang, Y., Li, H., & Ou, J. (2013). PZT/PVDF composites doped with carbon nanotubes. Sensors and Actuators A: Physical, 194, 228-231. https://doi.org/10.1016/j.sna.2013.02.005

19. Guo, L., & Lu, Q. (2017). Modeling a new energy harvesting pavement system with experimental verification. Applied Energy, 208, 1071-1082. https://doi.org/10.1016/j.apenergy.2017.09.045

20. Jiao, P., Egbe, K. J. I., Xie, Y., Matin, A. N., & Alavi, A. H. (2020). Piezoelectric sensing techniques in structural health monitoring: A state-of-the-art review. Sensors, 20(13), 3730. https://doi.org/10.3390/s20133730

21. Kepler, R. G., & Anderson, R. A. (1978). Piezoelectricity and pyroelectricity in polyvinylidene fluoride. Journal of Applied Physics, 49(8), 4490-4494. https://doi.org/10.1063/1.325454

22. Kumar, Y., Trivedi, A., & Shukla, S. K. (2024a). Damage evaluation in pavement-geomaterial system using finite element-scaled accelerated pavement testing. Transportation Infrastructure Geotechnology, 1-12. https://doi.org/10.1007/s40515-023-00309-y

23. Kumar, Y., Trivedi, A., & Shukla, S. K. (2024b). Deflections governed by the cyclic strength of rigid pavement subjected to structural vibration due to high-velocity moving loads. Journal of Vibration Engineering and Technologies, 1-20. https://doi.org/10.1007/s42417-023-01063-8

24. Kumari, N., & Trivedi, A. (2019). Vibration control of flexible retention systems. In Advances in Computer Methods and Geomechanics: IACMAG Symposium (2), 529-539. Springer, Singapore. https://doi.org/10.1007/978-981-15-0890-5_44

25. Kumari, N., & Trivedi, A. (2022). Factors influencing piezoelectric response of horizontally and vertically embedded PZT patch in confined granular fills. Advances in Materials Science and Engineering, 2022(1), 7860273. https://doi.org/10.1155/2022/7860273
26. Kumari, N., & Trivedi, A. (2022b). The effect of confined granular soil on embedded PZT patches using FFT and digital static cone penetrometer (DSCP). Applied Sciences, 12(19), 9711. https://doi.org/10.3390/app12199711
27. Kumari, N., & Trivedi, A. (2022). A review on modelling and techniques used for piezoelectric power generation from vibration of geo-structures. E-Prime-Advances in Electrical Engineering, Electronics and Energy, 100076. https://doi.org/10.1016/j.prime.2022.100076
28. Lee, U., Kim, D., & Park, I. (2013). Dynamic modeling and analysis of the PZT-bonded composite Timoshenko beams: Spectral element method. Journal of Sound and Vibration, 332(6), 1585-1609. https://doi.org/10.1016/j.jsv.2012.06.020
29. Liu, P., Zhao, Q., Yang, H., Wang, D., Oeser, M., Wang, L., & Tan, Y. (2019). Numerical study on influence of piezoelectric energy harvester on asphalt pavement structural responses. Journal of Materials in Civil Engineering, 31(3), 04019008. https://doi.org/10.1061/(ASCE)MT.1943-5533.0002640
30. Maity, K., Mahanty, B., Sinha, T. K., Garain, S., Biswas, A., Ghosh, S. K., &

Mandal, D. (2017). Two-dimensional piezoelectric MoS2-modulated nanogenerator and nanosensor made of poly(vinylidene fluoride) nanofiber webs for self-powered electronics and robotics. Energy Technology, 5(2), 234-243. https://doi.org/10.1002/ente.201600419

31. Mahapatra, S. D., Mohapatra, P. C., Aria, A. I., Christie, G., Mishra, Y. K., Hofmann, S., & Thakur, V. K. (2021). Piezoelectric materials for energy harvesting and sensing applications: Roadmap for future smart materials. Advanced Science, 8(17), 2100864. https://doi.org/10.1002/advs.202100864
32. Mario, P., & Young, H. K. (2019). Structural dynamics: Theory and computation (Vol. 6). Springer Science & Business Media, Switzerland.
33. Petroff, C. A., Bina, T. F., & Hutchison, G. R. (2019). Highly tunable molecularly doped flexible poly(dimethylsiloxane) foam piezoelectric energy harvesters. ACS Applied Energy Materials, 2(9), 6484-6489. https://doi.org/10.1021/acsaem.9b01061
34. Ragab, M., Abo-Dahab, S. M., Abouelregal, A. E., & Kilany, A. A. (2021). A thermoelastic piezoelectric fixed rod exposed to an axial moving heat source via a dual-phase-lag model. Complexity, 20(21), 1-11. https://doi.org/10.1155/2021/5547566
35. Rhimi, M., & Lajnef, N. (2012). Tunable energy harvesting from ambient vibrations in civil structures. Journal of Energy Engineering, 138(4), 185-193. https://doi.org/10.1061/(ASCE)EY.1943-7897.00000
36. Roopa, T. S., Murthy, H. N., Harish, D. V. N., Jain, A., & Angadi, G. (2021).

Properties of PVDF films stretched in machine direction. Polymers and Polymer Composites, 29(3), 198-206. https://doi.org/10.1177/0967391120910592

37. Roshani, H., Dessouky, S. (2015). Feasibility study to harvest electric power from highway pavements using laboratory investigation. Department of Civil and Environmental Engineering, University of Texas at San Antonio, USA.
38. Roshani, H., Dessouky, S., Montoya, A., & Papagiannakis, A. T. (2016). Energy harvesting from asphalt pavement roadways vehicle-induced stresses: A feasibility study. Applied Energy, 182, 210-218. https://doi.org/10.1016/j.apenergy.2016.08.116
39. Roshani, H., Jagtap, P., Dessouky, S., Montoya, A., & Papagiannakis, A. T. (2018). Theoretical and experimental evaluation of two roadway piezoelectric-based energy harvesting prototypes. Journal of Materials in Civil Engineering, 30(2), 04017264. https://doi.org/10.1061/(ASCE)MT.1943-5533.0002112
40. Saxena, P., & Shukla, P. (2021). A comprehensive review on fundamental properties and applications of poly(vinylidene fluoride) (PVDF). Advanced Composites and Hybrid Materials, 4, 8-26. https://doi.org/10.1007/s42114-021-00217-0
41. Sezer, N., & Koç, M. (2021). A comprehensive review on the state-of-the-art of piezoelectric energy harvesting. Nano Energy, 80, 105567. https://doi.org/10.1016/j.nanoen.2020.105567

42. Singh, B., Varandani, D., & Mehta, B. R. (2013). Effect of conductive atomic force microscope tip loading force on tip-sample interface electronic characteristics: Unipolar to bipolar resistive switching transition. Applied Physics Letters, 103(5), 051604. https://doi.org/10.1063/1.4817380
43. Singh, H. H., Singh, S., & Khare, N. (2017). Design of flexible PVDF/NaNbO3/RGO nanogenerator and understanding the role of nanofillers in the output voltage signal. Composite Science and Technology, 149, 127-133. https://doi.org/10.1016/j.compscitech.2017.06.013
44. Tasaka, S., Miyata, S. (1981). The origin of piezoelectricity in poly(vinylidene fluoride). Ferroelectrics, 32(1), 17-23. https://doi.org/10.1080/00150198108238668
45. Tasaka, S., Niki, J., Ojio, T., & Miyata, S. (1984). Structure and piezoelectricity of poly(vinylidene fluoride) films obtained by solid-state extrusion. Polymer Journal, 16(1), 41-48. https://doi.org/10.1295/polymj.16.41
46. Vinogradov, A., & Holloway, F. (1999). Electromechanical properties of the piezoelectric polymer PVDF. Ferroelectrics, 226(1), 169-181. https://doi.org/10.1080/00150199908230298
47. Verruijt, A. (2009). An introduction to soil dynamics (Vol. 24). Springer Science & Business Media.
48. Wang, B. T., Chen, P. H., & Chen, R. L. (2006). Finite element model verification for the use of piezoelectric sensor in structural modal analysis.

Journal of Mechanics, 22(2), 107-114. https://doi.org/10.1017/S1727719100004408

49. Wei, C., & Jing, X. (2017). A comprehensive review on vibration energy harvesting: Modelling and realization. Renewable and Sustainable Energy Reviews, 74, 1-18. https://doi.org/10.1016/j.rser.2017.01.073
50. Xin, Y., Sun, H., Tian, H., Guo, C., Li, X., Wang, S., & Wang, C. (2016). The use of polyvinylidene fluoride (PVDF) films as sensors for vibration measurement: A brief review. Ferroelectrics, 502(1), 28-42. https://doi.org/10.1080/00150193.2016.1232582
51. Zou, F., Benedetti, I., & Aliabadi, M. H. (2013). A boundary element model for structural health monitoring using piezoelectric transducers. Smart Materials and Structures, 23(1), 015022. http://doi.org/10.1088/0964-1726/23/1/015022

6

Chapter

Development of a Novel Piezo-Sensor for Sensing and Energy Harvesting Applications

---

Highlights

- In this chapter, Flexible PVDF and PVDF–MoS_2 nanocomposite patches were synthesized to enhance piezoelectric performance for vibration-based energy harvesting.
- Hydrothermal synthesis produced MoS_2 nanoflakes, while drop-casting formed PVDF and PVDF–MoS_2 films with varied thicknesses.
- XRD and Raman analyses confirmed the successful synthesis and the improved electroactive β-phase in the composite films.
- The PVDF–MoS_2 patches generated up to 16.2 V, nearly four times higher than pristine PVDF and exceeding Pb- and rGO-based nanogenerators.
- The results highlight the potential of PVDF–MoS_2 composites as eco-friendly, efficient piezoelectric sensors for energy harvesting in geostructural applications.

6.1 Background

Research into the thickness-dependent, piezoelectric, pyroelectric, and ferroelectric properties of polymer-based piezoelectric materials has been driven by the increasing applications of polyvinylidene fluoride (PVDF) and its copolymers (Kepler & Anderson, 1978; Singh et al., 2023). The PVDF is inherently polar; however, the overall polarity of the compound in its natural state is zero because the crystals are arbitrarily arranged (Dunn & Carr, 1989). The PVDF's piezoelectric properties are verified to be much superior to those of organic materials. It seems that PVDF components outperform piezoceramic ones in terms of piezoelectric output as well (Gandhi & Thompson, 1992). As a result, the PVDF has the advantage in terms of a useful sensor and energy harvester. Piezoelectric nanogenerators (PENGs) provide an improved amount of energy and flexibility in integration into systems for confined geostructures experiencing dynamic loads (Anton & Sodano, 2007), and an investigation has been conducted on the impact of excitation frequency on PZT implanted in constrained geostructures both vertically and horizontally (Kumari & Trivedi, 2022a). The existing research suggests a diverse use of PENGs produced by inorganic materials with enhanced coefficients of piezoelectricity. Nevertheless, the published research cannot be considered acceptable due to its poisonous lead component, expensive processability, and brittle characteristics (Guan et al., 2013). To address these constraints, scientists have created a piezoelectric polymer, i.e., PVDF, that is non-toxic, very flexible, and cost-effective (Tasaka et al., 1984; Fukada, 2000). The polymer PENGs, especially PVDF, have been observed to produce less electrical output. This limitation can be overcome by nucleating the PVDF with nano-fillers. The nucleation of nano-fillers enhances the β-phase and increases the performance of the PVDF without compromising the flexibility (Pan et al., 2012). The Di-chalcogenides of two-dimensional layered transition metals have been gaining much interest among scientists, practitioners, and engineers due to their improved piezoelectric performance and non-toxic nature (Gheibi et al., 2014; Peng et al., 2018). Among the TMDs, scientists and practitioners have adopted the Molybdenum Di-sulphide for its versatility in lubrication, batteries, and catalysis in chemical reactions (Malard et al., 2013; Wu et al., 2014; Yu et al., 2018). The centrosymmetric structure of TMDs in bulk form prohibits piezoelectric performance. However, the piezoelectricity in TMDs can be observed in thin monolayers of TMDs because of their fragmentary inversion symmetry. The voltage output of PVDF and its co-polymers embedded in confined geostructure under vibratory loads has been studied to a very limited extent, and its use remains elusive in geotechnical engineering (Kumar et al., 2024). Considering these research gaps, the objectives mentioned below were set for this research:

- To synthesize the bulk of molybdenum di-sulfide (MoS_2) nanoflakes and pristine patches of polyvinylidene difluoride (PVDF) with varied thicknesses and composite PVDF-MoS_2 piezoelectric patches, and
- To examine the influence of vibratory load on the efficiency of PVDF and PVDF-MoS_2 composite patches embedded in confined geostructures.

6.2 Materials and Methods

Fig. 6.1 has been conceptualized to illustrate a system for energy harvesting through coupled mechanisms (Kumari & Trivedi, 2022b). The coupling enables the simultaneous conversion of different energy forms, namely, mechanical force, vibrations, or motion, into electrical energy. Integrating multiple transduction mechanisms maximizes energy output across a range of frequencies and input conditions.

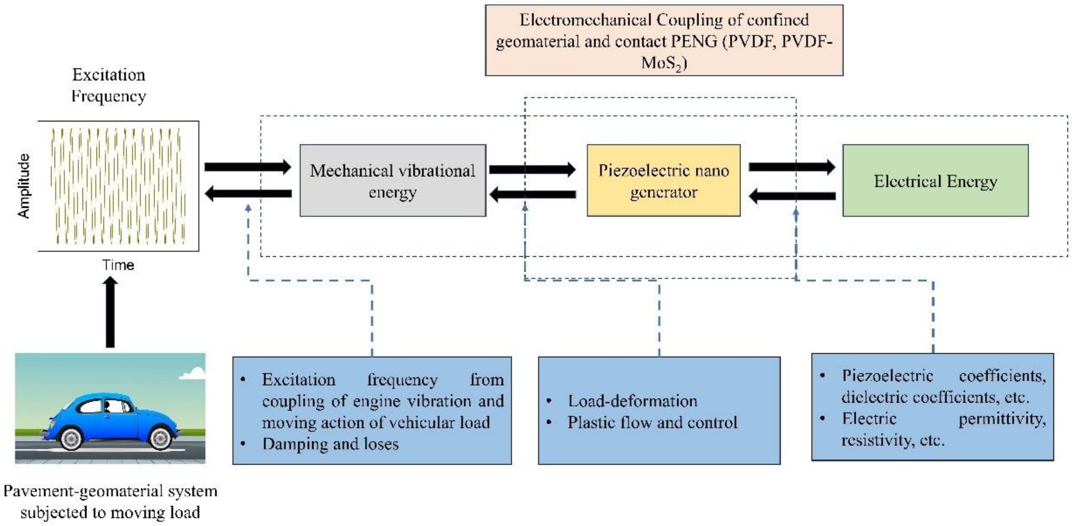

Figure 6.1 Flow diagram for the conceptualization of electromechanical Coupling of confined geomaterial in pavement geomaterial system and contact PENG (PVDF, PVDF-MoS_2)

The hydrothermal method has been adopted to synthesize the bulk MoS_2, the drop-casting method was used to synthesize the PVDF patches of varied thicknesses and composite PVDF-MoS_2, and the experimental testing setup has been provided as a supplementary file. The testing on confined geomaterial has been idealised to a condition of paving geostructure. An artistic representation of the energy harvesting setup, as shown in Fig. 6.2, includes a digital storage oscilloscope, dynamic shaker, confined geomaterial, PVDF/MoS_2 nanogenerator, and power amplifier cum signal generator.

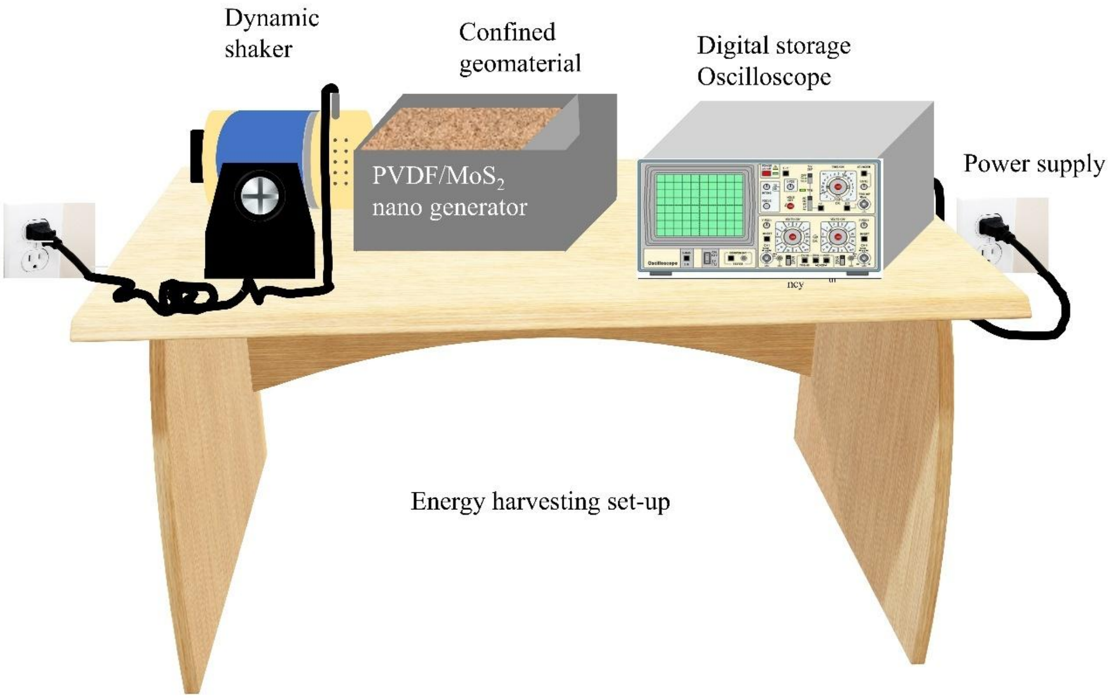

Figure 6.2 Artistic representation of the energy harvesting setup consisting of a digital storage oscilloscope, a dynamic shaker, confined geomaterial, a PVDF/MoS_2 nanogenerator, and a power amplifier cum signal generator

6.3 Results and Discussion

6.3.1 Characterization of the Bulk of Synthesized Molybdenum Disulphide and Piezoelectric Nanogenerator Patches

The synthesis of MoS_2 has been confirmed by the XRD analysis, as shown in Fig. 6.3 (a). The peaks at 13.79°, 32.26°, 35.65°, 43.09°, and 57.23° confirm the presence of (002), (100), (101), (103), and (110) planes of the synthesized hexagonal 2H-MoS_2. A total of two active peaks have been identified from Raman spectra (Fig. 6.3 (b)). The Raman E^1_{2g} mode at 376.19 cm^{-1} confirms the Mo-S atoms in a layered structure, and the 403.73 cm^{-1} Raman shift corresponds to the vibration of Sulphur atoms, confirming the presence of

A_{1g} mode. Hence, XRD and Raman spectra establish that bulk MoS_2 is successfully synthesised and maps well with the literature available (Chaudhary et al., 2018).

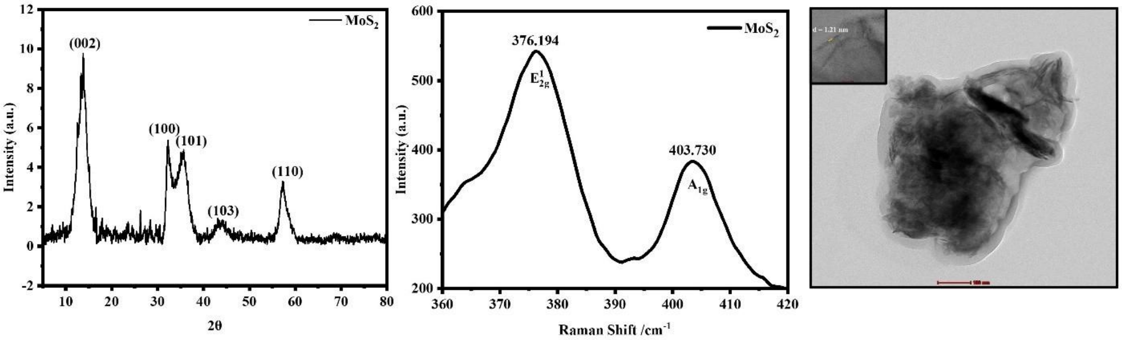

(a) (b) (c)

Figure 6.3 Characterisation of MoS_2 using (a) x-ray diffraction, (b) Raman spectrum, and (c) TEM

Transmission electron spectroscopy has been conducted to reveal the crystal morphology of MoS_2. It can be seen from Fig. 6.3 I that MoS_2 nanosheets have been synthesized. The inserted fringe pattern confirms a 1.21 nm lattice distance in the (002) plane of synthesized hexagonal MoS_2.

In PENGs, the XRD confirms the presence of non-polar (α) and polar (β) phases (Fig. 6.4 (a)). The 18.5° peak shows the non-polar (α) phase, and the 20.1° shows the polar (β) phase of PENGs. X-ray diffraction of the PVDF-MoS_2 composite patch shows increased electroactive β phase, whereas α-phase decreases with the doping of MoS_2. Figure 6.4 (b) shows the FTIR absorption spectra of the fabricated PENGs. The presence of the β-phase in PVDF enhances the piezoelectric capabilities of the PENGs; higher β-phase concentration results in a larger dipole moment. The FTIR absorption spectra reveal the presence of both α and β phases of the developed PENGs. The peaks representing the nonpolar α and polar β phases of the PENGs are shown in Figure 6.4(b).

Lambert-Beer law has been used to determine the β-phase as shown below:

$$F_\beta = \frac{A_\beta}{\left(K_\beta/K_\alpha\right) A_\alpha + A_\beta} \tag{6.1}$$

Here, F(β) denotes the β-phase content in the PENGs, $K_\beta = 7.7 \times 10^4$ cm^2/mol at 840 cm^{-1}, and $K_\alpha = 6.1 \times 10^4$ cm^2/mol at 760 cm^{-1}. Absorption at K_β and K_α is denoted by A_α and A_β respectively. The β-phase was 53.94 % for the PVDF patch and enhanced up to 60.78 % after the inclusion of MoS_2. Figure 6.4(c&d) shows the FE-SEM image of pristine PVDF and composite PVDF-MoS_2 patches. As illustrated, the spatial arrangement of MoS_2 nano-fillers within the polyvinylidene fluoride (PVDF) matrix exhibits a uniform distribution, potentially contributing to the enhanced electroactive β-phase observed in the composite PVDF-MoS_2 patches.

6.3.2 Voltage Response of Piezoelectric Nanogenerator Patches

Fig. 6.5 (a) and (b) show the voltage variation with time for varied thicknesses (0.02-0.10 mm) of the PENGs embedded in the geomaterial. The PENGs have been subjected to a 3-12 Hz input frequency with an interval of 3 Hz. A compounded variation in voltage output has been observed on the real-time scale of 10 seconds. The researchers have observed a cyclic, repeating voltage output when the PENGs are subjected to direct contact loading. Randomness in the output of voltage results is observed in the present research; this may be due to the fact that the PENGs are embedded in geomaterial, and there is a rebound effect causing the damping in the voltage. This rebound of forces in the geomaterial is developing a cushioning to the contact surface of PENGs. Moreover, this damping produces a constructive and destructive interference of the voltage output.

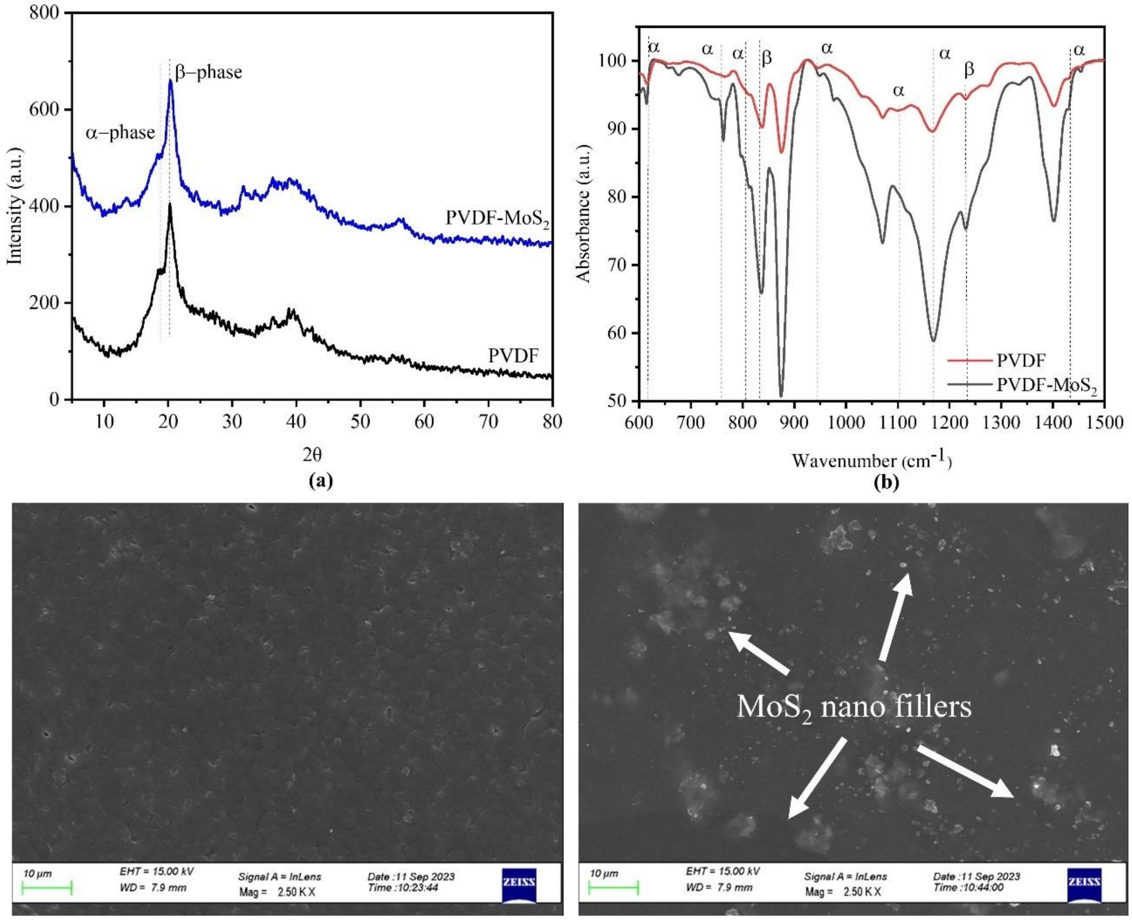

(a) (b)

(c) (d)

Figure 6.4 (a) X-ray diffraction and (b) FTIR spectra of PVDF and PVDF-MoS$_2$ patches, and FE-SEM images of (c) PVDF and (d) PVDF-MoS$_2$ patches

To understand this effect, the peak voltage of the PENGs and their corresponding voltage magnification factors (V_{mf}) have been recorded. The voltage related to the PVDF patch with a thickness of 0.02 mm has been selected as the reference value. Corresponding to this offset value, the magnification in the magnitude of voltage is calculated with a rise in the thickness of the PVDF patch. Mathematically, the V_{mf} can be expressed as:

$$V_{mf} = \frac{V_{(t=\sum_{i=0.02}^{0.10} t_i)}}{V_{t_c}} \tag{6.2}$$

where $V_{(t=\sum_{i=0.02}^{0.10} t_i)}$ is the maximum output voltage obtained from the varied thickness of the PVDF and PVDF-MoS$_2$ composite patch and V_{t_c} is the base value of voltage, i.e., the voltage output of a 0.02 mm PVDF patch.

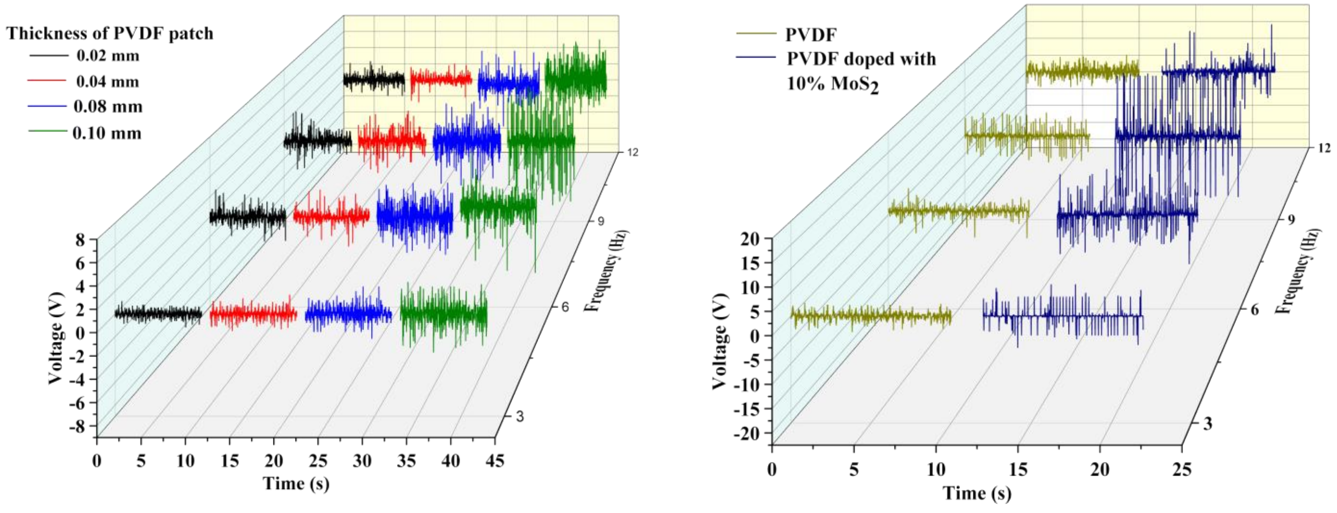

(a) (b)

Figure 6.5 Experimental observations of variation in voltage for a thickness of (a) 0.02 – 0.10 mm PVDF patches and (b) 3-10 % MoS$_2$ in PVDF patch subjected to 3-12 Hz frequency

Figures 6.6 (a) and (b) show the experimentally observed peak values of voltage and their corresponding magnifications with an input frequency of 3-12 Hz. The peak voltage ranges from 1.24 to 7.2 V and 11 to 16.5 V for the pristine PVDF and PVDF-MoS$_2$ composite patches, respectively. The maximum voltage has been achieved for a 10%

concentration of MoS_2 in the PVDF-MoS_2 patch. A threshold input of 9 Hz frequency has been identified, whichh gives rise to a maximum voltage of 16.50 V. An exponential rise in voltage ranging from 9% to 119% has been observed when the thickness of the PVDF patch is increased. A 396% amplification in voltage has been reported for the PVDF-MoS_2 composite patch (Fig. 6.6 (b)). This indicates that increasing the thickness and doping of MoS_2 increases the output voltage in the PENGs.

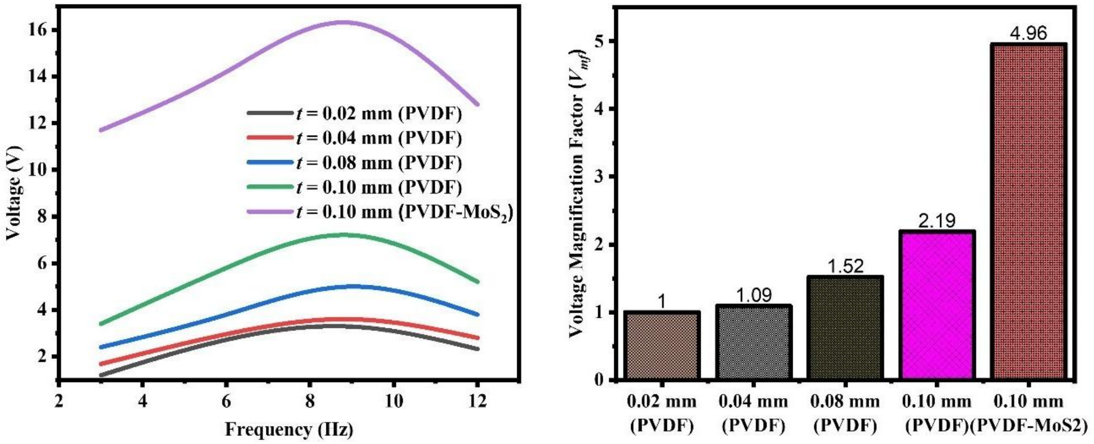

(a) (b)

Figure 6.6 Departure of (a) voltage with frequency and (b) voltage magnification factor for the selected set of PVDF and PVDF-MoS_2 patches

Table 6.1 shows the engineering application, PENG patch thickness, voltage output, synthesis technique, and environmental implications of the PENGs. It has been observed that PENGs considered in this research generate a maximum voltage of 16.2 V, which is notably higher than the voltage generated by the PENGs created with toxic lead (Pb) and reduced graphene oxide (rGO). Therefore, this work introduces a novel approach to developing an eco-friendly piezoelectric nanogenerator in geostructures for the purpose of energy generation and sensor applications.

Table 6.1 Assessment of synthesis technique, engineering application, voltage output, and environmental implications of the synthesized PENGs and piezoelectric generators reported in the literature

PENG	Synthesis technique	Engineering application	Output voltage (V)	Environmental implications
PZT [a]	Commercially procured	Confined geostructures (indirect loading conditions)	0.56	Toxic (Pb) [e]
PVDF* (0.02-0.10 mm thick)	Dropcasting	Pavements/ confined geostructures	3.10-7.20	Non-toxic
PVDF/ SrGO [b]	Dropcasting	Prismatic member	01.91	Non-toxic
PVDF/ ZCNT [c]	Electrospinning	Finger-tapping prismatic member	15.50	Non-toxic
PVDF/ ZnS [d]	Electrospinning	Finger-tapping prismatic member	15.00	Non-toxic
PVDF/ MoS_2* (10% MoS_2)	Dropcasting	Pavements/ confined geostructures	16.20	Non-toxic

[a] Kumari and Trivedi (2022a); [b] Aanand et al. (2020); [c] Khalifa et al. (2022); [d] Ali et al. (2024); [e] Iyer et al. (2015); *Present Work

As shown in Table 6.2, the present work demonstrates appropriateness for energy harvesting by showing a significant voltage output range (3–16 V) using a PVDF and PVDF/MoS_2 composite under realistic mechanical excitation via a dynamic shaker. The power range has been arbitrarily calculated for a voltage output of 16.20 V across resistances ranging from 10 Ω to 50 Ω, increasing by 10 Ω each step ($P=V^2/R$). The power calculated is comparable to or exceeds several previously reported PENG systems, indicating its potential for practical energy harvesting applications. Furthermore, the calculated outputs are based on a reasonable voltage (16.20 V) and resistance range (10–50 Ω), aligning with real-world load conditions. These results suggest that the material system and setup used in this study can effectively convert mechanical energy into usable electrical energy, supporting its use in energy harvesting.

Table 6.2 Comparison of operating conditions, voltage, resistance, and power output for various piezoelectric nanogenerators (PENGs)

PENG type	Loading agency	Voltage (V)	Resistance (Ω)	Power (mW)
PZT*	Wind	02.00-335.00	02.00-50.00	0.14-22.00
PZT*	Water	2.80-65.00	30.00-495.00	0.01-5.50
PZT*	High-speed rotation	8.00-88.81	1.80-240.00	3.10-78.87
PZT*	Frequency up-conversion mechanism	5.00-7.50	14.00	0.13-521.00
PVDF and PVDF-MoS_2**	Dynamic shaker	3.10-16.20	10.00-50.00	5.25-26.24

* Xiao et al. (2025); ** Present work (power has been arbitrarily calculated for a voltage output of 16.20 V across resistances ranging from 10 Ω to 50 Ω, increasing by 10 Ω each step, we can use the formula for electrical power: $P=V^2/R$)

6.4 Conclusions

Based on the results and discussion presented earlier, the following conclusions can be drawn:

- The inclusion of the bulk molybdenum disulphide (MoS_2) nanoflakes into the PVDF matrix significantly increases the electroactive β-phase content from 54.26% in pristine PVDF to approximately 76% in PVDF-MoS_2. This results in four times the increase in output voltage, achieving up to 16.2 V.
- The piezoelectric performance has increased with PVDF patch thickness. Among all selected sets of PVDF patches, the 0.10 mm PVDF patch delivered the highest voltage output (7.2 V) in pristine form.

- A 10% concentration of MoS_2 in the PVDF matrix demonstrated the optimal piezoelectric performance, with an increase of 396% compared to the thinnest PVDF patch.
- The PVDF and PVDF-MoS_2 patches outperformed conventional piezoelectric materials such as lead-based (PZT) and reduced graphene oxide (rGO) based generators, both in terms of output voltage and environmental impact, affirming their potential for safer and more effective applications in dynamic geostructure environments.

This study presents a specific and comprehensive evaluation of each contributing factor. The findings underscore the viability of PVDF-MoS_2 composites as efficient, flexible, and environmentally friendly piezoelectric materials for energy harvesting and sensing in confined geostructures. This is because the dynamic loads on geostructures are often used in energy generation using thin patches containing PZTs and rGOs. The patches are proven to be toxic to human health. Therefore, the current research has established a future avenue for investigating non-toxic PVDF as an alternative to toxic Pb and rGO-based nanogenerators in geo-structure sensing technologies and renewable energy.

References

[1] Ali, N., Faid, A. H., & Gad, S. (2024). Improving energy harvesting through femtosecond laser surface modification of PVDF/ZnS composite nanofibrous nanogenerators for electronic applications. Materials Chemistry and Physics, 327, 129916. https://doi.org/10.1016/j.matchemphys.2024.129916

[2] Anand, A., Meena, D., Dey, K. K., & Bhatnagar, M. C. (2020). Enhanced piezoelectricity properties of reduced graphene oxide (rGO) loaded polyvinylidene fluoride (PVDF) nanocomposite films for nanogenerator application. Journal of Polymer Research, 27, 1-11. https://doi.org/10.1007/s10965-020-02323-x

[3] Anton, S. R., & Sodano, H. A. (2007). A review of power harvesting using piezoelectric materials (2003–2006). Smart Materials and Structures, 16(3), R1. https://doi.org/10.1088/0964-1726/16/3/R01

[4] Dunn, P. E., & Carr, S. H. (1989). A historical perspective on the occurrence of piezoelectricity in materials. MRS Bulletin, 14(2), 22-31. https://doi.org/10.1557/S0883769400063405

[5] Fukada, E. (2000). History and recent progress in piezoelectric polymers. IEEE Transactions on Ultrasonics, Ferroelectrics, and Frequency Control, 47(6), 1277-1290. https://doi.org/10.1109/58.883516

[6] Gandhi, M. V., & Thompson, B. D. (1992). Smart materials and structures. Chapman & Hall, Springer Science & Business Media.

[7] Gheibi, A., Bagherzadeh, R., Merati, A. A., & Latifi, M. (2014). Electrical power generation from piezoelectric electrospun nanofibers membranes: Electrospinning parameters optimisation and effect of membranes thickness on output electrical voltage. Journal of Polymer Research, 21, 1-14. https://doi.org/10.1007/s10965-014-0571-8

[8] Guan, X., Zhang, Y., Li, H., & Ou, J. (2013). PZT/PVDF composites doped with carbon nanotubes. Sensors and Actuators A: Physical, 194, 228-231. https://doi.org/10.1016/j.sna.2013.02.005

[9] Kepler, R. G., & Anderson, R. A. (1978). Piezoelectricity and pyroelectricity in polyvinylidene fluoride. Journal of Applied Physics, 49(8), 4490-4494. https://doi.org/10.1063/1.325454

[10] Kumari, N., & Trivedi, A. (2022a). Factors influencing piezoelectric response of horizontally and vertically embedded PZT patch in confined granular fills. Advances in Materials Science and Engineering, 2022, 7860273. https://doi.org/10.1155/2022/7860273

[11] Kumari, N., & Trivedi, A. (2022b). A review on modelling and techniques used for piezoelectric power generation from vibration of geo-structures. e-Prime-Advances in Electrical Engineering, Electronics and Energy, 2, 100076. https://doi.org/10.1016/j.prime.2022.100076

[12] Pan, H., Na, B., Lv, R., Li, C., Zhu, J., & Yu, Z. (2012). Polar phase formation in poly(vinylidene fluoride) induced by melt annealing. Journal of Polymer Science Part B: Polymer Physics, 50(20), 1433-1437. https://doi.org/10.1002/polb.23146

[13] Peng, Y., Que, M., Tao, J., Wang, X., Lu, J., Hu, G., et al. (2018). Progress in piezotronic and piezo-phototronic effect of 2D materials. 2D Materials, 5(4), 042003. https://doi.org/10.1088/2053-1583/aadabb

[14] Petroff, C. A., Bina, T. F., & Hutchison, G. R. (2019). Highly tunable molecularly doped flexible poly(dimethylsiloxane) foam piezoelectric energy harvesters. ACS Applied Energy Materials, 2(9), 6484-6489. https://doi.org/10.1021/acsaem.9b01061

[15] Rhimi, M., & Lajnef, N. (2012). Tunable energy harvesting from ambient vibrations in civil structures. Journal of Energy Engineering, 138(4), 185-193. https://doi.org/10.1061/(ASCE)EY.1943-7897.0000077

[16] Roshani, H., Dessouky, S. (2015). Feasibility study to harvest electric power from highway pavements using laboratory investigation. Department of Civil and Environmental Engineering, University of Texas at San Antonio.

[17] Roshani, H., Dessouky, S., Montoya, A., & Papagiannakis, A. T. (2016). Energy harvesting from asphalt pavement roadways vehicle-induced stresses: A feasibility study. Applied Energy, 182, 210-218. https://doi.org/10.1016/j.apenergy.2016.08.116

[18] Roshani, H., Jagtap, P., Dessouky, S., Montoya, A., & Papagiannakis, A. T. (2018). Theoretical and experimental evaluation of two roadway piezoelectric-based energy harvesting prototypes. Journal of Materials in Civil Engineering, 30(2), 04017264. https://doi.org/10.1061/(ASCE)MT.1943-5533.0002112

[19] Singh, A., Singh, J., Sinha, M. K., & Kumar, R. (2023). Ferrous-metal matrix composites: A review on status, scope and challenges. International Journal of Interactive Design and Manufacturing, 17(6), 2807-2829. https://doi.org/10.1007/s12008-023-01517-z

[20] Tasaka, S., Niki, J., Ojio, T., & Miyata, S. (1984). Structure and piezoelectricity of polyvinylidene fluoride films obtained by solid-state extrusion. Polymer Journal, 16(1), 41-48.

[21] Vinogradov, A., & Holloway, F. (1999). Electromechanical properties of the piezoelectric polymer PVDF. Ferroelectrics, 226(1), 169-181. https://doi.org/10.1080/00150199908230298

[22] Wu, W., Wang, L., Li, Y., Zhang, F., Lin, L., Niu, S., et al. (2014). Piezoelectricity of single-atomic-layer MoS_2 for energy conversion and piezotronics. Nature, 514(7523), 470-474. https://doi.org/10.1038/nature13792

[23] Xiao, Y., Han, Q., & Wu, N. (2025). Piezoelectric energy harvesting: A review of energy sources, structures, and working mechanisms in high-frequency excitations and operations. Smart Materials and Structures, 34, 023001. https://doi.org/10.1088/1361-665X/adadcc

[24] Yu, S., Rice, Q., Tabibi, B., Li, Q., & Seo, F. J. (2018). Piezoelectricity in WSe_2/MoS_2 heterostructure atomic layers. Nanoscale, 10(26), 12472-12479. https://doi.org/10.1039/C8NR04394A

7

Chapter

Conclusion, Future Scope, and Socio-Environmental Impact

7.1 Conclusions

This thesis has undertaken a comprehensive investigation into the dynamic behavior of pavement–soil systems under moving loads and the development of sustainable piezoelectric sensors for structural monitoring and energy harvesting. The research integrates theoretical modeling, numerical simulation, and experimental validation into a unified framework to bridge the gap between computational mechanics and smart material applications in transportation infrastructure. The major conclusions from Chapters 2–6 are as follows:

1. **Development of a Generalised Finite Element Framework**

   A finite element-based numerical framework was successfully developed to simulate the dynamic response of pavement–soil systems subjected to moving loads. A novel *Generalised Dissipation Mechanism (GDM)* was introduced, defined by three dissipation parameters (α, β, γ) and two empirical coefficients (η, ϑ), which collectively enhanced damping stability and noise reduction. The approach minimized numerical noise from 16% to nearly negligible levels as the damping ratio approached 0.03. Dynamic amplification analyses revealed up to a 70% increase in load and 46% in displacement compared to static loading, offering a more realistic prediction of field conditions. This model forms a dependable computational foundation for velocity-sensitive pavement design.

2. **Velocity-Induced Dynamic Response of Pavement–Soil Systems**

   A finite-element-based cyclic response model was developed to quantify the velocity-induced stress and displacement in rigid pavements. The study introduced the *Vibrational Compounded Stress Transfer Mechanism (V-CSTM)*, correlating vehicle velocity, pavement stiffness, and load intensity. Results showed low-, moderate-, and high-influence zones that define velocity thresholds for resonance and amplification. Rigid pavements exhibited cyclic strength between 0.01 to 0.2% of the characteristic strength, capable of withstanding approximately 10^{15}–10^{9} load cycles, confirming their resilience under repetitive high-velocity traffic conditions. These findings have practical significance for estimating pavement service life and optimizing layer configuration under high-speed conditions.

3. **Dynamic Load-Induced Flow Behavior and Damage Mechanism**

   A new plastic damage model was formulated to characterize post-elastic and flow-controlled damage behavior in geomaterials under dynamic excitation. The *Vibrational Mechanism of Stress Transfer (VMST)* was introduced to explain the nonlinear propagation of stress waves and energy dissipation during plastic deformation. Three mechanistic zones, namely, elastic, transition, and post-elastic, were identified, with equivalent plastic strains ranging from 10^{-16} to 10^{-3}% in the granular base and 10^{-16} to 10^{-4}% in the subgrade. The model demonstrated that higher vehicle velocities redistribute stresses, thereby reducing permanent deformation and improving resilience. This framework enhances understanding of failure progression in pavement–soil systems under cyclic loading.

4. **Experimental and Numerical Evaluation of PVDF Films:**

   Experimental investigations on PVDF films (0.02 to 0.10 mm thick) embedded in confined geomaterials subjected to vibrations at 3 to 12 Hz revealed clear relationships among stress, deflection, and output voltage. The 0.10 mm thick PVDF film generated a peak open-circuit voltage of 7.2 V, while stress magnification reached 411% and deflection amplification 203% with increasing frequency. Numerical modeling corroborated these results, predicting deflections of 0.001–0.01 mm and stresses of 0.9–12 kPa. The findings confirm that PVDF thickness and excitation frequency have a strong influence on voltage output, providing crucial insights for optimizing sensors in pavement applications.

5. **Development of PVDF–MoS_2 Nanocomposite Sensors:**

   Flexible PVDF and PVDF–MoS_2 nanocomposite films were synthesized using drop-casting and hydrothermal methods. Structural characterization (XRD, Raman) verified a significant increase in electroactive β-phase content (from

54% in pristine PVDF to 76% in PVDF–MoS_2). The hybrid composite generated a voltage of 16.2 V to nearly four times that of pure PVDF, demonstrating superior piezoelectric sensitivity and energy conversion efficiency. These eco-friendly, lead-free sensors not only outperform traditional PZT-based counterparts but also exhibit enhanced flexibility, stability, and environmental compatibility, marking a major step toward sustainable smart infrastructure technologies.

The integration of finite element modeling, damping-controlled dynamics, and nanocomposite sensing advances the state of knowledge in pavement dynamics. The research establishes a *multiscale electromechanical framework* that connects macroscopic structural responses with microscopic energy transduction mechanisms, offering predictive capability for both performance assessment and energy harvesting in transportation systems.

7.2 Future Scope

The findings of this study provide a robust foundation for several future research directions:

1. **Field Implementation and Calibration**

   The numerical and experimental models should be extended to full-scale field testing to validate response predictions and establish calibration constants for varying traffic and climatic conditions.

2. **Integration into Smart Infrastructure Systems:**

   Embedding piezo-sensors into pavements can facilitate real-time monitoring of structural responses, enabled by self-powered data acquisition.

7.3 Social and Environmental Impact

This research holds profound implications for sustainable infrastructure and societal advancement:

1. **Green and Sustainable Technology:**

   By replacing toxic lead-based ceramics with recyclable, flexible polymers, this work directly supports Sustainable Development Goals (SDG 9: Industry, Innovation, and Infrastructure; SDG 11: Sustainable Cities and Communities).

2. **Energy-Efficient Transportation Systems:**

   Piezoelectric energy harvesting from vehicular-induced vibrations can provide decentralized power for sensors, lighting, or communication systems, fostering energy self-sufficiency in transportation networks.

3. **Enhanced Public Safety and Maintenance:**

   Smart sensors embedded in pavements can detect early signs of fatigue, rutting, or settlement, allowing timely interventions that reduce accident risk and maintenance costs.

4. **Economic and Environmental Savings:**

   The combined use of predictive modeling and self-powered sensing can extend pavement life, lower maintenance frequency, and reduce lifecycle carbon emissions.

5. **Educational and Technological Advancement:**

   The interdisciplinary integration of civil engineering, materials science, and electronics provides a replicable framework for academic and industrial innovation, training future engineers in the design of sustainable, smart infrastructure.

In addition, this thesis contributes a unified understanding of dynamic pavement–soil interaction and piezoelectric sensing through theoretical, numerical, and experimental lenses. The developed models and materials bridge gaps between simulation and real-world performance, offering pathways toward *self-sensing, self-powered, and sustainable transportation infrastructure* that aligns with the global vision of smart and resilient infrastructure.